Structural analysis of low speed, high torque electrical generators for direct drive renewable energy converters

Alasdair Stewart McDonald

Doctor of Philosophy (PhD)

The University of Edinburgh

2008

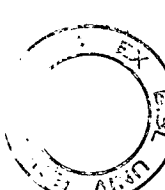

Abstract

This thesis focuses on electrical generators 'directly driven' by the mechanical output of renewable energy converters such as wind turbines. Renewable energy and the different ways of converting it into electricity are reviewed.

Direct drive renewable energy converters provide a low speed, high torque input to the electrical generator. As a result these generators must be larger than their high speed counterparts. Because of this size and the large airgap-closing force, the structural design must be stiff and robust. This typically results in heavy generators, with structural ('inactive') material dominating the electromagnetically 'active' material.

Design tools are set out, validated and used to model the inactive material in high torque axial-flux and radial-flux type machines. Simple optimisations on generator aspect ratios are carried out to find lighter designs. Axial-flux and radial-flux permanent magnet synchronous machines for wind turbines are compared in terms of mass and a cost criterion, with and without the inactive mass.

Some machines are designed in such a way that the normal force is nonexistent or significantly smaller than in conventional electrical generators. The design and modelling of a special air-cored permanent magnet machine is described. Discussions and conclusions highlight impacts on direct drive design philosophy.

Declaration

I hereby declare that this thesis has been composed by myself, that the work is my own and that the work has not been submitted for any other degree or professional qualification.

Alasdair McDonald, February 2008

Acknowledgements

I would like to thank my principal supervisor, Markus Mueller who gave me the opportunity, support and freedom to carry out the research contained within this thesis. Without his moral and technical contributions, this thesis would not have been possible.

I am grateful to my second supervisor, Ewen Macpherson for his support and excellent proof-reading.

My gratitude goes to friends and colleagues (which I must point out are not two mutually exclusive groups) at the Institute for Energy Systems at the University of Edinburgh, for help and diversion. Tom Davey, Brian Sellar and Paul Stott are due particular thanks.

During my research I was helped by a Royal Academy of Engineering Research Student Development Fellowship. This helped me attend several conferences and carry out work at TU Delft. I thank them for this financial assistance. I also thank Henk Polinder for hosting me during my time in the Netherlands.

On a more personal note, I would like to thank my family for encouraging me to embark on this journey; and also for not asking too often how long it would take me to arrive.

Finally, but most importantly, I would like to thank my wife Amy, who supported me throughout my time working on and writing this thesis. Her patience and love has meant that engineering stress and strain is the only type that I have ever had to worry about.

Table of Contents

List of Figures

List of Tables

Nomenclature

Roman letters

a_r	rotor disc outer radius, m
a_s	stator disc outer radius, m
$a_{i,j,...}$	polynomial function coefficient
A	electrical loading at inner stator radius, A/m
A_g	airgap area, m^2
b_r	rotor shaft radius, m
b_s	stator disc inner radius, m
B_g	airgap flux density, T
B_r	remanent flux density, T
c	airgap clearance, m
c	scale factor
c_p	coefficient of performance
c_{str}	cost of a reference structure, €
C	cost criterion, €
C_{active}	cost of active material, €
$C_{inactive}$	cost of inactive material, €
C_{kWh}	price of energy, €
C_n	circular plate constants (a, b)
C_{str}	cost of generator structure, €
d	arm thickness, m
d_g	airgap diameter, m
d_{ref}	diameter of a reference structure, m
d_{se}	generator diameter, m
D	plate constant, Nm
e	eccentricity, m
E	Young's modulus, Pa
E_d	annual energy loss, kWh

f	radial force per unit length, N/m
F_n	cylindrical shell functions
F_{bmp}	balanced magnetic pull, N
F_d	air gap force, N
F_{ump}	unbalanced magnetic pull, N
g	acceleration due to gravity, 9.81 m/s^2
g	magnetically effective airgap width, m
h_m	magnet height, m
h_{sa}	support arm height, m
h_{yr}	rotor back thickness, m
h_{ys}	stator back thickness, m
H	resultant thrust, N
H_0	midspan tangential thrust, N
i	gearbox transmission ratio
I	current, A
I	second moment of area, m^4
J	current density, A/mm^2
k	radius of gyration, m
k	shape factor
k_{mag}	ratio of magnet width to pole pitch
k_r	ratio of inner radius of rotor permanent magnets to rotor disc outer radius
K_n	cylindrical shell constants
K_{rad}	ratio of axial length to airgap diameter
l	axial length of machine, m
l_m	magnet length, m
l_{ref}	length of a reference structure, m
l_s	stack (axial) length of machine, m
l_{sa}	support arm length, m
l_{shaft}	rotor shaft length, m
l_{tot}	generator length, m

L_n	circular plate loading constants (a, r_o)
m_{act}	active mass, kg
m_b	mass of support beams, kg
m_c	mass of cylindrical shell casing, kg
m_{in}	inactive mass, kg
m_r	mass of rotor disc, kg
m_s	mass of stator disc, kg
$m_{str,st}$	mass of stator structure, kg
m_{tot}	total mass, kg
M	resultant moment, Nm
M_A	reaction end moment of beam at A, Nm
M_{ra}	unit radial bending moment at outer radius (force-length per unit of circumferential length), N
M_{rb}	unit radial bending moment at shaft, N
M_0	moment applied at midpoint of each beam, Nm
n	number of stages
n_b	number of beams
n_{disc}	number of rotor discs
N	number of turns
N	rotational speed, rpm
p_r	circumferential stress, Pa
p_θ	radial stress, Pa
P	period of comparison, years
P	power rating, W
q	normal component of Maxwell stress, Pa
Q_b	unit shear force at shaft (force per unit of circumferential length), N/m
r_s	stator radius, m
r_0	inner radius of rotor permanent magnets and iron cores, m
R	resistance, Ω
R	airgap radius, m
R	circular beam radius, m

R_A	vertical end reaction at A, N
R_{ring}	support arm ring outer radius, m
R_{rot}	rotor outer radius, m
R_{shaft}	rotor shaft rotor, m
S	reluctance, At/Wb
S	sum of squared errors, m^2
t	plate thickness, m
t	cylinder thickness, m
t_c	cylinder casing thickness, m
t_d	disc thickness, m
t_w	winding thickness, m
t_r	rotor disc thickness, m
t_s	stator disc thickness, m
t_{sa}	support arm thickness, m
T	point force, F
T	torque, Nm
u	deflection, m
u_{an}	analytical deflection, m
u_d	disc deflection, m
u_{FE}	finite element analysis deflection, m
U	strain energy, J
U_a	strain energy in the arm, J
U_B	strain energy due to bending of the rim, J
U_C	strain energy due to tangential compression of the rim, J
v_w	wind speed, m/s
V_r	rotor volume, m^3
w	uniformly distributed load, N/m
w_m	magnet width, m
W	uniform annular line load, N/m
x	distance along beam, m
x_n	n^{th} input parameter

y	radial deflection, m
y_a	deflection at a, the outer rotor radius, m
y_A	deflection at A, m
y_b	deflection at b, the inner stator radius, m
y_{b1}	deflection at b, due to stator disc bending, m
y_{b2}	deflection at b, due to beam bending, m

Greek letters

α	distance from beam end of moment application, m
ε	mechanical strain
θ	angular displacement, radians
θ	half angle between adjacent arms, radians
λ	cylindrical shell parameter, m^{-1}
λ	tip speed ratio
μ_0	permeability of free space, $4\pi \times 10^{-7}$ Wb/Am
μ_r	relative permeability
ν	Poisson's ratio
ρ	density, kg/m^3
σ	airgap shear stress, Pa
φ	tilt angle, radians
Φ	flux, Wb
ψ	meridional slope, radians
ψ_A	meridional slope at A, radians
ω	rotational speed, radian/s

Abbreviations

AC	alternating current
AFPM	axial-flux permanent magnet machine
CAD	Computer Aided Design
DC	direct current
DFIG	doubly fed induction generator

FEA	Finite Element Analysis
IEA	International Energy Agency
OECD	Organisation for Economic Co-operation and Development
RMS	root mean square
rpm	revolutions per minute
PM	permanent magnet
SRF	Scottish Renewables Forum
udl	Uniformly distributed load
WEC	Wave energy converter

Chapter 1

Introduction

1.1 Introduction

THERE is a pressing need for renewable energy: to reduce carbon dioxide (and other) emissions, to exploit native energy resources, to avoid long term storage of hazardous wastes and to reduce the consumption of finite fossil fuel resources [36]. The UK government is aiming for a varied portfolio of different energy types, of which renewable energy will make up a significant proportion.

Wind and wave resources tend to be greatest offshore and so large scale renewable energy developments will increasingly be placed further away from land. Lifting operations offshore cost in the orders of £10k-100k a day, so lightweight generator design - which can be lifted with smaller, cheaper vessels - along with maintenance and robustness of design will become more and more important. Maintaining and replacing gearboxes (or other intermediate power take off equipment) offshore is costly, so direct drive systems - where the electrical generator is directly coupled to the slow moving prime mover and where there are the least possible mechanical moving parts and no electrical slip rings or brushes - are attractive. The problems with wind turbine gearboxes can be readily seen at Scroby Sands, one of the UK's first offshore wind farms. Between January and December 2005, 27 intermediate speed and 12 high speed gearbox bearings of the Vestas V-80 wind turbines had to be replaced [35]. In 2003 Vestas took over NEG Micon - another large wind turbine manufacturing company - after the latter had to replace and refurbish 1250 wind turbine gearboxes [85].

Figure 1.1. Vestas V-80 at Scroby Sands

These are some wind turbine design considerations taken from another manufacturer's website [57]:

- Low-maintenance requirements
- Easy access to key components, particularly in extreme weather conditions
- Excellent power quality characteristics
- Erection with a relatively light, inexpensive crane

The company in question – Harakosan – decided that direct drive machines are better placed to meet most of these requirements than the most popular current gearbox/induction machine systems. However, most direct drive designs and machines have been heavy so far [44].

A typical approach to reducing the weight of direct drive designs is to compare competing machine types based on optimised torque density (torque per unit mass). The problem with these comparisons is that they are

normally based only on electromagnetically active mass (such as the copper in the windings, the iron in the rotor and stator and the permanent magnets). However inactive material makes up the majority of mass in these (low speed, high torque) direct drive machines. Hartkopf *et al.* note that for radial-flux machines about two thirds of the mass is made up of supporting structure [59].

1.2 Thesis statement

"If there is to be a fair comparison to find the best topology for direct drive generators and if each topology is to be optimised for minimum mass and cost, then the inactive mass must be included."

1.3 Aims of thesis

The main aim of this thesis is to advance the understanding of low speed, high torque/force electrical machines for direct drive renewable energy converters, with particular reference to structural aspects of these machines. Objectives include:

- To produce design tools which can be used early on in the design process to quickly model forces and machine structures
- To demonstrate the importance of structural design in low speed, high torque permanent magnet machines
- To optimise both the active and inactive (structural) parts of these machines with a view to reduce mass
- To compare different machine topologies when inactive material is included in the analysis
- To explore the structural and mechanical aspects of an unconventional permanent magnet machine topology

1.4 Layout of thesis

The next chapter will introduce the reader to renewable energy and renewable energy converters, review power take off and electrical machines and include a review of the literature in these fields.

Chapter 3 introduces design tools for modelling the inactive part of axial-flux permanent magnet synchronous machines. These will be used to carry out some simple optimisations of the active and inactive mass of slotless TORUS machines.

In chapter 4, mechanical finite element analysis is used to predict deflections in simple structures of radial-flux permanent magnet machines. These results are then modelled with a polynomial method, so that the inactive mass can be quickly estimated for design purposes.

Instead of using finite element techniques for radial-flux in chapter 4, the work in chapter 5 returns to the use of analytic expressions to model the inactive part of radial-flux machines.

Chapter 6 lays out some modifications and improvements to the structural modelling in chapters 3, 4 and 5. This includes accounting for secondary deflection and relating the simple structural models to commercial designs. Also in chapter 6, axial-flux and radial-flux PM machines for wind turbines will be compared in terms of mass and a cost criterion with and without the inactive mass.

Some machines are designed in such a way that the normal force is nonexistent. In Chapter 7, other mechanical design considerations will be examined for such an 'air-cored' machine.

Chapter 8 will further discuss the work in this thesis, draw some conclusions and highlight impacts on design philosophy.

Chapter 2

Literature review

CONVENTIONAL electrical generation has been provided in the past by large synchronous generators in thermal (coal, oil, gas or nuclear) power stations located centrally on a national or international electrical grid. These generating units produce electrical power at specified voltage and frequency - they are 'synchronised'. Synchronous machines in these power plants are normally run at 1500rpm (2-pole pair machines on a 50Hz grid), that is a constant, high speed.

The introduction of renewable energy brings with it two challenges. Generation is decentralised and spread out (where the wind, tide, wave and other resources are to be found) and the input power is variable. Integration of renewable energy must not produce any discernible difference (in terms of voltage and frequency) to the electricity delivered to the consumer. This means that renewable generation must make use of different electrical machines and power converter topologies.

This chapter also describes the efforts - present and future - to produce lightweight direct drive electrical generators for wind, wave and tidal energy converters. Because low mass is one of the fundamental aims of this work, the research must plant a foot firmly in both electrical and mechanical engineering disciplines. At the same time, the specified applications are quickly developing in a context where there is much debate about energy and renewable energy in particular. A wide range of literature has been produced, some of which is detailed below.

2.1 Renewable energy

Boyle *et al.* define renewable energy sources as those that are "continuously replenished by natural processes... [they are] essentially *flows* of energy". Fossil and nuclear fuels in contrast are finite "*stocks* of energy" [11]. On its website, the UK Department for Trade and Industry describes it as "energy flows that occur naturally and continuously in the environment, such as energy from the wind, waves or tides. The origin of the majority of these sources can be traced back to either the sun (energy from the sun helps to drive the earth's weather patterns) or the gravitational effects of the sun and the moon. This means that these sources are essentially inexhaustible" [37]. Renewable energy sources include: hydroelectricity, solar thermal and photovoltaics, wind, wave, tidal, geothermal, and combustible fuels including wood, biomass and biogas.

According to the International Energy Agency, Renewable Energy accounted for 17.9% of the world's Electricity Production and 13.1% of the world's Total Primary Energy Supply in 2004 (see Fig. 2.1) [61]. The Renewable Electricity is dominated by hydroelectric generation, but the Primary Energy Supply is dominated by combustible renewables and renewable waste. Between 1971 and 2004, the annual growth in all renewables (2.3%) slightly outpaced that of the global Total Primary Energy Supply. 'New' renewables (classed by the IEA as solar, wind, ocean and geothermal) had a combined annual growth of 8.2% (with wind and solar growing annually by 48.1% and 28.1% respectively). Two-thirds of these 'new' renewable sources are located in OECD nations.

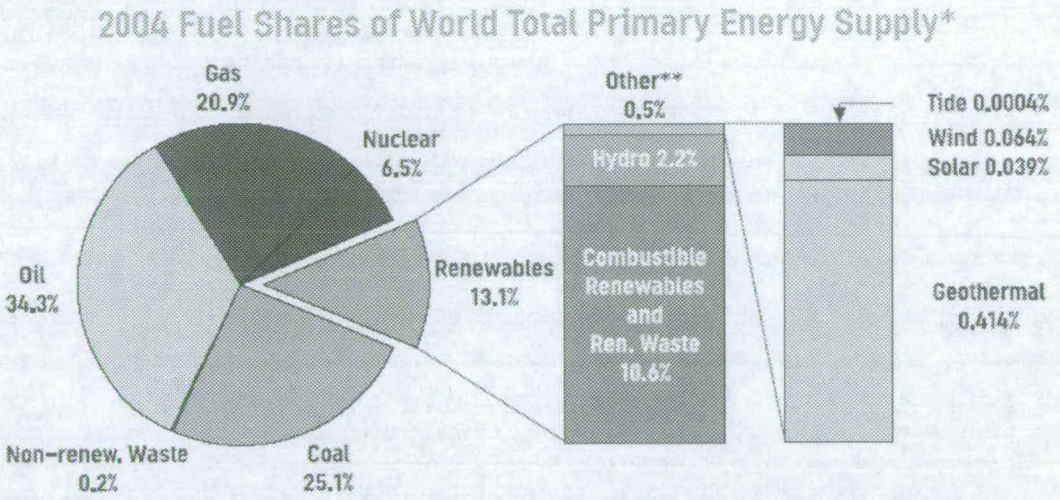

Figure 2.1. 2004 Fuel share of world's total primary energy supply [61]

The UK government signed the Kyoto Protocol in 1997 and committed itself to a 12.5% reduction in greenhouse gas emissions in the period 2008-12 and it seeks to reduce emissions further to 20% below 1990 levels by 2010 [37]. In the 2003 Energy White Paper the government pledged to cut CO_2 in the UK by 60% by 2050 [36]. To help achieve these aims, the government set a target of 10% renewable electricity production by 2010 along with an aspiration of 20% by 2020. In March 2003, the Scottish Executive aspired to the target of producing 40% of Scotland's electricity from renewable sources by 2020 [106].

Of the renewable energy types outlined above, it is wind, wave and tidal energy sources (and the energy converters that harness them) that interest the designer of new electrical machines. Hydroelectric schemes, solar thermal, geothermal and combustion plant can employ traditional synchronous machines; solar photovoltaic panels do not require electrical machines. In contrast, wind and ocean energy sources are movements of fluid (air, water) normally at low speed (in comparison to the normal speeds that are typically used in conventional electrical machines). Some thought has to be put into the 'power take off', the apparatus or method used to convert the kinetic energy of these fluid movements into electricity. The

remainder of this section will dwell on these three renewable energy sources and some of the energy converters that have been designed to harness them. The next section will look at power take off strategies in greater detail.

2.1.1 Wind energy

The winds above the surface of the Earth are caused by differences in the amount of heat that is absorbed by the Earth in different regions. At the equator (which is nearer to the Sun) the mean temperature is higher than at the poles. Warm air rises in the atmosphere over hot land masses and sinks back to the Earth's surface in colder areas. Different local terrain influences these air movements to produce what we call 'wind'.

The global wind industry has an estimated annual turnover of £5.5 billion, 84% of which is based in Europe [47]. According to SRF (the Scottish Renewables Forum) wind energy is the second most popular renewable energy (after hydroelectricity) in Scotland in 2006 [108]. The Sustainable Development Commission noted that "onshore wind power is already one of the cheapest forms of renewable energy per kWh" in their *Wind Power in the UK* report. They then went on to state "current predictions are that electricity supply companies will meet their Renewable Obligation to 2010 from wind power". An addition of 9.5 GW (at a 30% capacity factor) of new wind turbines to existing renewable plant would provide 10% of the UK's electricity supply [120]. In a more detailed examination (but for Scotland only) Boehme *et al.* found that 6 GW of onshore wind could, on average, make up 40% of Scotland's electricity supply in 2020 [107]. In an alternative scenario they found that 3 GW of offshore wind could provide 23% of Scotland's electricity supply by the same year. It is for this reason that the emphasis of the research in this thesis will be on electrical machines for wind turbines.

Although there are many different possible wind turbine designs, there has been a convergence on a design with three pitchable blades, placed upwind of the tower on a horizontal axis, such as the Vestas turbines shown in Fig. 1.1. In 2004 the average global installed wind turbine was 1.3 MW [42]. Fig. 2.2 shows how typical wind turbine designs have grown in the last 25 years [47]. In 2006 a European Union funded project called UpWind was launched to investigate future turbine designs up to 20 MW [123].

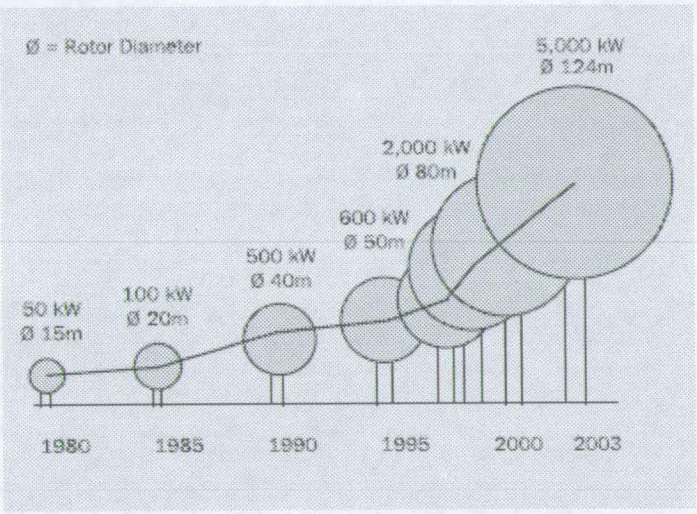

Figure 2.2. Growth in scale of commercial wind turbines [47]

2.1.2 Wave energy

The action of the wind on the sea surface produces waves: the initial tangential stress on the water surface causes waves to form and grow; then turbulence causes variations in shear stress and pressure fluctuations; as the waves grow further the wind can exert more and more force on the upwind side of the wave. The power of the waves (and their ability to destroy mighty cliffs and sweep away manmade structures) has captured the imagination of many inventors over the last few centuries, and hence there are a plethora of different designs to harness the waves. The reader is referred to [122] to explore some of these. Because of its location on the edge of the Atlantic Ocean, the UK and the West coast of Scotland in particular enjoys one of the most energetic wave climates in the world.

Boehme *et al.* predicted that 3 GW of electricity (20.4% of the overall Scottish electricity demand) could be generated from waves in Scotland in 2020 [107]. The wave energy industry is made up of lots of small companies all at the research, development and pre-commercial demonstration phases. In May 2005, a Portuguese consortium led by Enersis (a renewable electricity company) placed an order for three Pelamis wave energy converters, heralding the start of the first significant grid connected wave farm in the world [88].

2.1.3 Tidal energy

The movement of the earth and the moon produce the twice daily high and low tides. Between these times there are significant flows of sea water, particularly where there are natural constrictions (narrow straits, sea lochs and estuaries). Tidal mills (where a pool is topped up and closed off at high tide and then at low tide the head of water is used to drive a water mill) have been used for centuries. An extension of this simple principle is the tidal barrage at La Rance near St Malo in France (see Fig. 2.3). This scheme was built between 1961 and 1967 and includes a 740 m long barrage with 24 turbines, each rated at 10 MW. The tidal range is up to 12 m, with typical 5m head [11]. Because of the large civil engineering costs and environmental impact of large dam works, newer tidal energy developments are turning to 'tidal current' devices. Most of these designs are similar to a typical wind turbine design (horizontal axis with 3 blades), although open-centered ducted machines [87], oscillating hydroplanes [45] and vertical axis machines [96] have been tested.

In Scotland the potential for exploiting tidal energy is less than that of either wind or wave. Boehme *et al.* estimated that 750 MW of tidal-current plant could supply about 5% of Scotland's electricity demand. The advantage of tidal energy (over say wind or wave) is that the tidal flow is entirely

predictable and that the best sites concentrate the energy close to land masses.

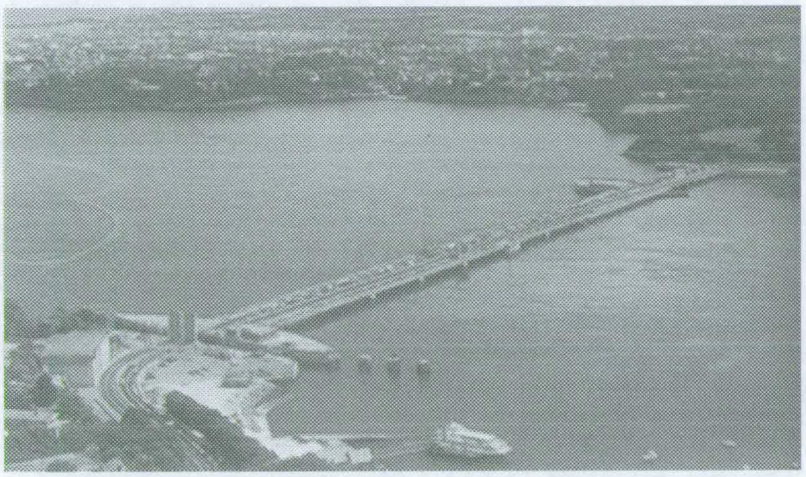

Figure 2.3. La Rance tidal barrage

2.2 Power take off

It is generally assumed in this thesis that these renewable energy devices will be used to produce electricity and not pump or desalinate water or produce liquid fuels. 'Power take off' describes the method of converting the kinetic energy of the primary displacing element into electricity.

The fluid movements in wind, waves and tides are slow (in the order of 10 m/s for wind, 2 m/s for tidal flows and 1 m/s for waves). Conventional electrical machines – such as synchronous and induction machines – run at high speeds. For example a 4 pole induction machine with a 1m airgap diameter (with 50 Hz) rotates at approximately 1500 rpm – in this case, a tangential speed of 79m/s. Either the designer can bridge this gap by using an intermediate step (through mechanical, hydraulic or pneumatic means) or else a novel electrical machine (designed to run at low speed) can be employed. This section outlines the most important power take off methods.

2.2.1 Mechanical

Gearboxes are widely used in wind turbines to step up speed from the slowly rotating rotor blades (≈30 rpm for a 1.5 MW turbine) to the high speed electric machine. At the same time, the torque is stepped down by the same ratio. About 85% of the wind turbines installed in the world in 2005 used multistage gearboxes [35]. Figure 2.4 shows a typical wind turbine with gear drivetrain.

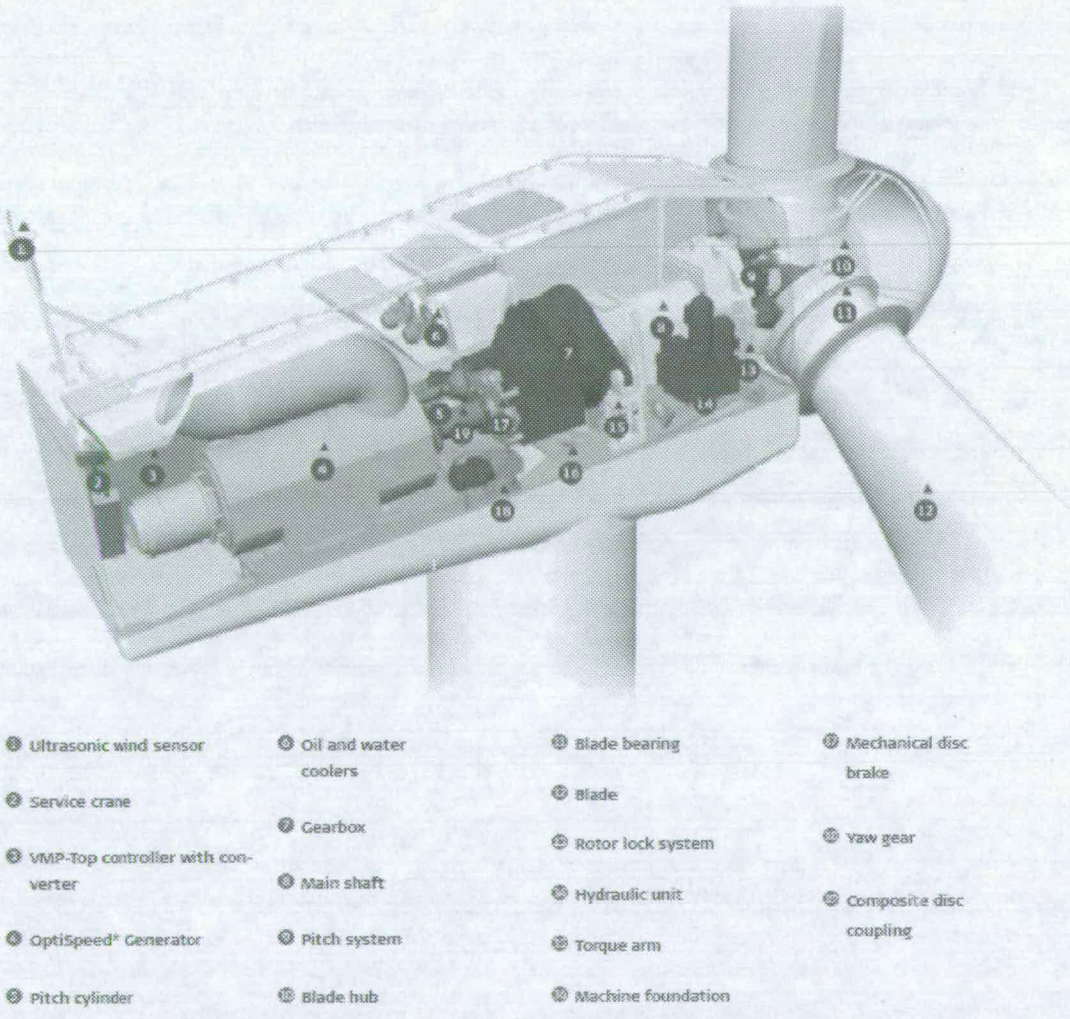

Figure 2.4. Typical wind turbine with drivetrain (Vestas V52) [127]

A number of different combinations of gear systems are used in modern wind turbines, including:

- 1 planetary step/ 2-step parallel axle gears (Vestas V52 – 850 kW)

- 2 planetary and 1 helical stage (Vestas V90 - 3 MW)
- 2 helical stages and a double helical spur gear stage (REPower 5 MW)
- 3 stage planetary helical design (Siemens SWT-3.6 MW-107)
- 3 stage planetary spur gear system (GE 2.X MW)
- 1 planetary stage / 2 helical stages (Gamesa G90 - 2.0 MW)

A smaller generator can be used when a gearbox is utilised (as the speed is stepped up, the torque is stepped down, and as the size of electrical machines is proportional to the torque developed smaller and cheaper electrical machines can be used). It is interesting to see how the mass of the gearbox dwarfs the mass of the induction generator in the REPower 5M wind turbine [97]: the gearbox is 63 tonnes whilst the 6 pole doubly-fed induction generator is only 17 tonnes.

The gearbox is widely acknowledged as a problem in the wind turbine industry - it has been a major cause of failures and has in the past led one manufacturer - NEG Micon, subsequently bought by the Vestas group - to carry out large scale gearbox replacement schemes, incurring multi-million pound costs [85].

Table 2.1 shows estimated gearbox replacement and repair costs for 650-900 kW class turbines [20]. These costs increase as turbines grow and are installed offshore. The WindPACT study - funded by the US Department of Energy through the National Renewable Energy Lab - also states that the predicted mean time between failures is 12-15 years for a well maintained gearbox. Gearboxes must be well lubricated, requiring an 8-12 month lubrication interval [8]. Some wind turbine manufacturers have opted for 'heavy duty' (large mass, expensive but robust) to avoid some of the costs of failures. With high fluctuations of rotor torque due to wind gusts, gearboxes must be designed for at least twice the rated torque [61].

	Costs (US$)	Comments
Developer X	~$50,000-$60,000 replacement ~$30,000 minimum repair	~$10,000 minimum to transport crane to site
Manufacturer R	$50,000-$70,000 replacement $10,000-$20,000 repair	
Manufacturer W	~$60,000	
Consultant U	$75,000 replacement	Additional $35,000 for crane

Table 2.1. Estimated gearbox costs for 650 to 900 kW onshore turbines [20]

Jöckel points out that with a constant blade tip speed (around 70m/s, speeds much higher lead to noisy operation which cannot be permitted onshore), as rotor diameters increase, rotational speed must decrease. This leads to more unfavourable (i.e. greater) transmission ratios [61]. Each gearbox stage is limited to i=5 or 6 [68], so that greater transmission ratios lead to more stages and thus reduced efficiency. Gear losses are 3-5% depending on the number of stages [61].

The operation and maintenance costs of gearboxes led the WindPACT team to choose a direct drive wind turbine design [20]. In a recent Renewable Energy World article, a wind turbine gearbox expert, Jan van Egmond (Managing Director of Quality in Wind), was asked about his experience of gearbox failures [35]. These included:

- Insufficient rigidity of the machine chassis, resulting in misalignment of gearbox and generator shafts leading to failure.

- Substantial knowledge gaps with regard to determination of real turbine design loads, combined with a structural demand for top head mass reduction and system compactness.
- Under-dimensioning of specific components leading to insufficient gearbox housing rigidity properties.
- Problems with lubrication and oil filtration.
- Excessive heating in gearbox hot spots (often the fast-speed output-shaft-bearing located on the gearbox rear side). Cyclic loading during gusty weather leads to frequent axial load changes on the third high-speed parallel stage helical gears. The combined effect of rapid load variation and misalignment can result in excessive loads and high bearing temperatures.

Others argue that it is the high speed stages of the gearbox that are most prone to failure, thus they propose a single stage gearbox and a medium speed generator, the so-called 'Multibrid' concept [109]. This has been adopted by WinWinD (see Fig. 2.5 [137]) of Finland for their 1 MW turbines and PROKON Nord Group for their Multibrid M5000 5 MW machine [84]. It must be noted that the WindPACT study considered this concept but found that it gave a higher cost of energy than a true direct drive system.

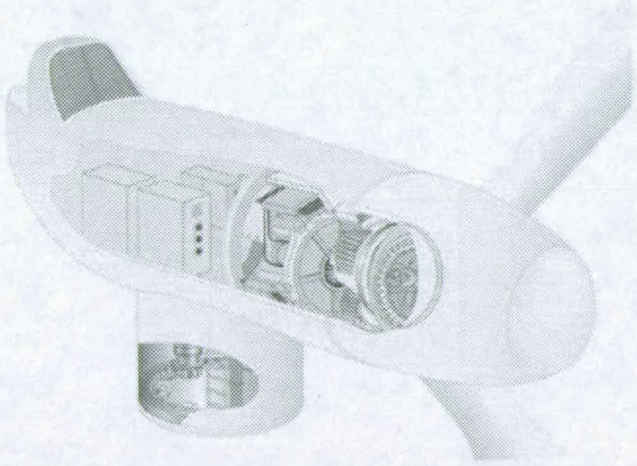

Figure 2.5. Multibrid concept, WinWind

2.2.2 Hydraulic

Hydraulics have been proposed in power take-off, mostly for wave energy converters. A few companies have suggested using hydraulic gearboxes in wind turbines such as that in [6] and [131] to turn a slow, reciprocating motion into a high speed rotary motion suitable for a DFIG. The added benefit of such a hydraulic gearbox is that some energy can be stored in accumulators and then the hydraulic output can be smoothed.

There are two main ways that hydraulic power take off can be used in marine energy: the use of the sea water in an overtopping device to act on a turbine [133], [135] which is coupled to a generator; and the conversion of wave or tidal current energy into hydraulic oil pressure that is used to drive a generator [45], [88], [104].

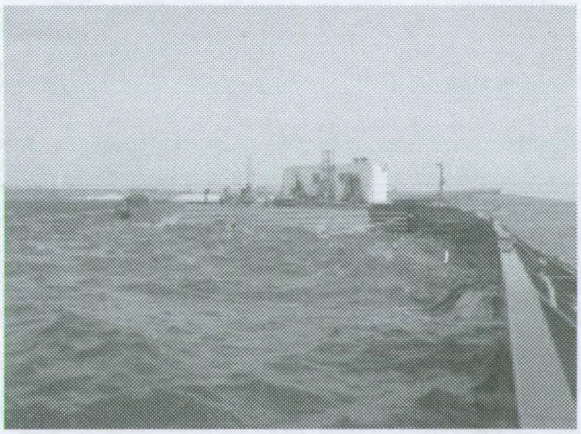

Figure 2.6. Wavedragon wave energy converter [133]

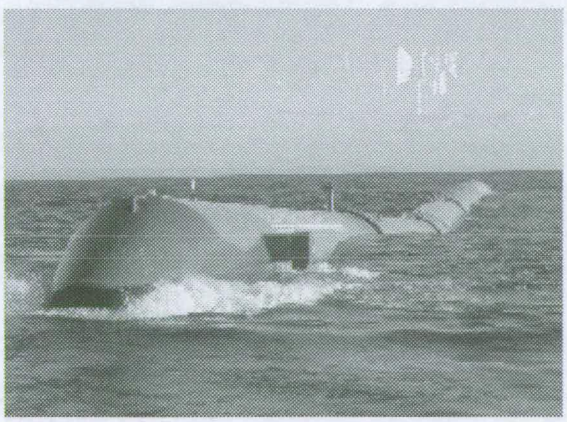

Figure 2.7. Pelamis wave energy converter [88]

The advantage of using seawater is that it is abundant, there is no need for a return pipe and any leakages will not cause any environmental problems [104]. There are disadvantages: sea water may contain abrasive particles which can damage seals and valves, and sediment can clog ducts. High pressure is suitable for Pelton turbines which are used in hose-pump devices [3]. Lower pressure designs make use of Kaplan turbines [133] (see Fig. 2.6). Reference [63] identifies a number of different options for turbine type, number and control strategies for water turbines in an over topping wave energy device.

The general features of hydraulic oil systems relevant to wave power applications include [117]:

- High specific force
- The finite life of seals and the consequent need for periodic service
- The inclusion of oil which is a potential pollutant to the sea
- Energy storage possibility
- Cannot transmit over a long distance
- Low velocity
- Compactness
- Established technology

A typical hydraulic system for a reciprocating wave energy converter will consist of:

- speed reducing linkage
- hydraulic ram/cylinder
- low pressure accumulator
- high pressure accumulator
- hydraulic motor

- hydraulic lines and valves

Such a system, outlined in [79] is shown in Fig. 2.8.

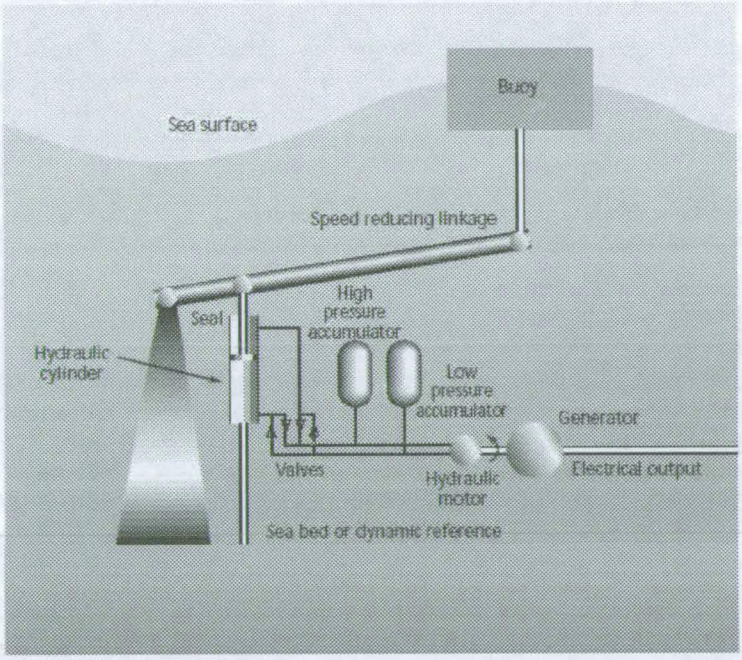

Figure 2.8. Hydraulic system in a wave energy converter [79]

A link from the buoy to the hydraulic ram is used to reduce the speed to 0.1 m/s or less, thereby prolonging the life of the seals. The hydraulic cylinder pumps oil from the low-pressure to the high-pressure accumulator which returns via the motor. This drives an electrical generator. The accumulators allow some energy storage and smooth the power output. Valves can be switched on and off to keep the motor speed constant.

It is likely that any configuration of a hydraulic power system would have the electrical plant close to the device, the advantage of remote shore based conversion being offset by the disadvantage of long, costly and inefficient pipework [7].

The following is a list of disadvantages of a hydraulic system [7]:

- Hydraulic systems are expensive and designed to operate at speeds lower than those of a typical wave energy converter (WEC).

- If oil is to be used then the marine environment strictly enforces its containment to prevent contamination, thus it requires a stringent limit on maintenance interval.
- The alternative to oil is to use fresh water, but as this is 1000th less viscous, the likelihood of leaks increases by 1000.
- Moving seals applications are limited to 0.5m/s; as the life of the seal is inversely proportional to speed and distance of application, most devices are limited to 0.1m/s [88].
- The requirement for non-return valves (for using accumulators) detracts from hydraulic efficiency.

2.2.3 Pneumatic

In some wave energy systems, such as the WaveGen Limpet oscillating wave column, the kinetic energy of the relatively slowly moving water surface is converted into kinetic energy of the air above the water surface. A change in duct area can increase the speed of the air flow and this drives a Wells turbine (which in turn is coupled to an induction generator through a gearbox) [134].

Although all wind turbines could be classed as 'pneumatic', it is rare for pneumatics to be used in the power take off between the rotor blades and the electrical machine. One exception was the Andrea Enfield 100 kW wind turbine constructed in the early 1950s. This used 24m hollow blades, open at the tip, which as they rotated drew air up through the tower where another turbine drove a generator [19].

2.2.4 Direct drive

An alternative to complex mechanical, hydraulic and pneumatic power take off systems is to couple the primary displacing element directly to the electrical generator. Although this leads to a simple system with few components, it calls for the design of an unconventional electrical generator that must be capable of producing electricity efficiently with a low speed, high force input.

In terms of broad philosophy, engineers are taught that each stage of energy conversion usually introduces further inefficiencies. The direct drive option attempts to reduce the number of energy conversion steps and therefore increase the overall efficiency. Direct drive systems can be characterised as having a smaller part count than their equivalent hydraulic or mechanical systems [7] and hence increased reliability. This is best summarised by Spooner and Mueller (in a paper addressing wave energy devices):

> "Each stage of power conversion incurs capital cost and power loss, is a potential source of failure and may require periodic servicing. There is a strong motive therefore to eliminate intermediate stages of power conversion." [117]

In a paper on the Danish wave energy programme Meyer *et al.* outlined some typical efficiencies of wave power conversion systems, direct drive systems coming out at the top [75]:

- direct drive generators 85%
- water turbines 81%
- oil hydraulic systems 72%
- air turbines 54%

Direct drive generators for wind turbines (such as the Enercon machine in Fig. 2.9) are normally large and heavy, require a frequency converter, are more efficient than doubly-fed induction generators (DFIGs) over the whole operating range and are reliable [54].

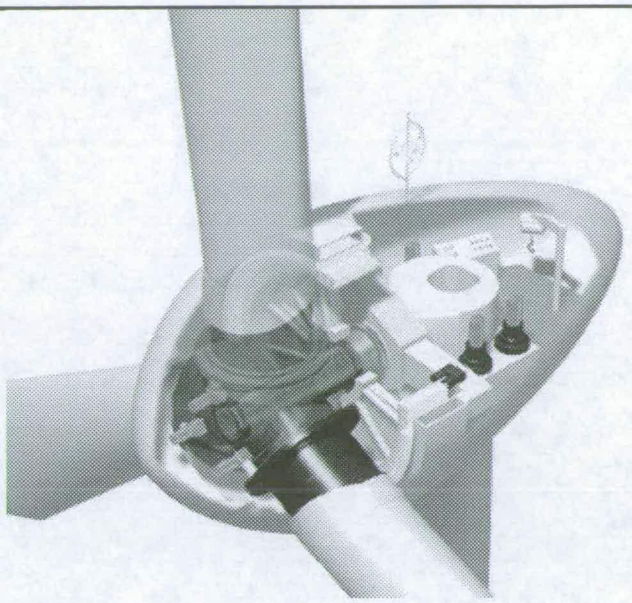

Figure 2.9. Enercon direct drive wind turbine [44]

Only one of the top ten wind turbine manufacturers – Enercon of Germany – uses direct drive technology. Grauers identified market barriers to generator development and the disinclination of wind turbine manufacturers to get involved in generator development as the reason that direct drive systems are not more widespread in the wind industry. The last few years has seen some of the large electrical machines companies providing direct drive generators for Zephyros/Harakosan (a 1.5-2.0 MW ABB machine) and Scanwind (a 3 MW Siemens generator), perhaps heralding a shift in interest.

2.3 Electrical machine types for renewable energy

As the most mature of the three renewable industries in section 2.1, the wind turbine market has seen an evolution in the power take off and type of electrical generators used, from the fixed speed Danish concept, through to variable speed with DFIGs and direct drive synchronous machines. At the same time, conventional synchronous and induction generators have been used in variable speed mode with the use of fully rated power converters. In this section each power take off and electrical machine combination will be reviewed and examples will be given.

After surveying these configurations, the focus will turn to permanent magnet topologies and other non-standard machines which can be used for direct drive such as variable reluctance machines. The arguments over generator topologies for wind turbines apply for most of the promising tidal current devices. Several wave energy devices call for the use of linear generators. Suitable machine types will be brought to the attention of the reader where appropriate.

2.3.1 Danish concept

The so-called 'Danish concept' makes use of a constant speed wind turbine with a squirrel cage induction (asynchronous) generator. This type of electrical machine is well known for being simple, rugged and cheap (25% cheaper than a doubly-fed induction generator [92]). A fixed ratio gearbox steps up the rotor speed to approximately 1500rpm for a 4 pole machine (on a 50Hz grid). This generator could be directly connected to the grid, although capacitors are normally used to provide some of the reactive power. The fixed speed approach has some drawbacks [92]:

- Wind gusts lead to torque fluctuations - thus heavy mechanical loading and increased maintenance and falling reliability.
- 'Flicker' is caused by variations in wind speed and tower shadow effect (Fig. 2.10). The turbine requires a stiff power grid to enable stable operation.
- Noise is generated by the wind turbine blades as tip speed does not match wind speed in fixed speed operation.
- The turbine is normally disconnected when there is a fault. This can lead to torque excursions, possibly damaging the gearbox on reconnection.
- Part load efficiencies of gearboxes and induction machines are poor.

Some variations of this configuration are used by wind turbine manufacturers. Bonus (now owned by Siemens) use stall regulated, constant rotor speed wind turbines with a pole convertible generator connected to the

grid in most of their turbines. At low winds (two-thirds of nominal speed) a small 6 pole generator winding is used for power production which is switched to 4 pole main winding at nominal speed [10]. This compensates some of the poor part load efficiencies. A cluster of other manufacturers have similar models:

- REPower 48/600 1523/1010 rpm 4/6 pole [97]
- Ecotecnia 62 1300 kW 1518/1012 rpm 4/6 pole [43]
- MADE AE-61 1320 kW 4/6 pole 1519/1010 rpm [50]
- Nordex N62/1300 kW 1500/1000 rpm 4/6 pole [86]

These turbines still produce flicker and suffer from challenging mechanical loadings. Vestas provide semi-variable operation with an electronically variable rotor resistance (this system is known as 'OptiSlip'). This allows the V80 turbine (for the US, 60 Hz market) a 10% speed variation from 1800 to 1980 rpm [127].

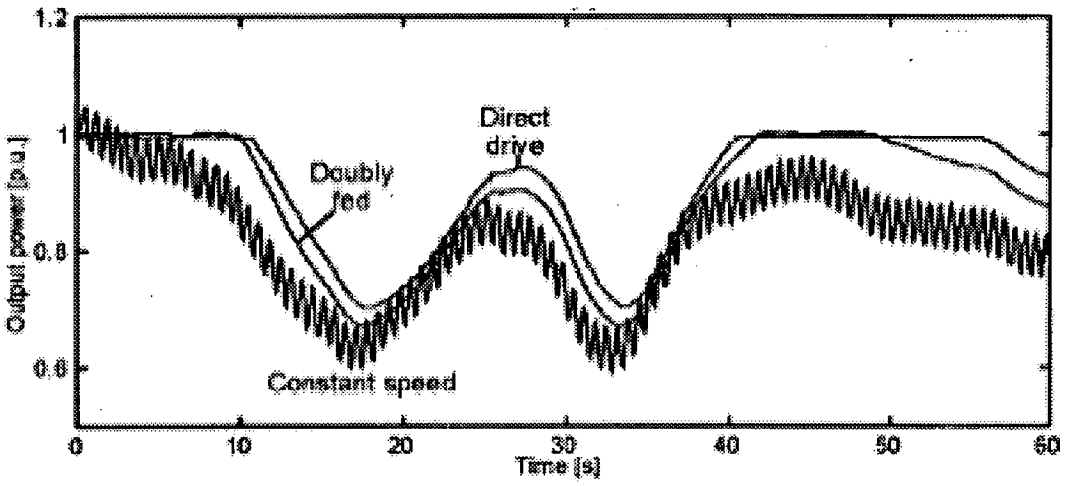

Figure 2.10 Torque flicker [92]

2.3.2 Variable speed wind turbine with doubly-fed induction generator

As turbine sizes have moved beyond the 1 MW mark, variable speed operation has become more and more popular and important. The most

popular approach has been with wound rotor induction machines in a doubly-fed configuration. A gearbox is used so that the generator rotor rotates at high speed (about 85% of nominal speed) [92]. Instead of a squirrel cage, the rotor winding is fed through a power converter (rated at about 35% of the turbine power) and brushes. The rotor currents can be used to control the speed of the rotor blades, preferably so that the optimum tip speed ratio λ is achieved, producing the maximum energy capture. A quick comparison of the Vestas 'OptiSpeed' DFIG system with the 'OptiSlip' semi-variable speed system shows that the V80 has a much greater speed variation: 1090 to 2300 rpm (60Hz). In most designs the blades are pitched to reduce the power captured at wind speeds above the rated wind speed.

The largest current DFIG turbine is the REPower 5M [97]. This 5 MW machine has a variable rotor blade speed of 6.9 to 12.1 rpm. A 63 tonne Winergy gearbox - with a total ratio of i = 97 - steps this up to 670 to 1170 rpm for the 4 m long, 2.2 m diameter induction machine.

Gearboxes have limited part load efficiency and high maintenance costs, especially when they are so large (much larger than the generator). The use of electrical brushes imposes further inspection and maintenance costs. Furthermore, power electronics produce harmonics that need to be filtered.

A paper by Polinder *et al.* suggests that a single stage gearbox and a larger doubly-fed induction generator will lead to a very high annual energy yield per total cost. This is mainly due to the lower rating of the converter and a subsequent reduction in converter cost and losses [93].

2.3.3 Variable speed with squirrel cage induction generator

A squirrel cage induction machine can be used for variable speed operation with a power converter. The new Bonus (now owned by Siemens) 3.6 MW wind turbine uses a 4-pole induction generator combined with a full converter [34]. This avoids the slip rings that must be used in wound rotor

machines, but still requires a gearbox. Although the squirrel cage machine is cheaper to manufacture, the wound rotor machine will give a higher energy yield and has a cheaper converter; on balance the DFIG is more economic [31].

2.3.4 Variable speed wind turbine with direct drive synchronous generator

In this system the rotor shaft directly drives the synchronous machine rotor. This avoids the problems posed by the gearbox (so that there is better part load efficiency, lower noise and better reliability). At wind speeds above the rated wind speed, the power is reduced by pitching the blades in most designs.

These generators tend to be large in order to produce a very large torque. The air gap force density of conventional machines is in the order of F_d = 25 - 50 kN/m^2. The rotor volume can be estimated using eqn. 2.1 [92]:

$$V_r = \pi r_s^2 l_s = \frac{P}{2\omega F_d} \tag{2.1}$$

For a given power rating P, the rotor volume increases as the rotor speed falls. As machine size is proportional to torque, a low speed machine must be larger than a high speed equivalent. Large generator size leads to large mass adding to tower and foundation structural costs and lifting costs and extra transportation difficulties (and hence costs).

Variable low speed operation means that the turbine cannot be directly grid connected. Instead the turbine power must go through a 100% rated converter - giving more losses and costs than the converter for DFIGs. Again, power electronics will produce harmonics that must be filtered.

The largest direct drive manufacturer is Enercon, with 15.8% of the world market in 2005 [16]. Enercon's turbines use a synchronous machine that is electrically excited (see Fig. 2.11) [44]. According to Jöckel, "the specific energy cost of the PM excited machines are definitely smaller compared to

those using conventional DC-excitation". He also notes that their active material is half of similar electrically excited machines [61]. Grauers points out that although permanent magnets are expensive, they eliminate the excitation losses and allow smaller pole pitches to be used [53]. Permanent magnet excitation also leads to high efficiency at part load, leading to a higher energy yield when the whole operating range is taken into account [93]. Other advantages include 50% less internal heat generation and no slip rings or brushes to manufacture and maintain [137].

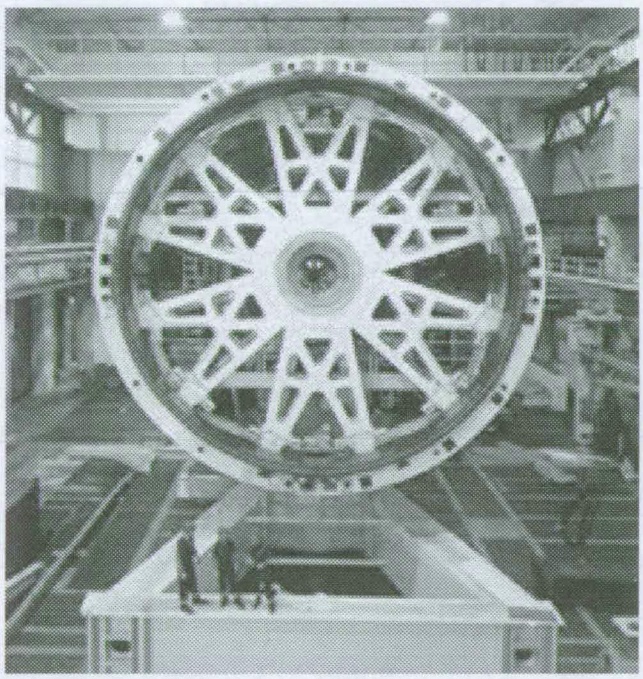

Figure 2.11. Construction of the E-112 Enercon nacelle [44]

Because of these advantages several companies are investigating the use of permanent magnets in synchronous machines for large wind turbines, including:

- Harakosan, Z72, 1.5/2.0 MW [57]
- Jeumont, J70/77, 1.5/2.0 MW [130]
- Leitwind, LTW 1.5 MW [65]
- Mitsubishi, MWT-2000S, 2.0 MW [76]

- MTorres, 1.5 MW [77]
- ScanWind, 3000 DL, 3.0 MW [105]
- Vensys 70, 1.5 MW [125]

A variation on the direct drive permanent magnet synchronous machine is the Multibrid system (section 2.2.1) used in the WinWinD and the Multibrid wind turbines. According to Polinder *et al.* this would lead to an improved annual energy yield per total cost (as compared to the direct drive version) as the generator is cheaper to construct [93]. The WindPACT study concludes that the cost of energy is less (than the Multibrid option) for the direct drive option when maintenance costs are taken into account [20].

2.4 Permanent magnet topologies

A number of authors have demonstrated that permanent magnet synchronous machines are more suitable than traditional wound rotor machines for use in wind turbine. There are a number of distinct synchronous topologies, each of which is attracting interest. The current research to date is summarised in the following subsections.

2.4.1 Radial-flux machines

'Radial-flux' refers to the direction of flux as it crosses the airgap. There are many similarities with wound rotor synchronous machines as these tend to be radial-flux machines.

2.4.1.1 In comparison to conventional generators

In his thesis, Grauers compares his designs of a radial-flux PM machine with conventional generators [53]. Compared to a constant speed geared induction machine the PM radial-flux machine is less efficient at rated power, but has a higher average efficiency (2.3% more for a 500 kW and 1.6% more for a 3 MW machine). The electrically excited Enercon synchronous machine has a 94% larger diameter and 50% greater rotor volume than the Grauers PM equivalent. Bianchi and Lorenzoni found that PM designs are

more efficient than wound rotor designs [9]. Hartkopf *et al.* noted that PM excited machines had a lower mass than electrically excited machines [59]. Dubois found that PM excitation is more cost-effective for pole pitches shorter than about 100mm [41].

Vilsbøll *et al.* note that in contrast to an induction generator with gearbox, the efficiency of their PM machine increases with decreasing load as far down as quarter load [129].

2.4.1.2 Commercial examples

An increasing number of manufacturers of medium to large direct drive permanent magnet wind turbines are emerging. Of these, the majority are using the radial-flux topology [65], [76], [105], [125]. One 1.5 MW design by the Dutch company Harakosan is shown below in Fig. 2.23 [57]. This generator is rated at 18.5 rpm, has an outer diameter of 4 m and weighs 47.2 tonnes [126].

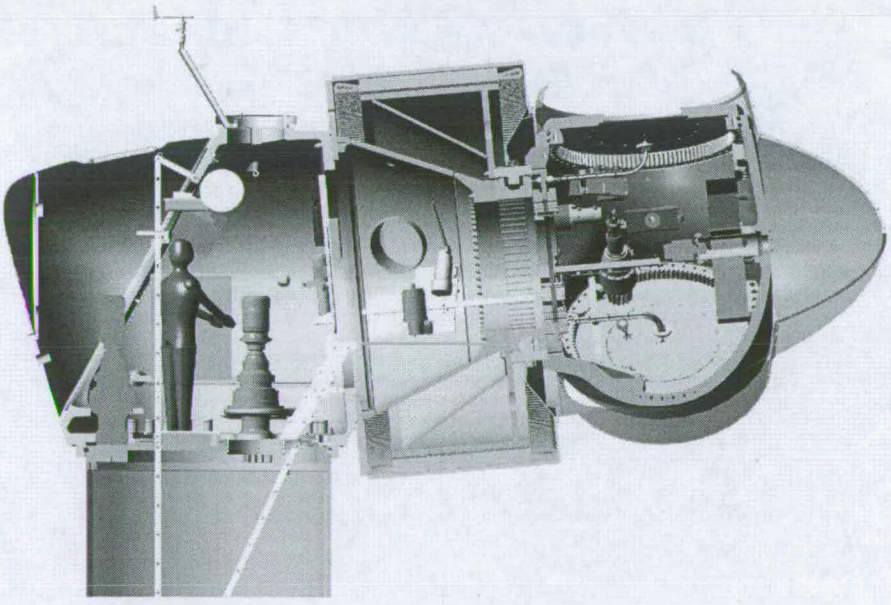

Figure 2.12. Cutaway section of Harakosan Z72 nacelle [57]

2.4.1.3 Surface mounted or buried magnets

The permanent magnets can either be surface mounted onto or buried in the rotor. Surface mounted configurations use high energy magnets such as NdFeB, which have a remanent flux density which exceeds the desired airgap flux density. These are expensive but produce a lightweight design. As they are mounted on the rotor, they must be mechanically protected and coated as NdFeB magnets are highly susceptible to corrosion [115].

With flux concentration, buried ferrite magnets can be used. These lower energy magnets are much cheaper (perhaps a tenth of the cost per unit mass as suggested by [30]), but more have to be used (5 times as much magnetic material compared to an equivalent surface mounted machine [115]). The assembly is more complicated and costly.

Vilsbøll *et al.* concluded in favour of the use of NdFeB rather than ferrite magnets as this would reduce the overall mass, dimensions and price of a 20kW generator for a wind turbine [129].

Lampola investigated various rotor designs for the radial-flux PM machine: curved and rectangular surface-mounted magnets as well as rectangular magnets equipped with pole shoes. The optimisation showed that the lowest cost of active materials and the highest pull-out torque per cost of active materials is found in the design with curved surface-mounted magnets [64].

2.4.1.4 Inner or outer rotor

From a thermal point of view, most heat is generated in the stator windings so an inner rotor allows the shortest cooling path. Most wind turbine manufacturers have chosen an inner rotor with permanent magnets. The Vensys wind turbines use a generator with an outer rotor, claiming that they can reduce the outer diameter [125]. Chen *et al.* also presented an outer rotor design [27]. When the rotor rotates, the centrifugal force of the magnets

applies pressure to the outer rotor and improves the reliability of the glued joints.

2.4.1.5 Modular machines

A modular construction could reduce manufacturing costs which are likely to be high in large radius machines. Spooner *et al.* proposed a modular radial-flux PM synchronous design for a wind generator in [115]. Standard sized stator and rotor modules were proposed for a wide range of machine designs. Modularisation can lead to less material waste, an easier assembly (avoiding rotor threading), economies of scale in manufacturing, small stock (machines with different poles numbers can use the same spare parts) and easier on site repair (replacing only the damaged modules). A design comparison with an equivalent 'continuous-core' design showed that the modular machine would have 15% less active material whilst providing high efficiency at partial and full load.

Loss mechanisms with this topology are identified by Spooner and Williamson [116], the dominant one being rotor eddy current loss. A redesign of the rotor modules based on laminated flux concentrators would lead to high efficiency. Experiments by Carlson *et al.* [24] on a 40 kW modular prototype achieved 85% efficiency at full load and 90% at part load.

A modular topology can have different noise and vibration characteristics to conventional machines. These can be reduced by using stator modules on the same support beam to cancel these effects depending on physical and electrical phase difference [51].

Gordon examined a modular design of a Segmental Electrical Machine using laser-cut plate. The work successfully demonstrated the concept and highlighted the practical challenges of creating a constant airgap when building such a machine [52]. Modular construction has also been considered for axial-flux machines, notably [25] and [83].

2.4.1.6 Unconventional radial-flux topologies

Evolving Generation is developing an ironless stator winding machine with a large diameter, lightweight spoked rotor and stator (similar to that shown in Fig. 2.13) [52], [118], [119]. A lightweight structure is possible because there is no direct magnetic attraction between rotor and stator. Evolving Generation's design would be 25-50% lighter than conventional machines [48]. An ironless stator generally means low airgap flux density (because of the large effective airgap) and low shear stress, which is why a large airgap radius is needed. Eddy-current and aerodynamic losses are likely to be higher than for a more conventional design. Despite this, efficiency as high as 94% is claimed. An overall 15-20% reduction in cost per kWh of electricity over existing wind turbines is predicted [48].

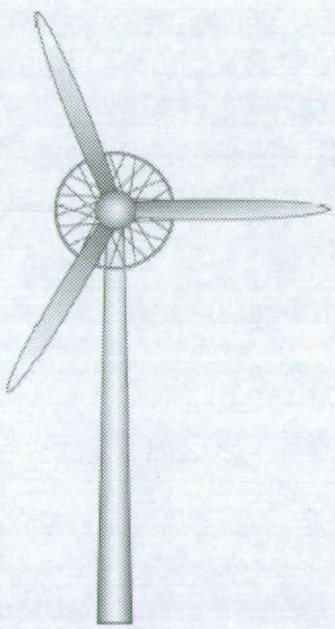

Figure 2.13. Evolving Generation wind turbine generator [119]

2.4.1.7 Linear PM synchronous machines

This is the linear analogue of the radial-flux permanent magnet synchronous machine. One has been used in the Archimedes Wave Swing [4]), designed by Polinder *et al.* [91]. In his paper on electrical generators for direct drive wave energy converters, Mueller found that because of its inferior shear

stress compared to the transverse-flux topology, this machine had a greater active mass [78]. There are considerable forces across the airgap that must be carried by the translator and stator structures. To reduce this, Baker investigated a permanent magnet aircored tubular machine which had a high power factor and no cross airgap forces [7].

In the design study for the Archimedes Wave Swing, the linear PM machine still came out with the lowest cost and highest efficiency for the conventional machines, although the double-sided moving iron transverse-flux machine gave similar results [94].

2.4.2 Axial-flux machines

2.4.2.1 General

A review of axial-field machines is presented in [1], in particular axial-flux permanent magnet machines. Axial-flux machines are different to conventional machines because of the following:

- airgap is axial, conductors are radially aligned
- stator and rotor are discs
- a higher percentage of the stator winding produces torque
- rotating discs with mounted magnets act as fans
- high power to mass ratio with larger diameter to length ratio
- floor space for manufacture and assembly is less
- larger diameter produces a higher inertia

Axial-flux machines have been proposed for a number of different applications, both at high and low speeds: portable generator systems [113], direct drive in-wheel motors [21], [67], generator units in vehicles [14], for propulsion and generators on ships [25] and for aircraft drives [60].

2.4.2.2 Axial-flux machines in wind turbines

A number of authors have suggested axial-flux permanent magnet machines for use in direct drive wind turbines. The French company Jeumont-Framatome built 50 units of their J48 750 kW, 25 rpm axial-flux permanent magnet generator wind turbines [130]. A number of design studies comparing permanent magnet topologies have been produced: Rovio *et al.* on very small 230W axial- and radial-flux machines [103]; Chen *et al.* on 2 radial- and 5 axial-flux topologies [28]; Dubois in his review of electromechanical conversion in wind turbines [38], with further comparison of generator topologies for direct drive wind turbines based on cost/torque and torque/volume [39] and also an examination of axial- and radial-flux slotted machines [40]; and Söderlund *et al.* at Tampere in Finland present both axial- and radial-flux designs of 100 and 600 kW machines [112].

2.4.2.3 Topologies

TORUS machines

Spooner and Chalmers introduced this topology [113]. In this topology two rotors – upon which are mounted a set of alternately axially-aligned NdFeB permanent magnets – sandwich a steel toroidal core, with a slotless winding.

The design, construction and test of two prototype three-phase, 16 pole TORUS generators, nominally 50kW at 4000rpm is reported in [17]. This report along with [14] gives useful design equations. Caricchi *et al.* detail work at Durham, UMIST and La Sapienza universities on two 5kW prototype machines examining stator thickness, conductor arrangements and axial-force [23]. Reference [26] describes the design, build and test of a 5kW, 200rpm direct drive wind turbine. A slotless, airgap winding gives low values of mutual and leakage inductances. Axially directed end windings are relatively short, yielding low resistance – hence voltage regulation under load is acceptable. Absence of slots leads to a very low noise machine with negligible cogging torque.

A large number of phases is preferable to individual coils in parallel (there is a high probability of circulating currents) and subdivided, twisted fine strands (with a reduced copper section gives increased I^2R losses) [110]. In the work at Tampere [62], [110], [111] the rotor discs were made from an aluminium alloy, with an extra ring of back iron mounted on the rotors.

Work at Tampere on TORUS designs for wind turbines includes: a Vihriälä *et al.* study on reducing costs of wind power with gearless 50, 100, 225, 500 and 1000 kW axial-flux PM generators [128]; Söderlund *et al.* report on 5 and 10kW prototype machines and a 100 kW, 60rpm design [110], [111]; and Keppola *et al.* report the performance of this 100 kW TORUS machine [62].

Slotted machines

[28] found that a double rotor slotted axial-flux machine gave the greatest torque per unit volume of active material. Dubois *et al.* also found that slotted axial-flux machines compare favourably with their radial-flux equivalents on a torque per unit volume basis [40].

Multistage

In order to increase the power produced by an axial-flux machine without exceeding a certain outer diameter several engineers have looked into multistage topologies. Caricchi *et al.* noted that with n stages there are n stator windings and $(n+1)$ rotor discs [21]. This means that there is a reduction in structural mass compared to the case when n identical machines are coupled together. Braid *et al.* found that adding a second stage improved the power to mass ratio by 15.7% [12]. Mbidi *et al.* used a double stage configuration in a coreless axial-flux machine [69]. Hill-Cottingham *et al.* have designed a 3-stage machine for aircraft motors [60]. Caricchi *et al.* include a 4-stage machine design for ship propulsion [25]. There are problems with unbalanced load sharing in multistage machines [13]. Only outside rotors must have magnetic properties for return flux path - the

others are for mechanical support and so can be fabricated from aluminium [22].

Air-cored/ironless

This topology has no iron core and the flux is driven by magnets to cross axially from a north to a south pole. With no iron core losses, this type of machine can potentially run at higher efficiencies [132]. The losses in the Stellenbosch machine were approximately ¼ eddy-current, ¼ copper and ½ mechanical. Eddy-current losses in the copper – the stator copper is exposed to full magnetic field – can be reduced with Litz wires [55]. These machines have a large airgap length, so a large volume of magnet is needed to establish an adequate airgap flux density [66]. These produce low noise and zero cogging torque. An ironless arrangement leads to a very low machine inductance and so an acceptable voltage regulation is achieved due to negligible armature reaction.

2.4.3 Transverse-flux machines

The transverse-flux principle means that the path of the magnetic flux is perpendicular to the direction of the rotor rotation. Very high current loadings are possible (in the order of 300 kA/m) and high force densities are achievable, thus making this family of machine a prime candidate for direct drive applications.

Dubois reviewed prototypes in literature and found that transverse-flux PM machines could bring higher torque/mass and lower cost/torque compared to the conventional radial-flux PM synchronous machine [38]. Weh *et al.* designed a 5.8 kW, 195 rpm machine for a direct drive wind turbine. This was a two-phase generator that fed into a DC link by means of a rectifier bridge. A linear model with flux concentration achieved a force density in excess of 100 kN/m^2 [136].

Like radial-flux machines, transverse-flux machines can use surface mounted or flux-concentrating topologies. Dubois chose the flux-concentrating version because of the higher contribution of PM volume elements to the no-load flux and hence a reduced requirement for magnets [41]. Arshad *et al.* designed a surface mounted, single sided, outer rotor transverse-flux machine for a wind turbine with torque per total active mass of 12.8 Nm/kg [5].

The transverse-flux machine with toothed rotor (developed by Dubois) with diameters of 1.0 m and lower produced greater torque/cost values than a radial-flux equivalent. However, diameters larger than 1.0 m favoured the conventional PM synchronous machine. The degradation of performances of transverse-flux machines at diameters above 1.0m is due to the larger airgap used in the calculations in those cases. In a transverse-flux machine larger airgaps create significant flux leakage [41]. Dubois' research is now being commercialised by Éocycle Technologies in Canada [46].

The main drawback of these machines is the inherent low power factor. Efforts to improve the low power factor reduce the torque density [58]. Power factors in the range 0.35 - 0.55 are typical. This has the effect of increasing the power rating required for the power converter.

Mueller found that machines in the variable reluctance permanent magnet family (which the transverse-flux machines belong) offer the best potential in terms of physical size, mass and efficiency for linear machines in direct drive wave energy converters. However, compensation is required to overcome the high inherent inductance in these machines. The use of fixed capacitors at low electrical frequencies and active compensation at high electrical frequencies is one solution to this problem with transverse-flux machines [78].

Polinder *et al.* proposed a double-sided moving-iron transverse-flux for the Archimedes Wave Swing [94]. This topology has the advantage of having both the magnets and windings on the stator, allowing a long translator made out of cheap laminations and making the best use of the expensive materials and permitting the designer to choose a long stroke. The design is slightly cheaper and more efficient than the conventional linear PM synchronous machine.

2.4.4 Comparison of permanent magnet topologies

Dubois provides a review of permanent magnet topologies in the context of generators for wind turbines [38]. The work compares these topologies based on torque density and cost per unit torque using reports of prototypes [39]. Chen *et al.* give a comparison of permanent magnet topologies for a range of wind turbines up to 200 kW, including five axial-flux topologies: double (slotted) stator, double (slotted) rotor, single sided (with stator balance), single sided (with rotor balance) and TORUS [28]. The criteria used for comparison are torque density, active material mass, outer radius, total length, total volume and efficiency.

The problem with these types of comparison is that they are based only on active mass (such as the copper in the windings, the iron in the rotor and stator and the permanent magnets). However inactive material makes up the majority of mass in these (low speed, high torque) direct drive machines. Hartkopf *et al.* note that for radial-flux machines,

> "about two thirds of the machine is made up of supporting structure" [59].

If there is to be a comparison to find the best permanent magnet topology, then this inactive mass (which is chiefly needed to maintain the structural integrity of the machines) must be included.

2.4.4.1 Structural mass in radial-flux machines

Grauers used an approximate model to estimate the cost of the structure of his designs. The amount of material used and difficulty of manufacturing and assembly increase as the diameter and length increase [53]. Based on this, a cost function was developed in eqn. 2.2,

$$C_{str} = \frac{c_{str}}{2}\left[\left(\frac{d_{se}}{d_{ref}}\right)^{a} + \left(\frac{l_{tot}}{l_{ref}}\right)^{a}\right], \tag{2.2}$$

where the constants c_{str}, d_{ref} and l_{ref} are the cost, diameter and length of a reference structure and d_{se} and l_{tot} are the diameter and length of the generator in question. Grauers used an exponent a = 3. This is calculated by assuming that a 1 m long structure with 2m diameter costs 20 kECU and that a smaller structure (0.5 m long with a 1m diameter) costs 2.5 kECU. There is no detail of where these numbers come from or if other structures were used. The justification for using this level of approximation (using a function for interpolation and extrapolation based on only two points) is that the structural costs are much smaller than the active costs and costs of losses. However since 1996 (when this analysis was carried out) the cost of magnets has fallen (Grauers used magnets costing more than 25 times the same mass of iron; in 2005 the magnets were only 10 times the cost of iron [93]). As the cost of the structure becomes more important, then more accurate and realistic methods of modelling the cost of the structure are needed.

One of the reasons that Grauers chose the radial-flux topology is that

> "it is easier to make a rotor stiff in the radial direction than in the axial direction".

It follows that it is easier to make radial flux generators with a small airgap. He concedes that thermal expansion of the rotor and stator may lead to airgap closing. Jöckel concludes his paper by stating that

> "efforts in reducing the required mechanical airgap width are absolutely necessary when further developing wind generators",

because larger airgaps require greater PM material [61].

Lampola states that

> "the relative weight of the non-active parts of the low-speed generators is higher than that in the four pole induction generator, 62–65% and 33% of the total weight, respectively".

This is because of the high torque and large radius in direct drive machines [64].

Hartkopf *et al.* examined radial loads of balanced magnetic pull and unbalanced magnetic pull due to eccentric rotor position given by eqns. 2.3 and 2.4 respectively,

$$F_{bmp} = \frac{A_g B_g^2}{2\mu_o} \tag{2.3}$$

$$F_{ump} = \frac{A_g B_g^2}{2\mu_o} \frac{e}{g} \tag{2.4}$$

The unbalanced load is proportional to the relative eccentricity e/g (the ratio of absolute eccentricity to magnetically effective airgap width). The airgap consists of the mechanical airgap width plus magnet height, leading to about four times lower radial magnetic loads for the permanent magnet design than electrically excited design. Hartkopf used mechanical finite element analysis to ensure that the designs did not deflect radially by more than 10% of the airgap.

2.4.4.2 Structural mass in axial-flux machines

Several papers refer to the large axial force that must be reckoned with in the construction phase of axial-flux machines: 2.8 kN in a 15 kW machine [66], 10kN in a 5 kW machine [26], 17.5 kN in a 300 kW machine [69], and 14.7 kN in a 150 kW machine [132].

Deflection of rotor discs is critical according to Wang *et al.* because:

- Running clearance between rotor and stator closes
- Permanent magnets can break due to bending

- Airflow area is reduced and thus cooling capacity decreases
- There will be a non uniform airgap causing a drift in electrical performance from the optimum.

Structural finite element analysis can be used to ensure that the deflection is no more than a specified amount. Mbidi *et al.* found that most bending of the disc happens in a very narrow diameter between that of the support structure diameter and the inner diameter of the magnets. A tapered disc uses 10% less iron, and produces negligible extra deflection [132]. For the 300 kW design, the use of strengthening ribs was examined. The lowest mass combination is 19.5 kg with sixteen (10 mm thick) ribs on a 7 mm disc - however taking manufacturing costs into account a 12 mm disc with no ribs is better. These mechanical considerations require extra mass reducing the power/active mass ratio by 33% [69].

Söderlund *et al.* estimate structural costs using an expression from [53]. The structural cost depends on outer diameter and length and is found to be more than the cost of the active parts in a 600 kW AFPM design [112]. Some authors have assumed that the weight of the supporting structure is the same as the active material in preliminary calculations [128].

The research at Tampere has used aluminium alloys to reduce mass. Hill-Cottingham *et al.* describes the design of a lightweight axial-flux motor for an unmanned aircraft [60]. The design uses carbon fibre for the chassis and rotor shaft alongside a structural plastic (Ketron PEEK) for the stator and rotor discs. Even in this very lightweight construction, the structural materials make up 50% of the total mass.

2.5 Some early conclusions

As renewable energy becomes more and more prevalent and takes on a more important role in the UK's energy mix, wind energy devices will increasingly be placed offshore. Here the need for reliable power take-off will become

more important and so the "direct drive" option may be favoured more in the future. In order to encourage this move to gearless drivetrains, engineers are trying to reduce the mass of direct drive generators. One way to do this is to use permanent magnet excitation, thus reducing the active mass. The next step is to optimise the torque density, but so far this has been based on active mass only. Including the inactive mass in this optimisation process would lead to a more lightweight design. Some way of predicting the inactive, structural mass is needed for this to be achieved, and the next few chapters explore ways of estimating the inactive mass.

The work in this thesis will concentrate on rotating generators, concentrating on machines for wind turbines. Many of the conclusions will be applicable to tidal energy converters and a few wave energy devices.

Chapter 3

Axial-flux machine modelling

3.1 Introduction

AXIAL-flux permanent magnet (AFPM) machines have been considered for a number of applications such as motors in electric vehicles, ship propulsion and wind turbine generators. These machines differ from conventional permanent magnet synchronous generators because the magnetic flux passes across an airgap axially rather than radially (see Fig. 3.1). In certain cases axial-flux machines are preferred over radial-flux machines because they can give a higher power to mass ratio and their large diameter to length ratio is useful. A number of different variations of the axial-flux topology have been proposed, including slotted, slotless, iron-cored, ironless stator, single stage and multistage machines. The following subsections introduce some of these variants.

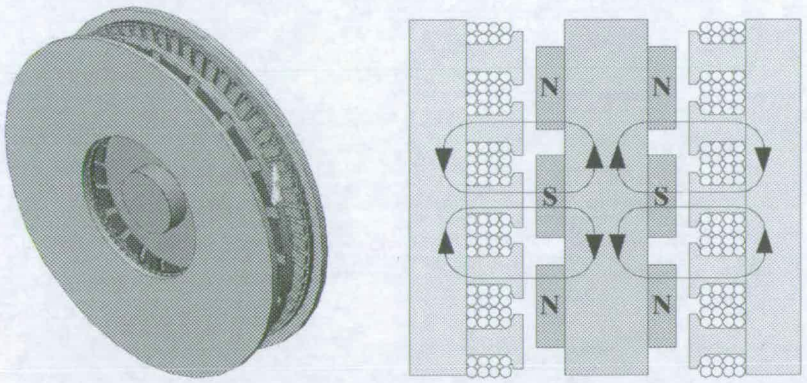

Figure 3.1. Slotted axial-flux machine. (a) Whole machine with stator and rotor discs (light grey), permanent magnets (dark grey) and windings. (b) Diagram (top view) showing simplified magnetic flux directions in TORUS machine.

3.1.1 Slotted machines

In this topology - shown in Fig. 3.1. - the windings are mounted on the slotted stator. The flux is channelled through the teeth and hence between the coils. Chen *et al.* found that a double rotor slotted axial-flux machine gave the greatest torque per unit volume of active material in their comparison of PM machines for wind applications [28]. Dubois *et al.* also found that slotted axial-flux machines compare favourably with their radial-flux equivalents on a torque per unit volume basis [40].

3.1.2 Slotless machines

In this topology two rotors sandwich a steel toroidal core. Mounted on the rotors are a set of alternately axially-aligned NdFeB permanent magnets. In this case the predominant flux crosses the airgap axially, turns perpendicularly and flows circumferentially through the toroidal core before recrossing the airgap at the next pole (see Fig. 3.2). The coils are wrapped around this core. The main type of slotless machine is known as the TORUS and is introduced and described in detail by Spooner and Chalmers in [113].

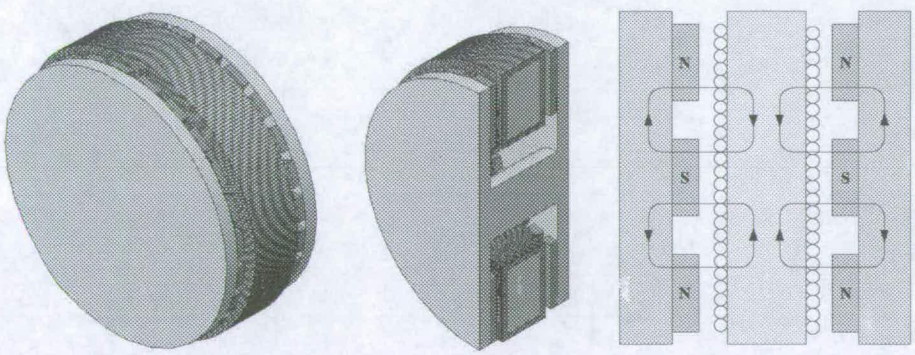

Figure 3.2. TORUS axial-flux machine. (a) Whole machine with rotor disc (light grey), permanent magnets (dark grey) and windings. (b) Section view of machine showing rotor shaft and toroidal stator core. (c) Diagram (top view) showing simplified magnetic flux directions in TORUS machine.

3.1.3 Air-cored machines

This topology dispenses with the iron core and the flux is driven by magnets to cross axially from a north to a south pole as in Fig. 3.3. The air-cored stator runs between the two sets of magnets. The lack of iron in the stator means that the airgap flux density is lower than in similarly proportioned iron-cored machines. To compensate for this more permanent magnet material and a larger radius may be used if the same torque (as an iron-cored machine) is required. With very small iron core losses, this type of machine can potentially run at higher efficiencies [132].

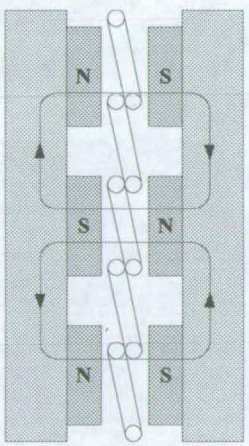

Figure 3.3. Air-cored axial-flux machine (top section view).

3.1.4 Multistage machines

Moving to a multistage design allows the designer to produce the same torque as an equivalent single stage machine, but now with a smaller disc diameter. Rotor discs can have permanent magnets mounted on both sides, meaning that there is a reduction in structural mass compared to the case when n identical machines are coupled together. As mentioned in Chapter 2, Braid *et al.* found that adding a second stage improved the power to mass ratio by 15.7% [12].

3.1.5 Structural mass

All of these topologies have axially magnetised permanent magnets mounted on circular rotor discs. If the stator contains iron, there will be an attractive force between the rotor permanent magnets and the stator iron; if not then there will be forces between the permanent magnets on adjacent rotors. The stator disc covers the same area as the permanent magnet ring and is supported at its outer radius.

Fig. 3.4 shows a cross section of a single rotor, single stator arrangement in which permanent magnets are mounted on one side of the rotor disc. If the stator contains iron there is an attractive force acting on the rotor disc and the stator. Alternatively in a single rotor, double stator arrangement (such as the slotted machine in Fig. 3.1) magnets are mounted on both sides of the rotor disc which is placed between two stators (a cross section of which is shown in Fig. 3.5). There are two equal and opposite attractive forces on the rotor, which can cancel if the rotor is placed exactly midway between the stators. However, both stator discs experience a force.

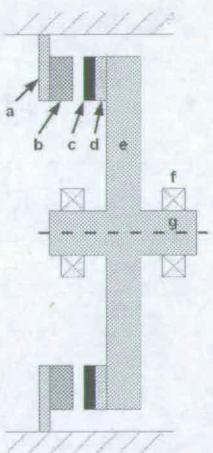

Figure 3.4. Single rotor, single stator axial-flux machine. (a) stator support structure, (b) slotted stator and copper winding, (c) permanent magnet, (d) rotor iron core, (e) rotor disc, (f) bearing, (g) rotor shaft.

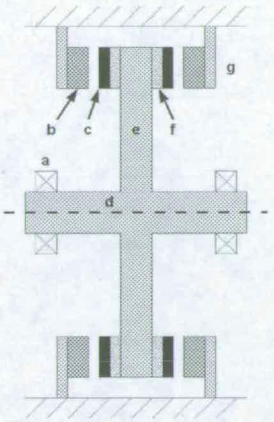

Figure 3.5. Single rotor, double stator axial-flux machine. (a) bearing, (b) slotted stator and copper winding, (c) permanent magnets, (d) rotor shaft, (e) rotor disc, (f) rotor iron, (g) stator support structure.

In a double rotor single stator machine (such as the TORUS machine in Fig. 3.2) two mirrored rotor discs are mounted on a shaft, with the permanent magnets mounted on the inner sides. The stator is suspended between the two rotor discs (Fig. 3.6). In an iron-cored machine the rotors are attracted to the stator. If the stator is not exactly midway between the rotors then there exists a net force on it [62]. An air-cored machine (such as the one in Fig. 3.3) has no force on the stator and a smaller rotor force (between the permanent magnets on the two facing rotors) because of the larger effective airgap.

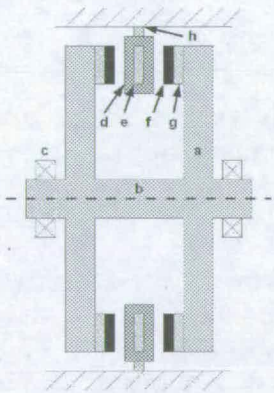

Figure 3.6. Double rotor, single stator axial-flux machine. (a) rotor disc, (b) rotor shaft, (c) bearing, (d) copper winding, (e) stator iron core, (f) permanent magnet, (g) rotor iron core, (h) stator support structure.

The double rotor, single stator configuration is essentially a single stage machine. In multistage topologies the number of rotors is one more than the number of stators (Fig. 3.7). There are two types of rotor: external (permanent magnets on one side of the rotor only) and intermediate (permanent magnets on both sides of the rotor). External rotors and iron-cored stators can be analysed as in the double rotor, single stator case. The intermediate rotors are the same as those in single rotor, double stator case.

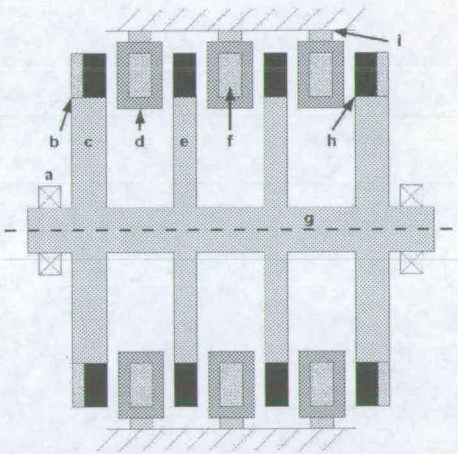

Figure 3.7. Multistage axial-flux machine. (a) bearing, (b) rotor iron core, (c) external rotor disc, (d) copper winding, (e) intermediate rotor disc, (f) stator iron core, (g) rotor shaft, (h) permanent magnet, (i) stator support structure.

The maximum force on the stator will be during the assembly process, when one rotor is brought up towards a stator. A conservative design would assume that there is no force cancelling and so the structures have to cope with this assembly force all of the time. This policy is adopted in this thesis.

In all of the designs described above the engineer must take into account the effect of the magnetic attraction forces in the structural design of the machine. The deflection of rotor discs is critical according to Wang *et al.* because:

- Running clearance between rotor and stator closes.
- Permanent magnets can break due to bending.

- Airflow area is reduced and thus cooling capacity decreases.
- There will be a non-uniform airgap causing a drift in electrical performance from the optimum.

Structural finite element analysis can be used to ensure that the deflection is no more than a specified amount [69] and [132]. This is normally carried out after the electromagnetic optimisation. For example, Mbidi *et al.* found that the structural considerations require extra mass reducing the power/active mass ratio by 33% [69].

In order to optimise both the electromagnetic and structural mass of the machine the designer needs some analytical expressions that link the maximum allowable deflection to structural dimensions and hence structural mass.

Before selecting a particular machine for an application the design engineer will normally go through a paper design study comparing different topologies, but such optimisations have tended only to focus on the electromagnetic design and either completely ignore the structural interaction or use very crude approximations to model the structure. For instance, Söderlund *et al.* estimated structural costs using an expression from [53]. The structural cost depends on outer diameter and length and is found to be more than the active part mass in a 600 kW AFPM design [112]. Some authors have assumed that the weight of the supporting structure is the same as the active material in preliminary calculations [128]. In references [28] and [39] different machine topologies are compared for wind energy converters, but in the comparison only the active mass (the mass of the iron in the magnetic circuit, the copper in the stator windings and permanent magnets on the rotors) is used. For the case of an axial-flux permanent magnet machine, previous studies reveal that this active mass is typically only a third of the total mass [62]. The remaining inactive mass - mostly structural mass which is required to maintain small airgaps between rotor discs and the

stator winding - will remain unoptimised. With direct drive wind turbines there is a requirement for low mass at the tower head [33], so that any design study comparing different machine topologies must include the structural mass.

The main aim of any design study is to provide the engineer with results rapidly and with a reasonable level of confidence. Classical analytical techniques are therefore used rather than more sophisticated numerical modelling techniques such as finite element analysis. The analytical expressions for the electromagnetic design are well known. In this chapter well established analytical expressions from circular plate, elastic beam and cylindrical shell theory are applied to calculate the structural mass of axial-flux permanent magnet machines rapidly but with a level of accuracy sufficient for the first stage in a design study. These expressions can be incorporated into basic electrical machine design procedures for comparative design exercises in order to ensure that both the active and inactive mass is optimised. Mechanical finite element models and previously reported results for axial-flux machines will be used to verify the analytical expressions introduced. In order to demonstrate the importance of including the structural mass analysis a series of direct drive wind turbines are designed and discussed. The chapter concentrates on the double rotor, single stator configuration both with iron (also known as a TORUS machine) and without iron in the stator.

3.2 Analytical models

The electromagnetic and structural designs are linked by the magnetic attraction force acting between the stator and rotor, which is commonly referred to as the Maxwell stress. Classical analysis of magnetic equivalent circuits can be used to determine the airgap flux density and hence the normal component of Maxwell stress is given as

$$q = \frac{B_g^2}{2\mu_0}, \qquad (3.1)$$

where B_g is the airgap flux density and μ_0 is the permeability of free space.

3.2.1 Rotor

There are two rotor discs in the single stage axial-flux permanent magnet machine shown in Fig. 3.6. Mounted on a shaft with a radius, b_r, these discs have a number of magnets fixed between an inner radius, r_0, and outer radius, a_r, as in Fig. 3.8. The parts covered by magnets experience a stress, q, given by eqn. (3.1). In reality the Maxwell stress is a wave distributed in a circular fashion (confined between the limits r_0 and a_r) with the same number of peaks as there are poles. Considering only the first harmonic of the airgap flux density then the stress will take the form $\frac{1}{2\mu_0}\hat{B}_g^2 \sin^2(n\theta)$ [121].

To simplify the analysis, it will be assumed that the stress, q, acts on the annulus area bounded by r_0 and a_r. The normal component of Maxwell stress is modified by multiplying it by the magnet width/pitch ratio and spread across the whole pole pitch, so that the overall force acting on the rotor disc remains constant (see Fig. 3.9).

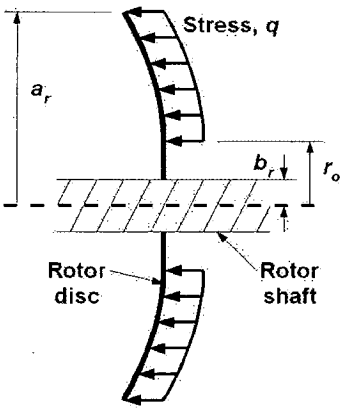

Figure 3.8. Circular plate model of axial-flux rotor disc.

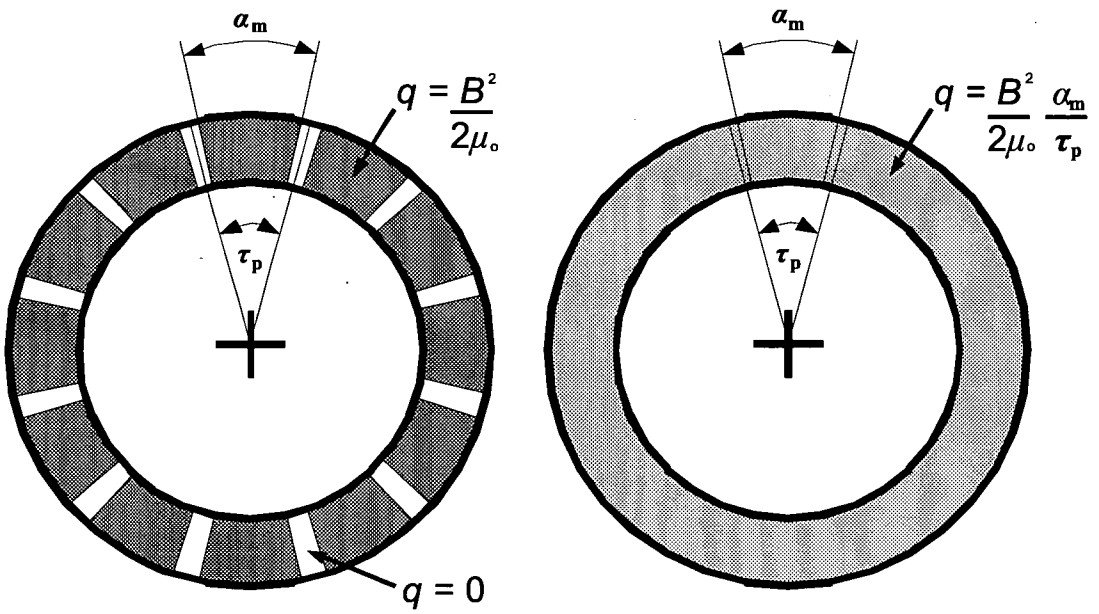

Figure 3.9. Rotor disc stress distribution. (a) Actual stress distribution on rotor disc, areas covered by permanent magnets in dark grey and spacing in white. (b) Assumed stress distributed across the active annulus in light grey

Circular plate theory can be used to model the rotor disc as a flat circular plate of constant thickness, t_r, with its outer edge free and the inner edge fixed [98]. The maximum deflection is at the outer radius, a_r. This deflection into the airgap, y_a, can be found from

$$y_a = M_{rb}\frac{a_r^2}{D}C_2 + Q_b\frac{a_r^3}{D}C_3 - q\frac{a_r^4}{D}L_{11}, \tag{3.2}$$

where the unit radial bending moment at the shaft, M_{rb}, is

$$M_{rb} = \frac{-qa_r^2}{C_8}\left[\frac{C_9}{2a_r b_r}\left(a_r^2 - r_0^2\right) - L_{17}\right], \tag{3.3}$$

and the unit shear force at the shaft, Q_b, is

$$Q_b = \frac{q}{2b_r}\left(a_r^2 - r_0^2\right). \tag{3.4}$$

Constants C_2, C_3, C_8, C_9, L_{11} and L_{17} are given in Appendix A. The plate constant, D, is a function of plate thickness, t,

$$D = \frac{Et^3}{12\left(1-\nu^2\right)}. \tag{3.5}$$

By specifying the maximum allowable deflection at a, y_a, the rotor thickness, t_r, can be found,

$$t_r = \sqrt[3]{\frac{12a_r^2(1-\nu^2)}{Ey_a}\left[M_{rb}C_2 + Q_b a_r C_3 - qa_r^2 L_{11}\right]}. \tag{3.6}$$

Thus the mass of the rotor discs is expressed in eqn. (3.7).

$$m_r = n_{disc}\rho\pi\left(a_r^2 - b_r^2\right)\sqrt[3]{\frac{12a_r^2(1-\nu^2)}{Ey_a}\left[M_{rb}C_2 + Q_b a_r C_3 - qa_r^2 L_{11}\right]}, \tag{3.7}$$

where n_{disc} is the number of rotor discs.

3.2.2 Stator

The stator disc is also modelled using circular plate theory (in section 3.2.2.1). Its outer radius is attached to a multiple beam structure (analysed in section 3.2.2.2) or a cylindrical shell structure (analysed in section 3.2.2.3). These potential stator structures are based upon structures that have been seen in the published literature. To simplify the model the stator is modelled as one piece of iron connected directly to a structure (beams or casing) which in turn is fixed at both ends to baseplates. Equations are developed to predict the thickness of the stator and supporting structures so that the deflection into the airgap is kept within defined limits when the largest Maxwell stress, q, is applied, which occurs during assembly when the stator is moved into position opposite one rotor disc.

3.2.2.1 Stator disc

Flat circular plates with outer edge fixed and inner edge free are modelled in [98] as shown or the general case in Fig. 3.10. A stress q (3.1) acts on the stator between r_0 (which is equal to b_s in the case of the stator disc) and a_s which is equal to the rotor outer radius a_r plus a running clearance. This simplification (where q is applied over a greater area than that of the rotor as in section 2.1) leads to a slightly conservative design.

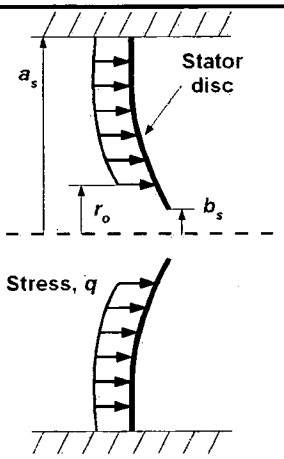

Figure 3.10. Circular plate model of general disc case.

The maximum deflection is at the inner radius and is given by

$$y_{b1} = \frac{-qa_s^4}{D}\left(\frac{C_1 L_{14}}{C_4} - L_{11}\right), \tag{3.8}$$

where C_1, C_4 and L_{14} are given in Appendix A. By combining eqn. (3.5) with eqn. (3.8) and rearranging, the minimum stator thickness (from a mechanical perspective) can be determined and is

$$t_s = \sqrt[3]{\frac{12qa_s^4(1-\nu^2)}{Ey_{b1}}\left(\frac{C_1 L_{14}}{C_4} - L_{11}\right)}. \tag{3.9}$$

It should be noted that magnetic circuit requirements may require a greater stator thickness. The mass of the stator disc due to structural needs is given in eqn. (3.10).

$$m_s = \rho\pi\left(a_s^2 - b_s^2\right)\sqrt[3]{\frac{12qa_s^4(1-\nu^2)}{Ey_{b1}}\left(\frac{C_1 L_{14}}{C_4} - L_{11}\right)}. \tag{3.10}$$

3.2.2.2 Beam structure

The model of the stator disc gives a deflection assuming that the stator disc is connected to a solid structure (at the top and bottom of Fig. 3.10). This structure is needed to react the moment per circumferential length given in eqn. (3.11) and hold the stator core in position [98].

$$M_{ra} = -qa_s^2\left(L_{17} - \frac{C_7}{C_4}L_{14}\right). \tag{3.11}$$

Several configurations have been used in [18] and [23], one of these is shown in Fig. 3.11. The axial-flux machine is shown on the right of the figure. In this analysis, the iron core is made up of two toroidal halves fixed to a toroidal plate sandwiched between them. This plate has several tabs which are held in position by beams, the ends of which are fixed to two baseplates (Fig. 3.12a). Assuming that the total circumferential moment is equally shared by all the n_b beams, then the moment on each beam is expressed in eqn. (3.12).

$$M_0 = \frac{2\pi a_s M_{ra}}{n_b}. \tag{3.12}$$

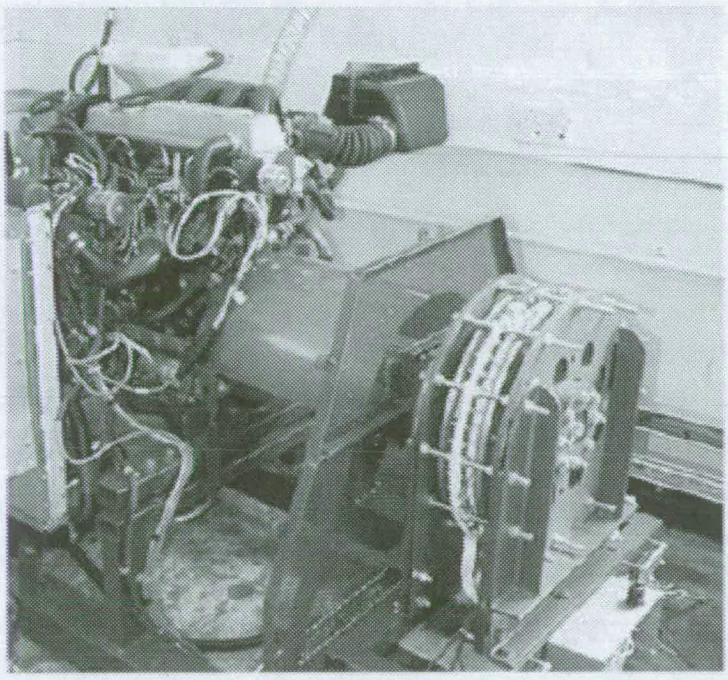

Figure 3.11. Axial-flux machine showing beam structure [18]

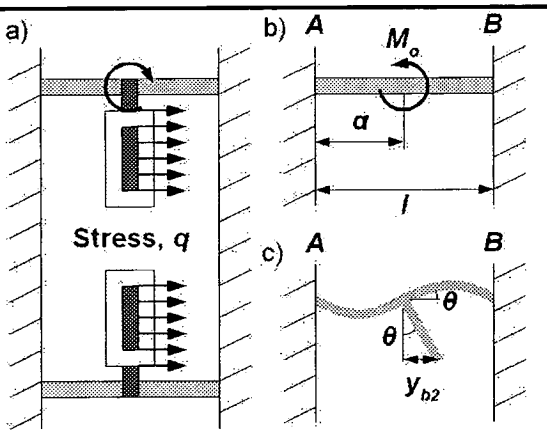

Figure 3.12. a) Stator and beam model b) Beam reacting moment M_0 at mid point c) Deflection, y_{b2}, due to beam bending.

Modelling the beams (Fig. 3.12b) as elastic straight beams with both ends fixed, this moment is applied at $\alpha = l/2$ m along the beam and leads to an angular displacement at distance, x, along the beam [99] given in eqn. (3.13)

$$\theta = \frac{M_A x}{EI} + \frac{R_A x^2}{2EI}, \tag{3.13}$$

where

$$M_A = \frac{-M_0}{l^2}\left(l^2 - 4\alpha l + 3\alpha^2\right), \tag{3.14}$$

and

$$R_A = \frac{-6M_0\alpha}{l^3}(l-\alpha). \tag{3.15}$$

If the beams have a circular cross section then the second moment of area, $I = \pi R^4/4$. By combining eqns. (3.13-3.15), the beam radius (to give a specified angular displacement, θ, at $x = \alpha$) is given in eqn. (3.16).

$$R = \left(\frac{-4M_0\alpha}{\pi l^2 E\theta}\left[l^2 - 4\alpha l + 3\alpha^2 + \frac{6(l-\alpha)\alpha}{2l}\right]\right)^{1/4}. \tag{3.16}$$

Fig. 3.12c shows how this angular displacement produces a deflection into the airgap. For a given axial deflection, y_{b2}, the angular displacement is expressed in eqn. (3.17)

$$\theta = \tan^{-1}\frac{y_{b2}}{b_s - a_s}. \tag{3.17}$$

Thus the mass of the structural support beams follows,

$$m_b = n_b \rho l \pi \sqrt{\frac{-4M_0\alpha}{\pi l^2 E\theta}\left[l^2 - 4\alpha l + 3\alpha^2 + \frac{6(l-\alpha)\alpha}{2l}\right]}. \tag{3.18}$$

3.2.2.3 Cylindrical casing

Instead of attaching the stator to beams, the stator could be hung off the machine casing. This casing can be modelled as a short thin-walled cylindrical shell with an intermediate applied moment shown in Fig. 3.13 [100]. As in the beam case, the angular displacement must be limited to keep the axial deflection into the airgap less than y_{b2} given by eqn. (3.17).

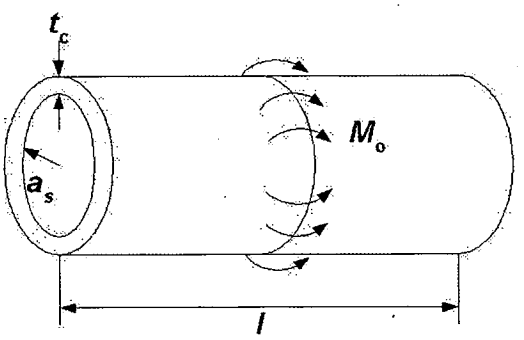

Figure 3.13. Cylindrical shell model of machine casing.

For cylindrical shells, the angular displacement of the cylinder surface halfway along the cylinder is

$$\psi = \psi_A F_1 - y_A \lambda F_4, \tag{3.19}$$

where

$$\psi_A = \frac{-M_0}{D\lambda}\frac{K_2K_{a1} + K_3K_{a4}}{K_{11}}, \tag{3.20}$$

$$y_A = \frac{M_0}{2D\lambda}\frac{2K_3K_{a1} + K_4K_{a4}}{K_{11}}, \tag{3.21}$$

$$\lambda = \left(\frac{3(1-\nu^2)}{a_s^2 t_c^2}\right)^{1/4}. \tag{3.22}$$

Cylindrical shell constants K_2, K_3, K_4, K_{11}, K_{a1}, K_{a4} and functions F_1 and F_4 are given in Appendix A. The thickness of the cylinder, t_c, can be altered so that $\psi = \theta$. Thus the mass of the machine casing is

$$m_c = \rho l \pi\left(t_c^2 + 2a_s t_c\right). \tag{3.23}$$

3.3 Finite element models

Structural finite element analysis is used in this section to model the maximum deflection due to the stress q. These deflections will be compared with those predicted by the analytical equations in section 3.2. Table 3.1 gives the relevant dimensions for a number of different iron-cored machines based on the design by Söderlund *et al.* in [111], each of which have been modelled using finite element analysis and the analytical expressions developed previously. Finite element results have been previously reported for a double rotor, coreless stator machine built by Wang *et al.* [132]. Commercial finite element software is used to develop the structural models in this chapter [29].

Rotor				*Stator*			*Support structures*		
a_r, m	b_r, m	r_0, m	t_r, mm	a_s, m	b_s, m	t_s, mm	l, m	R, mm	t_c, mm
1.20	0.240	1.09	37.4	1.26	1.09	4.74	0.173	5.34	3.13
2.39	0.477	2.17	74.3	2.50	2.17	9.44	0.288	10.2	6.43
3.26	0.651	2.96	101	3.42	2.96	12.9	0.366	13.6	9.04
5.14	1.03	4.67	160	5.40	4.67	20.3	0.520	20.9	15.3
7.66	1.53	6.96	238	8.04	6.96	30.3	0.717	30.6	24.8

Table 3.1 Parameters of iron-cored machines.

3.3.1 Rotor disc

3.3.1.1 Coreless machine

Full details and results of a finite element model developed by Wang *et al.* are given in [132]. Briefly, they constructed a one sixteenth model of the disc using 4-node shell elements with symmetry conditions (so that the model did not deflect circumferentially). Results from the model were used to calculate the maximum deflection of a rotor disc with a_r = 360 mm, b_r = 165 mm, r_0 = 250 mm, t_r = 17 mm and q = 69.8 kPa machined from steel with mechanical properties E = 200 GPa and ν = 0.3. This result is used below to verify the analytical method.

3.3.1.2 Iron-cored machine

In this section, a similar one sixteenth shell element model is recreated in a finite element solver to model a number of sample machines based on the Söderlund machine design in [111]. The relevant dimensions used in the finite element and analytical models are given in Table 3.1. In the finite element model the inner edge is constrained (no translation or rotation) and a stress q = 28 kPa (equivalent to B_g = 0.33 T, with a magnet width/pitch ratio of 0.653) is applied to find the axial deflection at the outer rotor disc radius (Fig. 3.14) for all machine cases in Table 3.1. The Söderlund machine uses rotor discs made of an aluminium alloy with mechanical properties E = 69 GPa and ν = 0.33 for the structural part of the rotor.

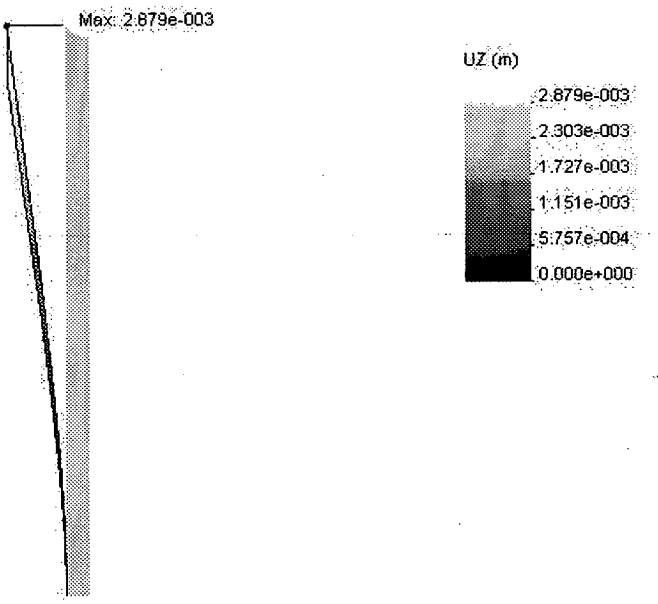

Figure 3.14. One sixteenth finite element model of rotor disc showing deflection when a_r = 1.2m.

3.3.2 Stator

3.3.2.1 Stator disc

Again, a one sixteenth model with 4-node shell elements and symmetry conditions is shown, this time in Fig. 3.15, with the outer edge constrained.

The same stress q is applied to find the deflection at the inner stator disc radius for the stator parameters in Table 3.1.

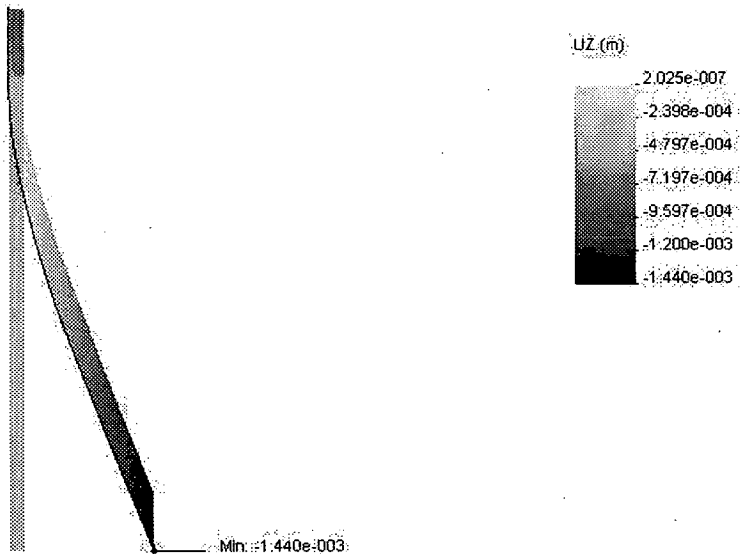

Figure 3.15. One sixteenth finite element model of stator disc showing deflection when a_s = 1.26m.

3.3.2.2 Beam structure

A similar one thirtieth model (because the number of beams, n_b = 30) of a section of the stator disc with a beam of radius R (Table 3.1) joined midway along at radius, a_s, is shown in Fig. 3.16. The ends of the beam are constrained and the deflection at the inner stator disc radius is found when q is applied to the stator disc.

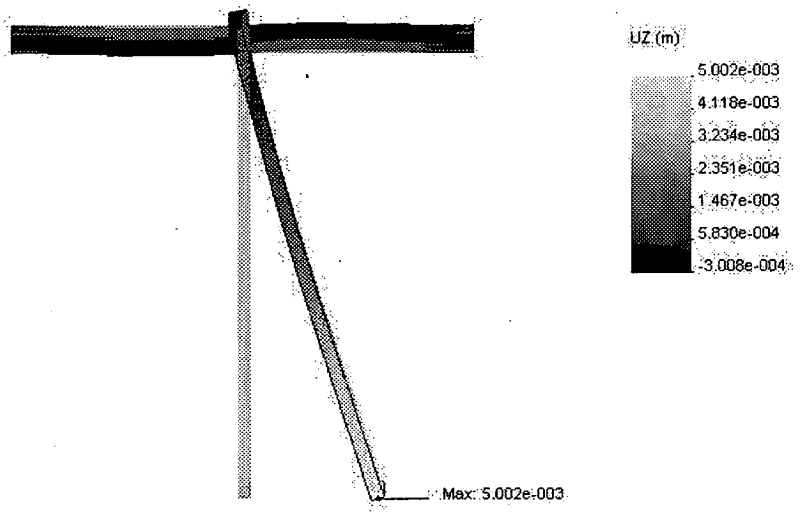

Figure 3.16. One thirtieth finite element model of stator disc and beam support showing deflection when R = 5.34mm.

3.3.2.3 Cylindrical casing

In this case the one thirtieth model with 4-node solid mesh consisted of a section of the stator disc and the cylindrical casing with thickness, t_c, from Table 3.1. The ends of the cylinder are constrained and the deflection is found (Fig. 3.17).

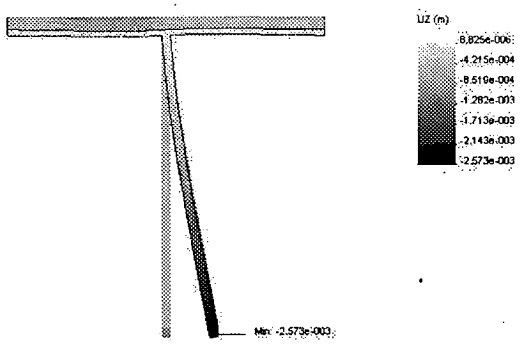

Figure 3.17. One thirtieth finite element model of stator disc and cylindrical casing showing deflection when t_c = 3.13 mm.

3.4 Results

3.4.1 Rotor disc

By rearranging eqn. (3.6) the maximum deflection, y_a, can be found in terms of rotor thickness, t_r. For the coreless machine, y_a = 0.1475 mm if the plate thickness, t_r = 17 mm, which compares favourably to the deflection of 0.145mm reported by Wang *et al.* The analytic and finite element deflections for the iron-cored machine designs in Table 3.1 are shown in Fig. 3.18, which also show excellent correlation.

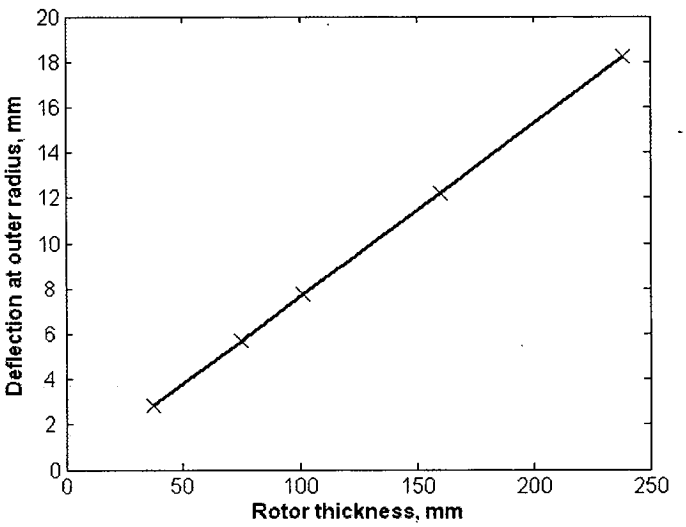

Figure 3.18. Maximum deflection of rotor disc found analytically (–) and for five points with finite element analysis (×).

3.4.2 Stator

3.4.2.1 Stator disc

Rearranging eqn. (3.9) gives the maximum deflection at the inner stator core radius with stator thickness, t_s. The analytic and finite element deflections of the stator for the iron-cored machines are shown in Fig. 3.19.

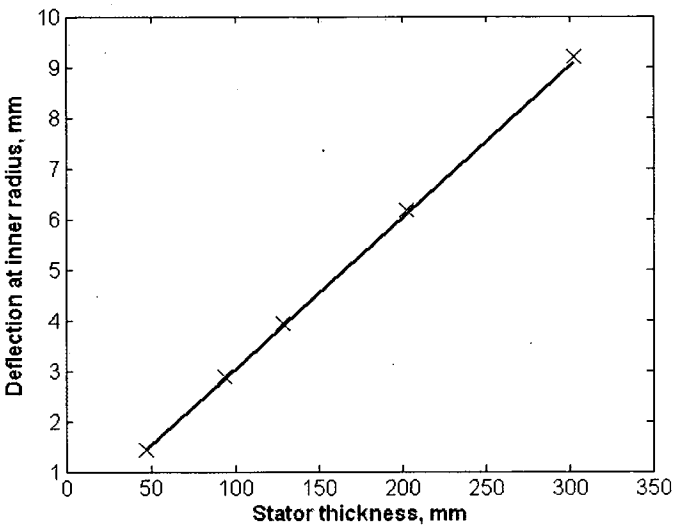

Figure 3.19. Maximum deflection of stator disc found analytically (–) and for five points with finite element analysis (×).

3.4.2.2 Beam structure

Combining eqn. (3.16) and eqn. (3.17) gives the radius, R, of the support beams needed to limit the maximum combined deflection, y_b. The analytic and finite element deflections of the stator with beam structure for the iron-cored machines are shown in Fig. 3.20.

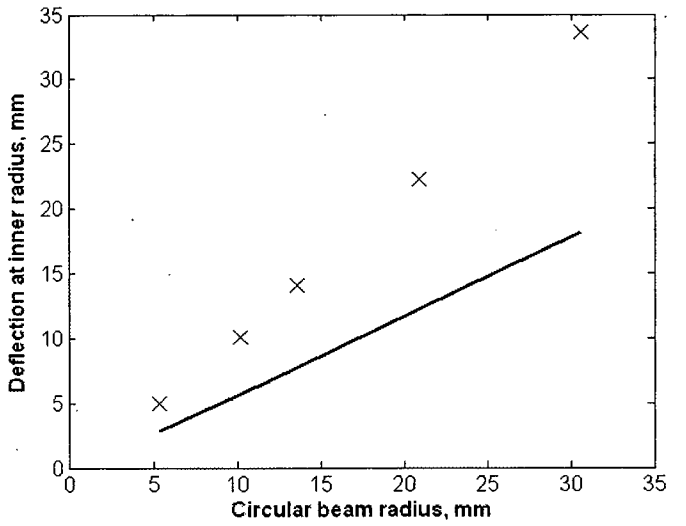

Figure 3.20. Maximum deflection of stator disc with beam structure found analytically (–) and for five points with finite element analysis (×).

3.4.2.3 Cylindrical casing

Using eqns. (3.17) and (3.19-3.22) the maximum combined defection, y_b, can be found when the casing has a thickness of t_c. The analytic and finite element deflections of the stator with casing structure for the iron-cored machines are shown in Fig. 3.20.

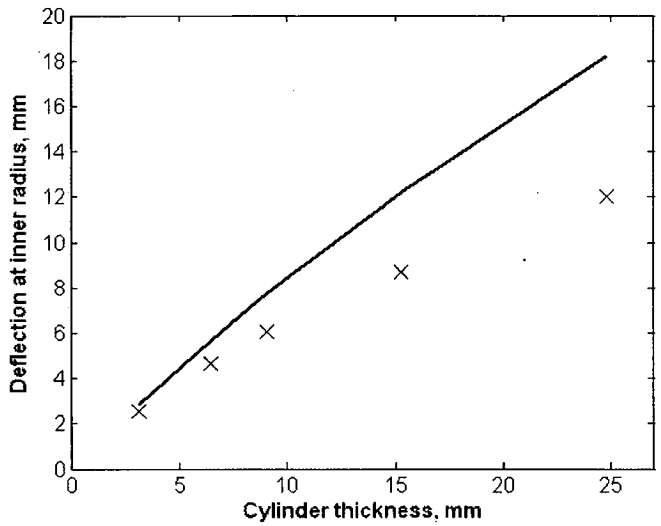

Figure 3.20. Maximum deflection of stator disc with cylinder casing found analytically (–) and for five points with finite element analysis (×).

3.4.3 Discussion

3.4.3.1 Cylinder plate theory for rotor and stator discs

Both the analytical models for the rotor and stator discs give maximum deflections that are within 2% of those produced in the finite element analysis reported in this chapter and elsewhere. These disc models can be applied to all axial-flux topologies, not just the double rotor, single stator configuration.

It should be noted that these are both models based on the same assumptions and simplifications. In reality there are more forces at work in the machine. It is appropriate to neglect these in an early stage design study because the normal component of Maxwell stress is by far the largest force. In practice

the designer should carry out a full finite element analysis to check that the running clearance does not close too much.

3.4.3.2 Beam vs. cylindrical shell model

The stator plate model assumes that the outer radius is constrained. The applied stress, q, produces a moment per circumferential length. In the beam model this constraint is badly approximated by the beams, giving a much larger deflection in the finite element analysis than predicted by the analytical model. A cylindrical shell model with an intermediate moment per circumferential length (at the point that the stator is fixed to the casing) predicts the deflection more closely than the beam equations, although the model over-predicts the required cylinder thickness, particularly at large radii.

3.4.3.3 Subsequent deflection

These machines suffer from 'magnetic negative stiffness' as defined in [121]. This means that as the rotor and stator discs deflect, the airgap narrows and the flux density and the normal component of Maxwell stress increase and so there will be a subsequent deflection. This must be coped with by increasing the structural dimensions, such as the disc thickness. This phenomenon and its implications will be analysed in Chapter 5, but it will be neglected in this chapter.

3.5 Direct drive wind turbines

To show how these models can be used, the designs of a series (0.1, 0.5, 1, 1.67, 2.5 and 5 MW) of wind turbines based on [62], [111] are presented below. The speed of each machine is based on current commercial designs [44], [127]. The power rating and nominal speed of E-33, E-48, E-82 and E-112 were plotted and a logarithmic curve was fitted to the results. Speeds for the desired power ratings were interpolated using the function, giving N as

shown in Table 3.2. The required rated torque, T, was then found from $T = P/\omega$. Torque produced by a TORUS machine is given in [23] as

$$T = 2\pi a_r^3 B_g A k_r \left(1 - k_r^2\right). \tag{3.24}$$

With typical magnetic and electrical loadings of B_g = 0.33 T and A = 28 kA/m and a ratio of inner-to-outer permanent magnet radius (aspect ratio) $k_r = r_0/a_r$ = 0.91, the outer radius, a_r, at each rating is given in Table 3.2. For the 0.1, 0.5, 1, 2.5 and 5 MW machines the number of pole pairs is set to produce a frequency of 45 Hz at rated speed. For comparison purposes the pole pair number of the 1.67 MW machine is set to produce 9.25 Hz at rated speed. During the design the ratios of the airgap running clearance to rotor outer radius (c = $0.0095a_r$) and the shaft radius to rotor outer radius are kept constant (b_r = $a_r/5$). A radial clearance of 5% of the rotor outer radius is added to give the stator outer radius. Changing the thickness of the permanent magnets and the number of turns per coil gives the required airgap flux density and the electrical loading at the stator core inner radius. The permissible rotor and combined stator deflections are 25% of the airgap running clearance in each case. Thus during the worst case scenario of assembly (with the stator and only one rotor), the running clearance is reduced to 50% of its original value.

P, kW	a_r, m	N, rpm	T, kNm	**Active Mass, kg**	**Inactive Mass, kg**	**Total Mass, kg**
100	1.20	60.0	15.9	485 (33.8%)	951 (66.2%)	1440
500	2.39	38.0	126	2260 (23.6%)	7320 (76.4%)	9570
1000	3.26	30.0	318	4520 (19.7%)	18500 (80.3%)	23000
2500	5.14	19.0	1260	12100 (14.3%)	72300 (85.7%)	84400
5000	7.66	11.5	4150	28000 (10.4%)	241000 (89.6%)	269000
1670	4.54	18.5	866	27700 (34.9%)	51600 (65.1%)	79300

Table 3.2. Design parameters and masses of axial-flux machines for direct drive turbines.

Based upon the results in the previous section the disc model is used for the rotor and the cylindrical shell is used for the stator. The latter provides an overestimate, but it is better to be conservative during the initial stages of design.

3.5.1 Results and comparison with existing direct drive generators.

In order to gain some confidence in the use of the electrical machine design procedure taken from [15] and [17] and the application of the structural equations, the designs are compared to the 100 kW machine in [62] in this section. Row 1 in Table 3.2 shows the results obtained for the Söderlund machine calculated using the models presented in this chapter. In [62] the total mass of the 100 kW machine is stated as 1900 kg, which is 32% greater than calculated using the proposed model. However, it is not possible to reproduce the exact design and the actual structure used is unclear from the paper, so the error is not unexpected. The ratio of active-to-total mass shows better agreement - 33.4% is reported in [62]. Although the total mass calculation exhibits significant error, the fact that there is good correlation between the ratio of active-to-total mass provides some confidence in the use of the analysis. The difference between nominal and maximum torque ratings in the 100 kW machine may also account for the difference in mass.

The results of active and inactive mass for the range of typical wind turbine power ratings are shown in Table 3.2. The active mass is made up of the copper windings, iron cores (one for the stator, two on the rotors) and two sets of permanent magnets modelled using [15] and [17]. The inactive mass is the sum of the rotor discs, stator support and machine casing. Figs. 3.22 and 3.23 show the breakdown of active and inactive mass respectively at each rating. These results show that the structural requirements play a dominant role in the total mass of axial-flux machines especially at greater ratings (and hence larger outer radii). From Fig. 3.23 the rotor mass dominates inactive

mass at powers greater than 1 MW, so that any errors in the stator structural model observed in section 3.4 will have a negligible impact on the total mass.

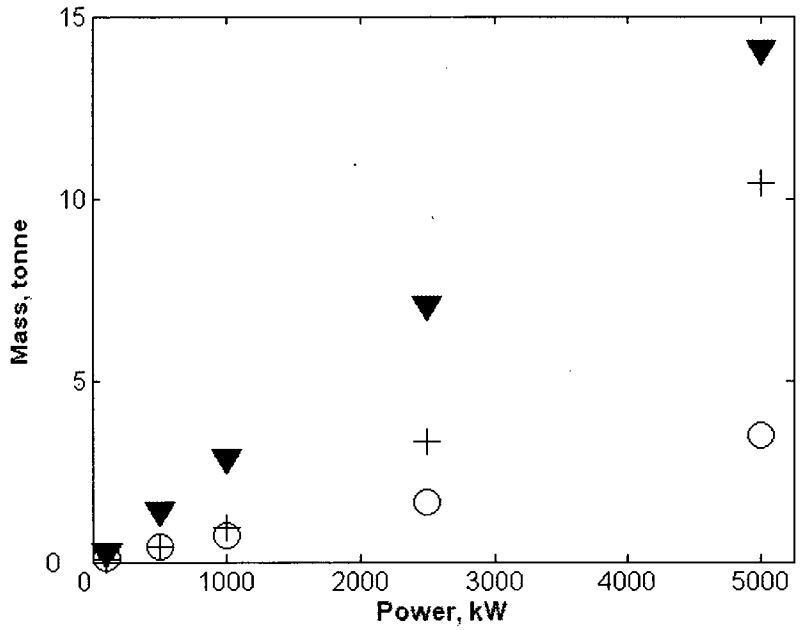

Figure 3.22. Breakdown of active mass: (▼) Iron, (+) Permanent Magnet, (O) Copper.

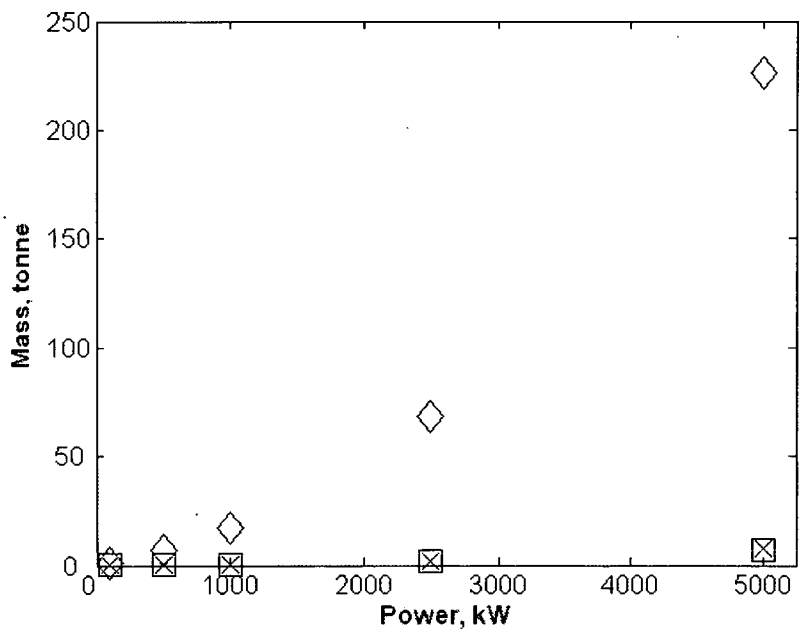

Figure 3.23. Breakdown of inactive mass: (◊) Rotor disc (□) Cylinder casing (×) Stator disc.

It is not easy to compare these results with existing megawatt direct drive wind turbines to give confidence in the results. The only large axial-flux generator used in wind turbines is in the Jeumont J48 750kW. There are no figures available for the mass of the generator in this turbine. However, the results are of the right size. For example the 1.8 MW and 4.5 MW machines built by Enercon have a nacelle weight (including rotor) of 133 and about 220 tonnes respectively [20]. It is not clear what proportion of the nacelle weight is equal to the generator only. Enercon generator technology is based on the field wound synchronous machine, which is expected to be heavier than PM machines. Given the uncertainties in the data on the Enercon machines it can be concluded that the results obtained using this model for the 1.8 MW and 4.5 MW ratings are comparable with similar direct drive machines. A Dutch company, Harakosan, has built a low speed radial-flux permanent magnet synchronous machine rated at 1.67 MW and according to [126] has a total mass (including inactive) of 47.2 tonnes. The axial-flux equivalent machine is 67% heavier. It must be noted that this is a comparison of an unoptimised and an optimised design and that the shaft radii and the allowable airgap deflections are very different. The model used gives masses of the right size and hence can be used with some confidence to provide a first order estimate of the structural mass of axial-flux PM machines.

3.5.2 Machine optimisation

When designing an axial-flux machine for a direct drive wind turbine, the machine designer is faced by a number of constraints and choices. The maximum rotor speed, ω, is often set by the tip speed of the rotor blades, leaving the designer to vary the torque, T, according to eqn. (3.24). The current loading, A, is limited by the Joule loss and the outer radius, a_r, must be small enough to fit into the wind turbine nacelle. Nacelle size is limited by transportation, lifting and aerodynamics requirements. Eqn. (3.24) implies that the maximum torque is produced when $k_r=1/\sqrt{3}$, however most

designers opt for a higher value (0.7-0.8) to reduce active material costs. In an application where the mass needs to be minimised, the designer is less interested in high torque and more keen on maximising torque per unit mass. The following discussions demonstrate why structural mass must be considered when minimising mass based on a_r, k_r and B_g.

3.5.2.1 Outer radius, a_r and PM radii ratio, k_r

A 100 kW machine running at 60 rpm must produce a torque of 15.9 kNm. A line of this constant torque based on eqn. (3.24) is plotted on a k_r vs. a_r chart (the thick line in Fig. 3.24a) with B_g = 0.33 T and A = 28 kA/m. The designer must choose an outer radius and the ratio of inner-to-outer radii somewhere on this line. To find where the lowest mass is visually, the torque per unit active mass is plotted on the same figure (the thin numbered contours). Based on active mass only, the value of k_r, which maximises the torque per unit active mass, is approximately equal to 0.47. Including the rotor structural mass in the torque per unit mass calculation gives Fig. 3.24b, from which the torque density is optimum when k_r=0.40.

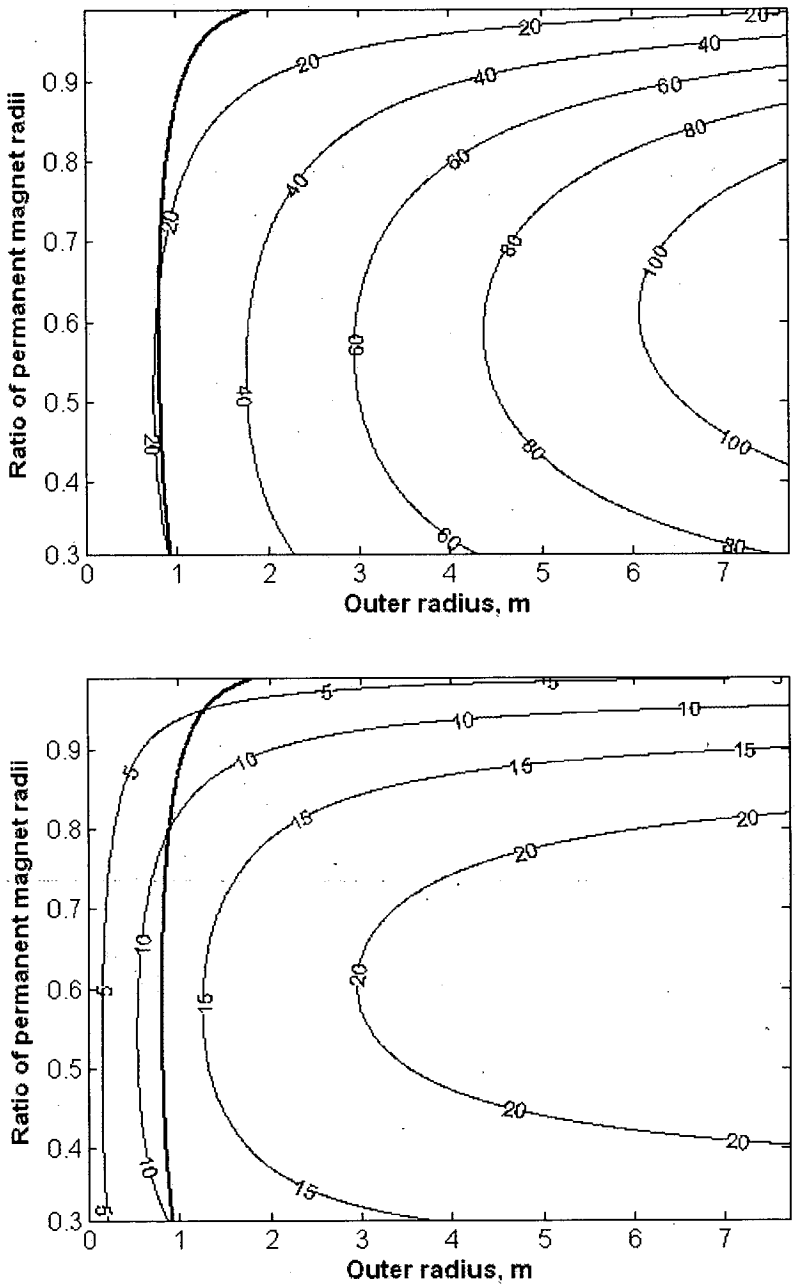

Figure 3.24. Torque and torque density plots (a) Active mass only (b) Active and inactive mass. Line of constant torque, T = 15.9 kNm (thick line), and contours of torque per unit mass (numbered), Nm/kg plotted for 100 kW machine at 60 rpm. Vertical axis: k_r, ratio of inner radius of rotor permanent magnets to rotor disc outer radius. Horizontal axis: a_r, rotor disc outer radius, m.

For the larger 2.5 MW machine (running at 19 rpm and producing a torque of 1.26 MNm), Fig. 3.25 shows the torque density contours with constant torque

lines for 1, 2 & 3 stages. The standard axial-flux machine with two rotors has one stage. For the single stage machine the torque density is optimised for an aspect ratio, k_r, equal to 0.74 based on active mass only (Fig. 3.25a). However, including the structural rotor mass (which dominates the stator structural mass) the designer would choose a smaller value of k_r = 0.63 (Fig. 3.25b). A torque per unit rotor structural mass plot has been generated for the 2.5 MW machine (Fig. 3.26), which is independent of machine design speed. This graph shows that considering only rotor inactive mass, a value of k_r = 0.63 results in the maximum torque per unit rotor inactive mass for all outer radii. This is not very different to the case when the total mass is considered because the inactive mass dominates.

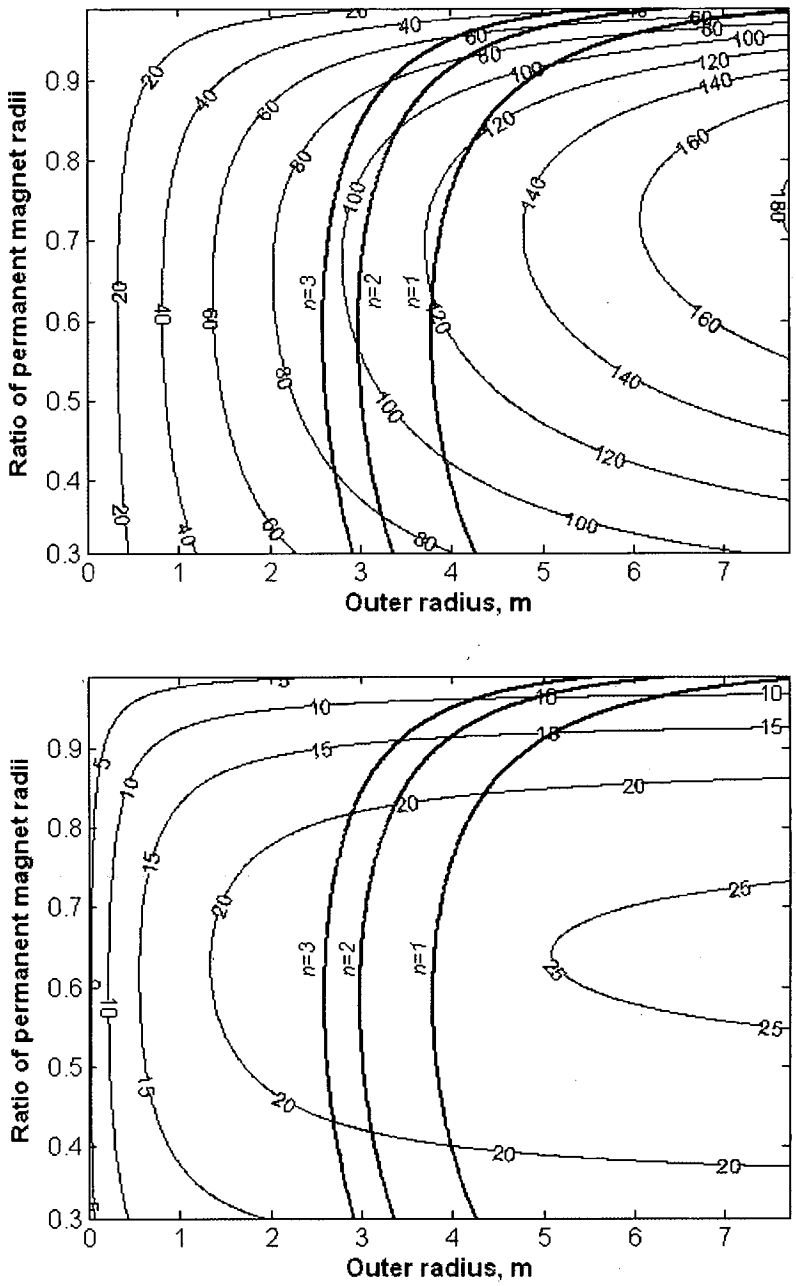

Figure 3.25. Torque and torque density plots. Line of constant torque, T = 1.26 MNm, $T_{n=2}$ = 628 kNm, $T_{n=3}$ = 419 kNm (thick lines) and contours of torque per mass (numbered), Nm/kg plotted for 2.5 MW machine at 19 rpm. Vertical axis: k_r, ratio of inner radius of rotor permanent magnets to rotor disc outer radius. Horizontal axis: a_r, rotor disc outer radius, m. (a) Active mass only (b) Active and inactive mass.

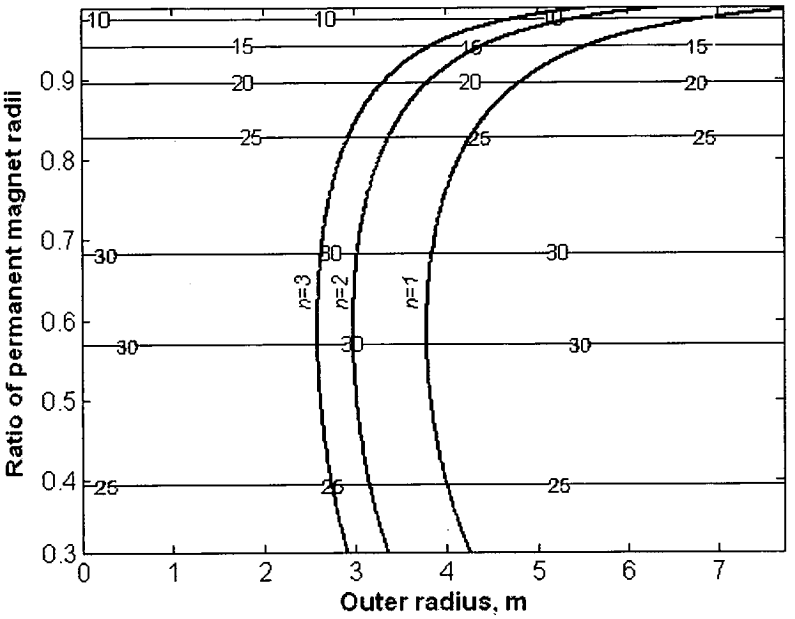

Figure 3.26 Torque and torque density plot for inactive mass. Line of constant torque, T=1.26MNm, $T_{n=2}$=628kNm, $T_{n=3}$=419kNm (thick lines) and contours of torque per inactive mass (numbered), Nm/kg plotted for 2.5 MW machine at 19 rpm. Vertical axis: k_r, ratio of inner radius of rotor permanent magnets to rotor disc outer radius. Horizontal axis: a_r, rotor disc outer radius, m.

On Fig. 3.25 lines of constant torque are included for multi-stage options. If the design is based upon the active mass only (Fig. 3.25a), the torque per unit mass is largest far to the right of the torque line. By introducing n identical machines coupled together, each producing 1.26 MNm/n torque, the designer would then shift the design to a lower torque per unit active mass. However, if the inactive mass is included (Fig. 3.25b), the torque per unit overall mass is fairly constant as the new machines are introduced. Hence if there are diameter restrictions a multi-stage design is an attractive option, without a significant increase in mass.

A true multistage design reduces the number of rotor discs that are required, as permanent magnets are mounted on both sides of the rotor (see Fig. 3.7 for an illustration). For example with two stages (n = 2), the number of rotor discs is n_{disc} = 3 (not $2n$ = 4 which would be the case if 2 similar machines

were coupled together); when n = 3, n_{disc} = 4 (Fig. 3.7). Table 3.3 shows the mass savings that would be produced when moving to a multistage design of a 2.5 MW machine (with k_r = 0.63). If circumstances allow sufficient axial length, then the designer would opt for a multistage machine based on this analysis.

Number of stages, n	**Torque per stage,** MNm	a_r, m	**Torque per unit mass,** Nm/kg	**Mass of rotor,** tonne	**Mass with $2n$ rotors,** tonne	**Mass with n_{disc} rotors,** tonne
1	1.26	3.90	24.2	20.7	52.0	52.0
2	0.628	3.10	23.4	10.4	53.8	43.4
3	0.419	2.71	22.9	6.94	55.1	41.2
4	0.314	2.46	22.5	5.18	55.8	40.3

Table 3.3. Multistage design mass savings for a 2.5 MW machine (k_r = 0.63).

3.5.2.2 Outer radius, a_r, and airgap flux density, B_g

Fig. 3.27 shows the variation of torque density with a_r and B_g for a fixed value of k_r, which is equal to 0.91 for the machine used in [111]. The constant torque line for this machine is also plotted. The torque per unit active mass plot (Fig. 3.27a) suggests that a low value of $B_g \approx 0.1$ T gives the highest torque density and hence lowest mass. However, including the inactive mass leads the designer to choose a higher value of $B_g \approx 0.22$ T (Fig. 3.27b). Both of these flux density values are surprisingly low, as most designs would have greater magnetic loading. One reason for this is that a lot of the main electrical parameters have been fixed to the Söderlund design, another is that space limitations may force designers to generally choose larger B_g values as opposed to a large outer radius. The low B_g is easily in the range of air-cored machines and there could be scope to further reduce active mass by eliminating the iron in the stator.

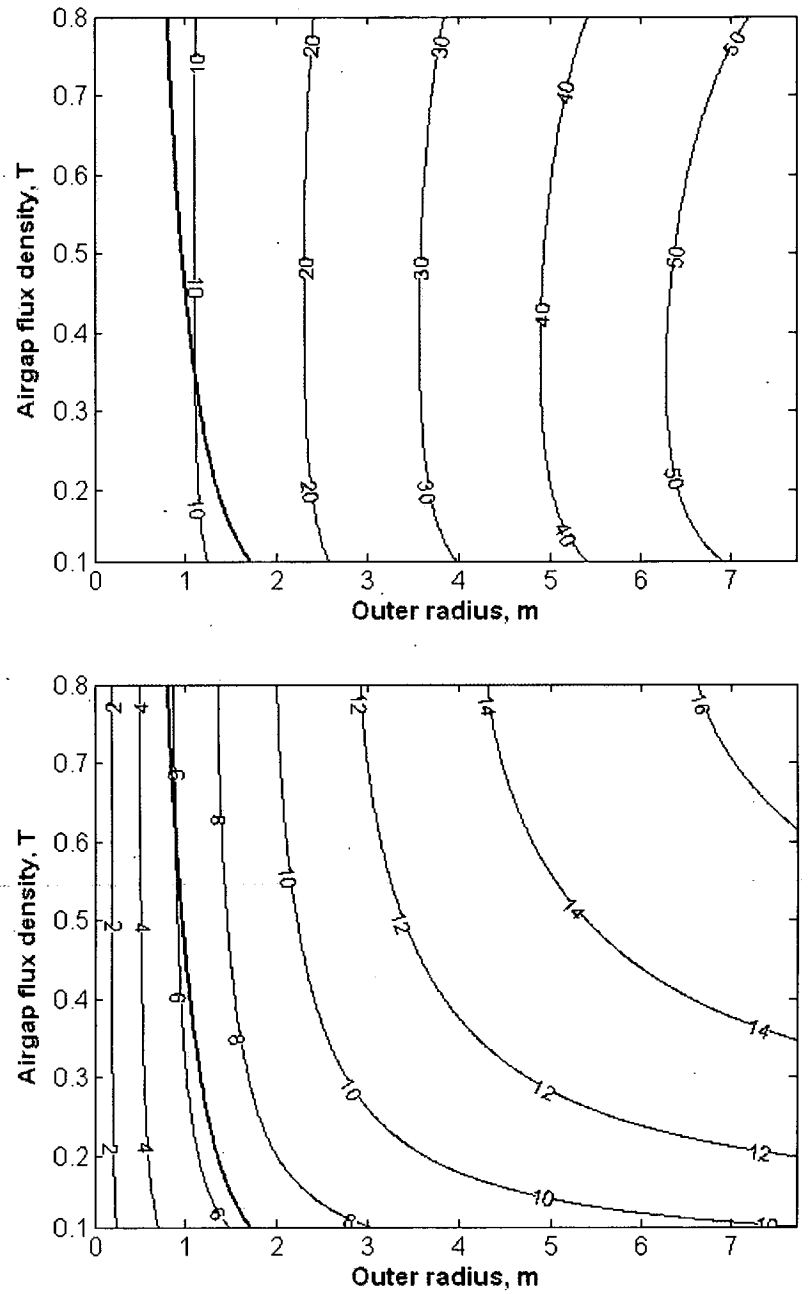

Figure 3.27. Torque and torque density plot. Line of constant torque, *T*=15.9 kNm (thick line), and contours of torque per unit mass (numbered), Nm/kg plotted for 100 kW machine at 60 rpm. Vertical axis: B_g, airgap flux density, T. Horizontal axis: a_r, rotor disc outer radius, m. (a) Active mass only (b) Active and inactive mass.

3.6 Conclusions

In this chapter the importance of including the inactive mass in the design of axial-flux machines has been demonstrated, particularly in determining key dimensions such as the ratio of rotor inner-to-outer radius to optimise the torque density. Well established analytical structural models have been modified and applied to link airgap deflections to key parameters such as rotor and stator disc thickness and the size of support structures. A comparison of the proposed analytical structural models with finite element models and existing machines shows that the expressions presented can be used with confidence in the early stages of the design process. Rotor and stator disc models presented in this chapter give excellent results compared with finite element models and published results. The beam and casing models provide less convincing results, but as the rotor disc mass dominates, the overall effect is to closely predict the proportion of mass needed to limit airgap deflection. Using the structural models in the design of a series of typical ratings for wind turbines it has been shown that a significant reduction in mass can be achieved by using multiple stages, but this conclusion could only have been arrived at if the inactive mass is included in the design calculations.

Chapter 4

Radial-flux machine polynomial modelling

4.1 Introduction

In Chapter 3, structural dimensions and the normal component of Maxwell stress were linked to airgap deflection in axial-flux machines. By using circular plate theory from solid mechanics, the impact of electrical and magnetic design on inactive and overall mass was investigated. Most low speed, high torque generators for direct drive wind turbines are of the radial-flux type. Fig. 4.1. shows a wind turbine with a wound rotor radial-flux machine produced by Enercon and another wind turbine with a permanent magnet machine sold by Harakosan.

Radial-flux machines are typically made up of an inner rotor and an outer stator (Figs. 4.2). The machine rotor is generally a cylinder (with the electrical field winding or permanent magnets) connected to the shaft by a solid disc. Surrounding this is the stator which is also made up of a cylinder held by a 'spider' of six to eight support arms (for example those shown in Figs. 4.3 and 4.4) [20],[59]. Fig. 4.5 represents a typical example and there are likely to be variations depending upon manufacturer. The rotor could equally employ a spider construction rather than a disc. Two different structures were chosen to demonstrate the technique. It should also be noted that this technique is being proposed for the first stage in the design process, when the designer simply wants a first order estimate of machine mass.

Figure 4.1. Enercon E-88 2MW wound rotor direct-drive wind turbine *(left)* and Harakosan Z-72 2MW permanent magnet direct-drive wind turbine *(right)*.

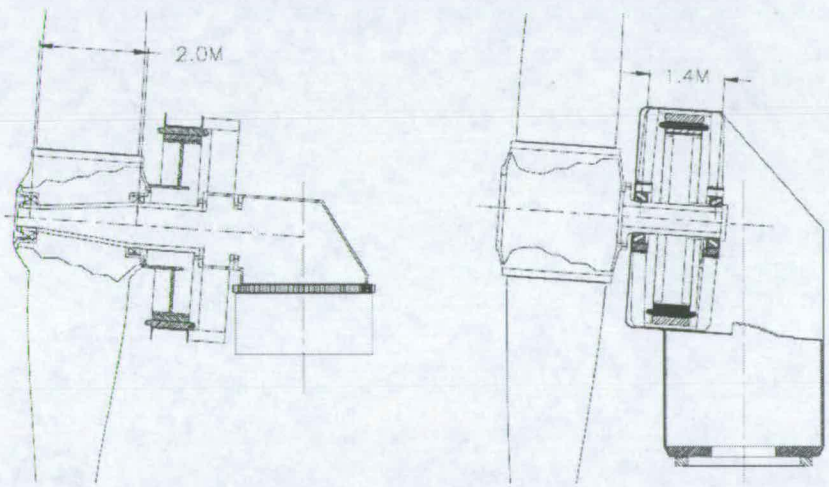

Figure 4.2. Alternative direct-drive configurations [20], inner rotor (*left*) and outer rotor (*right*)

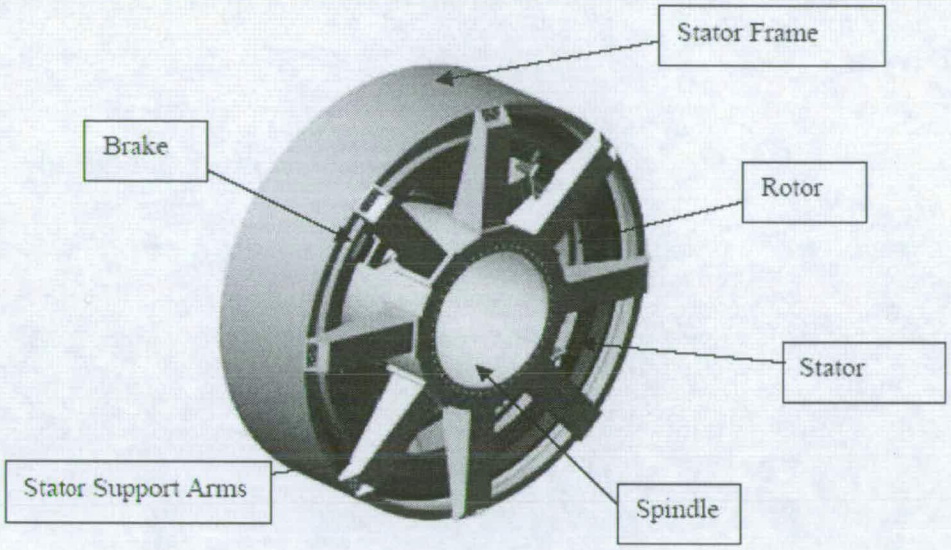

Figure 4.3. Permanent magnet direct drive generator from WindPACT drive train study [20].

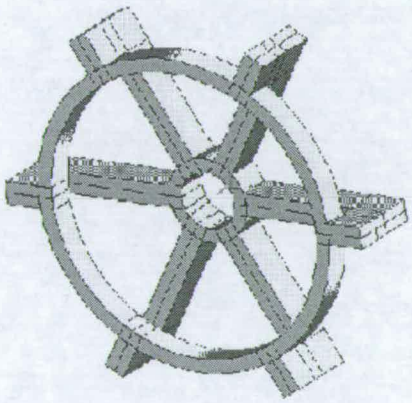

Figure 4.4. Geometry model of stator supporting structure [59].

The structure of the radial-flux machine is more complex than that of the axial-flux machine and so it is not possible to apply one analytical technique to the whole machine (as is the case with the axial-flux machine, in which circular plate theory was used). However, solid mechanics provides us with some techniques for treating similar solid shapes. A thin-walled cylindrical pressure vessel (that is when the radius to cylinder thickness ratio R/t>10) gives a deflection, u, according to [101],

$$u = \frac{qR^2}{Et} \quad (4.1)$$

where R is the radius, q is the pressure, t is the cylinder thickness (in machine terms the rotor or stator back thickness) and E is the Young's Modulus. There are several reasons that this expression is insufficient. There is no term for the length of the cylinder - it is expected that as the axial length increases so too will the problems caused by the weight of the structure itself. Another problem is that the size of the rotor disc and the stator support arms are effectively ignored. These parts deal with the shear stress (shown in Fig. 4.6) and gravity. Any asymmetry in the rotor or stator can lead to a tipping moment (Fig. 4.7).

Instead of traditional analytical expressions such as eqn. (4.1) a different strategy is needed. In this chapter a polynomial modelling technique taken from [56] is used to model the deflection. This function linking the structure and forces to airgap deflection is synthesised from the results of many pre-analysed finite element models.

To examine the effectiveness of this technique a 1.5 MW permanent magnet synchronous generator for a wind turbine is modelled (active parts are based on a design presented by Versteegh in [126], inactive parts are found with more intensive finite element analysis). Following this benchmarking step, the polynomial technique is used in the design of a range of direct drive wind turbines. Although the designs presented here are for permanent magnet machines, this technique is equally applicable to radial-flux machines which have a wound rotor.

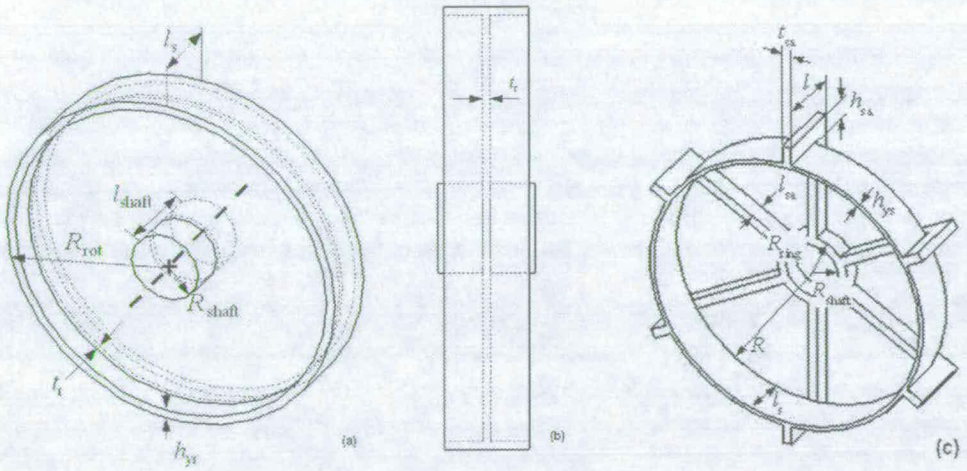

Figure 4.5. Radial-flux machine models showing dimensions: (a) Rotor; (b) Rotor from side; (c) Stator.

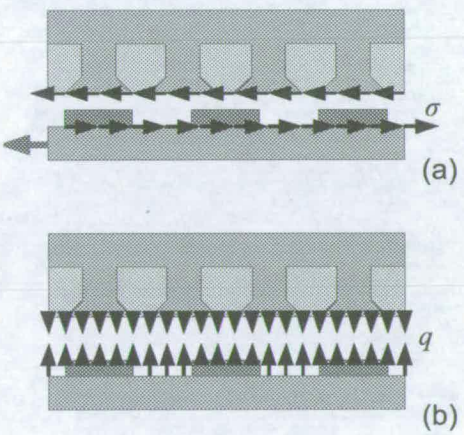

Figure 4.6. Shear stress, σ, and normal component of Maxwell stress, q, on section of radial-flux machine.

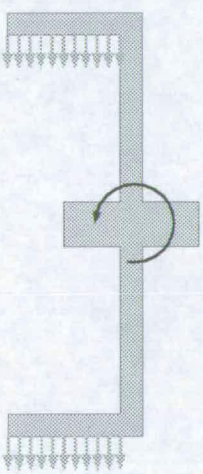

Figure 4.7. Tipping moment due to rotor asymmetry and gravity.

4.2 Structural Modelling

In order to model the structures shown in Fig. 4.5 a finite element based approach is used, but utilised such that it can be used rapidly in the design office. The approach is based upon taking a large number of experimental or simulation results and synthesising a simple function. An alternative to this would be to generate a look-up table from pre-analysed models, but this would require many more input data points (particularly as the number of variables increases). This section of the chapter lays out this method as applied to the radial-flux machine structure.

There is an unlimited range of possible rotor and stator structure designs and so one design was arbitrarily chosen for each. The dimensions that describe these models can be categorised into those that are fundamental variables and those variables that are derived from these fundamental variables. For both models four fundamental dimensions are chosen to keep the polynomial modelling simple later on. The rotor (Fig. 4.5(a,b)) is described by axial length, l_s, the airgap radius, R, rotor disc thickness, t_r, and rotor back thickness, h_{yr}. The stator (Fig. 4.5(c)) is similarly described by axial length, l_s, the airgap radius, R, support arm thickness, t_{sa}, and stator back thickness, h_{ys}. Derived dimensions are shown in Table 4.1.

A normal stress q is applied to the outside of the rotor cylinder and to the inside of the stator cylinder (as shown in Fig. 4.6) bringing the total number of parameters that describe each model to five.

Dimension	Expression
Rotor	
Rotor outer radius, R_{rot}	$R_{rot} = 0.995R$
Rotor shaft radius, R_{shaft}	$R_{shaft} = 0.2R$
Rotor shaft length, l_{shaft}	$l_{shaft} = 2R_{shaft} + t_r$
Stator	
Stator support arm height, h_{sa}	$h_{sa} = 2t_{sa}$
Stator support arm length, l_{sa}	$l_{sa} = 2t_{sa}$
Stator support arm ring outer radius, R_{ring}	$R_{ring} = R_{shaft} + h_{sa}$
Stator total length, l	$l = l_s + l_{sa}$

Table 4.1. Rotor and stator derived dimensions.

The main role of the machine structure is to maintain the airgap clearance; it follows that the performance quantity is the deflection into the airgap, u. It is normal for the designer to stipulate beforehand the permissible deflection as a percentage of the airgap clearance, c. This research is primarily interested in multi-MW direct drive machines so the range of parameters was chosen accordingly (shown in Table 4.2). The rotor and stator back thicknesses include active material and inactive material, which is why the maximum values are so large.

Parameter	Minimum	Maximum
q (10^3 Pa)	40	700
R (m)	0.5	5.5
l_s (m)	0.5	1.5
h_{yr} (m)	0.002	0.03
h_{ys} (m)	0.002	0.28
t_r (m)	0.01	0.14
t_{sa} (m)	0.03	0.7

Table 4.2. Parameter ranges.

Generalised models of the rotor and stator were created in a 3D CAD program (SolidWorks) and then transferred to a finite element package (COSMOSWorks). Here the appropriate constraints and forces (Maxwell stress q and gravity g) were applied and material constants were assigned. In this case the axis of the machine is set at 5° to the horizontal (this models the tilt which is found in most wind turbines). 648 models (for both the rotor and stator) were analysed using the FE package. The results were extracted and saved. In this case a polynomial is used to model the results. The deflection u is a multiple sum of products of a set of coefficients and the 5 design parameters along with a dummy parameter $x_0 = 1$. In the rotor case then $x_1 = q$, $x_2 = R$, $x_3 = l_s$, $x_4 = t_r$ and $x_5 = h_{yr}$. The quadratic function is shown in eqn. (4.2),

$$u_p = \sum_{i=0}^{5}\sum_{j=i}^{5} a_{i,j} x_i x_j \,. \tag{4.2}$$

Similar expressions can be found for cubic and other higher order polynomial functions. At this stage the coefficients (denoted in eqn. (4.2) by $a_{i,j}$) are unknown. The method of least squares is used to find the polynomial which gives the best fit to the results.

First the square of the difference between the input data point u and the value given by the polynomial u_p is calculated. The sum of the 'squared errors' in eqn. (4.3) is differentiated by the polynomial coefficients and in turn set these differentials to zero (eqn. (4.4)). The polynomial coefficients $a_{i,j}$ can then be easily calculated using matrix algebra as in [56].

$$S = \sum_n (u_p - u)^2 \tag{4.3}$$

$$\frac{\partial S}{\partial a_{i,j}} = 0 \tag{4.4}$$

With 5 input variables, the number of coefficients for each polynomial is given in Table 4.3:

Polynomial order	Number of coefficients
Linear	6
Quadratic	21
Cubic	56
4th order	126
5th order	252
6th order	462

Table 4.3. Number of coefficients for 5 variable polynomials

To ensure a good fit it is necessary to use about twice as many input data points as there are coefficients [56]. So, for example, to produce a 5 variable quadratic $2 \times 21 = 42$ input data points should be used.

These different models were based on 8 radius values (R = 0.5, 1.0, 1.5, 2.0, 2.5, 3.5, 4.5 and 5.5 m) and 3 values for each of the other parameters. With the coefficients of each polynomial established, the polynomial function

coefficients can be used in a spreadsheet to quickly analyse the performance of the machine structure.

4.3 Results

4.3.1 Benchmark case study: 1.5MW wind turbine

The rotor and stator of a 1.5 MW machine (based on the design introduced in [126]) is modelled in this section. In this case, three of the five input parameters are specified as: R = 1.6 m, l_s = 1.2 m and q = 224 kPa (corresponding to B_g = 0.75 T). This leaves t_r, h_{yr}, t_{sa} and h_{ys} unspecified (two parameters each for the rotor and stator). Also the designed deflection into the airgap is unknown, but results for different deflections will be presented. The minimum inactive mass can be found by plotting the airgap deflection and the inactive mass with the two unspecified parameters on the horizontal and vertical axes. Eqns. (4.5) and (4.6) give the inactive mass of the rotor and stator respectively. The density of iron, ρ is taken to be 7850 kg/m^3.

$$m_{\text{in,rot}} = \rho\pi\left(t_r R_{\text{rot}}^{\ 2} + l\{2R_{\text{rot}}h_{yr} - h_{yr}^2\}\right) \tag{4.5}$$

$$m_{\text{in,stat}} = \rho\{12t_{sa}^2(\tfrac{4}{5}R + h_{ys} + l_s) + \pi[h_{ys}l_s(2R+1) + 2t_{sa}^2(\tfrac{R}{5} + t_{sa})]\} \tag{4.6}$$

Separate finite element models were also run to provide additional benchmarking for this case study. These had R, l_s and q values fixed as above, but with 10 values each of the unspecified parameters (10 different t_r values and 10 different h_{yr} values giving 100 combinations for the rotor case). The contours of the inactive mass and the airgap deflection can be plotted on a graph similar to Fig. 4.8 and compared with the results of the polynomial modelling.

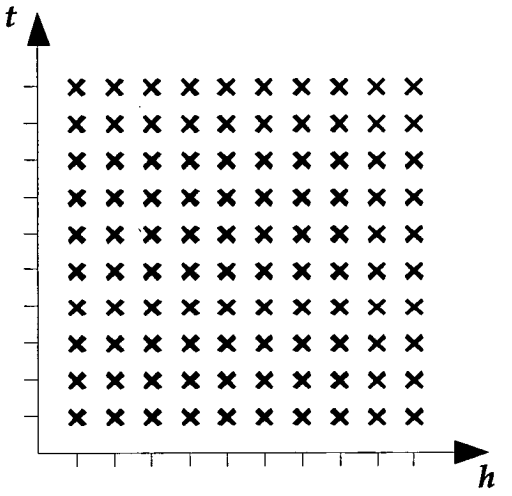

Figure 4.8. Design points for comparison contours.

According to Versteegh the airgap clearance, c is 3 mm for this machine. Curves for a design deflection of u = 0.75 mm (a quarter of the airgap clearance) will be plotted along with curves of u = 0.5 mm and u = 1 mm.

4.3.2 Rotor Modelling

Fig. 4.9 (a) shows the results of a cubic polynomial - for a machine with R = 1.6 m, l_s = 1.2 m and q = 224 kPa - generated from a large data set (425 points with 6 radii values ranging from R = 0.5-5.5 m). The thin lines show the rotor inactive mass labeled in kg; the 3 thick contours give the airgap deflection labeled in m. This gives a minimum inactive mass of about 1×10^3 kg when h_{yr} = 0.004 m and t_r = 0.01 m. If the machine designer is not interested in the larger machine radii then a more compact data set may be more appropriate. Fig. 4.10 (a) gives the deflection estimated by a quadratic synthesised from a slightly smaller and more concentrated data set centered on R = 1.5 m (405 points with R = 0.5, 1.0, 1.5, 2.0 and 2.5 m). This time the polynomial predicts a larger inactive mass of slightly less than 1.9×10^3 kg with h_{yr} = 0.06 m and t_r = 0.023 m. Using fewer input data points is quicker both in terms of initial finite element runs and later processing. Fig. 4.11 (a) shows the quadratic produced from 243 input points (with R = 0.5, 1.5 and 2.5 m), giving a

minimum inactive mass of about 2.1×10^3 kg (with a design of h_{yr} = 0.07 m and t_r = 0.024 m). This final polynomial is the most economical and gives a similar error to that produced by the cubic in Fig. 4.9 (a). The deflection curves in Fig. 4.12 were found by running extra finite element analyses with fixed R, l_s and q parameters and varying h_{yr} and t_r and applying a contour function to the results. The u = 0.00075 m curve gives a minimum inactive mass of slightly more than 1.6×10^3 kg (when h_{yr} = 0.08 m and t_r = 0.014 m).

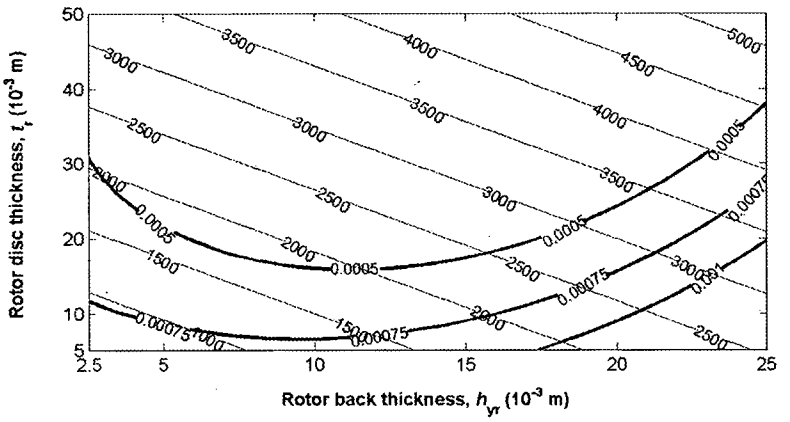

(a)

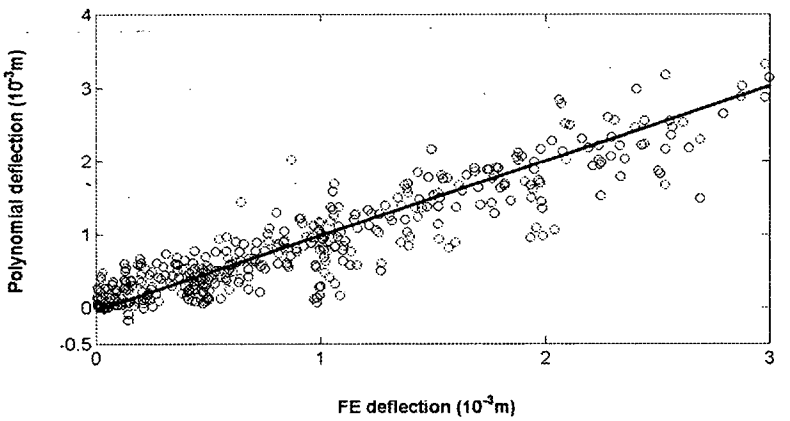

(b)

Figure 4.9. Rotor cubic polynomial (a) Deflection and mass plotted against t_r and h_{yr} (inputs with R = 0.5, 1.5, 2.5, 3.5, 4.5 and 5.5 m) (b) Polynomial deflection against FE deflection, RMS error = 33.6%.

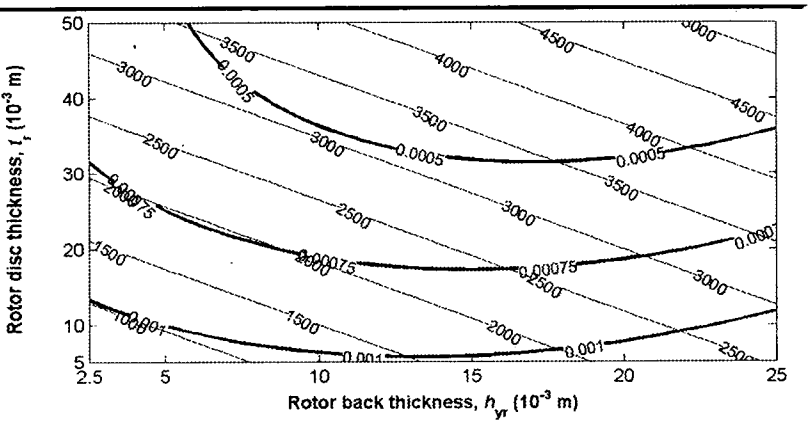

(a)

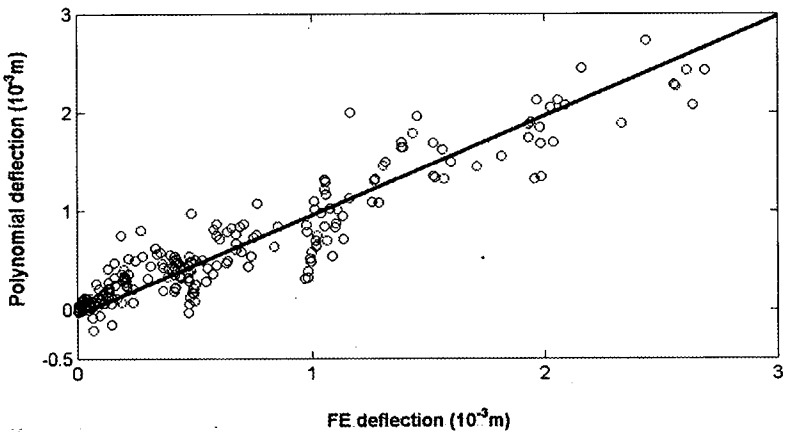

(b)

Figure 4.10. Rotor quadratic polynomial (a) Deflection and mass plotted against t_r and h_{yr} (inputs with R = 0.5, 1.0, 1.5, 2.0 and 2.5 m) (b) Polynomial deflection against FE deflection, RMS error = 43.9%.

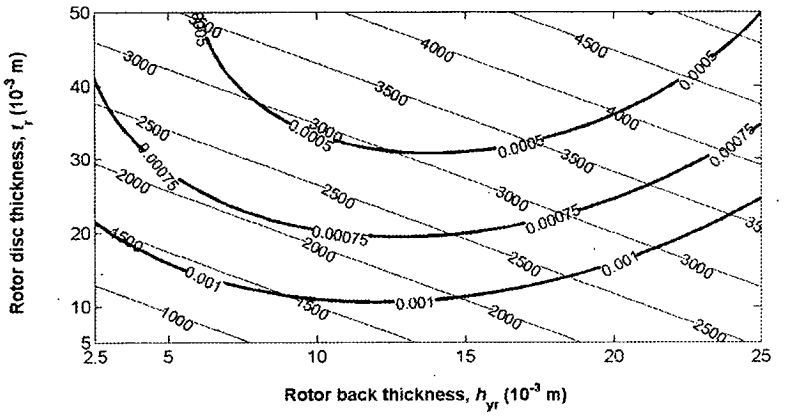

(a)

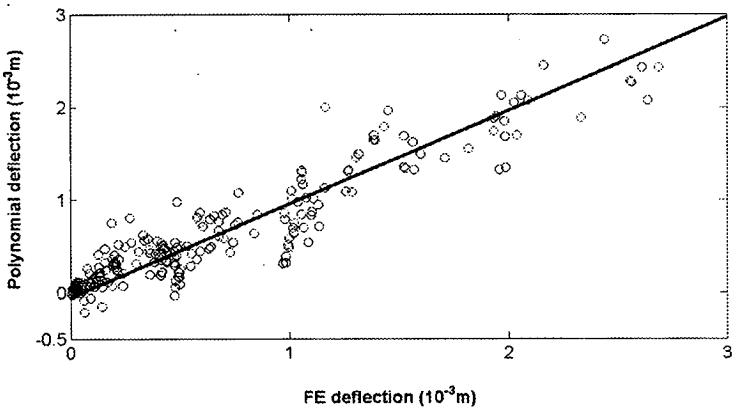

(b)

Figure 4.11. Rotor quadratic polynomial (a) Deflection and mass plotted against t_r and h_{yr} (inputs with R = 0.5, 1.5 and 2.5 m) (b) Polynomial deflection against FE deflection, RMS error = 35.1%.

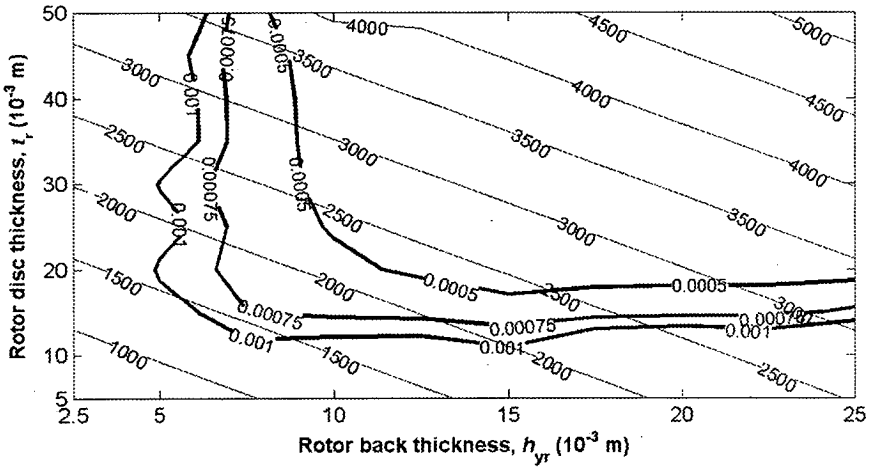

Figure 4.12. Graph showing contour plot of rotor deflection produced from finite element results with R = 1.6 m, l_s = 1.2 m, q = 224 kPa, h_{yr} = 0.0025-0.025 m and t_r = 0.005-0.05 m.

4.3.3 Stator Modelling

The stator can be investigated in a similar way to the rotor. Fig. 4.13 (a) gives the 5th order deflection curves for the stator produced from a relatively narrow input data set (351 data points with R = 0.5, 1.0, 1.5, 2.0 and 2.5 m centered on R = 1.5 m). The minimum inactive mass is just under 3.7×10^3 kg (with h_{ys} = 0.02 m and t_{sa} = 0.075 m). A similar set of curves is produced in Fig. 4.14 (a) from a smaller set of data (204 points with R = 0.5, 1.5 and 2.5 m centered on R = 1.5 m). Here the minimum mass is just over 5×10^3 kg, giving close agreement to that found directly with the finite element results in Fig. 4.15.

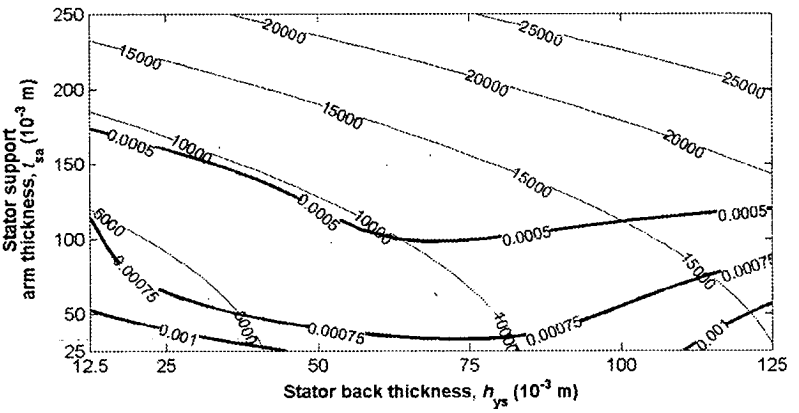

(a)

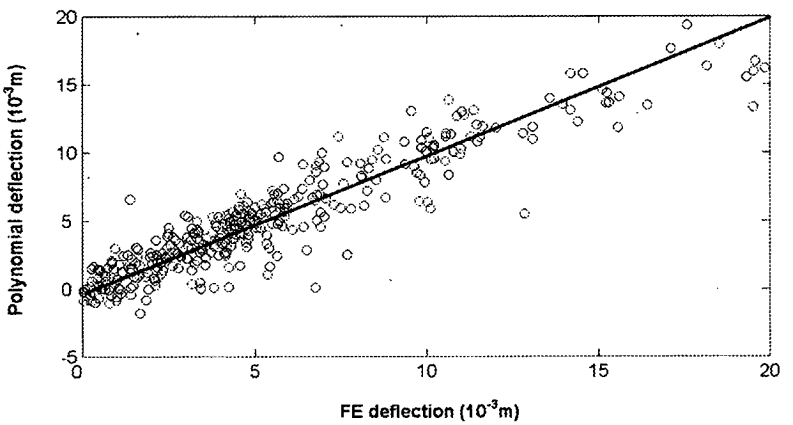

(b)

Figure 4.13. Stator 5th order polynomial (a) Deflection and mass plotted against t_{sa} and h_{ys} (inputs with R = 0.5, 1.0, 1.5, 2.0 and 2.5 m) (b) Polynomial deflection against FE deflection, RMS error = 29.8%.

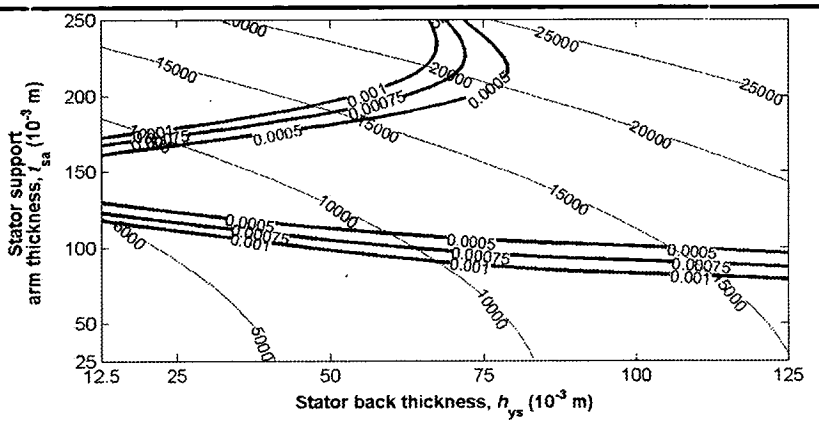

(a)

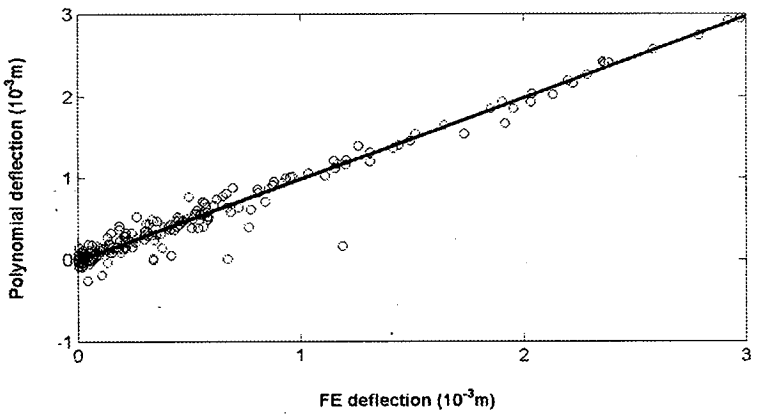

(b)

Figure 4.14. Stator 5th order polynomial (a) Deflection and mass plotted against t_{sa} and h_{ys} (inputs with R = 0.5, 1.5 and 2.5 m) (b) Polynomial deflection against FE deflection, RMS error = 23.9%.

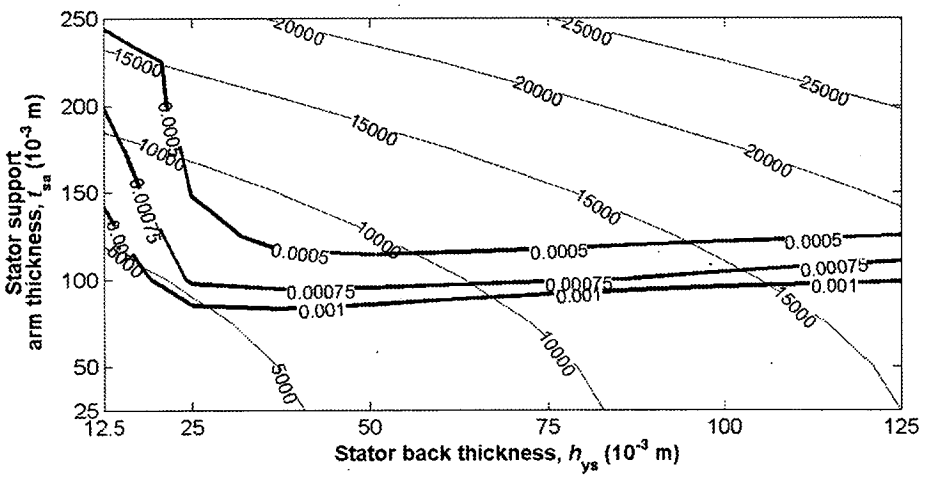

Figure 4.15. Graph showing contour plot of rotor deflection produced from finite element results with R = 1.6 m, l_s = 1.2 m, q = 224 kPa, h_{ys} = 0.0125-0.125 m and t_{sa} = 0.025-0.25 m.

4.3.4 Discussion

4.3.4.1 Trade off between accuracy and speed

Compared to the polynomial modelling in [56] the errors here are large (the best have an RMS error of 20-35%). This might be because these are quite sophisticated structures that have been reduced down to just 5 variables. The stator - which is structurally more complicated than the rotor - requires a polynomial of high order to minimise the error. Is this a problem? This technique was selected because it provides a quick estimation of inactive mass early on in the design process. As such, sacrificing some accuracy for speediness is appropriate.

There are some steps that can be taken to improve the quality of the polynomial modelling results. For example, the choice of size (and breadth) of data set has an effect on the results. By choosing a very large data set - as used in Fig. 4.9 - the designer has one polynomial for all the design space and so the modelling effort is reduced. In the stator case small deflections were swamped by the large deflections (often produced by the machines with the largest radii) and so narrower data sets were used. These smaller data sets, on the other hand, need several polynomials to cover the whole design space and therefore require more work. Generally, when using the same order of polynomial, better results are produced with smaller RMS errors using fewer and more concentrated values of R.

4.3.4.2 Choice of deflection value

The predicted overall mass (including the active mass) for the case study machine is 26.6×10^3 kg - significantly less than the 47.2×10^3 kg reported in [126]. It must be remembered that this is a different design, possibly with different materials. More importantly, an arbitrary deflection of 25% of the airgap clearance has been chosen - the inactive mass will be greater when the deflection is limited to a smaller value. The structure in [126] is probably designed for a smaller design deflection. Indeed this must be the case, as the

finite element results in Figs. 4.12 and 4.15 - not just the polynomial modelling - give very small mass. Table 4.4 shows the total mass found when the deflection, u, is limited to 10% and 5% of the airgap clearance, c. When both the rotor and stator are allowed to deflect by 5% into the airgap the total mass is 43.5×10^3 kg which is close to the machine generator mass in [126]. A deflection of 5% will be used henceforth in this chapter.

u/c	25%	10%	5%	Versteegh
Mass (10^3 kg)	26.6	31.9	43.5	47.2

Table 4.4. Mass and deflection comparison.

4.3.4.3 Materials

One of the shortcomings of this method is that the polynomial modelling is based on finite element analysis of two particular models. These are modelled with specific material properties such as density, Young's Modulus and Poisson ratio. Although once the polynomial coefficients are found the method is quick and easy, it can take a long time to carry out all of the finite element analysis. If the designer wants to use a different material then this method is quite inflexible, whereas an analytical method may be quicker to use.

4.4 Direct drive wind turbine designs

In this section a number of direct drive radial-flux permanent magnet generators are designed based on the machine in [126] using the design program in [41] and machine speeds from [80]. In addition, the model is used to investigate structural design parameters.

4.4.1 Range of wind turbine designs

The airgap flux density, current density, airgap clearance to airgap radius ratio and axial length to airgap diameter ratio are kept constant for all designs (B_g = 0.84 T; J = 2.1 A/mm^2; $c = R$ / 500; $K_{rad} = l_s$ / $2R$ = 0.375). Each design then has the same normal stress, q. Table 4.5 shows the details of the

machine designs. As the power rating increases from 500 kW to 5 MW the turbine speed decreases (to limit the tip speed of the turbine blades to about 75 m/s). This means that the torque rating increases at a greater rate than the power rating.

The inactive mass is found for each case as described in section 3. Stator inactive mass is much larger than the rotor inactive mass. For the lowest torque machine (500 kW) the active mass dominates the inactive mass. As the torque rating increases the inactive mass starts to dominate until it is 82% of the total mass (for the 5 MW machine).

Power (MW)	0.5	1.0	2.5	5.0
N (rpm)	38	30	19	11.5
T (kN·m)	126	318	1260	4150
l_s (m)	0.68	0.90	1.38	2.04
R (m)	0.90	1.20	1.84	2.72
u (10^{-3} m)	0.18	0.24	0.37	0.54
$m_{in,rot}$ (10^3 kg)	0.8 (9%)	1.6 (8%)	6.2 (9%)	20.1 (8%)
$m_{in,stat}$ (10^3 kg)	2.6 (31%)	8.8 (46%)	40.8 (60%)	195.9 (74%)
m_{act} (10^3 kg)	5.0 (60%)	8.9 (46%)	21.3 (31%)	46.6 (18%)
m_{tot} (10^3 kg)	8.3	19.3	68.3	262.6

Table 4.5. Rotor and stator inactive, active and total mass.

It should be noted that this is applicable only to this particular design, with a fixed electrical and magnetic loading, aspect ratio, structural design and permissible deflection: the ratio of active to inactive mass will change if these design parameters are altered.

4.4.2 Aspect ratio and the effect on total mass

In this section the structural model is used to help make a design decision. One choice that the machine designer faces is the aspect ratio, K_{rad} (the ratio of axial length to the machine diameter). A thin disc has an aspect ratio approaching zero, an object like a pencil has an aspect ratio approaching infinity. A typical radial-flux machine lies somewhere in between these extremes. In section 4.1 K_{rad} = 0.375 which is similar to that used in a commercial design [126].

In low speed machines the designer seeks the highest possible torque so as to produce high power. The torque can be increased by using high shear stress, σ, axial length, l_s, and airgap radius, R as shown in eqn. (4.7).

$$T = 2\pi\sigma l_s R^2 \tag{4.7}$$

Torque is proportional to the square of airgap radius because a greater R increases both the airgap surface area and the moment arm at which the force acts. A large airgap radius leads to lower shear stress requirements, meaning that the active mass can be reduced. It should be no surprise then that small aspect ratios yield the greatest torque per unit active mass. Dubois found that radial-flux permanent magnet machines with $K_{rad} \approx 0.1$ tend to give the optimum torque per unit active mass and cost per torque [41].

Often the machine designer is limited by the maximum outer radius (for example the size of transportation containers). If inactive mass is greater than active mass for the larger machine sizes then the designer needs to investigate the effect of K_{rad} on inactive mass. This will then lead to the design with the greatest torque per unit *total* mass.

Fig. 4.16 shows the active and inactive masses of a range of machines designed with K_{rad} = 0.1, 0.2, 0.3, 0.375 and 0.5. Comparing the active masses, m_{act}, the designs with K_{rad} = 0.1 are the lightest in each case (Fig. 4.16(a)). As the aspect ratio increases the rotor inactive mass tends to decrease (for a 5 MW machine in Fig. 4.16(b): with K_{rad} = 0.1 $m_{in,\,rot} = 28.1\times10^3$ kg; with K_{rad} = 0.5 $m_{in,rot} = 18.5\times10^3$ kg). This suggests that the inactive mass of the rotor is dependent on the machine radius (as the radius increases, the mass of both the cylinder and the disc parts of the rotor structure also grows). To reduce the rotor inactive mass then the designer should choose a larger aspect ratio.

However, as has been seen in section 4.1 the stator structure dominates the inactive mass. The trends in the stator structure are more difficult to discern for the smaller machines in Fig. 4.16(c) so this part of the discussion will

concentrate on the 2.5 and 5 MW machines. The maximum stator inactive mass is found when K_{rad} = 0.5 which is markedly different to the rotor. The stator is supported on one side only and as the axial length, l_s increases (with increasing K_{rad}) the center of mass moves further away from the spider and the support must be more rigid to prevent the stator from tipping into the airgap. This is compounded by the fact that the design deflection is a fixed proportion of the airgap radius and so designs with smaller radii (those with high K_{rad}) must produce smaller deflections. As K_{rad} approaches 0, the stator inactive mass also increases slightly. As the airgap radius, R, increases so too does the length and mass of the spider arms, but the allowable deflection is greater (and so the increase in mass is only slight). The minimum stator inactive mass for the 2.5 MW is at K_{rad} = 0.3 (34.3×10^3 kg) and at K_{rad} = 0.2 for the 5 MW machine (151×10^3 kg).

The total mass is dominated by the active and the stator inactive mass which are both minimum at low K_{rad} and so the curves in Fig. 4.16(d) are minimum at K_{rad} = 0.1-0.2 (the total mass curves are flat in this range). A machine designer would choose K_{rad} < 0.1 based on only the active materials (extrapolating K_{rad} towards 0 in Fig. 4.16(a)). The difference between the two K_{rad} values shows the importance of taking the inactive mass into account.

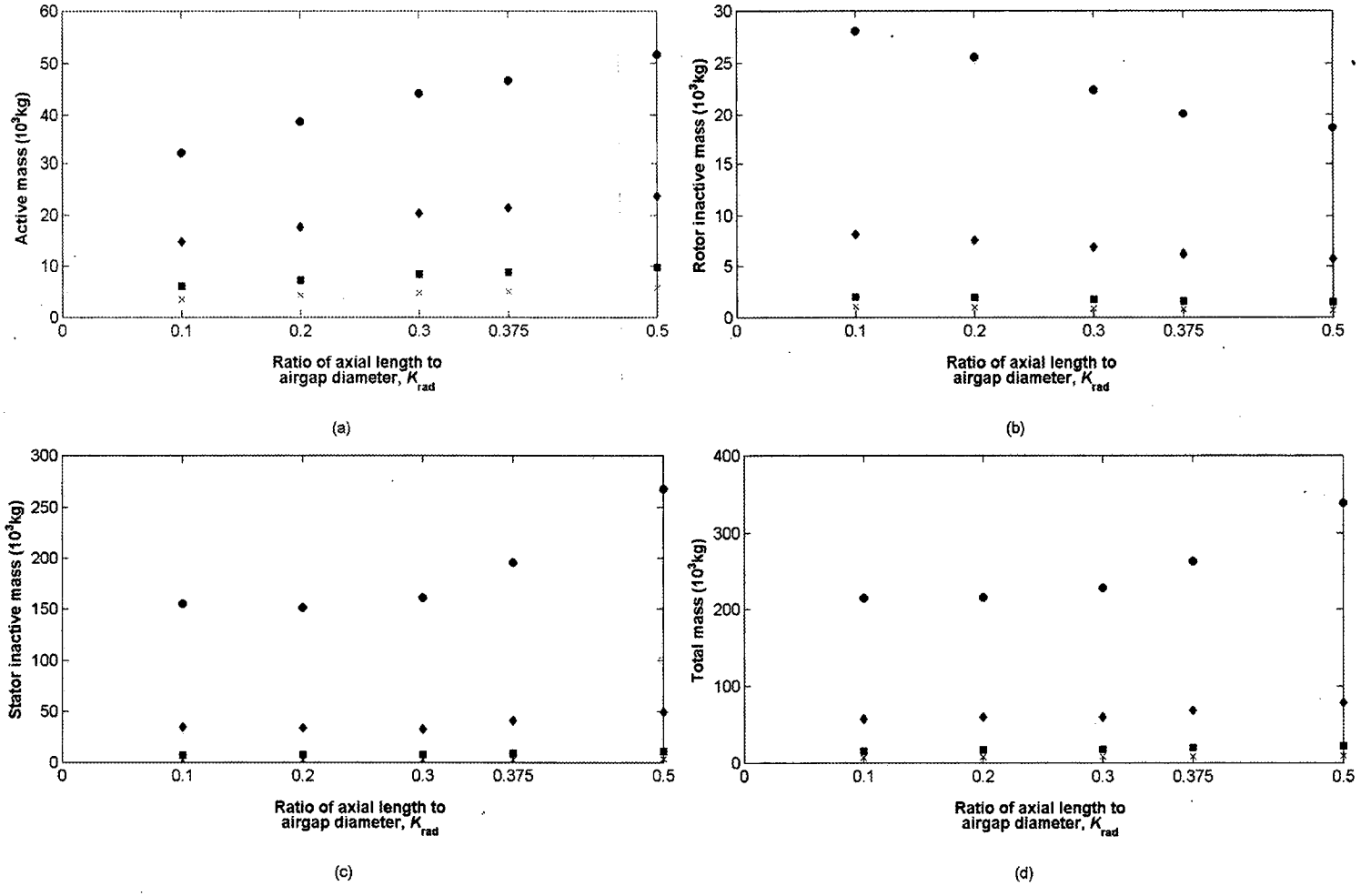

Figure 4.16. Machine mass plotted for a range of values of ratio of axial length to airgap diameter (a) Active mass (b) Rotor inactive mass (c) Stator inactive mass (d) Total mass. (×) 500kW (■) 1MW (♦) 2.5MW (●) 5MW

4.5 Conclusions

Direct drive wind turbines suffer because they require large and heavy generators. Inactive mass is a significant component of total mass in radial-flux machines, becoming dominant for high torque machines. An ability to estimate the total mass (including the inactive mass of the machine) early on in the design process is important when trying to produce a lightweight design. In this chapter a model of the structure based upon finite element analysis was used to investigate the impact of inactive mass on design. A range of machines (from 500 kW to 5 MW) were designed showing that the stator inactive mass is greater than that of the rotor inactive mass and that the combined rotor and stator inactive mass is at least 82% of the total mass for a 5 MW machine. It has been shown that the K_{rad} value that gives the optimum torque per unit mass is different depending on whether the inactive mass is included or not. The best torque per unit active mass is achieved with the lowest possible K_{rad} value; the maximum torque per unit total mass is achieved with K_{rad} = 0.1-0.2.

Chapter 5

Analytical treatment of radial-flux machine structures

In order to design lightweight direct drive generators for wind turbines, the designer must be able to model both active and inactive materials. In Chapter 4, the deflection of the radial-flux machine structure into the airgap was assessed using finite element analysis and a polynomial modelling technique. Generally the errors were large and the technique also had the disadvantage of being applicable to one material (Young's Modulus, E, mass density, ρ, and Poisson's Ratio, ν were all fixed). Different designers may choose different materials and also variations of the chosen design (e.g. different number of arms) so different approaches are used in this chapter. Instead of using the finite element analysis (FEA) method, analytical methods will be employed so that adequate structures can be designed and evaluated quickly.

Deflection into the airgap is the most important part although the axial deflection is also important. Rotor and stator structures with both discs and arms are considered - Fig. 5.1 shows the four variations that are modelled. Choosing generic structures such as these cannot perfectly represent the large number of feasible generator structures. However, the size and mass of these structures should be similar to most practical designs.

The areas of greatest deflection into the airgap are most critical to the design. These are at the bottom and at the top of the airgap (as shown for the two rotor designs in Fig. 5.2). At the bottom, the rotor deflection is maximum

(gravity and normal stress both act downwards) and the stator deflection is smaller (gravity and normal stress act in opposite fashions). At the top of the airgap, the rotor deflection is small and the stator deflection is maximum. In terms of 'armed' structures, the deflection of the back iron is maximum halfway along the 'rim' between two arms. It is minimum at the points where the arms meet the back iron cylinder. For disc structures, the deflection is greatest at the points furthest away from the points where the disc meets the cylinder. This means that for the rotor it is the parts of the cylinder at the axial extremes which deflect most. In the stator case the maximum deflection is found axially halfway along the cylinder, between the two discs.

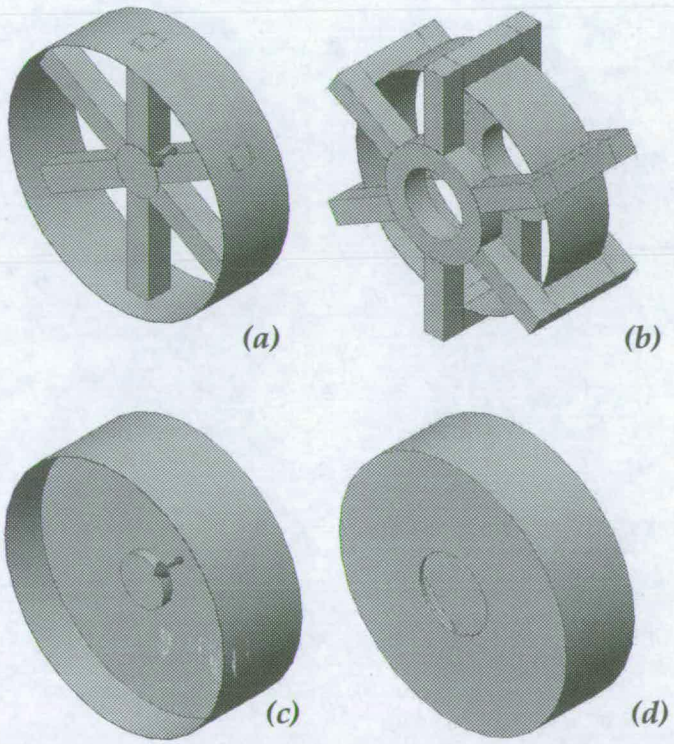

Figure 5.1. Variations of machine structure in Chapter 5: (a) Rotor with arms, (b) Stator with arms, (c) Rotor with disc and (d) Stator with discs

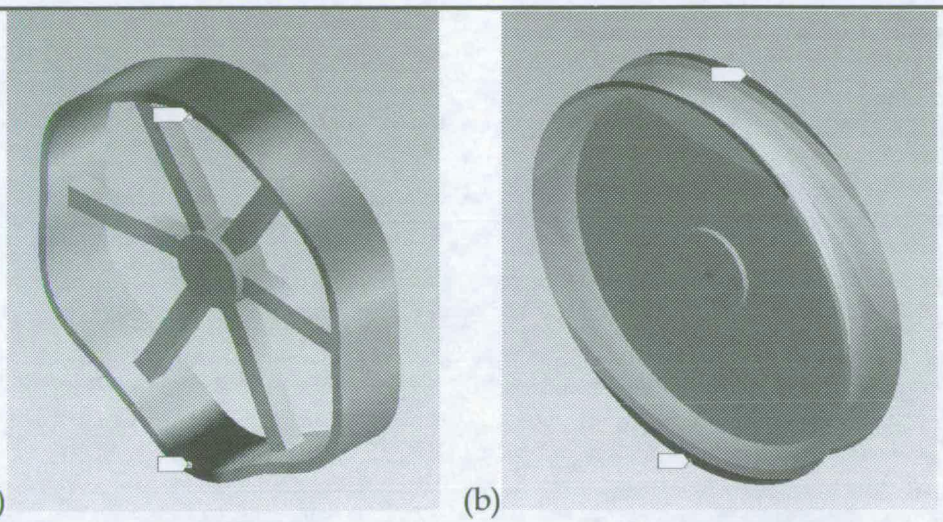

Figure 5.2. Maximum deflections for rotor subjected to normal component of Maxwell stress and gravity (a) Rotor with arms and (b) Rotor with disc

Different approaches are needed to address each structure and type of deformation. The armed structures will be analysed in section 5.1 as a wheel with rim and rigid arms. By splitting the cylinder and arms, compatibility equations can be used to calculate the forces that will close a virtual gap. These forces can then be used to find the deflection of the arms and, along with the cylinder equation, the deflection at the midspan. In section 5.2, the rotor and stator with discs are analysed, with the maximum deflection modelled with the cylinder equation and the minimum deflection (where the cylinder and disc meet) modelled using the compatibility of the cylinder and disc. Section 5.3 introduces techniques for modelling the deflection out of the radial plane due to gravity.

5.1 Deflection of rotor and stator back iron with arms

In this section the deflection of the rotor and stator structures shown in Fig. 5.1(a) & (b) will be examined. A uniform radial pressure, q, applied to a thin walled cylindrical pressure vessel (where the wall thickness is less than 10% of the radius) produces a radial deflection, u, according to eqn. (4.1) [101]

$$u = \frac{qR^2}{Et}. \tag{4.1}$$

Where R = radius of cylinder (m)

t = thickness of cylinder (m)

E = Young's modulus (Pa).

This cylindrical pressure vessel equation cannot be used in a straightforward manner in this case because the cylinder is constrained at the points that it meets the arms. As a result the deflection at the midpoint of the span will be less than that predicted by eqn. (4.1).

5.1.1 Normal loading of an armed structure

This method is adapted from Pippard [89]. A circular armed wheel is made up of a cylinder or rim connected to the shaft or fixed point by arms. A rotor structure with 6 arms is shown in Fig. 5.3. The cylinder corresponds to the 'yoke' or back iron. If a virtual 'cut' is made between the cylinder and the arms then the radius of the cylinder will increase by $u = \frac{qR^2}{Et}$. In reality the cylinder and arms are joined. To model this, a force T is applied outwards at the end of each arm and n forces each of magnitude T are applied inwards at the cylinder (at the points that the cylinder meets an arm). The resulting deformation will lead to some strain energy, U. Knowing the deflection and using Castigliano's theorem (whereby $\frac{\partial U}{\partial T} = u$) this force T can be calculated.

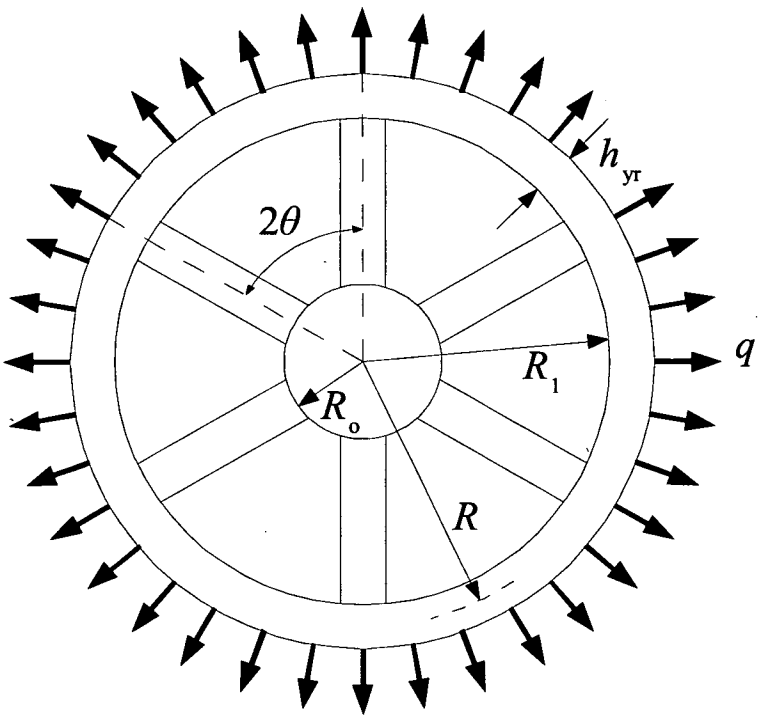

Figure 5.3. Rotor with arms, $\theta = 30°$

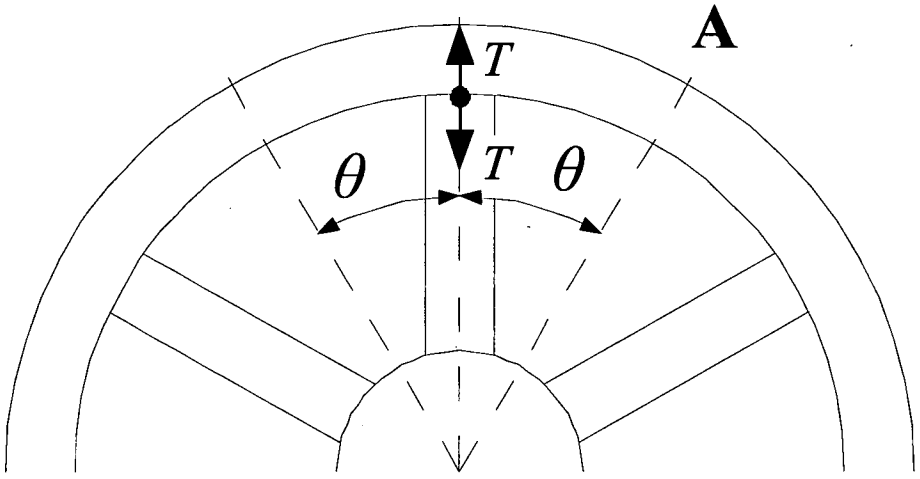

Figure 5.4. One arm or 2θ section of rotor

The first step is an examination of the forces in the rim. The angle between two arms is 2θ (see Fig. 5.4). At the midpoint **A** between any two adjacent arms there acts a moment, M_0, and a tangential thrust, H_0 (see Fig. 5.5). It is

possible to express these variables in terms of T, R, θ and m, where $m = \left(\frac{k}{R}\right)^2$ and k is the radius of gyration [89]:

$$M_0 = \frac{TR}{2}\left\{\frac{1}{\sin\theta} - \frac{1}{\theta}\left(\frac{1}{m+1}\right)\right\} \tag{5.1}$$

$$H_0 = \frac{T}{2}\frac{1}{\sin\theta} \tag{5.3}$$

At point X, at an angle α from this midpoint, there is a resultant moment, M, and a force, H. The moment is derived and expressed in terms of this angle α in eqn. (5.4) and the force in eqn. (5.5).

$$\begin{aligned} M &= M_o - \frac{TR}{2}\frac{(1-\cos\alpha)}{\sin\theta} \\ &= \frac{TR}{2}\left\{\frac{1}{\sin\theta} - \frac{1}{\theta}\left(\frac{1}{m+1}\right)\right\} - \frac{TR}{2}\frac{(1-\cos\alpha)}{\sin\theta} \\ &= \frac{TR}{2}\left\{\frac{\cos\alpha}{\sin\theta} - \frac{1}{\theta}\left(\frac{1}{m+1}\right)\right\} \end{aligned} \tag{5.4}$$

$$H = \frac{T}{2}\frac{\cos\alpha}{\sin\theta}. \tag{5.5}$$

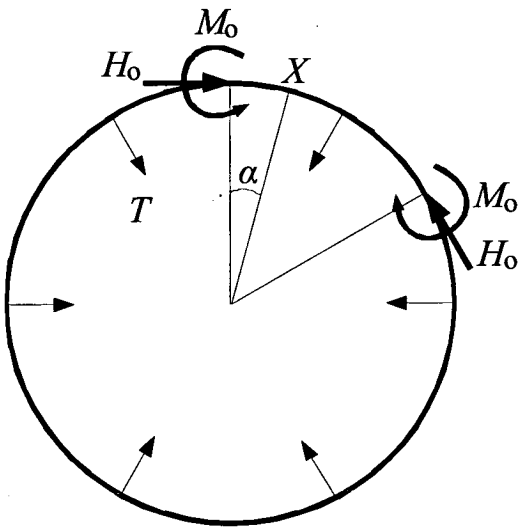

Figure 5.5. Forces in rim

The total strain energy is made up of strain energy due to bending of the rim, strain energy due to tangential compression of the rim and strain energy in

the support arm. The strain energy due to bending of the rim, U_B, (where k is the radius of gyration) is:

$$\begin{aligned} U_B &= \frac{2}{AE}\int_0^{\varphi}\left\{\frac{M^2}{2h}+H\left(\frac{HR}{2}-M\right)\right\}d\alpha \\ \frac{\partial U_B}{\partial T} &= \frac{2}{AE}\int_0^{\varphi}\left\{\left(\frac{M}{h}-H\right)\frac{\partial M}{\partial T}+(HR-M)\frac{\partial H}{\partial T}\right\}d\alpha \\ &= \frac{TR^3}{4EI}\left\{\frac{\theta}{\sin^2\theta}+\frac{1}{\tan\theta}-\frac{2}{\theta}\left(\frac{1}{m+1}\right)\right\} \end{aligned} \tag{5.6}$$

The partial derivative of strain energy due to the tangential compression of the rim with respect to the cut-closing force, T, is

$$\begin{aligned} \frac{\partial U_C}{\partial T} &= \frac{TR}{2AE}\int_0^{\varphi}\frac{\cos^2\alpha}{\sin^2\theta}d\alpha \\ \frac{\partial U_C}{\partial T} &= \frac{TR(2\theta+\sin 2\theta)}{8AE\sin^2\theta} \end{aligned} \tag{5.7}$$

where A is the cross sectional area of the rim.

The arms have a cross sectional area of a and each arm is R_1-R_o long. The strain energy in the arm is,

$$U_a = \tfrac{1}{2}\frac{T^2(R_1-R_o)}{aE}, \tag{5.8}$$

giving a partial derivative with respect to the closing force,

$$\frac{\partial U_a}{\partial T} = \frac{T(R_1-R_o)}{aE}. \tag{5.9}$$

The total partial derivative of strain energy with respect to the closing force, T is:

$$\begin{aligned} \frac{\partial U}{\partial T} &= \frac{\partial U_a}{\partial T}+\frac{\partial U_B}{\partial T}+\frac{\partial U_C}{\partial T} \\ &= \frac{T(R_1-R_o)}{aE}+\frac{TR^3}{4EI}\left\{\frac{\theta}{\sin^2\theta}+\frac{1}{\tan\theta}-\frac{2}{\theta}\left(\frac{1}{m+1}\right)\right\}+\frac{TR(2\theta+\sin 2\theta)}{8AE\sin^2\theta} \\ &= \frac{T}{E}\left\{\frac{R_1-R_o}{a}+\frac{R^3}{4I}\left\{\frac{\theta}{\sin^2\theta}+\frac{1}{\tan\theta}-\frac{2}{\theta}\left(\frac{1}{m+1}\right)\right\}+\frac{R(2\theta+\sin 2\theta)}{8A\sin^2\theta}\right\} \end{aligned} \tag{5.10}$$

With a virtual cut, the rim would deflect by the amount given in eqn. (5.1). Making the result given by eqn. (5.10) gives the force, T, which is necessary to the close the virtual cut:

$$\frac{dU}{dT} = \frac{T}{E}\left[\left(\frac{\theta}{\sin^2\theta}+\frac{1}{\tan\theta}\right)\left(\frac{R}{4A}+\frac{R^3}{4I}\right)-\frac{R^3}{2I\theta}\left(\frac{1}{m+1}\right)+\frac{R_1-R_o}{a}\right] = \frac{qR^2}{Et}$$

$$T = \frac{qR^2}{t\left[\left(\frac{\theta}{\sin^2\theta}+\frac{1}{\tan\theta}\right)\left(\frac{R}{4A}+\frac{R^3}{4I}\right)-\frac{R^3}{2I\theta}\left(\frac{1}{m+1}\right)+\frac{R_1-R_o}{a}\right]} \tag{5.11}$$

The rim sees two sets of forces: the normal stress, q, uniformly distributed around the rim and directed radially outwards and six point forces, T, separated by 2θ, each directed radially inwards. Adding the deflection due to the two different forces will give the total deflection.

Fig. 5.6 shows a ring under six equally spaced radial forces, taken from [102]. The change in radius at **A** is

$$\Delta R_A = \frac{-WR^3}{EI}\left[\frac{(\sin\theta-\theta\cos\theta)}{4\sin^2\theta}-\frac{1}{2\sin\theta}+\frac{1}{2\theta}\right] \tag{5.12}$$

where I is the second moment of area of the rim.

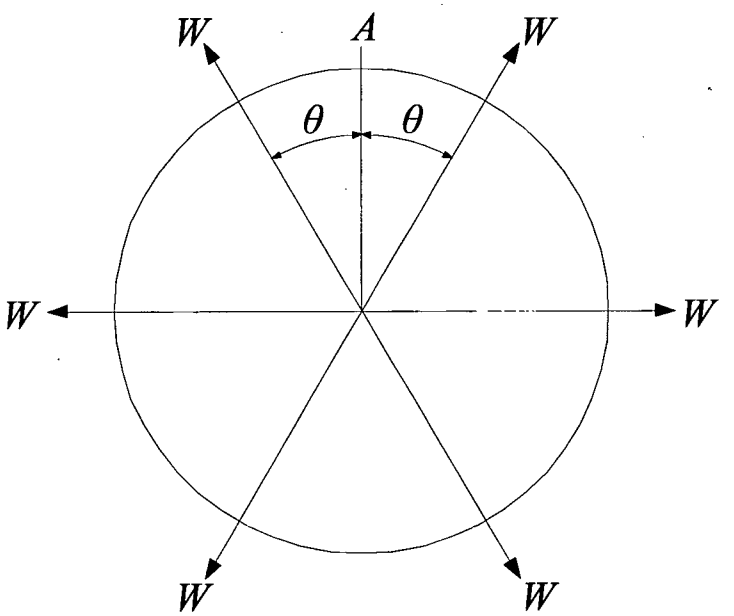

Figure 5.6. Ring under any number of equally spaced equal radial forces

In this case the radial forces, T, are directed inwards so that $W = -T$, hence,

$$u_A = u + \Delta R_A$$

$$u_A = \frac{qR^2}{Et} + \frac{qR^5\left[\frac{k_1(\sin\theta - \theta\cos\theta)}{4\sin^2\theta} - \frac{k_2}{2\sin\theta} + \frac{k_2^2}{2\theta}\right]}{EIt\left[\left(\frac{\theta}{\sin^2\theta} + \frac{1}{\tan\theta}\right)\left(\frac{R}{4A} + \frac{R^3}{4I}\right) - \frac{R^3}{2I\theta}\left(\frac{1}{m+1}\right) + \frac{R_1 - R_o}{a}\right]} \tag{5.13}$$

$$u_A = \frac{qR^2}{Et}\left(1 + \frac{R^3\left[\frac{k_1(\sin\theta - \theta\cos\theta)}{4\sin^2\theta} - \frac{k_2}{2\sin\theta} + \frac{k_2^2}{2\theta}\right]}{I\left[\left(\frac{\theta}{\sin^2\theta} + \frac{1}{\tan\theta}\right)\left(\frac{R}{4A} + \frac{R^3}{4I}\right) - \frac{R^3}{2I\theta}\left(\frac{1}{m+1}\right) + \frac{R_1 - R_o}{a}\right]}\right)$$

This can then be used to find the deflection at the midpoint, **A**, due to the radial (normal) stress, q.

5.1.2 Finite element comparison for rotor

Three cases of the same generic six armed rotor structure will be analysed using eqn. (5.13) and compared with results from finite element analysis. The first case is a steel structure for a 3 MW generator; the second case is a steel structure for a 5 MW generator and the third case is an aluminium structure for a 5 MW generator.

The 3 MW generator has a rotor volume, V_r = 22.5 m^3 (with airgap radius, r_g = 3 m and axial length, l_s = 0.797 m). In the case of the 5 MW generators, V_r = 48 m^3 (with the same airgap radius but with an axial length, l_s = 1.7 m). In all the cases, the normal stress is equal to 2.8×10^5 Pa (equivalent to a flux density of 0.84 T).

The steel structures have the following material properties: Young's modulus, E_{st} = 2.1×10^{11} Pa, Poisson's ratio, ν_{st} = 0.3 and mass density, ρ_{st} = 7850 kg/m^3. For the aluminium structure Young's modulus, E_{al} = 7.0×10^{10} Pa, Poisson's ratio, ν_{al} = 0.33 and mass density, ρ_{al} = 2600 kg/m^3.

5.1.2.1 Case 1

In this case a 3 MW generator with a steel rotor structure is analysed. With an airgap radius of 3 m the airgap clearance, c = 6×10^{-3} m and so a deflection

of $u = 3\times10^{-4}$ m is suitable. The rim thickness $h_{yr} = 100\times10^{-3}$ m and the support arm thickness $t_{sa} = 0.7$ m ($a = t_{sa}^2 = 0.49$ m^2). Fig. 5.7 shows the rotor structure analysed using a solid model restrained at the rotor shaft with a mesh size of 167 mm. The maximum deflection by finite element analysis is $u = 2.206\times10^{-4}$ m. From eqn. (5.13) $u = 2.150\times10^{-4}$ m, or 97.5% of the value found by FEA.

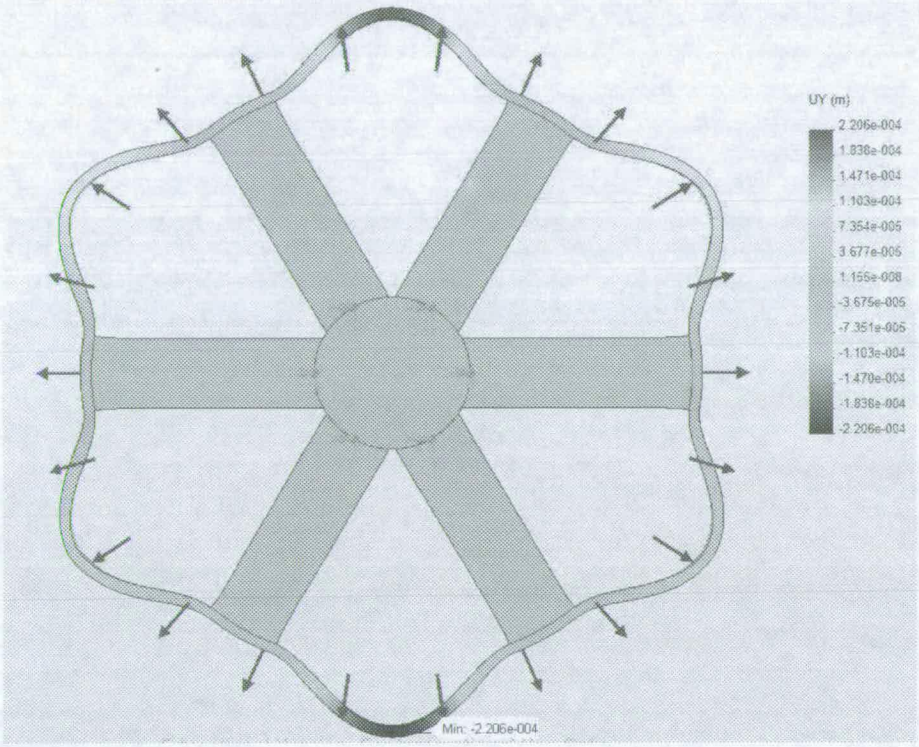

Figure 5.7. Deflection of Case 1 armed rotor due to normal stress, $u = 2.206\times10^{-4}$ m

5.1.2.2 Case 2

This case is a 5 MW generator with a steel rotor structure. The rim thickness is $h_{yr} = 110\times10^{-3}$ m, and the arm thickness is $t_{sa} = 0.6$ m. With the same mesh size as in case 1, the deflection $u = 1.956\times10^{-4}$ m by finite element analysis. From eqn. (5.13), $u = 1.924\times10^{-4}$ m, or 98.4% of the deflection found by FEA.

5.1.2.3 Case 3

A 5 MW generator with an aluminium rotor structure has a rim thickness of $h_{yr} = 200\times10^{-3}$ m and an arm thickness, $t_{sa} = 0.6$ m. Again analysed as cases 1

and 2, the deflection is u = 2.469×10^{-4} m by FEA and u = 2.809×10^{-4} m from eqn. (5.13).

5.1.3 Finite element comparison for stator

5.1.3.1 Case 1

For a 3 MW steel structure stator with h_{ys} = 130×10^{-3} m and t_{sa} = 0.5 m then using a 202 mm mesh a deflection u = 1.660×10^{-4} m was found using FEA. Equation 5.13 can be altered to take into account the double sided arm arrangement of the stator, by doubling the arm area, a (giving eqn. 5.13b). This then gives a deflection of u = 1.6045×10^{-4} m or 96.7% of the FEA value.

$$u_A = \frac{qR^2}{Et}\left(1+\frac{R^3\left[\frac{k_1(\sin\theta-\theta\cos\theta)}{4\sin^2\theta}-\frac{k_2}{2\sin\theta}+\frac{k_2^2}{2\theta}\right]}{I\left[\left(\frac{\theta}{\sin^2\theta}+\frac{1}{\tan\theta}\right)\left(\frac{R}{4A}+\frac{R^3}{4I}\right)-\frac{R^3}{2I\theta}\left(\frac{1}{m+1}\right)+\frac{R_1-R_o}{2a}\right]}\right) \quad (5.13b)$$

5.1.3.2 Case 2

For the larger (5 MW) steel structure, a rim thickness h_{ys} = 130×10^{-3} m was chosen along with a support arm thickness, t_{sa} = 0.5 m. Analysis with finite element mesh of 180 mm gave a maximum deflection of u = 1.615×10^{-4} m. A slightly smaller deflection of u = 1.5955×10^{-4} m was found using eqn. 5.13b.

5.1.3.3 Case 3

In the aluminium 5MW structure, h_{ys} = 210×10^{-3} m and t_{sa} = 0.55 m gave a deflection u = 2.397×10^{-4}m when analysed using finite element analysis. The analytical technique gave a slightly larger deflection of u = 2.677×10^{-4} m.

5.1.4 Discussion on modelling with armed structures

In this section a simple wheel and arm structure has been used to represent both the generator rotor and stator. The final equation (5.13) has been shown to give results close to those found by finite element analysis when the same design is considered, generally within 10%. This model allows the engineer

to design for a deflection limit by varying material, number of arms, rim dimensions, arm dimensions and airgap flux density.

The supporting cases are by no means exhaustive and do not examine different:

i. Airgap flux densities (and therefore normal stress levels).

ii. Materials other than steel and aluminium. Materials with linear deformation characteristics should give similar results as the same quantity is used in both the analytical and FEA models.

iii. Arm numbers. For small arm numbers there will be a larger unsupported region between adjacent arms. More arms give a much smaller unsupported region between adjacent arms. As an aside, an interesting investigation would be to look at which number of arms gives the required deflection with the least structural mass.

iv. Different rim cross sections.

It should be noted that for any designs which differ significantly from those shown in this section, eqn. (5.13) should be tested against a FEA model first, before use in an optimisation process or early design procedure.

5.2 Normal loading of a disc structure

5.2.1 Analytical model for disc structure

5.2.1.1 Rotor disc structure

In this section the use of a disc – rather than arms as in the previous section – to connect the rotor cylinder to the rotor shaft will be investigated. Again the loading is the normal stress, q, caused by the magnetic flux density. The cylinder will first be loaded as if 'free' from the disc and the deflection will be calculated. In reality the disc and the cylinder are connected and so a force can be defined which stretches the disc radially outwards and compresses the cylinder – or at least part of the cylinder – radially inwards, so that the

two pieces remain in contact. Applying this force to a thin-walled cylindrical shell model and superimposing the effect of the 'free' cylinder deflection will lead to the maximum deflection. Figure 5.8 shows a cross section of the rotor with disc structure.

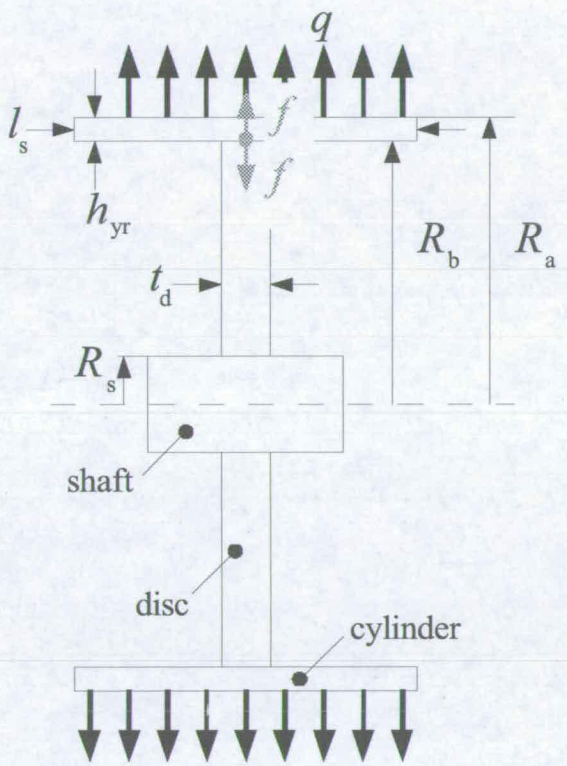

Figure 5.8. Compatibility of disc and cylinder in rotor

It has been seen that the deflection of a cylinder due to normal stress, q, on the outside of the cylinder is:

$$u = \frac{qR_b^2}{Eh_{yr}} \tag{5.1b}$$

If one makes a virtual cut between the cylinder and the disc, there must be a uniform outward radial force per unit length, f, around the outside of the disc. Since there is no resultant force around the junction the same inward radial pull, f, is found at the inner edge of the cylinder.

The disc will be stressed in such a way as shown in Fig. 5.9. The radial stress, p_θ'', is equal to the circumferential stress, p_r'', which is given by eqn. (5.14) from [90] as

$$p_\theta'' = \frac{1}{(R_1^2 - R_2^2)}\left\{p_1 R_1^2 - p_2 R_2^2 + \frac{(p_2 - p_1)R_1^2 R_2^2}{r^2}\right\}. \tag{5.14}$$

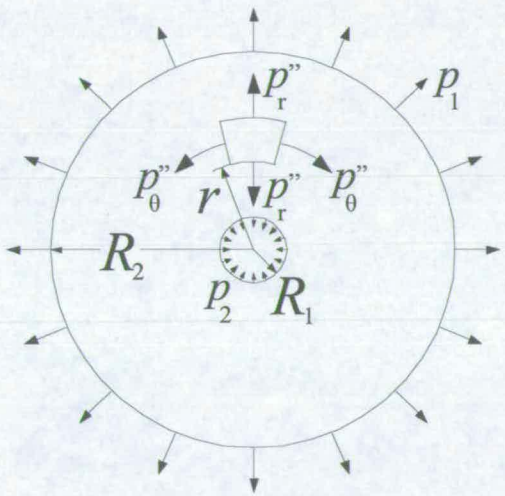

Figure 5.9. Stresses in a disc

At radius r the circumferential and therefore radial strain is $\frac{p_\theta'' - \nu p_r''}{E}$ and the increases in outer and inner radii of the disc are:

$$\begin{aligned} u_1 &= \frac{R_1}{E(R_1^2 - R_2^2)}\left[p_1\left\{(1-\nu)R_1^2 + (1+\nu)R_2^2\right\} - 2p_2 R_2^2\right] \\ u_2 &= -\frac{R_2}{E(R_1^2 - R_2^2)}\left[p_2\left\{(1+\nu)R_1^2 + (1-\nu)R_2^2\right\} - 2p_1 R_1^2\right] \end{aligned} \tag{5.15}$$

If the disc is keyed onto the shaft, then p_2=0. Substituting $p_1 = f_d$, $R_1 = R_b$, and $R_2 = R_s$ into eqn. (5.15), then the disc deflects by u_d,

$$u_d = \frac{R_b f_d}{E(R_b^2 - R_s^2)}\left[(1-\nu)R_b^2 + (1+\nu)R_s^2\right], \tag{5.16}$$

where

$$f_d = \frac{f}{t_d}. \tag{5.17}$$

The maximum radial deflection is at the axial extremes of the cylinder. According to Roark the radial deflection outwards, y, for a short thin-walled cylindrical shell under an intermediate radial load, f – as shown in Fig. 5.8 – is [100]:

$$y = y_A F_1 + \frac{\psi_A}{2\lambda} F_2 + LT_y \tag{5.18}$$

Where y_A and ψ_A are the radial deflection and meridonial slope at the axial extreme of the cylinder and LT_y is the radial load term. These are given in eqns. (5.19-5.21).

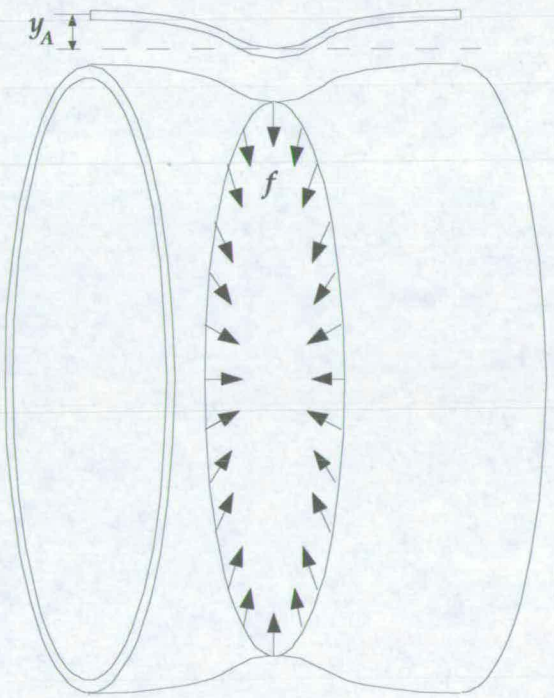

Figure 5.10. Short thin-walled cylindrical shell with intermediate radial load.

$$y_A = \frac{-f}{2D\lambda^3} \frac{C_3 C_{a2} - C_4 C_{a1}}{C_{11}} \tag{5.19}$$

$$\psi_A = \frac{f}{2D\lambda^2} \frac{C_2 C_{a2} - 2C_3 C_{a1}}{C_{11}} \tag{5.20}$$

$$LT_y = \frac{-f}{4D\lambda^3} F_{a4} \tag{5.21}$$

where $D, \lambda, C_2, C_3, C_4, C_{11}, C_{a1}, C_{a2}, F_1, F_2$ and F_{a4} are given in Appendix A.

Substituting these into eqn. (5.18) gives:

$$y = f\left[\frac{1}{4D\lambda^3}\frac{C_2C_{a2}-2C_3C_{a1}}{C_{11}}F_2 - \frac{1}{2D\lambda^3}\frac{C_3C_{a2}-C_4C_{a1}}{C_{11}}F_1 - \frac{1}{4D\lambda^3}F_{a4}\right] \tag{5.22}$$

To achieve continuity then

$$u_d = \frac{qR_b^2}{E(R_a - R_b)} + y \tag{5.23}$$

$$\begin{aligned}&\frac{R_b f_d}{E(R_b^2 - R_s^2)}\left[(1-\nu)R_b^2 + (1+\nu)R_s^2\right] \\ &- f_d t_d\left[\frac{1}{4D\lambda^3}\frac{C_2C_{a2}-2C_3C_{a1}}{C_{11}}F_2\left(x = l/2\right) - \frac{1}{2D\lambda^3}\frac{C_3C_{a2}-C_4C_{a1}}{C_{11}}F_1\left(x = l/2\right) - \frac{1}{4D\lambda^3}F_{a4}\left(x = l/2\right)\right] = \frac{qR_b^2}{E(R_a - R_b)}\end{aligned} \tag{5.24}$$

$$f_d = \frac{qR_b^2}{E(R_a - R_b)\left[\frac{R_b}{E(R_b^2 - R_s^2)}\left[(1-\nu)R_b^2 + (1+\nu)R_s^2\right] - t_d\left[\frac{1}{4D\lambda^3}\frac{C_2C_{a2}-2C_3C_{a1}}{C_{11}}F_2\left(x = l/2\right) - \frac{1}{2D\lambda^3}\frac{C_3C_{a2}-C_4C_{a1}}{C_{11}}F_1\left(x = l/2\right) - \frac{1}{4D\lambda^3}F_{a4}\left(x = l/2\right)\right]\right]} \tag{5.25}$$

This can then be substituted into eqn. (5.22) and when added to eqn. (5.1a) gives the maximum deflection.

$$u_{an} = \frac{qR_b^2}{E(R_a - R_b)} + \frac{f}{2D\lambda^3}\left[\frac{-F_1(x=0)}{C_{11}}(C_3C_{a2} - C_4C_{a1}) + \frac{F_2(x=0)}{2C_{11}}(C_2C_{a2} - 2C_3C_{a1}) - \frac{F_{a4}(x=0)}{2}\right] \tag{5.26}$$

5.2.1.2 Stator disc structure

For the stator there are two discs, one at either end of the cylinder (Fig. 5.11). The normal stress is orientated radially inwards, and the deflection of a cylinder can be modified to give the deflection towards the shaft as

$$u = \frac{qR_b^2}{Eh_{ys}}. \tag{5.1c}$$

Again by applying a virtual cut at the junction between the cylinder and a disc, it can be seen that there will be a force per unit length, f, on the disc (radially inwards, compressing the disc) and the cylinder (radially outwards, deflecting the cylinder as in Fig. 5.12). Equation (5.16) can be modified to take the change in direction of f into account,

$$u_d = -\frac{R_b f_d}{E(R_b^2 - R_s^2)}\left[(1-\nu)R_b^2 + (1+\nu)R_s^2\right]. \tag{5.16b}$$

According to Roark [100], the radial deflection due to a radial end load is

$$y = \frac{f}{2D\lambda^3}\left[\frac{C_{14}}{2C_{11}}F_2 - \frac{C_{13}}{C_{11}}F_1 - \frac{F_4}{2}\right]. \tag{5.27}$$

At one of end of the cylinder there will be a deflection effect due to f applied at that end ($x = 0$) and the other end ($x = l_s$). The resulting deflection at either end will be

$$y = \frac{f_d t_d}{2D\lambda^3}\left[\frac{C_{14}}{2C_{11}}\begin{pmatrix}F_2(x=0)\\+F_2(x=l_s)\end{pmatrix} - \frac{C_{13}}{C_{11}}\begin{pmatrix}F_1(x=0)\\+F_1(x=l_s)\end{pmatrix} - \frac{1}{2}\begin{pmatrix}F_4(x=0)\\+F_4(x=l_s)\end{pmatrix}\right]. \tag{5.28}$$

For continuity at the junction,

$$u_d = \frac{qR_b^2}{E(R_a - R_b)} + y\,. \tag{5.29}$$

Substituting eqns. (5.16b) and (5.28) into (5.29) and rearranging gives f_d:

$$f_d = \frac{qR_b^2}{E(R_a - R_b)\left[\frac{R_b}{E(R_b^2 - R_s^2)}\left[(1-\nu)R_b^2 + (1+\nu)R_s^2\right] + \frac{t_d}{2D\lambda^3}\left[\frac{C_{14}}{2C_{11}}\begin{pmatrix}F_2(x=0)\\+F_2(x=l_s)\end{pmatrix} - \frac{C_{13}}{C_{11}}\begin{pmatrix}F_1(x=0)\\+F_1(x=l_s)\end{pmatrix} - \frac{1}{2}\begin{pmatrix}F_4(x=0)\\+F_4(x=l_s)\end{pmatrix}\right]\right]} \tag{5.30}$$

The maximum deflection will be found at the midpoint of the cylinder (where $x = \frac{1}{2}l_s$). Equation (5.26) amended for the stator becomes

$$u_{an} = \frac{qR_b^2}{E(R_a - R_b)} - \frac{f}{D\lambda^3}\left[\frac{C_{14}}{2C_{11}}F_2(x = l_s/2) - \frac{C_{13}}{C_{11}}F_1(x = l_s/2) - \frac{1}{2}F_4(x = l_s/2)\right], \tag{5.31}$$

where C_{13}, C_{14} and F_4 are given in Appendix A.

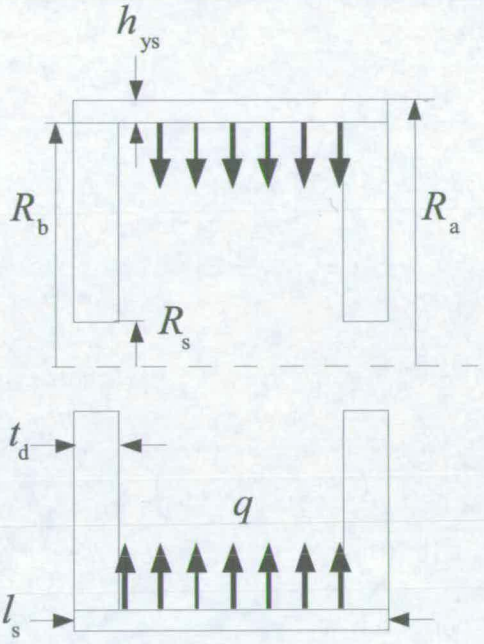

Figure 5.11. Cross section of disc stator

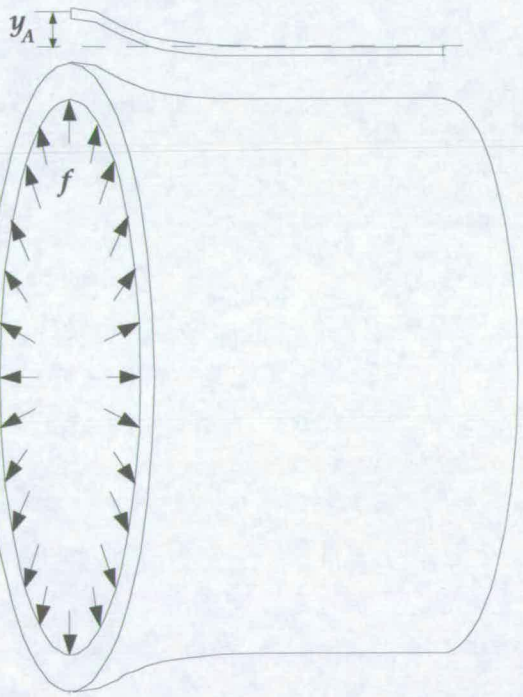

Figure 5.12. Short cylindrical shell with radial end load

5.2.2 Finite element analysis comparison for rotor

In this section the results of the deflection from eqn. (5.26) and deflection found using FEA are compared for the same three cases as described in section 5.1.2.

5.2.2.1 Case 1

In this case a 3 MW generator with a steel rotor structure is analysed. With an airgap radius of 3 m, a deflection of $u = 3\times10^{-4}$ m is suitable. The rim thickness $h_{yr} = 40\times10^{-3}$ m, the disc thickness $t_d = 40\times10^{-3}$ m and the stress q = 250 kPa is applied. For these dimensions, the maximum deflection found by finite element analysis is $u = 2.390\times10^{-4}$ m. From eqn. (5.26) $u_{an} = 2.488\times10^{-4}$ m, or 104% of the value found by FEA. Using the simple cylinder equation (5.1b), $u = 2.813\times10^{-4}$ m or 118% of the FEA value.

5.2.2.2 Case 2

Case 2 is a 5 MW generator, again with a steel rotor structure. The rim thickness is $h_{yr} = 50\times10^{-3}$ m, disc thickness $t_d = 50\times10^{-3}$ m and a stress, q = 250 kPa is applied. The resulting deflection $u = 2.867\times10^{-4}$m (by finite element analysis) and $u_{an} = 2.746\times10^{-4}$m (from eqn. (5.26)). The analytical value is 95% of the deflection found by FEA. The simple cylinder equation gives $u = 2.250\times10^{-4}$m or 78% of the FEA value.

5.2.2.3 Case 3

A 5 MW generator with an aluminium rotor structure has a rim thickness of $h_{yr} = 130\times10^{-3}$ m and disc thickness $t_d = 130\times10^{-3}$ m. Analysed as cases 1 and 2, the deflection is $u = 2.530\times10^{-4}$ m by FEA and $u_{an} = 2.594\times10^{-4}$ m from eqn. (5.26). This is 102% of the FEA value. The simple cylinder equation gives $u = 2.473\times10^{-4}$ m (98%).

5.2.2.4 Error with varying K_{rad}

In cases 1 and 2 the rotor design is similar with the exception of the axial length, l_s. With a radius of 3 m and a rim thickness of 50 mm, eqn. (5.1b)

predicts that both cases give a deflection of $u = 2.25\times10^{-4}$ m. Fig. 5.13 shows the deflection found using FEA when the axial length is varied to produce aspect ratios K_{rad} = 0.1, 0.132, 0.2, 0.25, 0.3, 0.4 and 0.5. It can be seen that there is a considerable change in deflection as the axial length changes. Fig. 5.14 shows two of the rotor designs, (a) with l_s = 1.5 m and (b) with l_s = 3 m. The first shows the ends of the cylinder 'turned up' so that the rotor rim resembles that of a pulley wheel. This gives the greatest deflection (at the edges). In the second design, even though the cylinder surface area is greater (and therefore the total force is larger than for the first design) the deflection is smaller. In this case the deflection is starting to converge to the value predicted by eqn (5.1b), i.e. the rim is starting to act as a simple cylinder. However, for most of the useful K_{rad} range, the simple cylinder equation is inadequate at describing the deflection.

Case 1 describes a rotor with K_{rad} = 0.132 and case 2 describes a rotor with K_{rad} = 0.5. The error given by eqn. (5.26) in cases 1-3 was sometimes positive and sometimes negative. Fig. 5.13 shows the analytical prediction, and Table 5.1 gives the u_{an}/u_{FE} values. The analytical technique shows good agreement over the whole K_{rad} range, particularly K_{rad} = 0.13-0.3.

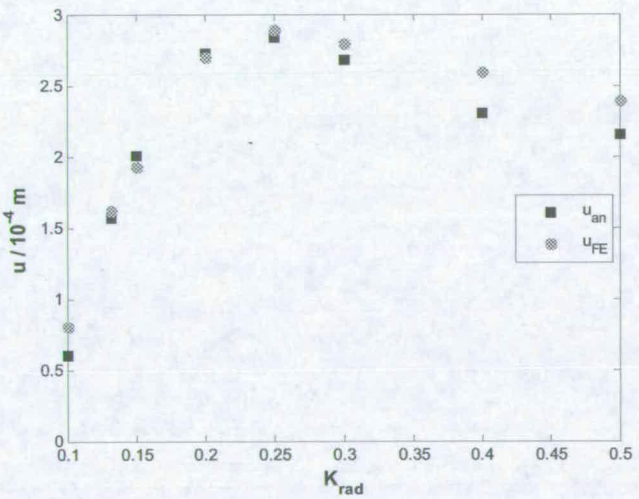

Figure 5.13. Deflection of rotor with varying axial length and aspect ratio (found with FEA and eqn. (5.26)). r_g= 3m, t_d=50mm, h_{yr}=50mm, steel.

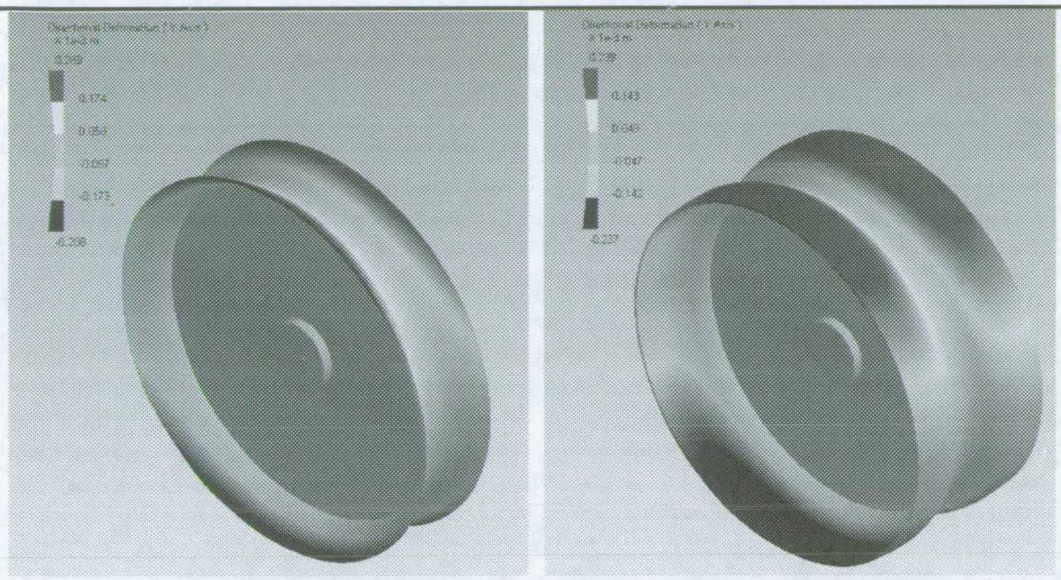

Figure 5.14. Deflection of rotor (found by finite element analysis) with varying aspect ratio (a) Rotor design l_s = 1.5m (Maximum deflection = 0.289mm) (b) Rotor design l_s = 3m (Maximum deflection = 0.239mm).

K_{rad}	0.1	0.132	0.15	0.2	0.25	0.3	0.4	0.5
l_s / m	0.6	0.797	0.9	1.2	1.5	1.8	2.4	3.0
u_{an}/u_{FE}	0.75	0.97	1.04	1.01	0.98	0.96	0.89	0.90

Table 5.1. Over and under prediction of rotor disc analytical method with varying aspect ratio.

5.2.3 Finite element comparison for stator

In this section the results of the deflection from eqn. (5.31) and deflection found using FEA are compared for the same three cases (i.e. same radius and axial length) as described in section 5.1.3.

5.2.3.1 Case 1

A steel stator ($E = 2.0\times10^{11}$ Pa, $\nu = 0.3$) with airgap radius $r_g = 3$ m and axial length $l_s = 0.797$ m, has cylinder thickness $h_{yr} = 40\times10^{-3}$ m and disc thickness $t_d = 40\times10^{-3}$ m. By FEA, the deflection is $u_{FEA} = 2.43\times10^{-4}$ m and with eqn. (5.30) $u_{an} = 2.60\times10^{-4}$ m (or 107% of the FEA value).

5.2.3.2 Case 2

A larger version of the stator in case 1 which has an axial length of l_s = 1.7 m, has a deflection of u_{FEA} = 3.27×10^{-4} m (found using a finite element solver). The deflection using eqn. (5.30) is u_{an} = 2.98×10^{-4} m (91% of the FEA value).

5.2.3.3 Case 3

A stator the same size as in case 2, but now with cylinder back thickness h_{yr} = 120×10^{-3} m and disc thickness t_d = 120×10^{-3} m and made from aluminium (E = 7.0×10^{10} Pa, ν = 0.33) analysed using the finite element solver gives a deflection u_{FEA} = 2.7526×10^{-4} m. Equation (5.30) gives the deflection as u_{an} = 2.6885×10^{-4} m (98% of the FEA value).

5.2.3.4 Error with varying K_{rad}

Figure 5.15 shows the deflection found analytically and with FEA of the stator shown in Fig. 5.16. When there is a small aspect ratio (i.e. K_{rad} = 0.1, the cylinder is axially short and the point of maximum deflection is relatively well supported by the two discs. As the aspect ratio increases to 0.25 (as shown in Fig. 5.16a), the deflection peaks. If the axial length increases further, then the deflection converges to the amount predicted by eqn. (5.1c). This can be seen with the 3m long stator in Fig. 5.16b, where there is a large dark area of fairly constant deflection. Table 5.2 shows that eqn. (5.30) agrees well with the finite element analysis over the whole range.

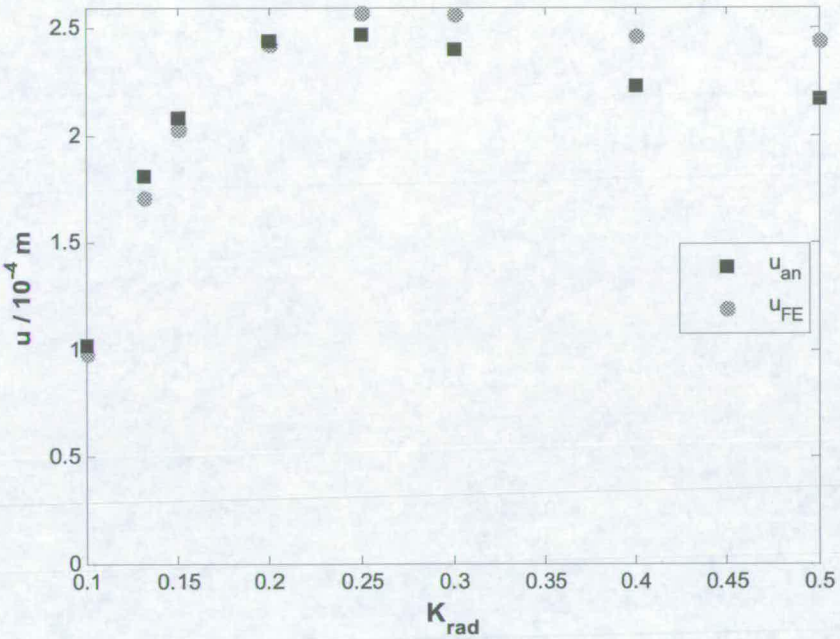

Figure 5.15. Deflection of stator with varying axial length and aspect ratio (found with FEA and eqn. (5.30)). r_g= 3m, t_d=50mm, h_{yr}=50mm, steel.

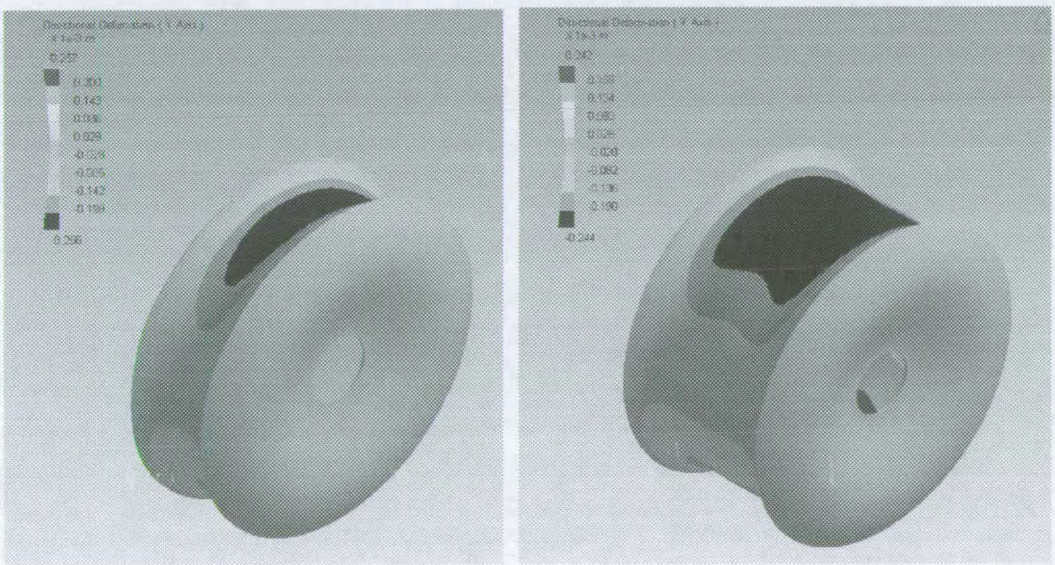

Figure 5.16. Deflection of stator (found by finite element analysis) with varying aspect ratio (a) Stator design l_s = 1.5m (Maximum deflection = 0.257mm) (b) Stator design l_s = 3m (Maximum deflection = 0.244mm).

K_{rad}	0.1	0.132	0.15	0.2	0.25	0.3	0.4	0.5
l_s /m	0.6	0.797	0.9	1.2	1.5	1.8	2.4	3.0
u_{an}/u_{FE}	1.04	1.06	1.03	1.01	0.96	0.94	0.91	0.89

Table 5.2. Over and under prediction of stator disc analytical method with varying aspect ratio.

5.3 Optimisation using normal component of Maxwell stress

The design equations developed in section 5.1 and 5.2 can be used to find the structural mass of rotor and stator structures. A particular radial-flux machine can produce torque according to eqn. (4.7). Figure 5.17 shows a plot of mass and deflection for a disc rotor suitable for a 5 MW wind turbine generator, with R = 4 m, l_s = 0.96 m, B_g = 0.84 T.

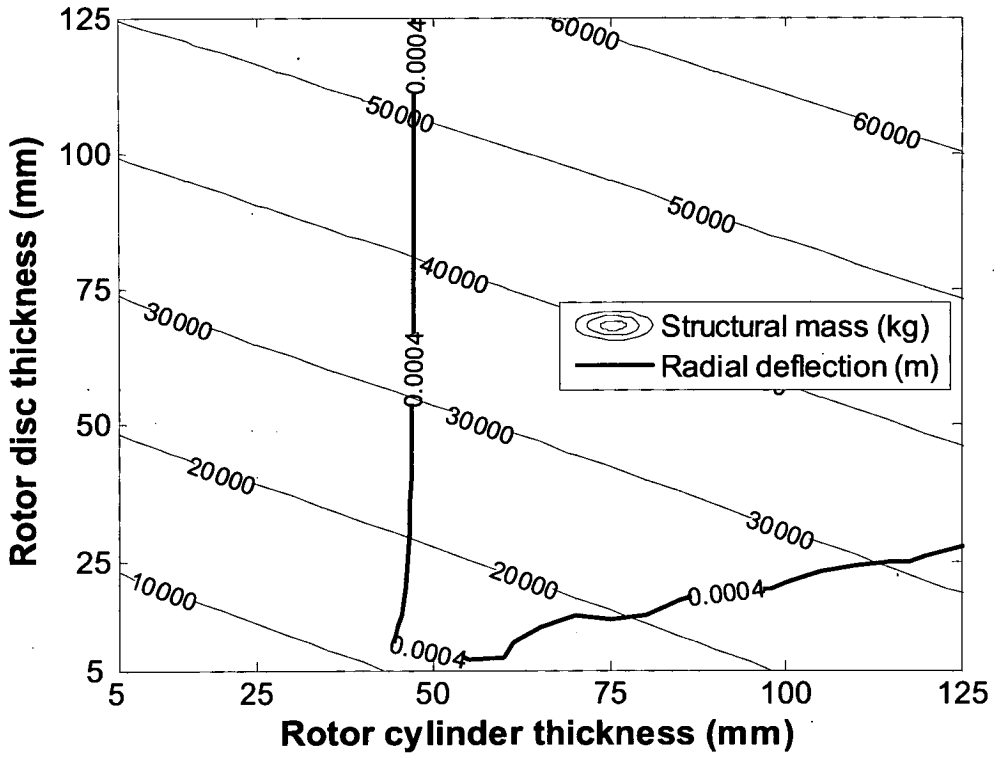

Figure 5.17. 2d optimisation for 5 MW rotor structure (R = 4 m, l_s = 0.96 m) with radial deflection criterion.

The rotor disc thickness and rotor cylinder thickness are independent variables here. Structural mass is plotted in thin black lines. Radial deflection equal to 10% of the airgap clearance is calculated and plotted (in thick black) according to eqn. (5.16). The minimum mass of the structure that meets this criterion is approximately 12 tonnes when h_{yr} = 45 mm and t_d = 10 mm. This would resemble the rotor shown in Fig. 5.18(a). Although this design may satisfy the deflection (due to Maxwell stress) criterion, there are other considerations that must be taken into account to give a practical solution. For example, analysing the structure with a finite element solver with gravity and the axis of the rotor tilted by 5° to the horizontal gives the axial deflection shown in Fig. 5.18(b). The maximum axial deflection of 9.1mm is too large and would mean that there would be axial misalignment between the rotor and stator (which has two discs). The next section will develop analytical tools so that the effects of gravity can be included in the optimisation process.

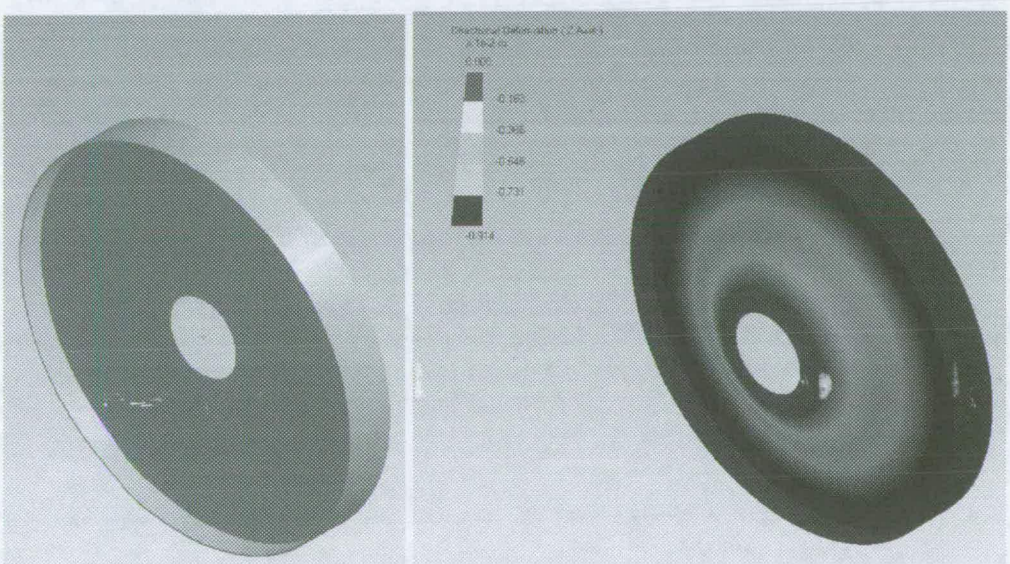

Figure 5.18. (a) Initial lightweight disc rotor structure solution (b) Axial deflection due to gravity.

5.4 Gravity loading

5.4.1 Introduction

The effect of gravity in the vertical direction is about two orders of magnitude less than that of the normal loading. The deflection of a six armed rotor with gravity is shown in Fig. 5.19. Table 5.3 compares the normal loading, q, over a range of flux densities with the gravity loading, w, for a range of cylinder thicknesses, h, of steel under acceleration due to gravity, g=9.81 m/s^2.

Machines with moderate flux density machine could see an increase in loading of 5-10% when the weight of the structure and active material is included.

For example, the case 1 rotor described in section 5.1.2.1 gives a deflection of u = 2.15×10^{-4} m due to a normal stress of q=250 kPa. The Maxwell and gravity loadings are only coincident at the bottom of the rotor and the top of the stator. However the normal loading model (in eqn. (5.13)) can be used to indicate the significance of gravity. Adding w to the loading in eqn. (5.13) for the case 1 rotor increases the deflection by 4.96×10^{-6} m (or an extra 2% of deflection).

Unlike the normal loading, the deflection of the rotor and stator will be in the same direction, so if they have the similar stiffness, then the relative deflection will approach 0. It is for this reason that the effect of the major component of gravity will be neglected.

B_g/T	q/kPa	h/mm	w/kPa
0.2	15.9	20	1.54
0.4	63.7	40	3.08
0.6	143	60	4.62
0.8	255	80	6.16
1.0	398	100	7.70

Table 5.3. Comparison of normal and gravity loading. $w=hg\rho_{st}$

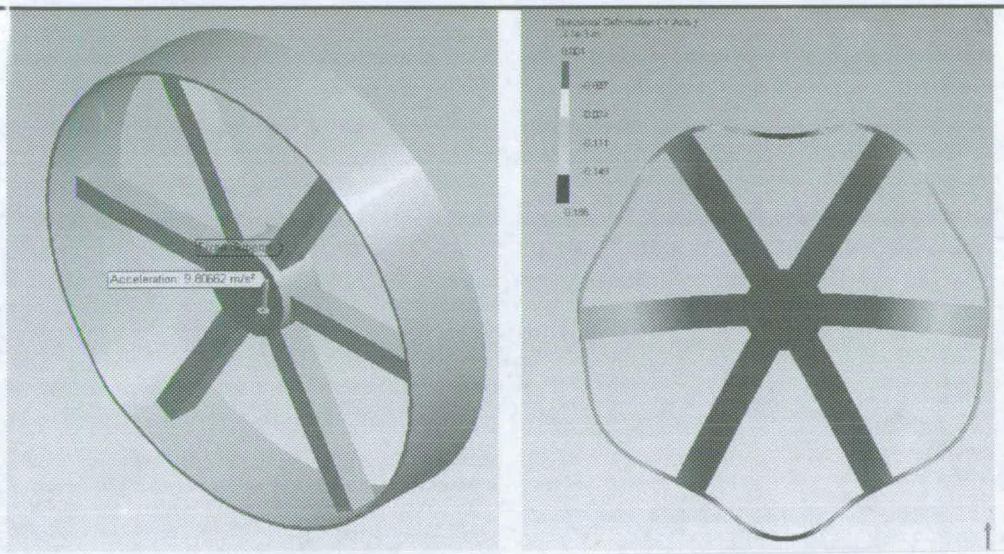

5.19. Model in finite element deflection solver of 6 armed rotor subjected to gravity and its subsequent deflection

5.4.2 Major and minor components of gravity

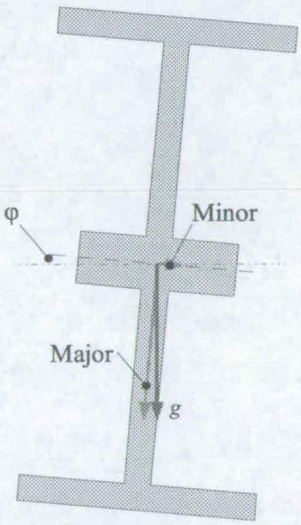

Figure 5.20. Major and minor components of gravity (due to tilt angle φ)

In wind turbines, it is common practice to incline the axis of the rotor blades and generator by a tilt angle, φ, so that when the wind deflects the rotor blades, they do not strike the tower. This tilt angle is of the order 5-10°.

As a result there will be two components of gravity, both of which are shown in Fig. 5.20. The result is typically a deflection similar to that in Fig. 5.17. The minor component is in the (generator) axial direction. This could lead to a

misalignment of the rotor and stator if there is a significant difference in stiffness.

5.4.3 Minor component of gravity

In this section, deflection in the axial deflection (due to the minor component of gravity) is modelled. The component of the gravity in this direction is $g\sin(\varphi)$. Circular plate theory is used to model the deflection of the rotor and stator with disc. The armed rotor and stator will be treated using cantilevered beams.

5.4.3.1 Rotor with disc

The loading is split into that due to the back iron cylinder and that due to the disc itself and applied to a disc with a fixed inner edge (representing the rotor shaft) and a guided outer edge. The outer edge is treated as guided because the back iron cylinder is relatively stiff resulting in a moment at the outer edge.

The deflection of an annular plate with a uniform annular line load $W = \rho g\sin(\varphi)(l_s\text{-}t_r)h_{yr}$ at a radius a_i (assumed to be equal to $r_{o,i}$), with the inner edge fixed and the outer edge guided, is shown in Fig. 5.21(i) and given in [98] and

$$y_{a,i} = \frac{-Wa_i^4}{bD}\left[\frac{C_2C_6}{C_5} - C_3\right]. \tag{5.32}$$

Deflection of the same plate with a uniformly distributed pressure $w = \rho g\sin(\varphi)t_r$ between b and a_{ii} with the inner edge fixed and the outer edge guided is shown in Fig. 5.21(ii) and given in [98] and

$$y_{a,ii} = M_{rb}\frac{a_{ii}^2}{D}C_2 + Q_b\frac{a_{ii}^3}{D}C_3 - \frac{wa_{ii}^4}{D}L_{11}, \tag{5.33}$$

where

$$M_{rb} = \frac{-wa_{ii}^2}{C_8}\left[\frac{C_9}{2a_{ii}b}\left(a_{ii}^2 - b^2\right) - L_{17}\right] \text{ and} \tag{5.34}$$

$$Q_b = \frac{w}{2b}\left(a_{ii}^2 - b^2\right). \tag{5.35}$$

The total axial deflection is $y = y_{a,i} + y_{a,ii}$.

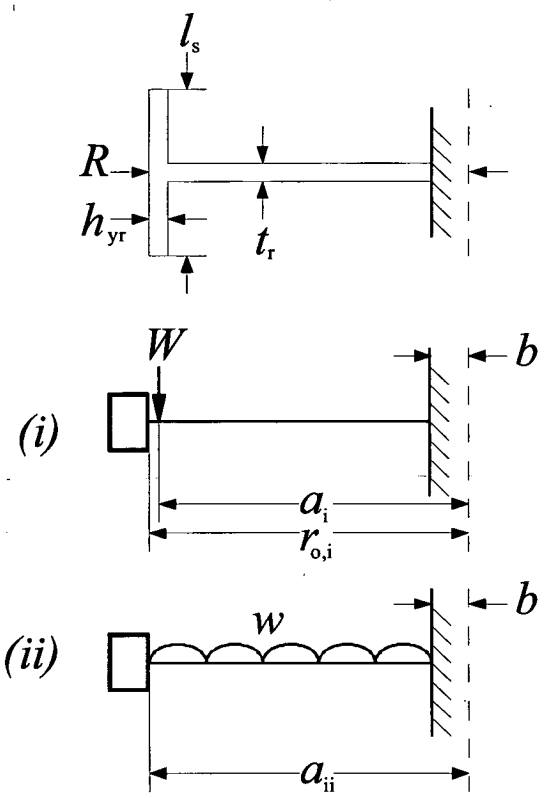

Figure 5.21. Cross section of rotor with disc with dimensions (*top*). (*i*) Weight component of the back iron. (*ii*) Weight component of the disc.

Table 5.4 shows deflection results for the case 1-3 rotors found using finite element analysis and also the equations (5.41) to (5.44) above. The analytical results are between 93% and 114% of the finite element deflection.

	FEA	Analytical
Case 1	7.603×10^{-4}m	7.067×10^{-4}m
Case 2	6.603×10^{-4}m	6.858×10^{-4}m
Case 3	8.007×10^{-5}m	9.115×10^{-5}m

Table 5.4. Finite element model and analytical axial deflection results for Case 1 to 3 rotor structures.

5.4.3.2 Stator with discs

Figure 5.22 shows the axisymmetric cross section of half of the stator with discs. It assumed that each of the stator discs carry the loading of half of the stator cylinder. As with the rotor with discs, a fixed inner edge and a guided outer edge are used. The total deflection, y, is made up of two components, $y_{a,i}$ (deflection due to the stator cylinder) and $y_{a,ii}$ (deflection due to the disc). These two models are shown in Fig. 5.22 (i) and (ii).

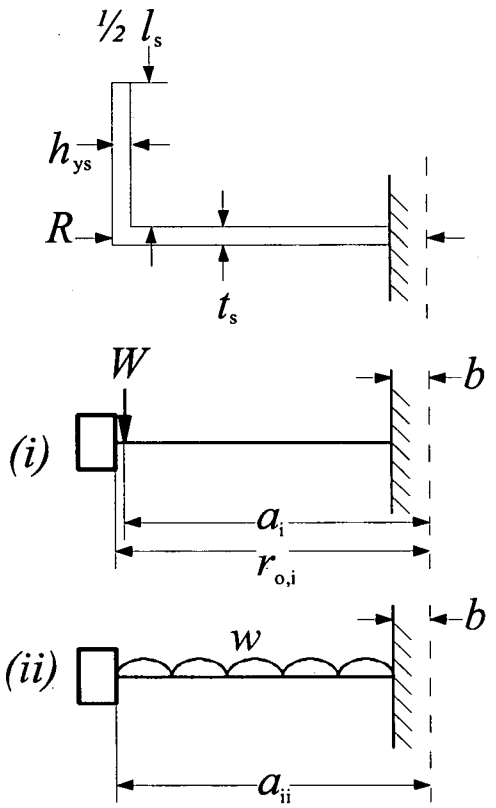

Figure 5.22. Cross section of half of stator with disc including dimensions (*top*). (*i*) Weight component of the back iron. (*ii*) Weight component of the discs.

$$y_{a,i} = \frac{-Wa_i^4}{bD}\left[\frac{C_2C_6}{C_5} - C_3\right], \tag{5.36}$$

where $W = \frac{1}{2}\rho g \sin(\varphi)(l_s - 2t_s)h_{ys}$ and

$$y_{a,ii} = M_{rb}\frac{a_{ii}^2}{D}C_2 + Q_b\frac{a_{ii}^3}{D}C_3 - \frac{wa_{ii}^4}{D}L_{11} \tag{5.37}$$

where $w = \rho g \sin(\varphi)t_s$ and

$$M_{rb} = \frac{-wa_{ii}^2}{C_8}\left[\frac{C_9}{2a_{ii}b_{ii}}\left(a_{ii}^2 - r_{o,ii}^2\right) - L_{17}\right], \tag{5.38}$$

$$Q_b = \frac{w}{2b_{ii}}\left(a_{ii}^2 - r_{o,ii}^2\right). \tag{5.39}$$

Table 5.5 shows deflection results for the case 1-3 stators found using finite element analysis and also the equations (5.45) to (5.48) above. The analytical results are between 103% and 116% of the finite element deflection.

	FEA	Analytical
Case 1	3.252×10^{-4}m	3.457×10^{-4}m
Case 2	4.476×10^{-4}m	4.637×10^{-4}m
Case 3	6.655×10^{-5}m	7.732×10^{-5}m

Table 5.5. Finite element model and analytical axial deflection results for Case 1 to 3 stator structures.

5.4.3.3 Rotor with arms

A cross section of the armed rotor in Fig. 5.1.(a) is shown in Fig. 5.23. An elastic straight beam with the right end fixed (at the rotor shaft) and the left end guided (modelling the connection to the rotor cylinder) is used to find the axial deflection, y. This is made up of two components, that due to $1/n^{th}$ of the weight of the rotor cylinder, W (shown in Fig. 5.23(i)) and that due to the weight of the rotor arm itself (represented by the u.d.l. w shown in Fig. 5.23(ii)).

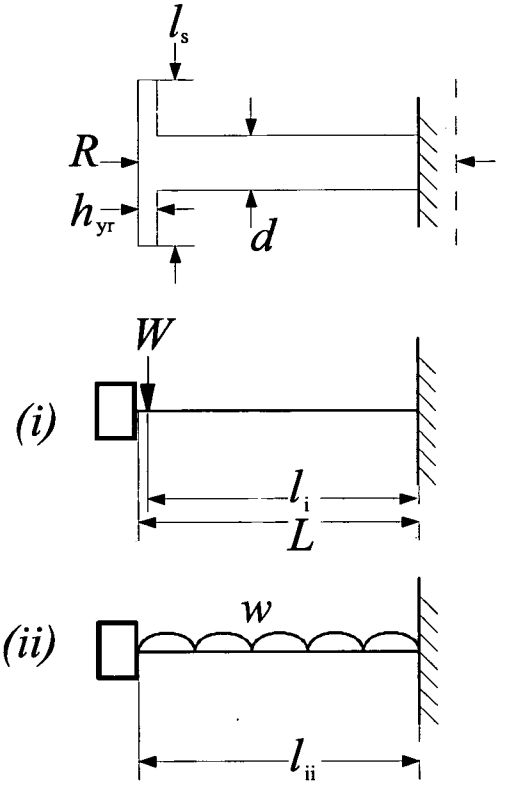

Figure 5.23. Cross section of rotor with arms including dimensions (*top*). (*i*) Weight component of the back iron. (*ii*) Weight component of the arms.

These deflections components are given in eqns. (5.40) and (5.41),

$$y_{a,i} = \frac{W l_i^3}{12EI}, \tag{5.40}$$

where $W = (2\pi R/n)\rho g \sin(\varphi) l_s h_{yr}$, $l_i = R - b - (h_{yr}/2)$ and I is the second moment of area of the rotor arm, and

$$y_{a,ii} = \frac{w l_{ii}^4}{24EI}, \tag{5.41}$$

where $w = \rho g \sin(\varphi) A$ and $l_{ii} = R - b$. The total axial deflection is $y = y_{a,i} + y_{a,ii}$.

Table 5.6 shows deflection results for the case 1-3 rotors found using finite element analysis and also the equations (5.40) to (5.41) above. The analytical results are between 83% and 118% of the finite element deflection.

	FEA	Analytical
Case 1	5.68×10^{-6}m	4.71×10^{-6}m
Case 2	1.05×10^{-5}m	1.15×10^{-5}m
Case 3	9.70×10^{-6}m	1.14×10^{-5}m

Table 5.6. Finite element model and analytical axial deflection results for Case 1 to 3 armed rotor structures.

5.4.3.4 Stator with arms

A cross section of the armed stator in Fig. 5.1.(b) is shown in Fig. 5.24. The stator arm is treated in the same way as the rotor in section 5.4.3.3 except for a difference in loading. In the stator case there are three loads: two point loads, W_i and W_{ii} (half of the beam joining the two stator arms and $1/n^{th}$ of the stator cylinder respectively) and w the u.d.l. of the stator arm weight.

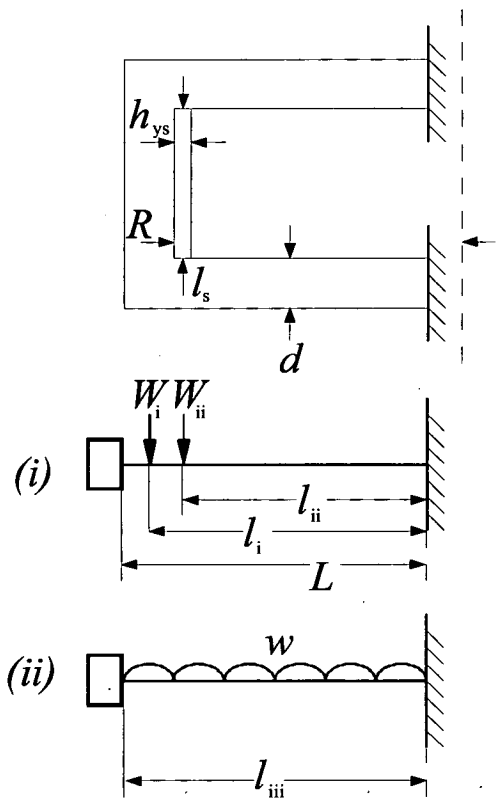

Figure 5.24. Cross section of stator with arms including dimensions (*top*). (*i*) Weight component of the back iron. (*ii*) Weight component of the arms.

The deflection components are

$$y_{a,i} = \frac{W_i l_i^3}{12EI}, \tag{5.42}$$

where $W_i = \frac{1}{2}\rho g \sin(\varphi) l_s d^2$, $l_i = R - b - \frac{1}{2}d$ and I is the second moment of area of the stator arm,

$$y_{a,ii} = \frac{W_{ii} l_{ii}^3}{12EI}, \tag{5.43}$$

where $W_{ii} = \frac{\rho g \sin(\varphi) l_s h_y \pi R}{n}$ and $l_{ii} = R - b - d - \frac{1}{2}h_{ys}$, and

$$y_{a,iii} = \frac{w l_{iii}^4}{24EI} \tag{5.44}$$

where $w = \rho g \sin(\varphi) A$ and $l_{iii} = R + d - b$.

Therefore the total axial deflection is $y = y_{a,i} + y_{a,ii} + y_{a,iii}$. Table 5.7 shows deflection results for the case 1-3 rotors found using finite element analysis and also the equations (5.42) to (5.44) above. The analytical results are between 77% and 108% of the finite element deflection.

	FEA	Analytical
Case 1	8.51×10^{-6}m	6.89×10^{-6}m
Case 2	1.20×10^{-5}m	9.29×10^{-6}m
Case 3	1.01×10^{-5}m	1.09×10^{-5}m

Table 5.7. Finite element model and analytical axial deflection results for Case 1 to 3 armed stator structures.

5.5 Discussion

In sections 5.1 and 5.2, radial deflection due to Maxwell stress was analysed for rotor and stator structures. In section 5.3, minimisation of structural mass was attempted using only the design equations from section 5.1 and 5.2. It can be seen that this produced a solution which would satisfy the deflection criterion based on the normal component of Maxwell stress, however it does

not produce a practical design when other forces such as gravity are included. Section 5.4 shows that the major component of gravity is typically very small compared to Maxwell stress, and it is noted that the deflection of the rotor and stator would likely be similar in both magnitude and direction and so cancel each other out. Consequently this has been neglected. The effect of the minor component of gravity was introduced and the deflection in the axial direction is analysed in section 5.4.

Figure 5.25 shows a plot of mass and deflection for the same rotor as that described in Section 5.3. In this case, the axial deflection equal to 1mm is plotted according to eqns. (5.40) and (5.41) in thick grey. The minimum mass of the structure that meets these two criteria is just over 30 tonnes when h_{yr} = 45 mm and t_r = 60 mm.

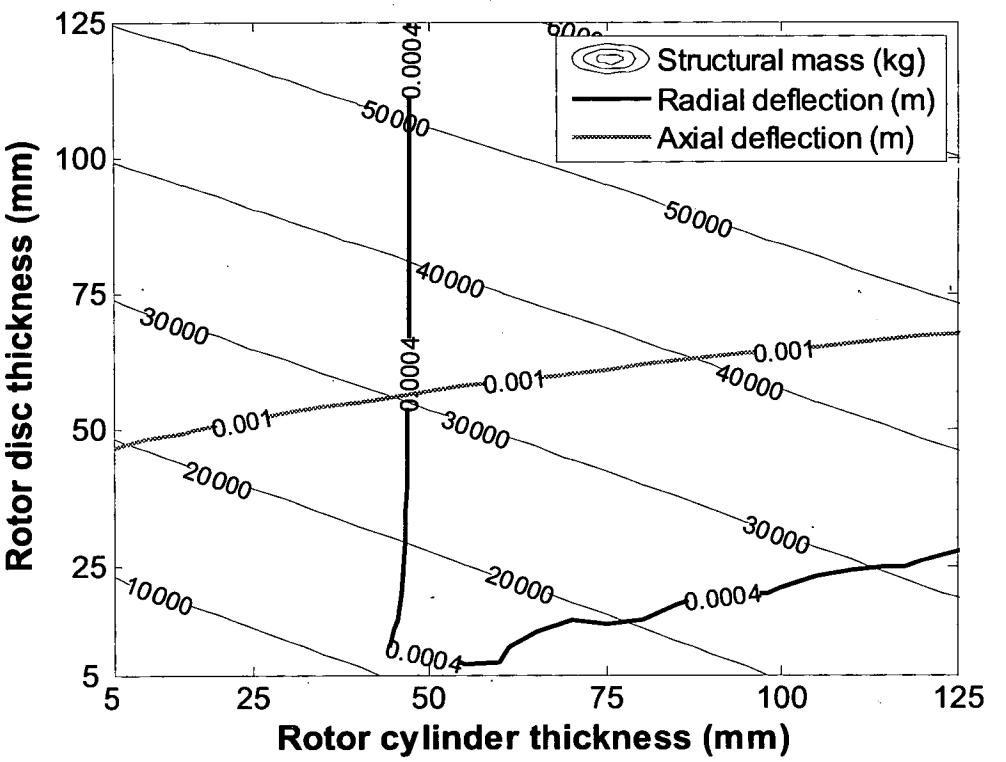

Figure 5.25. 2d optimisation for 5 MW disc rotor structure (R = 4m, l_s = 0.96m) with radial and axial deflection criteria.

This approach can also be used for the stator with discs and for the rotor and stator with arms. In Chapter 4, the aspect ratio was varied to see the impact on mass. Table 5.8 shows the variation of radial and axial dimensions for a 5MW generator taken from [72]. Figures 5.26 and 5.27 show the minimum structural mass for rotors and stators with arms and discs for a 5MW machine, found using a collection of 2d optimisation plots (similar to that shown in Fig. 5.25).

K_{rad}	0.02	0.06	0.12	0.28	0.96
r_g/m	7.0	5.0	4.0	3.0	2.0
l_s/m	0.31	0.61	0.96	1.70	3.82

Table 5.8. Radial and axial dimensions for a 5 MW generator.

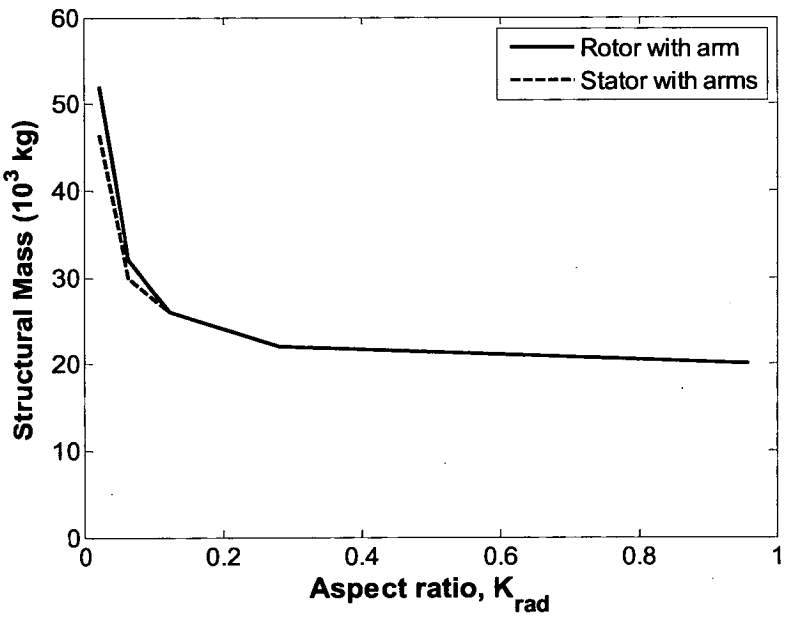

Figure 5.26. Structural mass for 5 MW rotor and stator with arms for varying aspect ratio, K_{rad}.

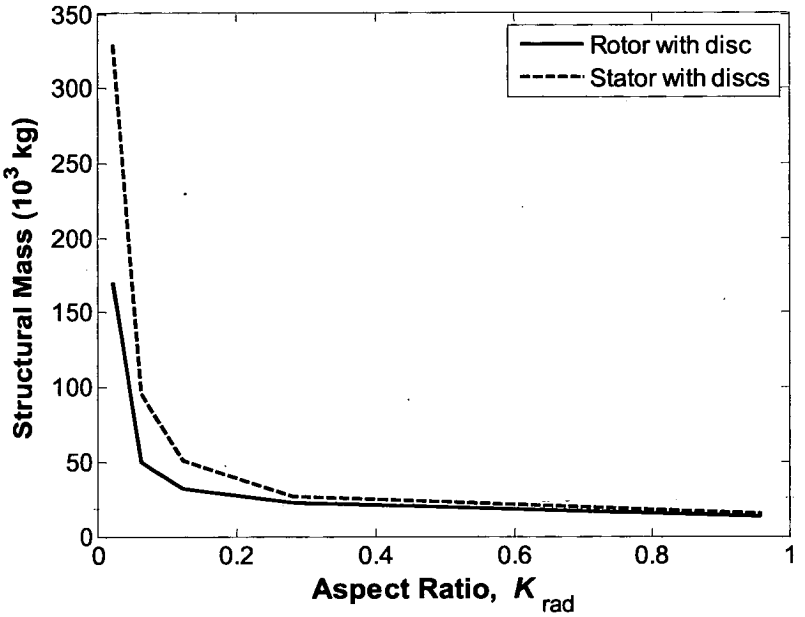

Figure 5.27. Structural mass for 5 MW rotor and stator with discs for varying aspect ratio, K_{rad}.

Both Fig. 5.26 and 5.27 show the structural mass decreasing as the aspect ratio increases. The rotor with disc is similar to results from Chapter 4 (Fig. 4.16) although the stator structural mass for a stator with arms has a different trend than that produce in Chapter 4. The main reason for this is that the stator in this chapter is symmetric (i.e. it has arms at both ends of the stator) whereas the stator in Chapter 4 is one-sided and is heavily affected by gravity at long axial lengths.

The structural masses are low, for what would be between 4 and 14 m diameter machines. At the very least this is due to the generous (and probably not very realistic) axial deflection that has been allowed. During assembly or positioning, the generator axis will probably pass through a tilt angle of 90°. The axial deflection then would be 5-10 times the value when in its final position, which would be too much. Choosing a stricter axial deflection criteria lifts the grey line in Fig. 5.25, and hence the structural mass for both the rotor and stator (with discs and arms).

5.6 Conclusions

In this chapter, analytical design tools for radial-flux generator rotor and structures have been introduced, verified with finite element analysis and finally applied in simple mass minimisations. Four general structures have been analysed: rotor with disc, rotor with arms, stator with discs and stator with arms. The radial deflection due to the normal component of Maxwell stress and the axial deflection due to gravity can now be found quickly for a wide range of dimensions and materials.

Chapter 6

Comparison of generator topologies

6.1 Introduction

A NUMBER of studies have compared different generator topologies for direct-drive renewable energy applications including wind turbines [28], [38] and wave energy devices [94]. These have typically compared the torque (or force) density and cost per unit torque (or unit force) of different prototypes for optimised designs based on active mass (iron, copper, and permanent magnets). However for both radial-flux and axial-flux topologies it has been shown that the active mass is dominated by the 'inactive' mass (two thirds of the total mass for the radial-flux [59] and up to 90% for the axial-flux machine in Chapter 3). The job of this inactive mass is to maintain the small airgap clearance and to hold the active mass in position subject to normal and shear stress in the airgap and the effect of gravity. For a fair comparison of different topologies the inactive mass must be included.

The work in Chapters 3, 4 and 5 has produced modelling techniques that link the electrical and magnetic design to the structural design of axial-flux and radial-flux permanent magnet machines. This work is enhanced in this chapter by introducing the concept of 'secondary deflection' and by linking the simple radial-flux structural models to commercial designs.

In this chapter, results of optimised designs based on a generator cost and loss cost criterion used in [93], adjusted here to include the cost of inactive

mass, is presented. This cost criterion is calculated for a typical wind speed profile so that the comparison includes partial load, not just the nominal full load rating. Radial-flux permanent magnet machines and slotted axial-flux permanent magnet machines are compared for 2, 3, and 5 MW ratings.

6.2 Methodology

6.2.1 Cost criterion for optimisation and comparison

The comparison is based on the costs and losses in a generator over 5 years for a range of multi-MW wind turbine designs. The cost criterion, C, in € is given by

$$C = C_{\text{active}} + C_{\text{inactive}} + PE_{\text{d}}C_{\text{kWh}}, \tag{6.1}$$

where C_{active} is the active material cost and C_{inactive} is the inactive material cost (both in €), P is the period of 5 years, E_{d} is the annual energy losses dissipated in the generator in kWh and C_{kWh} is the price of energy, taken here as 0.10 €/kWh. This cost criterion is fair because it includes both machine losses and cost – any additional investment in efficiency must be earned back in P years.

6.2.2 Annual Energy Yield

The annual energy yield is found by running a wind turbine model with a suitable wind speed distribution as used in [93]. This is modelled with a Weibull distribution. The Weibull probability density function is defined by two parameters, a shape factor, k, and a scale factor, c. The probability of seeing a wind speed, v_{w}, is

$$p(v_w) = \frac{k}{c}\left(\frac{v_w}{c}\right)^{k-1} e^{-\left(\frac{v_w}{c}\right)^k}. \tag{6.1}$$

The shape and scale factor can be derived from the mean wind speed and the standard deviation of the wind speed [68] and as such, different locations with different wind climates will be characterised by different Weibull curves. Figure 6.1 shows several distributions with the same scale factor (c =

7) and varying shape factor. The curve with the sharpest peak, k = 2.5, has the smallest wind speed variation.

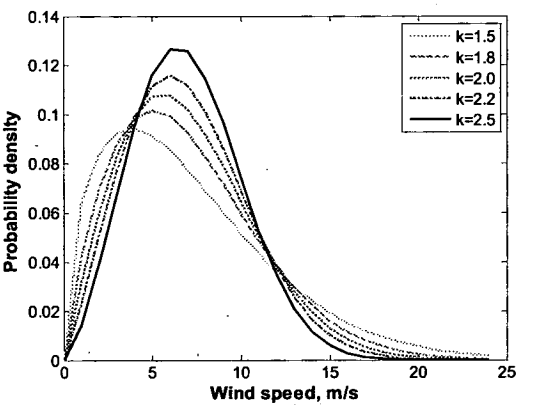

Figure 6.1. Weibull probability distribution curves with same scale factor but different shape factors.

The actual wind distribution is modelled using an average wind speed of 7 m/s (parameters in Table 6.1) and is shown in Fig. 6.2.

The shaft power, P delivered to the generator is given by

$$P = \tfrac{1}{2}\rho_{\text{air}} c_{\text{p}}(\lambda,\theta)\pi r^2 v_{\text{w}}^3, \tag{6.2}$$

where ρ_{air} is the density of air, c_{p} is the coefficient of performance (a function of the blade pitch angle θ and the tip speed ratio λ), r is the turbine blade radius and v_{w} is the wind speed. The different machine ratings – along with their rotor blade diameter and nominal speeds – are given in Table 6.2. The rated rotor speed, N_{nom} is fixed so that the maximum tip speed of the rotor blades is about 75 m/s – speeds above this will lead to noise problems. As Fig. 6.3 shows, this means that as the power rating increases, the rotor blade radius will increase and the rotational speed will fall at each increment of power rating. Figure 6.4 shows the rotor speed as a function of wind speed for the 3 MW wind turbine. At rotor speeds greater than N_{nom} = 16 rpm, the blades are pitched so as to reduce the coefficient of performance and hence the power does not increase further.

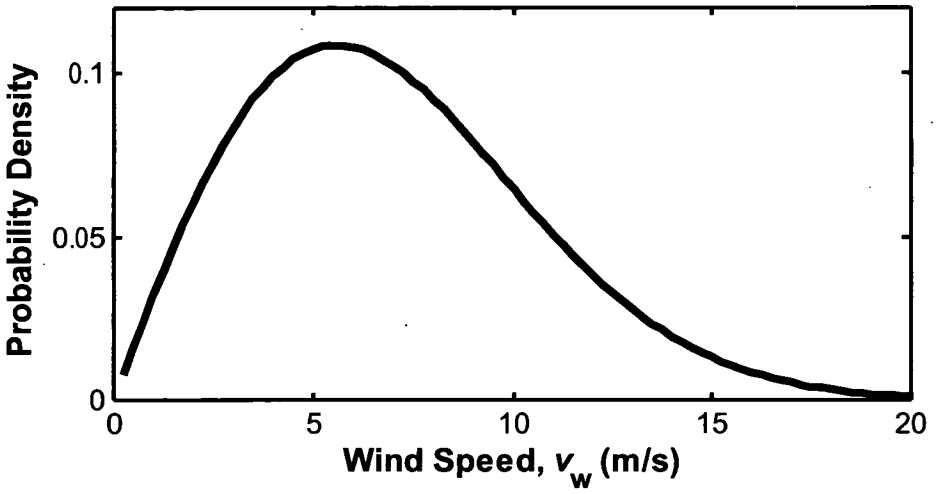

Figure 6.2. Weibull distribution with a 7 m/s average wind speed

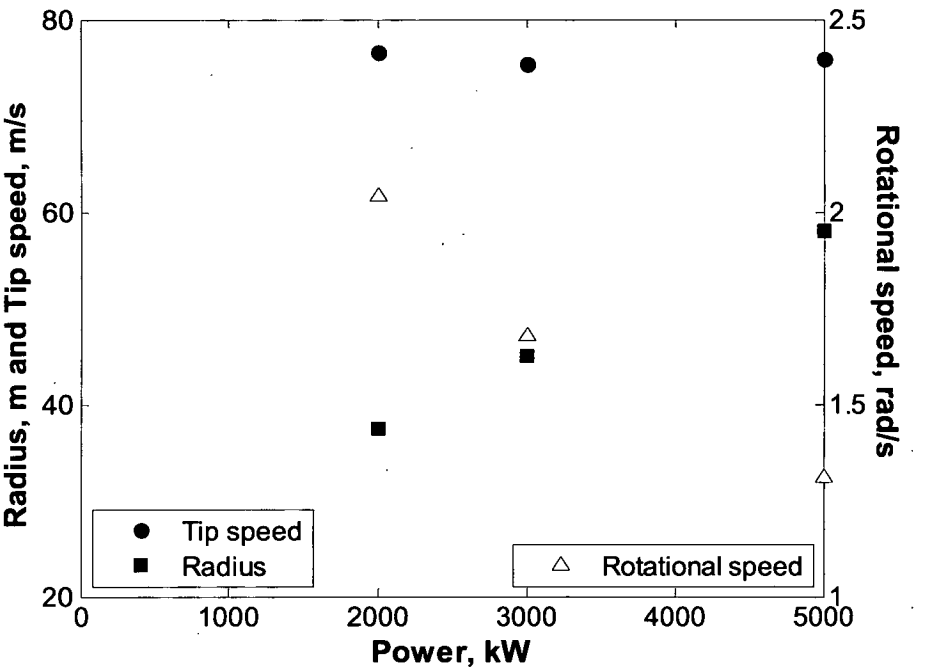

Figure 6.3 Rotor blade radius, tip speed and rotational speed against power rating.

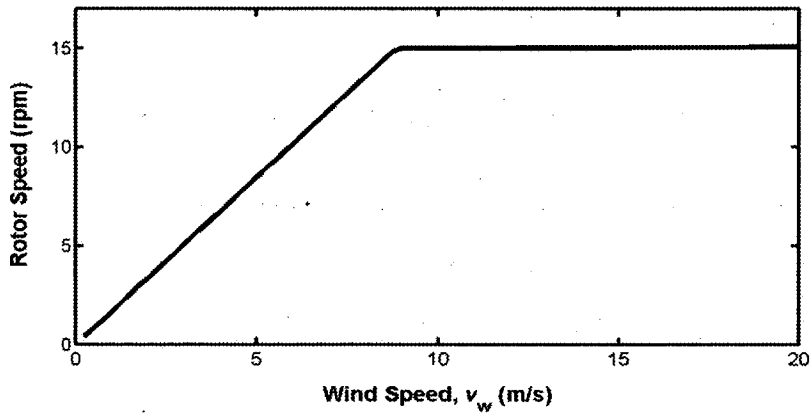

Figure 6.4 Rotor speed as a function of wind speed for the 3 MW wind turbine

Optimum tip speed ratio, λ	8
Maximum aerodynamic efficiency, c_p	0.48
Rated wind speed, $v_{w,rated}$ (m/s)	12
Weibull scale parameter	7.9
Weibull shape parameter	2
Mass density of air, ρ_{air} (kg/m^3)	1.225

Table 6.1. Wind and turbine characteristics

Rated grid power, P_{nom} (MW)	2	3	5
Rotor diameter, $2r$ (m)	75	90	116
Rated speed, N_{nom} (rpm)	19.5	16	12.5
Rated torque, T (MNm)	0.98	1.8	3.8

Table 6.2. Wind turbine ratings

6.2.3 Active Modelling

The modelling of the active part of these machines is based on [93] and the reader is referred there for a detailed explanation of the PM synchronous modelling used here. The key equations are reproduced in Appendix B.

In all machines the airgap clearance, c is kept as 1/1000th of the airgap diameter, d_g (as used by Grauers in his thesis [53]). The number of poles is changed with the airgap radius so that the same pole pitch and stator teeth layout (taken from [93]) is used in each case. The thickness of permanent magnets is varied so as to produce the same airgap flux density, B_g = 0.84 T.

The main differences for the axial-flux modelling are that ($a_r - r_0$) replaces l_s as the active length and that the saturation at the inner radius is taken into account (as in Dubois' thesis [41]).

The active cost modelling is achieved by multiplying the mass of each material by the costs in Table 6.3. Again the reader is referred to [93] and Appendix B for details of the loss modelling which leads to the annual dissipation (in Figs. 6.5 (a) and (b) for example) and the calculation of E_d, the annual energy lost in the electrical generator.

Structural steel cost (€/kg)	3
Laminations cost (€/kg)	3
Copper cost (€/kg)	15
Permanent magnet cost (€/kg)	25

Table 6.3. Cost modelling

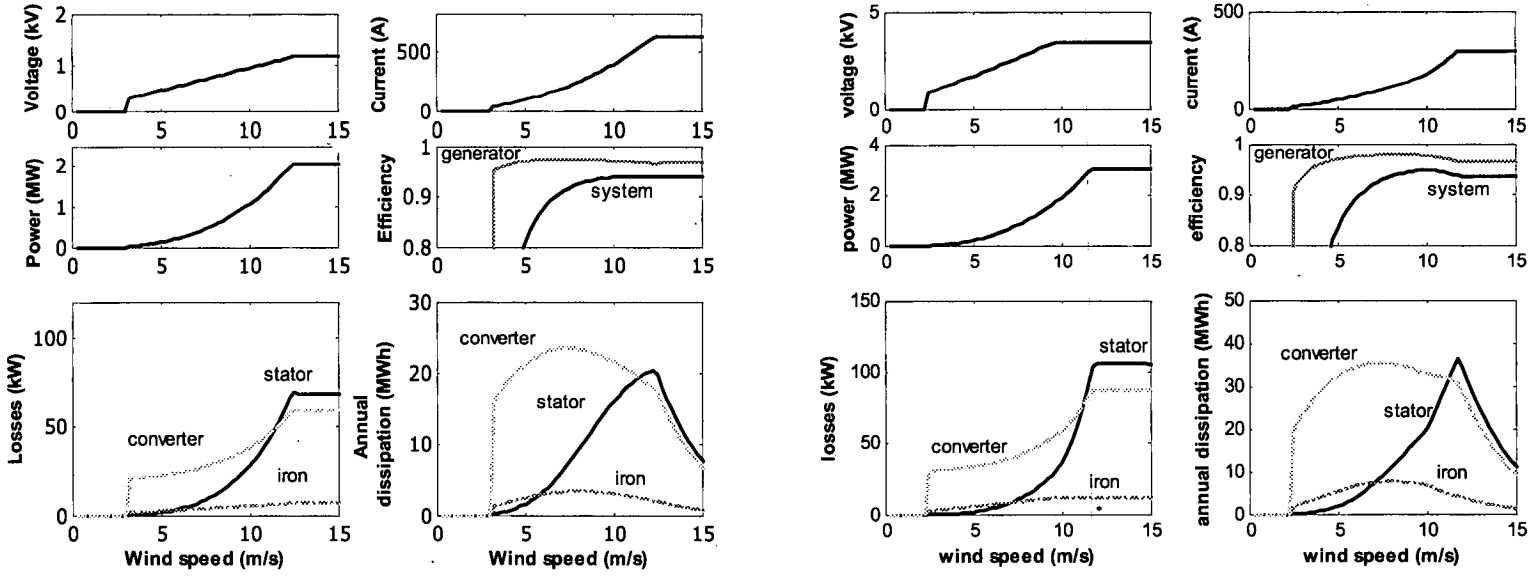

Figure 6.5. Active modelling examples: (a) Characteristics of 2 MW radial-flux PM generator with r_g = 2.5m and l_s = 0.63m and (b) Characteristics of 3 MW axial-flux PM generator with a_r = 3.1m and k_r = 0.7.

6.2.4 Structural Modelling

6.2.4.1 Normal stress

The largest force acting on the rotor and stator is the normal stress, q, which is found by

$$q = \frac{B_g^2}{2\mu_o} \tag{6.3}$$

where B_g is the airgap flux density and μ_o is the permeability of free space. The normal stress is usually an order of magnitude greater than that of the shear stress – consequently shear stress is neglected in this analysis. For both the radial-flux and the axial-flux cases the machine structure will be adjusted so that the total deflection into the airgap is 10% of the airgap clearance.

Normally the magnets that provide the flux density only cover part of each pole pitch. To simplify the analysis eqn. (6.3) is multiplied by k_{mag}, the ratio of magnet width to pole pitch, and the normal stress is assumed to act uniformly over the entire rotor area (and thus the total force on the disc is conserved).

6.2.4.2 Radial-flux machines

The structure used for the radial-flux machines is shown in Fig. 6.7 and is described in detail in Chapter 4. This is based on generator structural designs described in [20] and [59] and is similar to that of the Enercon E70 wind turbine generator (shown in Fig. 6.6).

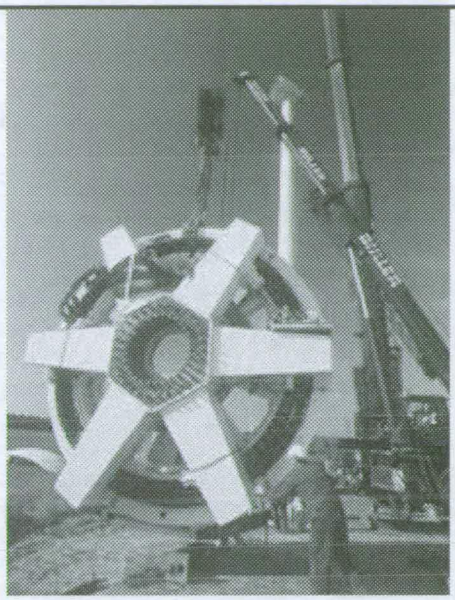

Figure 6.6. Enercon E70 generator

Here the machine structure is made up of an inner rotor (which can be thought of as a short cylinder wrapped around a circular disc) and an outer stator (a cylinder held by a 'spider' of 6 support arms).

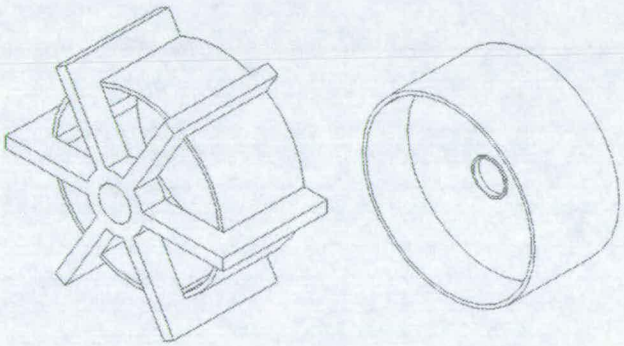

Figure 6.7. Radial-flux machine structure. Stator (left) and rotor (right).

A polynomial method – as outlined in Chapter 4 – is first used to find the structural dimensions (and estimate the minimum mass) that will give the permissible airgap deflection. Following this a number of finite element runs are performed to verify that the polynomial method has worked and refine the structural design so that the design with the minimum structural mass is found. The form of the cubic polynomial to find the deflection (in either the rotor or the stator) is given in eqn. (6.4),

$$u_{radial} = \sum_{i=0}^{5}\sum_{j=i}^{5}\sum_{k=j}^{5} a_{i,j,k} x_i x_j x_k \,. \tag{6.4}$$

where x_n are given in Chapter 4.

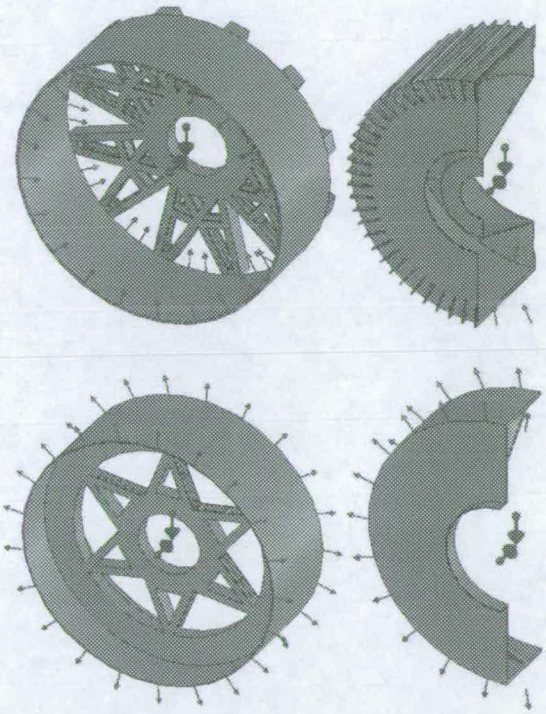

Figure 6.8. Commercial generator structures: (a) Stator 'E' (b) Stator 'Z' (c) Rotor 'E' and (d) Rotor 'Z'.

The stator model (Fig. 6.7) uses solid rather than hollow spider arms which is likely to lead to an overestimation of the inactive mass. A number of finite element models of commercial generator structures (shown in Fig. 6.8) were analysed and compared to the models used here. Table 6.4 shows relative deflections for an airgap radius of 2 m, with an aspect ratio, K_{rad} = 0.3. Generator 'E' is more similar to the model shown in Fig. 6.7 and is likely to display the same response to normal stress and gravity. Consequently this leads to a correction factor a_{st} = 0.5 to find the structural mass of the stator,

$$m_{str,st} = \alpha_{st} m_{str,st,pm} \,. \tag{6.5}$$

	Model	Generator 'E'	Generator 'Z'

Rotor relative deflection, u_{rel}	1	~1	~2
Stator relative deflection, u_{rel}	1	~½	~⅓

Table 6.4. Relative deflection of rotor and stator for generators 'E' and 'Z'

6.2.4.3 Axial-flux machines

In the case of the axial-flux machine the airgap deflection, u, can be found by using circular plate theory where the normal stress is applied between the inner and outer radii, r_0 and a_r. The deflection of the rotor (Fig. 6.9) is found using eqn. (3.2).

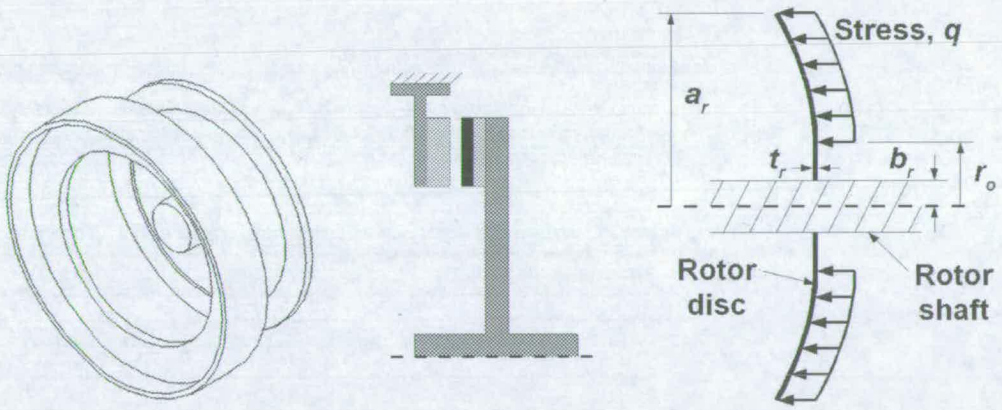

Figure 6.9. Axial-flux machine structure. (a) Isometric view (b) Side view (Light grey = laminations and windings; black = permanent magnets; dark grey = structures) (c) Rotor disc model

6.2.4.4 Secondary deflection

In both the radial-flux and axial-flux cases when the rotor and stator deflect and the airgap closes, there will be further (secondary) deflection because the airgap flux density will increase.

Secondary deflection modelling process

The deflection closes the airgap giving a new clearance of $c_2 = c_1 - u$. Flux density in the airgap for the axial-flux machine is given by eqn. (6.7) according to [113],

$$B_g = B_r \frac{h_m}{h_m + \mu_r (t_w + c)}. \qquad (6.7)$$

where h_m is the magnet thickness, t_w is the (slotless) winding thickness, B_r is the magnet remanence and μ_r is the magnet recoil permeability.

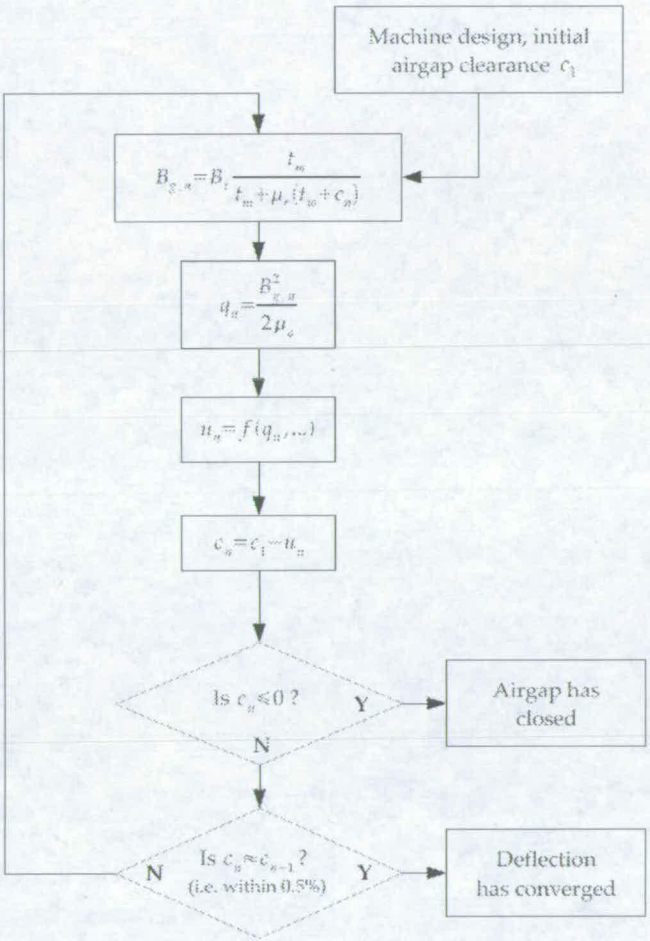

Figure 6.10. Process for iterative calculation for rotor deflection for axial-flux machine with slotless winding

A similar expression for the airgap flux density in a surface-mounted permanent magnet radial-flux machine is given in eqn. (6.8) [114],

$$B_g = B_r \frac{h_m}{h_m + \mu_r c}. \tag{6.8}$$

It follows that for both machine types B_g is a function of the airgap clearance c. As the airgap clearance reduces, so the normal stress q across the airgap increases. This is likely to cause further deflection.

To see whether this is the case an iterative calculation can be performed. The calculation process for the axial-flux case with winding in the airgap is shown in Fig. 6.10; a similar process can also be identified for the radial-flux machine by substituting eqn. (6.8) for (6.7).

Axial-flux rotor disc results

In the case of the axial-flux machine the rotor disc (which is the heaviest part) will be examined. Fig. 6.11 shows that a 2.5 MW design (with rotor disc thickness t_r) for a deflection of 25% of the airgap actually gives a final deflection of 47% (c_{final} / c_1 = 53% in Table 6.5) because of subsequent deflection. It is necessary to increase the disc thickness by 11% ($t_{r,adj}$ / t_r = 111% in Table 6.5), so that the design deflection can be achieved.

The reason for this secondary deflection can be clearly seen in Fig. 6.12. This shows the airgap stress increasing as the iterations advance (and the airgap clearance reduces). This example is for a 2.5 MW machine; Table 6.5 shows the results for a range of machine sizes (taken from designs in Chapter 3). For the larger machines, the extra mass needed to minimise the deflection can add up to 10% to the total machine mass.

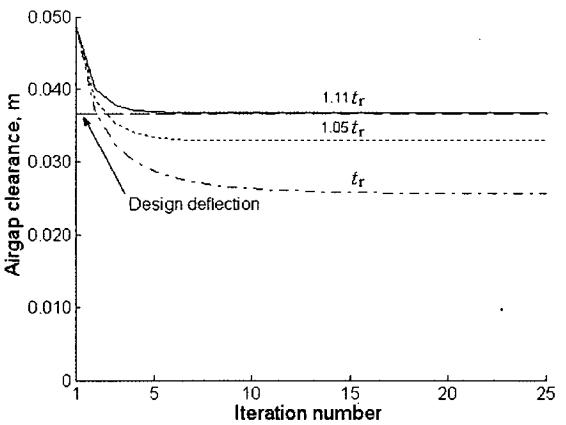

Figure 6.11. Deflection of 2.5 MW axial-flux rotor disc

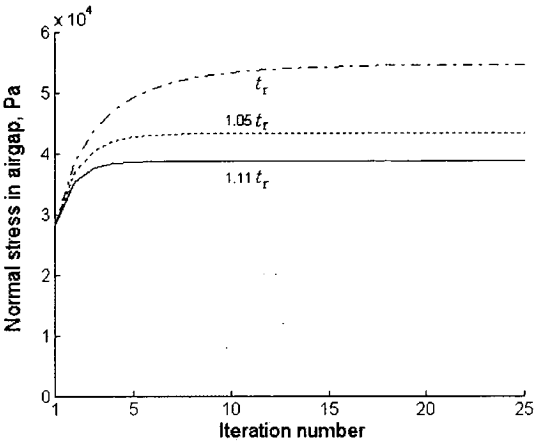

Figure 6.12. Airgap stress of 2.5 MW axial-flux rotor disc

Power, kW	c_{final} / c_1 , %	$t_{r,adj}$ / t_r , %
100	72	107
500	63	109
1000	59	110
2500	53	111
5000	airgap closes	112

Table 6.5. Airgap clearance and adjusted rotor disc thickness

Radial-flux results

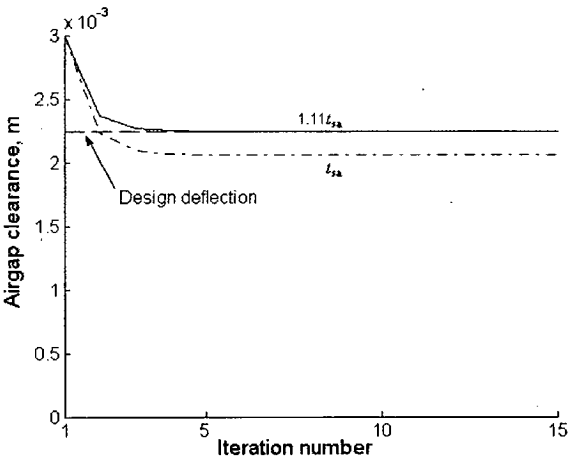

Figure 6.13. Deflection of 1.6 MW radial-flux stator structure

In the case of the 1.6 MW radial-flux machine stator, the support arm thickness must be increased by 11% (Fig. 6.13) in order to produce the

desired deflection. Because the stator inactive mass tends to dominate, this leads to an increase in total mass of about 5%.

6.2.5 Geometric ratios

One of the fundamental questions that a wind turbine generator designer faces is what shape of machine should be used. Which is better: a radial-flux machine which is axially short and large in diameter (such as the 6 MW E112 which is reported to have a 12m diameter [32]) or a machine which is longer in the axial direction but has a smaller diameter? The shape of a radial-flux machine is described by the aspect ratio, K_{rad}, the ratio of axial length, l_s, to airgap diameter, $d_g = 2r_g$

$$K_{rad} = \frac{l_s}{2r_g} \tag{6.9}$$

For the axial-flux machines the equivalent to this aspect ratio is k_r, the ratio of inner to outer radii, a_r and r_0

$$k_r = \frac{r_0}{a_r}. \tag{6.10}$$

In reality, these aspect ratios will be chosen as part of the overall wind turbine design. For example, the outer radius of the generator may be constrained by the nacelle design or transport requirements.

In this chapter, geometric ratios will be varied and used as the basis for the optimisation along with the cost criterion, C. The two ratios are illustrated in Fig. 6.14.

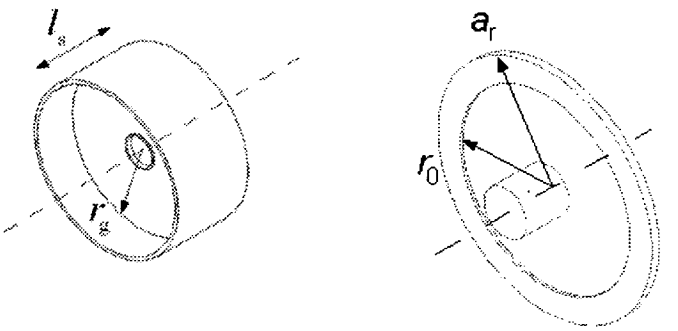

Figure 6.14. (a) Radial-flux and (b) axial-flux rotors showing dimensions important for geometric ratios.

A 2 MW machine that has a rated rotor speed N_{nom} = 19.5 rpm must develop a peak torque of at least 980 kNm. If the airgap force, F, is developed over the airgap surface area, A, by a shear stress, σ, then the torque is proportional to the rotor volume, V_r, as shown in eqn. (6.7). The same rotor volume can be produced by different combinations of K_{rad} and r_g as in eqn. (6.8).

$$\begin{aligned} T &= Fr_g \\ &= \sigma A r_g \\ &= 2\pi\sigma r_g^2 l_s \\ &= 2\sigma V_r \end{aligned} \tag{6.11}$$

$$V_r = 2\pi K_{rad} r_g^3 \tag{6.12}$$

In the case of the axial-flux machine if the same shear stress, σ, is developed between the inner and outer radii, r_0 and a_r, then the torque is

$$\begin{aligned} T &= 2\pi\sigma \int_{r_0}^{a_r} R^2 dR \\ &= \tfrac{2}{3}\pi\sigma(a_r^3 - r_0^3) \\ &= \tfrac{2}{3}\pi\sigma a_r^3(1 - k_r^3) \end{aligned} \tag{6.13}$$

The geometric ratios and their corresponding dimensions are shown in Table 6.4 for the radial-flux machines and in Table 6.5 for the axial-flux machines.

2MW	K_{rad}	0.07	0.13	0.25	0.58	1.97
	r_g (m)	3.00	2.50	2.00	1.50	1.00
	l_s (m)	0.44	0.63	0.98	1.75	3.93
3MW	K_{rad}	0.08	0.13	0.23	0.45	1.06
	r_g (m)	3.50	3.00	2.50	2.00	1.50
	l_s (m)	0.59	0.80	1.15	1.79	3.19
5MW	K_{rad}	0.02	0.06	0.12	0.28	0.96
	r_g (m)	7.00	5.00	4.00	3.00	2.00
	l_s (m)	0.31	0.61	0.96	1.70	3.82

Table 6.6. Radial-flux machine dimensions.

	k_r	0.5	0.55	0.6	0.7	0.8	0.9	0.95
2 MW	a_r (m)	2.31	2.34	2.39	2.54	2.80	3.41	4.22
	r_0 (m)	1.15	1.29	1.60	1.78	2.24	3.07	4.01
3 MW	a_r (m)	2.82	2.86	2.92	3.10	3.42	4.16	5.16
	r_0 (m)	1.41	1.57	1.75	2.17	2.74	3.75	4.90
5 MW	a_r (m)	3.63	3.68	3.76	3.99	4.40	5.36	6.64
	r_0 (m)	1.81	2.03	2.26	2.79	3.52	4.82	6.30

Table 6.7. Axial-flux machine dimensions.

6.3 Results

6.3.1 Radial-flux machines

6.3.1.1 Mass comparison

Inactive mass

The minimum inactive mass for all three machine ratings is in the range K_{rad} = 0.25 - 0.3. Figure 6.15 shows the inactive mass for the 5 MW radial-flux machine. The rotor inactive mass, $m_{in,r}$, is proportional (in the first order) to the area of the circular disc (which joins the cylinder to the shaft) and therefore to r_g^2. As K_{rad} approaches 0 the airgap radius increases steeply and so too does $m_{in,r}$, dominating the total inactive mass. In the case of the stator the inactive mass, $m_{in,st}$, is approximately proportional to the airgap radius r_g, (because the spider arms double in length when airgap radius doubles), hence there is a gentler increase in $m_{in,st}$ as $K_{rad} \rightarrow 0$. Above K_{rad} = 0.3 $m_{in,st}$ starts to increase. This is because the axial length is increasing so that the centre of mass moves further away from the support arms. The turning

moment effect of the stator weight increases approximately with the length of the stator length (this turning effect is shown in Fig. 6.16). This is compounded by the fact that as K_{rad} increases the airgap clearance, c, reduces and the permissible deflection is decreasing in magnitude (so that the structure can only deflect by a smaller amount requiring a more rigid structure).

Active mass

The active mass, m_{ac}, is smallest when the airgap radius is large (i.e. when $K_{rad} \rightarrow 0$). In the first approximation the active mass is proportional to the surface area of the airgap. When moving from, say, $K_{rad} = 0.1$ to $K_{rad} = 0.8$ the airgap radius, r_g, will halve and the axial length, l_s, will quadruple in order to give the same rotor volume, V_r. The surface area, $A = 2\pi r_g l_s$, will then double and so too will the active mass. This can be seen in Fig. 6.17.

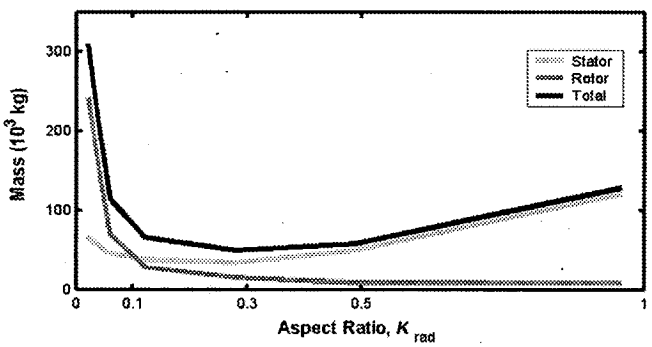

Figure 6.15. Stator inactive, rotor inactive and total inactive mass plotted against aspect ratio, K_{rad}, for a 5 MW radial-flux machine.

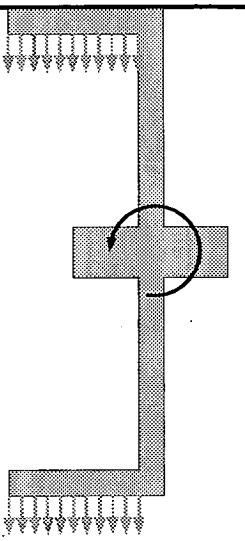

Figure 6.16. Gravity turning effect on stator.

Total mass

Figure 6.18 shows the total mass for the 2, 3, and 5 MW machines. The minimum mass is at K_{rad} = 0.2, 0.22, and 0.27 for the 2, 3, and 5 MW machines respectively. The curves are shallow and quite flat between K_{rad} = 0.1 and K_{rad} = 0.5. The minimum mass of the 5 MW machine is about 4 times that of the 2 MW machine – this is roughly the same ratio of the peak torque: 980 kNm to 3.84 MNm.

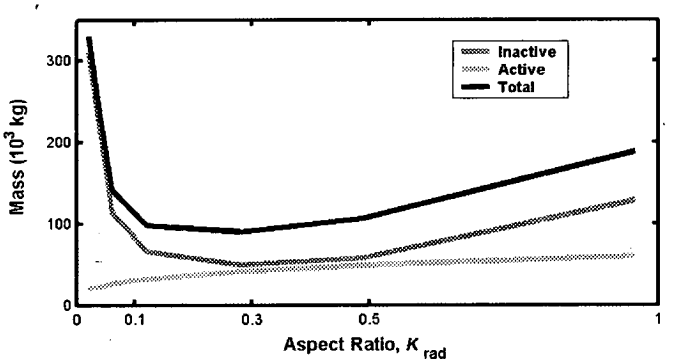

Figure 6.17. Inactive, active and total mass plotted against aspect ratio, K_{rad} for a 5MW radial-flux machine.

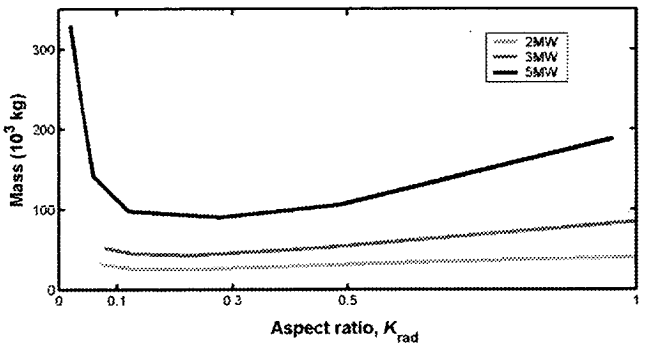

Figure 6.18. Total mass for 2, 3 and 5 MW radial-flux machines plotted against aspect ratio, K_{rad}.

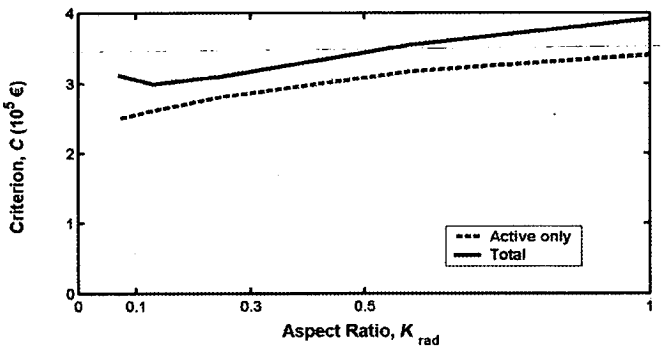

Figure 6.19. Cost criterion, *C*, for 2 MW radial-flux machine against aspect ratio, K_{rad}, calculated with the active mass only and total mass.

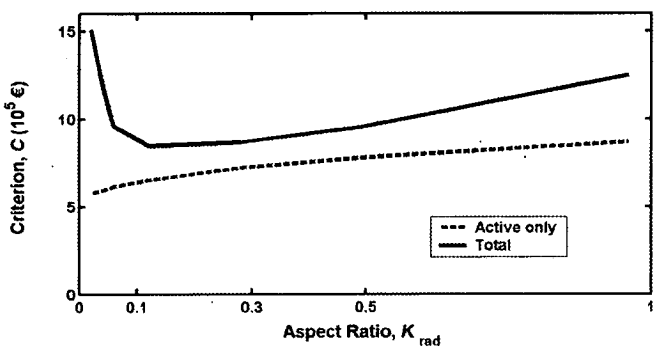

Figure 6.20. Cost criterion, *C*, for 5 MW radial-flux machine against aspect ratio, K_{rad}, calculated with the active mass only and total mass.

6.3.1.2 Cost criterion

Figures 6.19 and 6.20 show the cost criterion, *C*, plotted against the aspect ratio, K_{rad} for 2 and 5 MW designs calculated with only the active mass and then with the total mass. Considering the active mass only case first, in both

cases the cost criterion decreases as K_{rad} approaches 0. This is due to the decrease in active mass as seen in Fig. 6.17. Based on only the cost of the active mass the machine designer would choose a design with a very small K_{rad}.

The inactive material is cheaper than the active material – as shown in Table 6.3 – and so the inclusion of the cost of the inactive mass only makes a marginal effect when $K_{rad} > 0.3$. However when $K_{rad} < 0.2$ and the inactive mass becomes dominant then the cost criterion reaches a lower limit and then begins to increase (Figs. 6.19 and 6.20) as K_{rad} approaches 0. For the 2, 3, and 5 MW machines the minimum cost criterion, C, is 2.99×10^5, 4.67×10^5, and 8.48×10^5 € respectively and can be found when $K_{rad} = 0.12 - 0.13$.

6.3.2 Axial-flux machines

6.3.2.1 Mass comparison

Inactive mass

The airgap deflection, u, is greatly influenced by the airgap radius. In the case of the single stage machine (Fig. 6.21 shows the breakdown of mass for the 2 MW design) the inactive mass increases greatly as the permanent magnet radii ratio, k_r, increases from 0.5 to 0.95. Although at larger aspect ratios the area subjected to Maxwell stress is smaller, the mean radius is greater and consequently according to eqn. (6.6), the plate constant, D, must be greater. The rotor disc mass is greater than that of the stator disc and so the former dominates the total inactive mass.

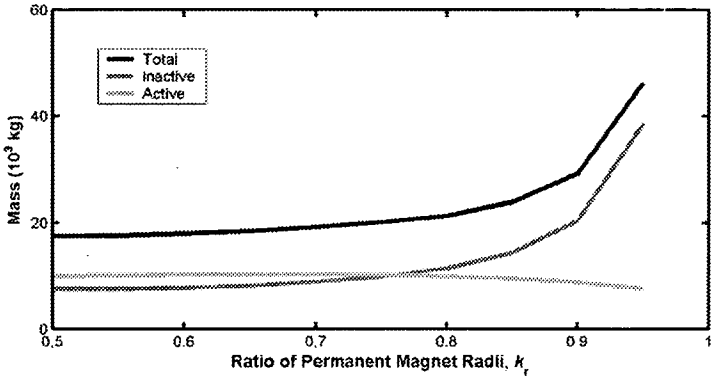

Figure 6.21. Active, inactive and total mass for a 2 MW axial-flux machine against aspect ratio, k_r.

Active mass

In general terms the active mass falls slightly as the permanent magnet radii ratio changes from 0.5 to 0.95, as illustrated in Fig. 6.21. At higher values of k_r the outer radius a_r is larger and so the same torque can be generated with less force (and hence a smaller surface area of active material).

Total mass

In the case of the 2 MW machine the active mass is greater than the inactive mass when $k_r < 0.76$. When $k_r > 0.76$ the inactive mass is greater than the active mass; at $k_r = 0.95$ the inactive mass is about 5 times the active mass.

The total mass for all three ratings is shown in Fig. 6.22. At $k_r = 0.5$, the 5 MW machine is 8 times the mass of the 2 MW machine; when $k_r = 0.95$ the 5 MW machine is 13 times heavier. The peak torque of the 5 MW machine is 4 times that of the 2 MW machine so as the torque increases the torque density falls because of the increasing inactive mass.

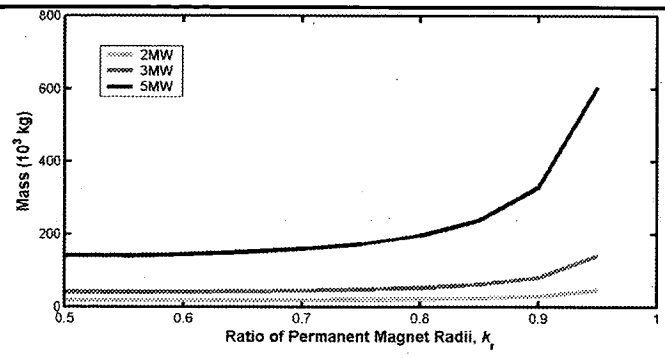

Figure 6.22. Total mass for 2, 3, and 5 MW axial-flux machines against aspect ratio, k_r.

6.3.2.2 Cost criterion

Fig. 6.23 shows the cost criterion, *C*, calculated for the 2, 3, and 5 MW machines with only the cost of the active material. The cost of the active material peaks at $k_r = 0.75$. Losses are maximum when $k_r < 0.5$, they decrease rapidly up to $k_r = 0.7$ and then more slowly up to $k_r = 0.95$. The result is that for each rating there is a maximum when $k_r < 0.5$ and then a minimum when $k_r = 0.95$. The minimum cost criterion for the 2 MW machine is 2.32×10^5 €.

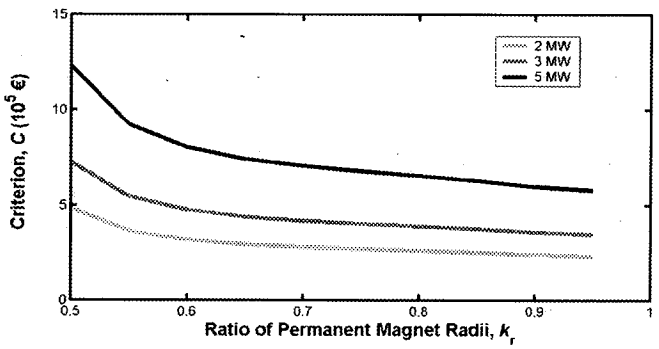

Figure 6.23. Cost criterion, *C*, for 2, 3, and 5 MW axial-flux machines against aspect ratio, k_r, calculated with the active mass only.

When the inactive mass is included in the cost criterion calculation in Fig. 6.24, the curves are all shifted up (the minimum cost criterion for the 2 MW machine is now 2.97×10^5 €). The minimum *C* is found when $k_r = 0.8$, 0.75 and 0.7 for the 2, 3, and 5 MW machines respectively. The main difference between Fig. 6.23 and Fig. 6.24 is that the cost criterion curves turn up as $k_r \rightarrow$

1 in Fig. 6.24. This is because the cost of the inactive material increases dramatically.

Double-sided machines

When $k_r = 0.7$ the 5 MW cost criterion increases from 7.05×10^5 € in Fig. 6.23 to 11.4×10^5 € when the inactive mass is included in Fig. 6.24. This shows that the inactive mass is dominant. One way that the machine designer can try to reduce the negative impact of this inactive mass is to use double-sided rather than single-sided machines.

For example in a double-sided machine the rotor disc can carry permanent magnets on both sides and two stators can be used (one either side of the rotor disc) as shown in Fig. 6.25. In this way, twice the torque can be produced with only slightly more inactive mass (although we assume here that the active mass doubles). If the aim is to reduce the inactive mass then the ratio of rotor discs to stator discs should be minimised. Every double-sided design will have a smaller outer radius than the equivalent single-sided machine and so generally there will be savings in inactive mass. The 5 MW single-sided machine (with $k_r = 0.7$) has an outer radius of 3.99 m; in comparison the double-sided machine has an outer radius of 3.17 m. Figure 6.26 shows the reduction in cost criterion brought about when this double-sided design is employed. The minimum cost criterion improves from 11.4×10^5 € (at $k_r = 0.7$) for the single-sided machine to 7.17×10^5 € (at $k_r = 0.85$) with a double-sided machine.

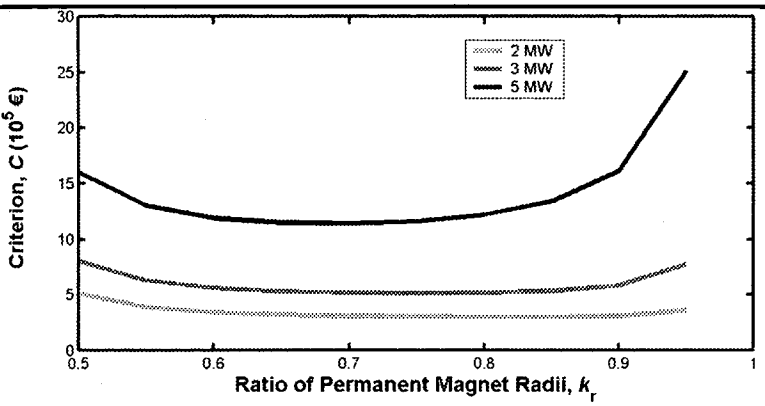

Figure 6.24. Cost criterion, C, for 2, 3, and 5 MW axial-flux machines as a function of the aspect ratio, k_r, calculated with the total mass.

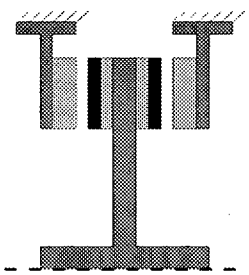

Figure 6.25. Double-sided axial-flux machine. Light grey = laminations and windings; black = permanent magnets; dark grey = structures.

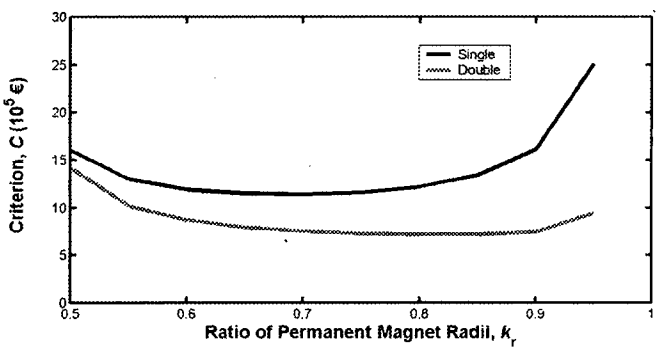

Figure 6.26. Cost criterion, C, for single- and double-sided 5 MW axial-flux machines against aspect ratio, k_r, calculated with the total mass.

6.4 Conclusions

A procedure for outlining a permanent magnet synchronous generator design for a direct drive wind turbine has been presented. The importance of

modelling both the active and inactive material has been demonstrated in both radial-flux and axial-flux cases. The generator cost and loss cost criterion is minimised based on K_{rad} and k_r. The inclusion of the structural mass leads to significantly different design decisions. The minimum mass for the radial-flux machine can generally be found when K_{rad} = 0.1-0.3; the minimum cost criterion when K_{rad} = 0.12-0.13. For the single-sided 5MW axial-flux machine the minimum cost criterion was found when k_r = 0.7; this changes to k_r = 0.85 for the double-sided machine.

Although it has been possible to find the lightest machines of a particular design, all of the machines that have been analysed in this chapter are large and heavy. Inactive mass is dominant and normal stress is the major factor influencing this inactive mass. In the next chapter, a new topology is introduced which copes with normal stress in a different manner, with a view to reducing the overall mass further.

Chapter 7

Development of an air-cored generator

In Chapter 6, conventional permanent magnet generators and their structures were optimised. Although some mass savings can be made by considering both the active and inactive material of 2, 3 and 5 MW rated machines, the generators are still heavy. An alternative approach, which is used in this chapter, is to use air-cored machines.

7.1 Introduction

In [73], iron-cored axial-flux permanent magnet machines are compared with air-cored machines. Air-cored machines have no iron in the stator. Although they have a poorer magnetic circuit (as the effective airgap is increased) the normal component of Maxwell stress is much reduced and so the stator structure can be much lighter because it no longer has to be as stiff. For a double rotor axial-flux machine the mechanical loading on the rotor discs is smaller too. Due to the reduced shear stress (which is proportional to airgap flux density) the air-cored machine must be larger than an iron-cored machine which is rated for the same torque. The simple study in [73] shows that air-cored machines are lighter for a range of power ratings (Fig. 7.1).

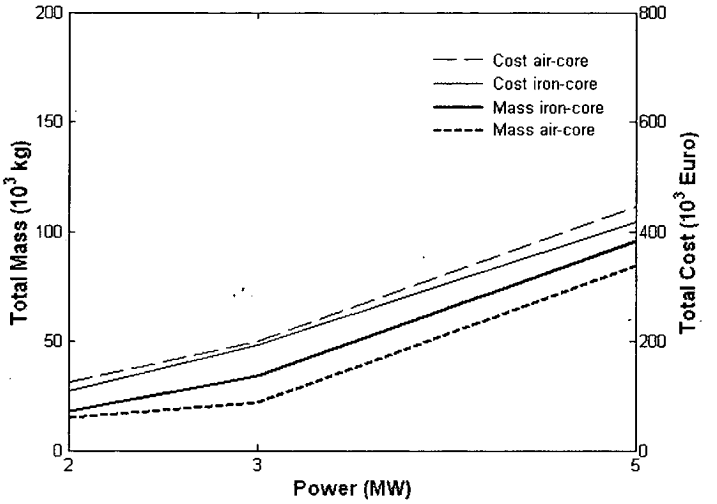

Figure 7.1. Material mass and cost of double sided axial-flux machines [73]

A logical development of such axial-flux disc machines in Fig. 7.2(a) is to increase the rotor shaft radius, thus leading to a reduced circumferential moment and enabling lighter discs to be used (see eqns. (3.2) to (3.6) and Appendix A). This is illustrated in Fig. 7.2(b). Taking this further leaves a 'C' cross section, where the limbs carry the magnets and the stator winding is held independently between them (Fig. 7.2(c)). A further step is to allow flux to cross the web of the 'C', and to make the rotor out of modules (Fig. 7.3) each carrying a pair of magnets. These can be handled easily and safely. If the winding is air-cored then there is no Maxwell force on the stator or on the rotor structure (there is a force on the facing rotor limbs of the 'C' core but outside these modules there is no net force transmitted to the rotor structure). By rotating the 'C' core modules by 90° a radial-flux machine can be produced.

This new topology is introduced in [82] and in the patent [81].

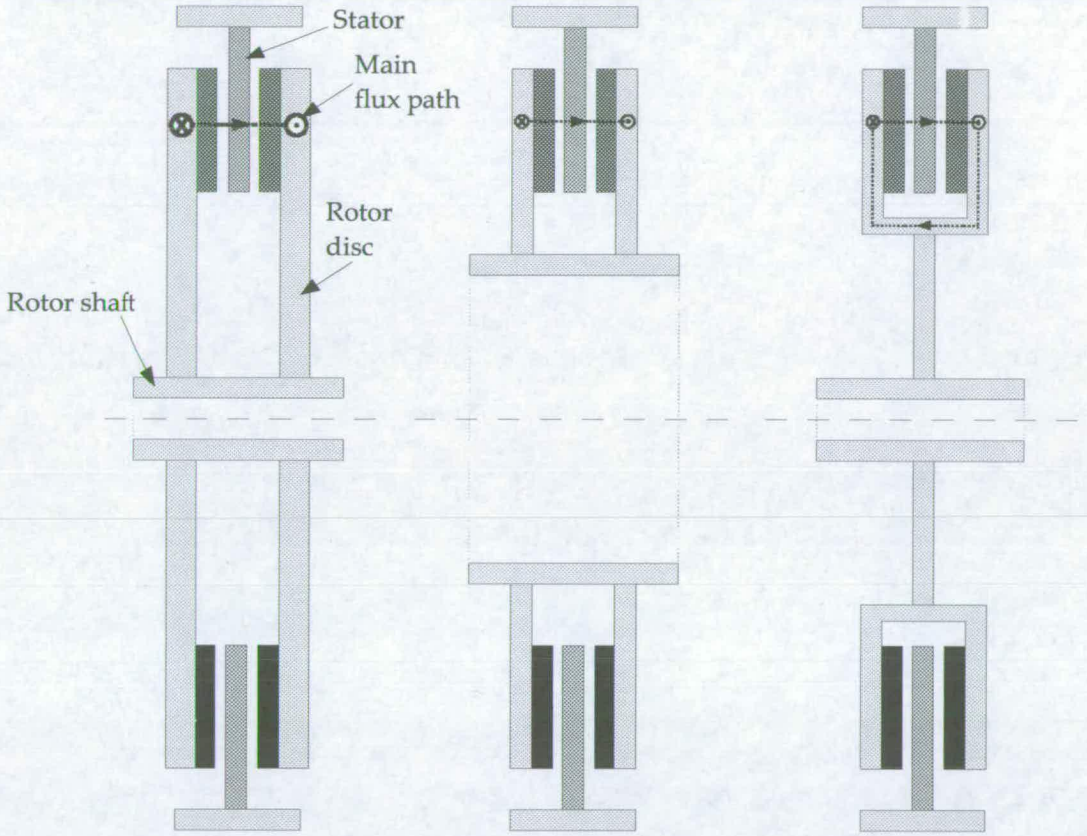

Figure 7.2. Cross section of double sided axial-flux machine: Baseline design (*left*); Increasing rotor shaft means that the thickness of the rotor discs can be reduced (*middle*); 'C' core machine with extra flux path (*right*)

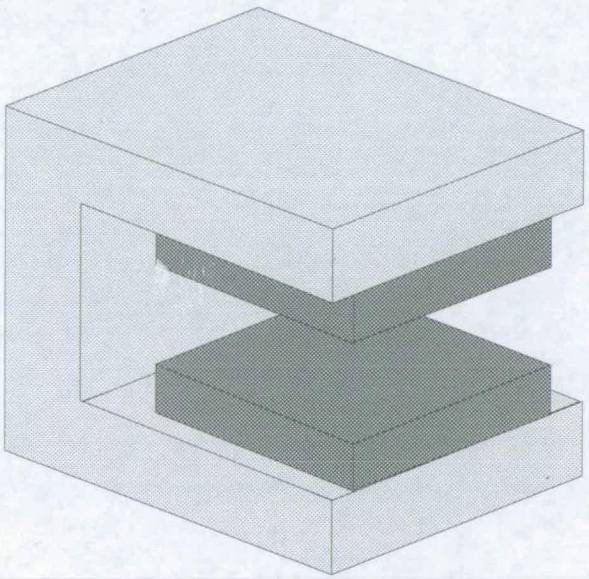

Figure 7.3. Steel 'C' core module with magnets.

This chapter explains the development of this concept. The first section concentrates on the structural modeling of the 'C' core modules, so that the 'C' core modules can successfully maintain the correct airgap clearance. The second section models the magnetic circuit of a radial-flux 'C' core machine, using a lumped parameter reluctance network. This is verified using a 3D magnetic finite element software package. Finally, large scale designs are introduced and the scaling laws of this topology are investigated.

7.2 Calculating the structural mass of a rotary 'C' core machine

7.2.1 Analytical models

Part of the rotating machine embodiment of the 'C' cored design is shown in Fig. 7.4. This is a 'radial-flux' version of the C-core machine. Each C-core is made up of three steel pieces, the top and bottom pieces either side of the airgap.

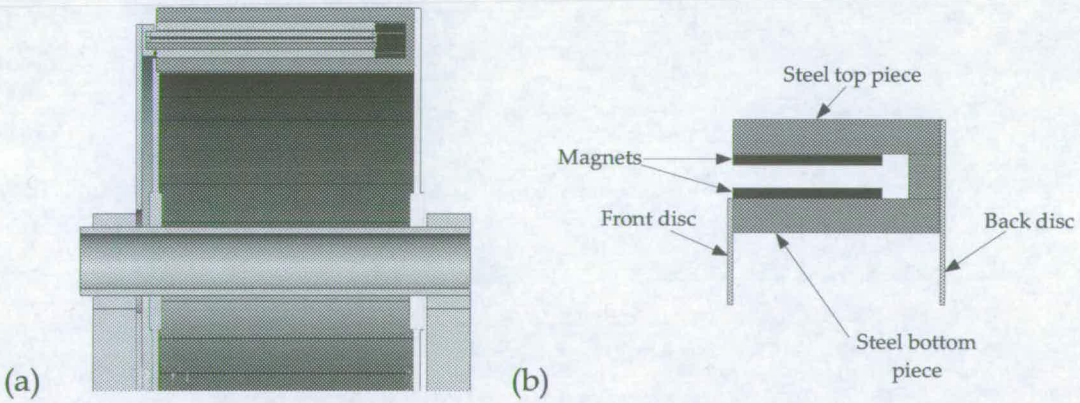

Figure 7.4. Part cross section of rotary C-core machine (a); (b) Rotor module.

The bottom steel piece is screwed to the front and back disc. It is assumed that the loading w is along the beam in the same area as the magnet, directed upwards. The connection to the back disc is assumed to be clamped (the middle and top steel pieces are screwed to the bottom piece) whereas the connection to front disc is assumed to be a simple support (providing no

moment reaction, as the deflection of the piece is likely to deflect the front disc). The deflection model is shown in Fig. 7.5.

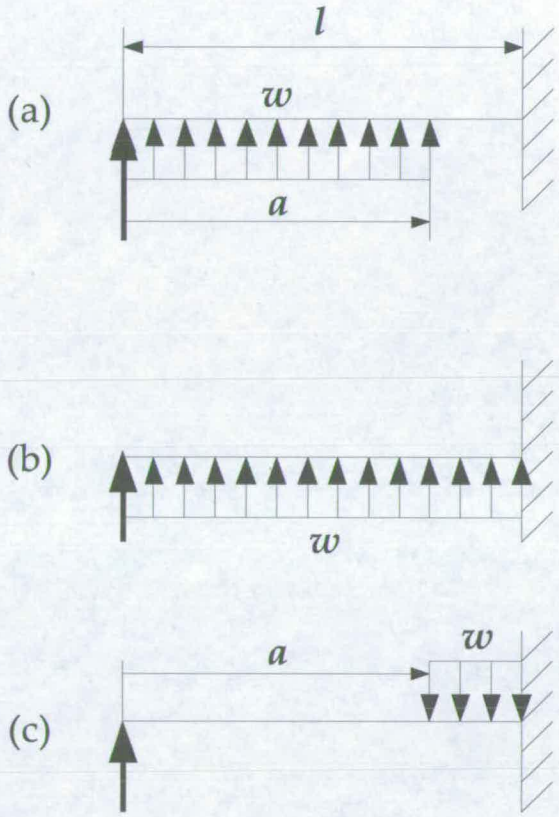

Figure 7.5. (a) Beam model of bottom steel piece. (b) and (c) show the submodels used to give the deflection when the udl is limited to *a* units along the beam.

According to Roark [99], the deflection of a beam simply supported at one end and clamped at the other, with a uniformly distributed load, udl covering a units of the beam (as shown in Fig. 7.5(c)) is

$$y = \theta_A x + \frac{R_A x^3}{6EI} - \frac{w}{24EI}\langle x-a\rangle^4 \tag{7.1}$$

where

$$\theta_A = \frac{-w}{48EIl}(l-a)^3(l+3a) \tag{7.2}$$

and

$$R_A = \frac{w}{8l^3}(l-a)^3(3l+a)\,. \tag{7.3}$$

In this case, eqns. (7.1) to (7.3) are applied twice, once with a=0 and w=qb and then with a=l_m and with w=-qb. The two resulting values of y are then added together to give the deflection at any point x along the beam.

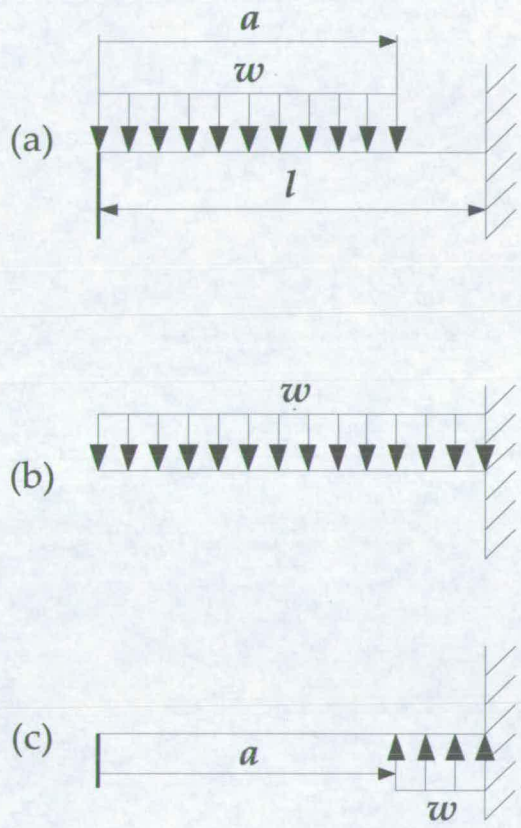

Figure 7.6. (a) Beam model of top steel piece. (b) and (c) show the submodels used to give the deflection when the udl is limited to *a* units along the beam.

The top steel piece is assumed to be cantilevered from the back disc, with the loading directed down (Fig. 7.6(a)). To begin with, the arch effect is neglected. (This is where each steel piece supports and is supported by its adjacent neighbours, as shown in Fig. 7.7). According to Roark, the deflection of a cantilevered beam due to a udl starting from a units from the free end is

$$y = y_A + \theta_A x - \frac{w}{24EI}\langle x-a\rangle^4 \qquad (7.4)$$

where

$$y_A = \frac{-w}{24EI}(l-a)^3(3l+a) \tag{7.5}$$

and

$$\theta_A = \frac{w}{6EI}(l-a)^3. \tag{7.6}$$

Figure 7.6. (b) and (c) show the submodels which are used to find the deflection.

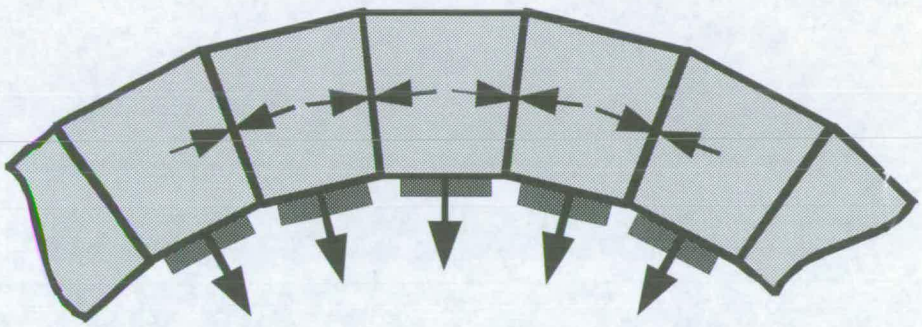

Figure 7.7. Arch effect on portion of rotor top steel pieces

Each steel piece has a trapezoidal cross section as shown in Fig. 7.8. The second moment of area about the neutral axis is

$$I_i = \frac{d^3}{36}\frac{b^2+4bc+c^2}{b+c}. \tag{7.7}$$

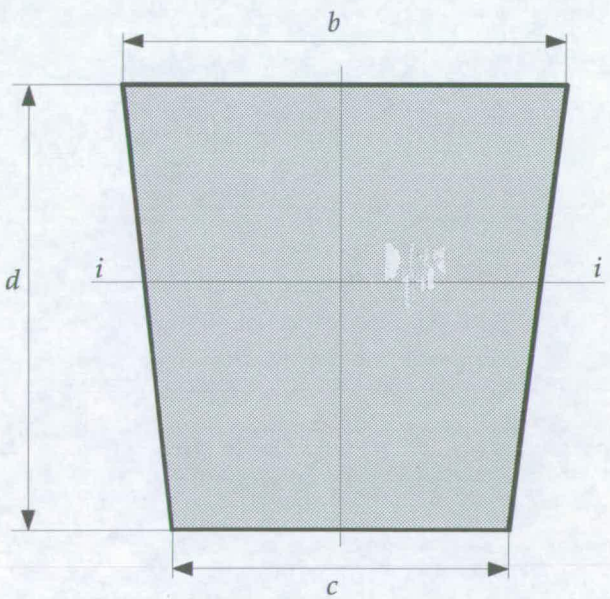

Figure 7.8. Cross section of steel piece for calculating second moment of area

7.2.2 Verification with finite element modelling

Figure 7.9 shows the top and bottom steel pieces for a 32 pole machine with a mean airgap radius of 0.5 m, h_m = 15 mm, l_m = 200 mm, l_{st} = 100 mm, c = 2mm, t_w = 26 mm, b_i = 110 mm, c_i = 104 mm, d_i = 30 mm, b_{ii} = 93 mm, c_{ii} = 87 mm, d_{ii} = 30 mm. By calculation, $I_i = 2.41\times10^{-7}$ m^4 and $I_{ii} = 2.02\times10^{-7}$ m^4. The normal stress is calculated using eqn. (3.1), with the assumption that the airgap flux density is 0.6 T (e.g. q = 143.2 kPa). Figure 7.10 shows the Ansys finite element analysis models for the steel pieces [2]. The maximum deflection into the airgap is given in Table 7.1.

	Analytical deflection	**FE deflection**
Bottom piece	1.646×10^{-5} m	1.069×10^{-5} m
Top piece	2.787×10^{-4} m	2.919×10^{-4} m

Table 7.1. Maximum deflection found analytically and with a finite element solver.

7.2.3 Discussion

Table 7.1 gives good agreement for the deflection. Both the analytical and finite element models assume that each rotor module exists on its own. However, in the case of the top piece, there is considerable interaction between it and its two neighbours – this is ignored by the cantilever beam analysis. This interaction is easily modelled in the finite element solver by adding two symmetry conditions on the long sides of the steel pieces (Fig. 7.11). A simplified approach to modelling this deflection is to assume that the steel pieces are merged together into a hollow cylinder, so that eqn. (4.1) can be used. The thickness of this cylinder is assumed to be that of the top steel piece. This predicts a deflection of 6.71×10^{-6} m, whereas the finite element model with symmetry constraints gives a deflection of 8.78×10^{-6} m. These are two orders of magnitude less than the deflection when the module is treated in isolation. This method will be used henceforth to model the deflection of the upper steel pieces.

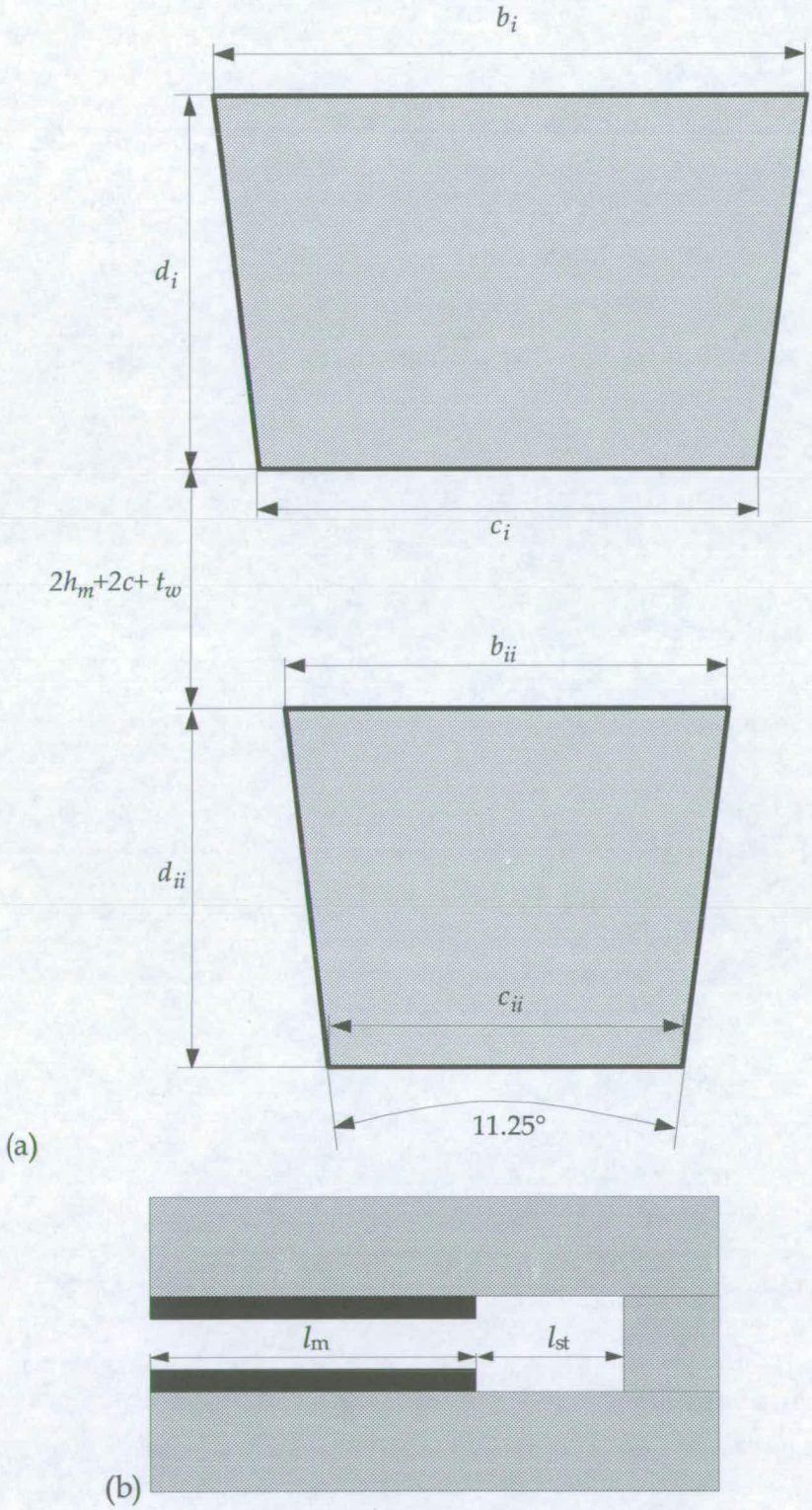

Figure 7.9 Steel rotor module dimensions: (a) Front view and (b) Side view

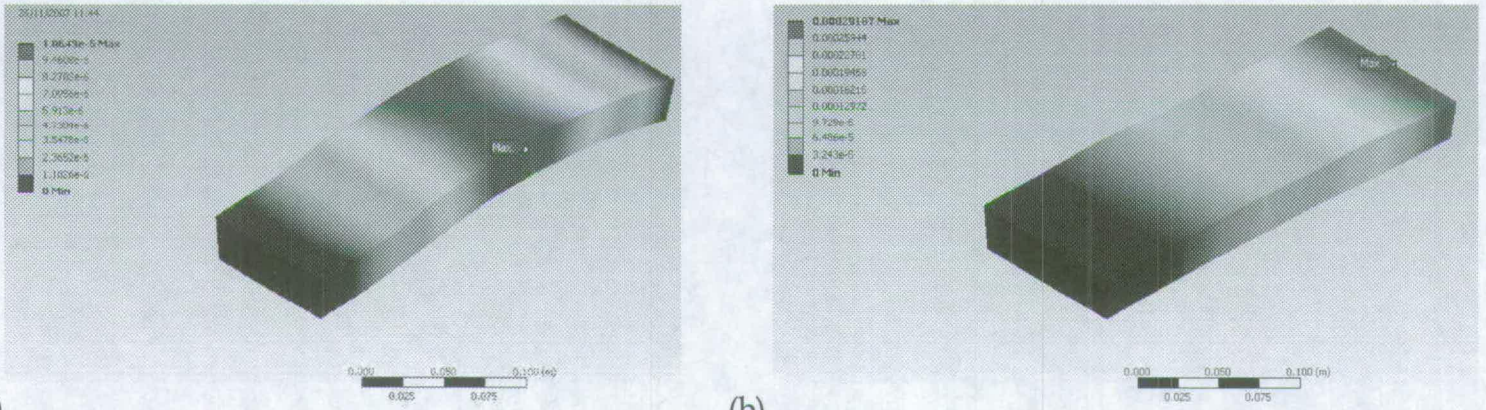

(a) (b)

Figure 7.10 Deflection of steel rotor module parts (a) Bottom piece (b) Top piece

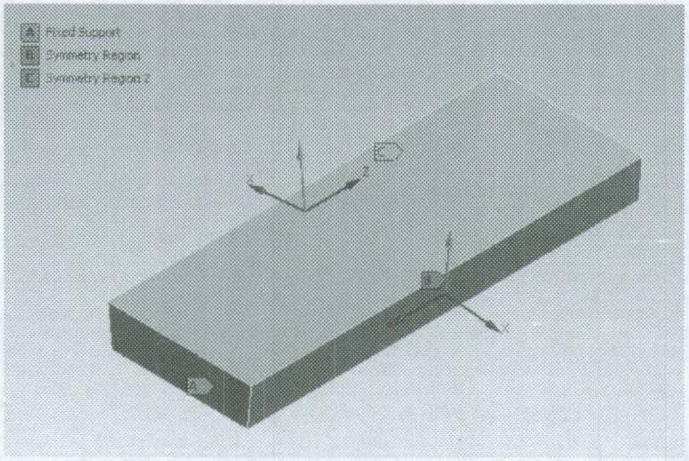

Figure 7.11 Symmetry conditions ('B' and 'C') on side of top steel part.

7.3 Flux modeling in 3D using a lumped parameter reluctance network

In this section a lumped parameter reluctance network is used to calculate the no load flux density in the airgap. The 3D flux in the C-core module can be visualised as two distinct flux paths (shown in Figure 7.12). The intermodule flux path can be considered as a longitudinal radial-flux path; the intramodule flux path can be considered as a transverse radial-flux path. If a C-core module were to be held in isolation, then this latter path would be the main path. When the modules are brought together into contact, the longitudinal flux comes into play. In reality, the flux paths are not distinct, and the flux is free to go where it pleases. The lumped parameter network (as outlined below) allows the quick calculation of the no load airgap flux density and a conservative prediction of saturation in the steel pieces.

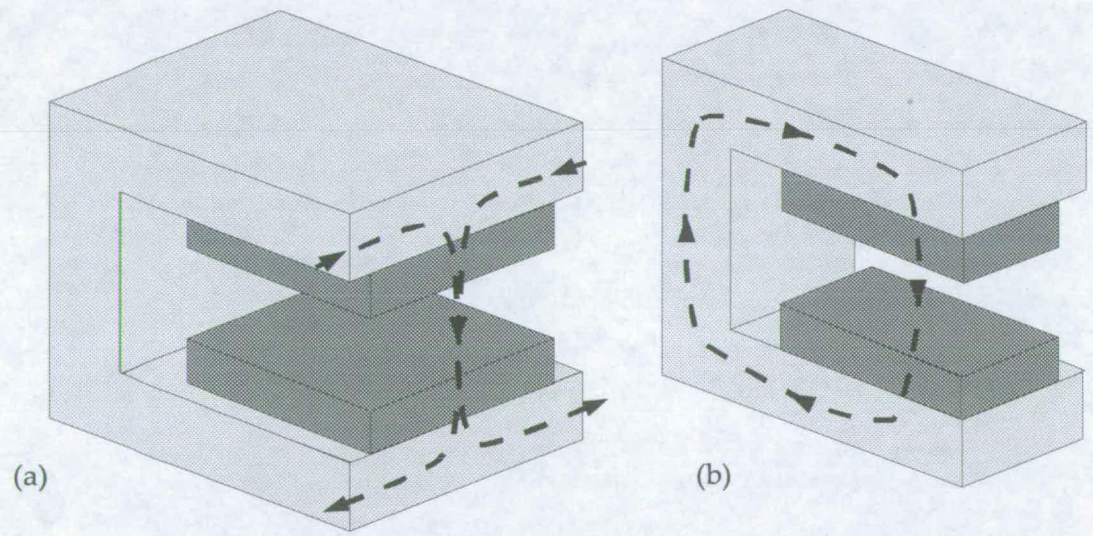

Figure 7.12. C-core flux paths (a) Intermodule (longitudinal) (b) Intramodule (transverse)

7.3.1 Analytical modelling

Figure 7.13 shows the magnetic circuit of 3 C-core modules from the front (the curvature of the modules has been removed for simplicity) and Fig. 7.14

shows the side view. The magnetic circuit model is made up of the following sources, reluctances and fluxes:

Sources

The mmf of the magnets is modelled as

$$NI = \frac{B_r h_m}{\mu_0 \mu_r}. \tag{7.8}$$

Reluctances

- Airgap reluctance, S_{ag}

$$S_{ag} = \frac{t_w + 2c}{l_m w_m \mu_0}, \tag{7.9}$$

where t_w is the winding height, c is the clearance between the winding and the magnets l_m is the axial length of the magnets and w_m is the average pitch of the magnets.

- PM reluctance, S_{PM}

$$S_{PM,T} = \frac{h_m}{l_m w_{m,T} \mu_r \mu_0} + \frac{\frac{1}{2} d_i}{l_m w_{m,T} \mu_{st} \mu_0}, \tag{7.10}$$

$$S_{PM,B} = \frac{h_m}{l_m w_{m,B} \mu_r \mu_0} + \frac{\frac{1}{2} d_{ii}}{l_m w_{m,B} \mu_{st} \mu_0}. \tag{7.10a}$$

where μ_r is the relative permeability of the PM material and μ_{st} is the relative permeability of the steel. The subscripts refer to the top (T) and bottom (B) magnets. The second fractions in (7.10) and (7.10a) refer to the reluctance between the steel edge and node **A**.

- Steel reluctance, S_{st}, is the reluctance of the intramodule steel,

$$S_{st} = \frac{\frac{1}{2} l_m + l_{st} + l_c}{\frac{1}{2} d_i (b_i + c_i) \mu_{st} \mu_0} + \frac{2h_m + t_w + 2c}{\frac{1}{2} (b_{ii} + c_i) l_c \mu_{st} \mu_o} + \frac{\frac{1}{2} l_m + l_{st} + l_c}{\frac{1}{2} d_{ii} (b_{ii} + c_{ii}) \mu_{st} \mu_o}. \tag{7.11}$$

- Spacer reluctance, S_{sp}, is the reluctance of the intermodule steel and any airgap between modules (distance c_{sp}),

$$S_{sp,T} = \frac{\frac{1}{2}(b_i + c_i)}{d_i l_m \mu_{st} \mu_0} + \frac{c_{sp}}{d_i l_m \mu_0}, \tag{7.12}$$

$$S_{sp,B} = \frac{\frac{1}{2}(b_{ii} + c_{ii})}{d_{ii} l_m \mu_{st} \mu_0} + \frac{c_{sp}}{d_{ii} l_m \mu_0}. \tag{7.12a}$$

Fluxes

- It is assumed that the PM flux, Φ_{PM}, is the same as the flux that crosses the airgap, Φ_{ag}.
- Steel flux, Φ_{st}, is the intramodule flux.
- Spacer flux, Φ_{sp}, is the intermodule flux.

Node **A** is where Kirchoff's Current (or the magnetic flux equivalent) Law can be applied:

$$\begin{aligned} 2\Phi_{sp} + \Phi_{st} &= \Phi_{PM} \\ \Phi_{sp} &= \tfrac{1}{2}\Phi_{PM} - \tfrac{1}{2}\Phi_{st} \end{aligned} \tag{7.13}$$

Kirchoff's Voltage (or mmf equivalent) Law can be applied first for loop **B**:

$$\begin{aligned} 4\frac{B_r h_m}{\mu_0 \mu_r} &= \Phi_{sp}(S_{sp,T} + S_{sp,B}) + 2\Phi_{PM}(S_{PM,T} + S_{PM,B}) + 2\Phi_{ag} S_{ag} \\ \frac{B_r h_m}{\mu_0 \mu_r} &= \tfrac{1}{4}\Phi_{sp}(S_{sp,T} + S_{sp,B}) + \tfrac{1}{2}\Phi_{ag}(S_{PM,T} + S_{PM,B} + S_{ag}) \\ &= -\tfrac{1}{8}\Phi_{st}(S_{sp,T} + S_{sp,B}) + \tfrac{1}{2}\Phi_{ag}(S_{PM,T} + S_{PM,B} + S_{ag} + \tfrac{1}{4}S_{sp,T} + \tfrac{1}{4}S_{sp,B}) \end{aligned} \tag{7.14}$$

and then for loop **C**:

$$\begin{aligned} 2\frac{B_r h_m}{\mu_0 \mu_r} &= \Phi_{st} S_{st} + \Phi_{PM}(S_{PM,T} + S_{PM,B}) + \Phi_{ag} S_{ag} \\ \frac{B_r h_m}{\mu_0 \mu_r} &= \tfrac{1}{2}\Phi_{st} S_{st} + \tfrac{1}{2}\Phi_{ag}(S_{PM,T} + S_{PM,B} + S_{ag}) \end{aligned} \tag{7.15}$$

Combining eqns. (7.13), (7.14) and (7.15) leads to the following results:

$$\frac{B_r h_m}{\mu_0 \mu_r}\begin{bmatrix} 1 \\ 1 \end{bmatrix} = \begin{bmatrix} \frac{1}{2}S_{st} & \frac{1}{2}(S_{PM,T} + S_{PM,B} + S_{ag}) \\ -\frac{1}{8}(S_{sp,T} + S_{sp,B}) & \frac{1}{2}(S_{PM,T} + S_{PM,B} + S_{ag} + \frac{1}{4}S_{sp,T} + \frac{1}{4}S_{sp,B}) \end{bmatrix}\begin{bmatrix} \Phi_{st} \\ \Phi_{ag} \end{bmatrix} \tag{7.16}$$

$$\Phi_{st} = \frac{\frac{1}{8}(S_{sp,T} + S_{sp,B})}{\frac{1}{4}S_{st}(S_{PM,T} + S_{PM,B} + S_{ag} + \frac{1}{4}S_{sp,T} + \frac{1}{4}S_{sp,B}) + \frac{1}{16}(S_{sp,T} + S_{sp,B})(S_{PM,T} + S_{PM,B} + S_{ag})} \frac{B_r h_m}{\mu_0 \mu_r} \tag{7.17}$$

$$\Phi_{ag} = \frac{\frac{1}{8}(S_{sp,T} + S_{sp,B}) + \frac{1}{2}S_{st}}{\frac{1}{4}S_{st}(S_{PM,T} + S_{PM,B} + S_{ag} + \frac{1}{4}S_{sp,T} + \frac{1}{4}S_{sp,B}) + \frac{1}{16}(S_{sp,T} + S_{sp,B})(S_{PM,T} + S_{PM,B} + S_{ag})} \frac{B_r h_m}{\mu_0 \mu_r} \tag{7.18}$$

$$\Phi_{sp} = \frac{\frac{1}{4}S_{st}}{\frac{1}{4}S_{st}(S_{PM,T} + S_{PM,B} + S_{ag} + \frac{1}{4}S_{sp,T} + \frac{1}{4}S_{sp,B}) + \frac{1}{16}(S_{sp,T} + S_{sp,B})(S_{PM,T} + S_{PM,B} + S_{ag})} \frac{B_r h_m}{\mu_0 \mu_r} \tag{7.19}$$

The flux densities at no load are then found by dividing these flux values by the minimum cross sections:

$$B_g = \frac{\Phi_{ag}}{l_m w_m}, \tag{7.20}$$

$$B_{st} = \frac{\Phi_{st}}{\frac{1}{2}d_i(b_i + c_i)}, \tag{7.21}$$

$$B_{sp} = \frac{\Phi_{sp}}{l_m d_i}. \tag{7.22}$$

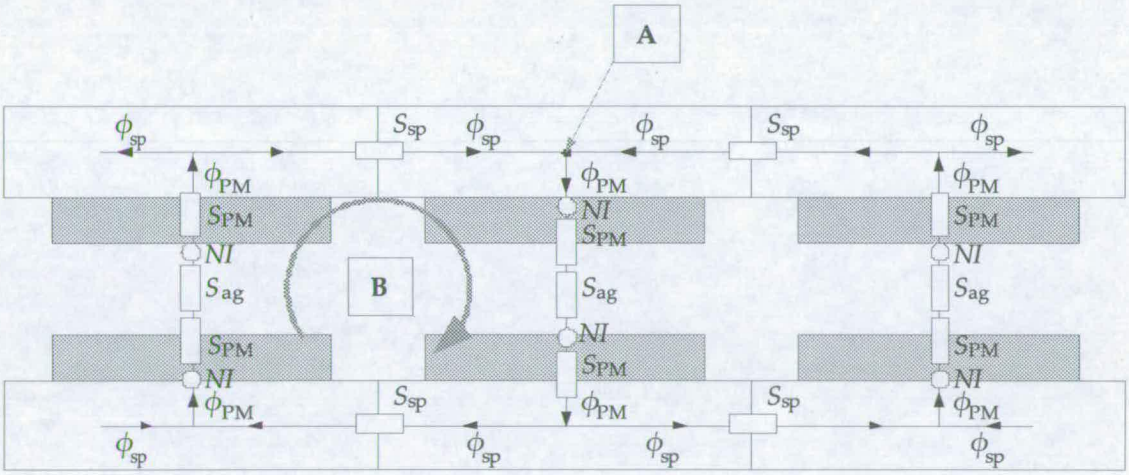

Figure 7.13. C-core (front) reluctance network

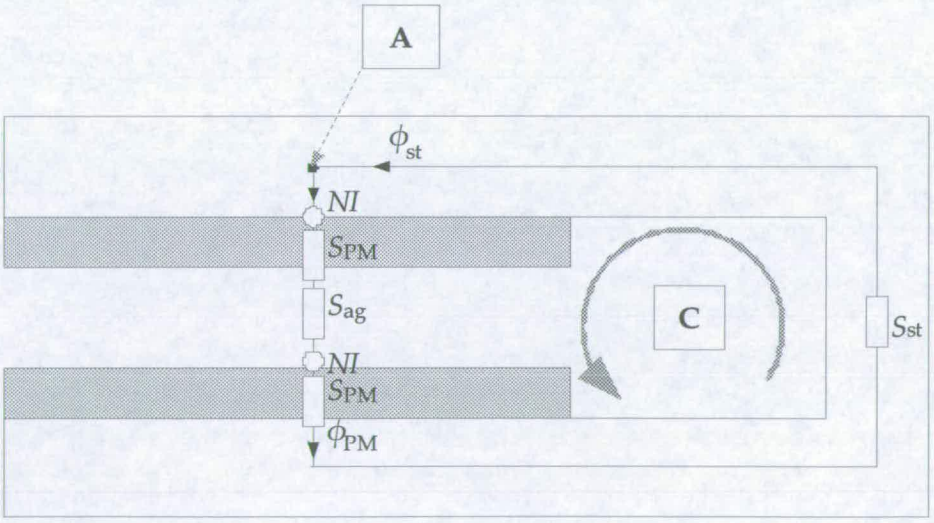

Figure 7.14. C-core (side) reluctance network

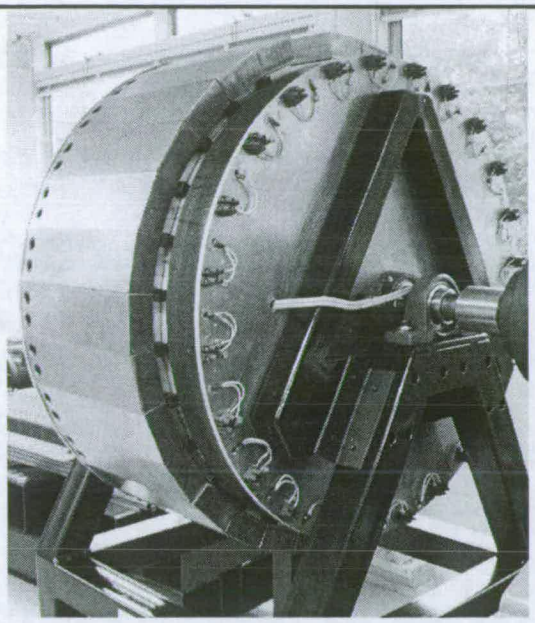

Figure 7.15. C-core generator prototype

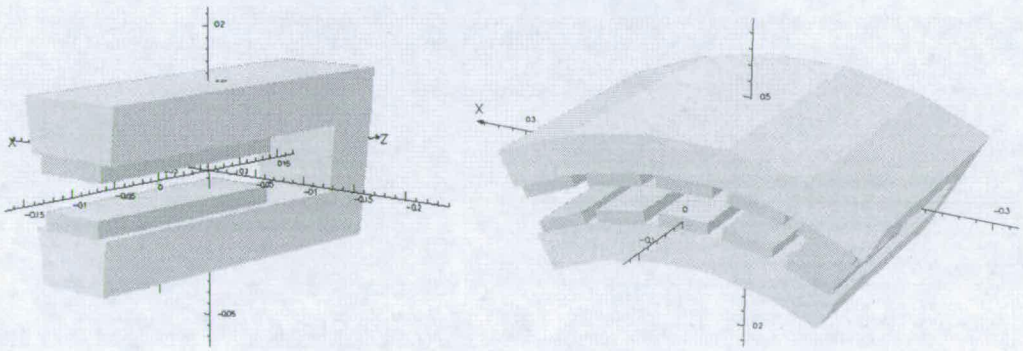

Figure 7.16. Finite element model (Opera TOSCA) of C-core modules

	Analytical method	Finite element method
Peak airgap flux density, isolated module	0.52 T	0.48 T
Peak airgap flux density, multiple modules	0.58 T	0.56 T

Table 7.2. Comparison of analytical and finite element method

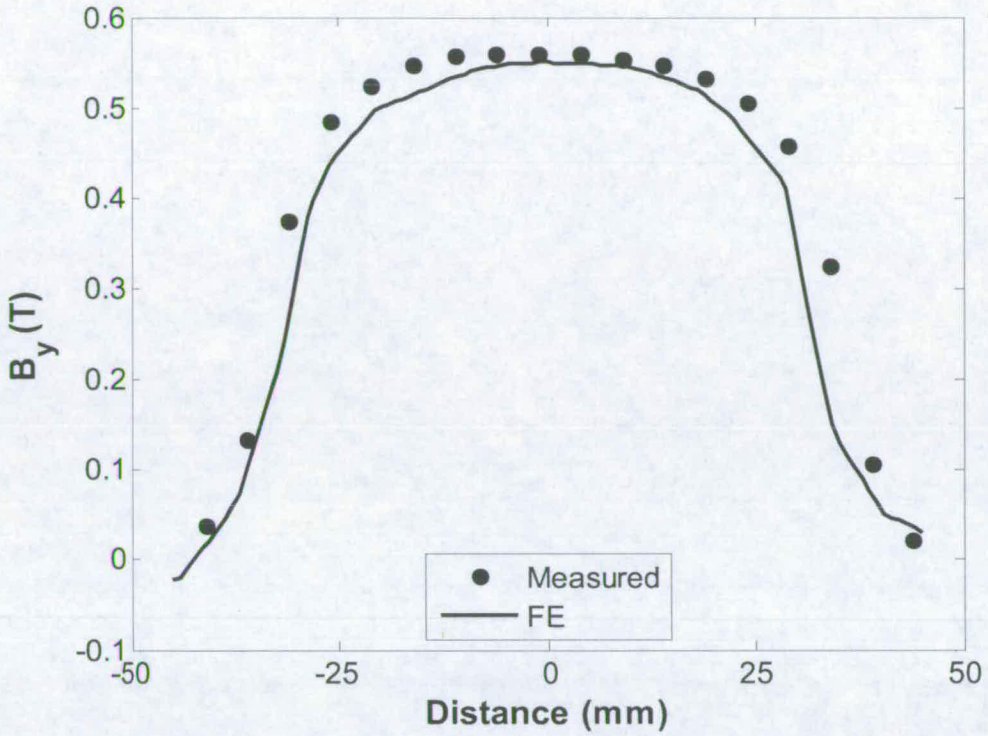

Figure 7.17. Radial no load airgap flux density distribution across a pole pitch (Z = 20mm)

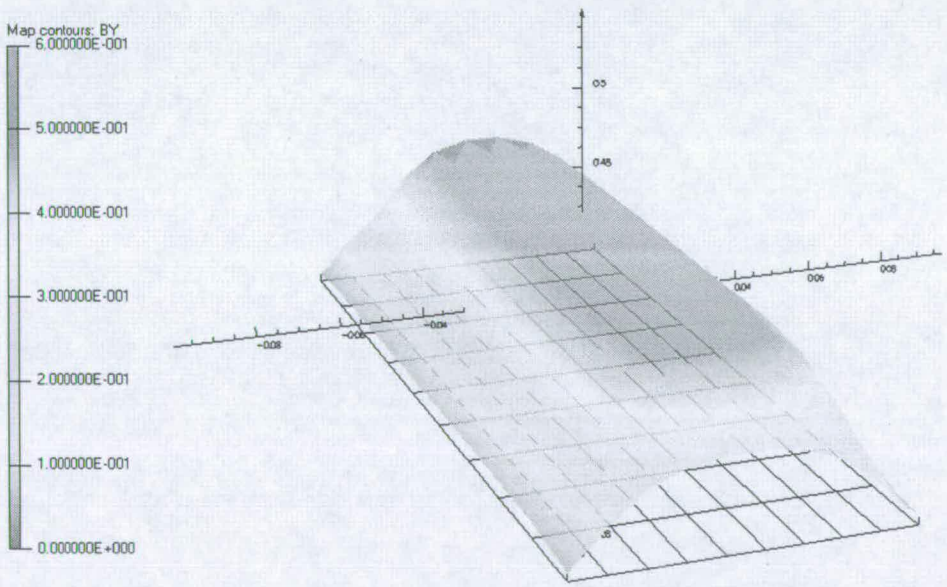

Figure 7.18. Radial flux density distribution mid way between two facing magnets

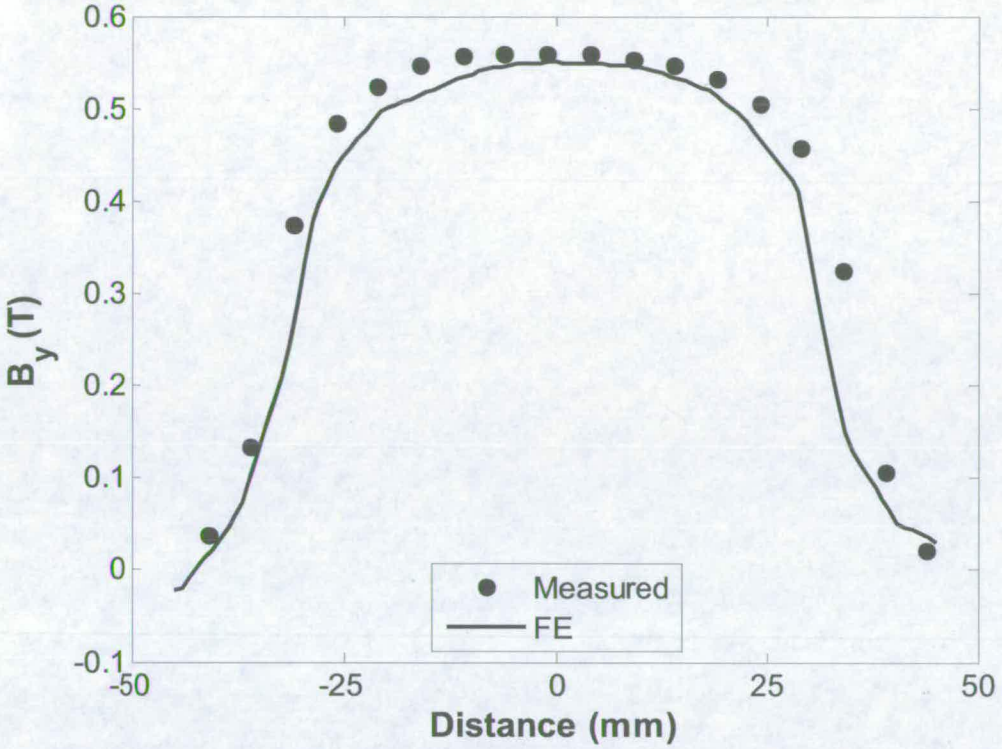

Figure 7.17. Radial no load airgap flux density distribution across a pole pitch (Z = 20mm)

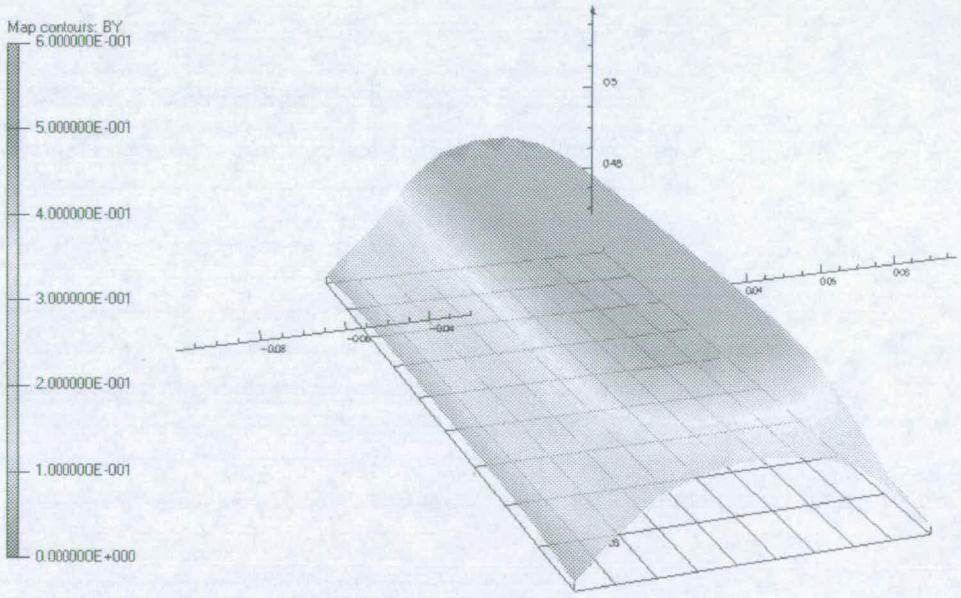

Figure 7.18. Radial flux density distribution mid way between two facing magnets

7.4 Large scale design and scaling laws

In this context, scaling laws can show how – with some assumptions and constraints – current technology will look when the power rating increases. First the scaling laws of radial-flux permanent magnet generators are set out and then the same is carried out for the C-core machine. Some C-core generator designs are set out for 100 kW up to 2 MW machines to illustrate these scaling laws, using the work in sections 7.2 and 7.3.

7.4.1 Conventional PM machine

Equation (4.7) gives the torque which is developed by a cylindrical radial-flux type electrical generator with a radius, R, axial length, l, and shear stress, σ,

$$T = 2\pi R^2 l\sigma . \tag{4.7}$$

Assuming that there is an optimum aspect ratio, K_{rad}, then l/R = constant. It follows then that

$$T \propto R^3\sigma . \tag{7.23}$$

Every electrical machine has a limited shear stress (decided by electrical loading, magnetic loading, pole layout, cooling opportunity, etc.). Assuming that the same value of shear stress is always chosen, then eqn. (7.23) can be restated more simply as

$$T \propto R^3 . \tag{7.24}$$

Equation (7.25) gives the mechanical power input to the generator, P, in terms of the machine torque, T, and rotational speed, ω,

$$P = T\omega . \tag{7.25}$$

In a wind turbine, this is subject to a maximum rotor blade tip speed, such that

$$r\omega = \text{constant}, \tag{7.26}$$

where r is the radius of the turbine rotor blades.

The mechanical power from the rotor blades is proportional to the area swept by the rotor blades so that,

$$P \propto r^2 . \tag{7.27}$$

Combining (7.26) and (7.27) and rearranging leads to the following result,

$$\omega \propto 1/\sqrt{P} . \tag{7.28}$$

Rearranging (7.25) and substituting eqn. (7.28) for ω gives the torque, T, in terms of power, P,

$$T \propto \frac{P}{1/\sqrt{P}} . \tag{7.29}$$
$$T \propto P^{3/2}$$

Alternatively, the torque, T, can be expressed in terms of rotor blade radius, r:

$$T \propto \frac{r^2}{1/r} . \tag{7.30}$$
$$T \propto r^3$$

Letting the right hand sides of eqns. (7.29) and (7.24) be equal then,

$$P^{3/2} \propto R^3 \tag{7.31}$$
$$P \propto R^2$$

This means that for a generator in a wind turbine, constrained by a maximum tip speed and a maximum shear stress, the power converted is proportional to the square of the generator airgap radius.

It can be assumed that there is an optimum pole layout which is relatively independent of the generator radius. If this is the case, then the active mass is proportional to the airgap surface area. With a constant aspect ratio, K_{rad}, then,

$$m_{act} \propto R^2 . \tag{7.32}$$

Combining eqns. (7.31) and (7.32) gives a constant P/m_{act} ratio†. As the power rating of the design increases then the active mass will increase accordingly.

For the inactive mass of a radial-flux machine, it can be assumed that the inactive mass has two components, the mass of a hollow cylinder, m_{cyl}, (which represents the rotor and stator back iron) and the mass of spokes, m_{sp} (for both the rotor and the stator).

Assuming that the airgap clearance is proportional to the airgap diameter [53], and that the amount of permissible deflection, u, is a fixed proportion of this clearance, then it can be said that u/R is constant. Eqn. (4.1) gives the deflection of a cylinder as

$$u = \frac{qR^2}{Et}. \tag{4.1}$$

It can be inferred from this that qR/Et is constant, and that because for a given design both the normal stress, q, and Young's Modulus, E, are constant, then R/t ought to be constant. The thickness of the cylinder, t, should increase in step with the airgap radius, R. The mass of a cylinder is

$$m_{cyl} = 2\pi l t R \rho. \tag{7.33}$$

With a constant aspect ratio and a R/t ratio, the relationship can be stated more basically as

$$m_{cyl} \propto R^3. \tag{7.34}$$

---

† The later assumption that the airgap clearance is proportional to the airgap radius means that to produce the same (no load) airgap flux density at larger radii, the magnetic loading must be greater than that at smaller radii. This in turn means that the height of the magnets will increase for the larger airgap radii. Although the magnetically active copper and steel follows the proportionality in eqn. (7.32), the mass of magnets is proportional to $R^2 h_m$, where $h_m \propto \frac{B_g c \mu_r}{B_r - B_g}$ and $c \propto R$. This implies that $m_{act} \propto R^n$ where $n > 2$ and that the active power density will drop as the airgap radius and power rating both increase.

For the spokes, the force at the end of each one, F, is equal to the total force on the outside of the cylinder divided by the number of spokes, n_{sp},

$$F = \frac{2\pi R l q}{n_{sp}}. \tag{7.35}$$

With constant aspect ratio, number of spokes and normal stress then,

$$F \propto R^2. \tag{7.36}$$

The stress in the arms is then proportional to R^2/A, where A is the cross section area of the spokes. For a material with a given Young's Modulus, the stress is proportional to the strain (which can be stated as u/R) and so,

$$\frac{R^2}{A} = \text{constant}, \tag{7.37}$$

or

$$A \propto R^2. \tag{7.38}$$

The mass of the spokes is then

$$\begin{aligned} m_{sp} &\propto n_p \rho A R \\ m_{sp} &\propto R^3 \end{aligned} \tag{7.39}$$

From eqns. (7.34) and (7.39), both elements of the structural mass follow the same relationship to airgap radius, and so combining them,

$$m_{str} \propto R^3. \tag{7.40}$$

Combining eqns. (7.31) with (7.40),

$$\frac{P}{m_{str}} \propto R^{-1} \propto P^{-1/2}. \tag{7.41}$$

For a conventional generator directly driven in a wind turbine (as described above), the power per unit structural mass will drop as the airgap radius (and power) increase. Given the above assumptions and taking the active and structural mass together one can see that the total generator power density will fall as wind turbines increase in power rating.

The ratio of active to structural mass comes from eqns. (7.31), (7.32) and (7.41) and shows that structural mass becomes more dominant at higher power ratings,

$$\frac{m_{act}}{m_{str}} \propto P^{-1/2}. \tag{7.42}$$

7.4.2 C-core machine

This subsection carries out the same scaling analysis as in the previous subsection, this time for the C-core machine. At each stage of analysis, results from C-core machine designs are used to illustrate the scaling laws. The C-core machine does not have an optimal aspect ratio, so instead the stack length is assumed to be constant at all values of R in the analysis. (This is illustrated for several axial lengths of magnets, l_m=0.4, 0.6, 0.8, 1.0 and 1.2 m).

Seven different power ratings are designed for: 100 kW, 250 kW, 500 kW, 750kW, 1 MW, 1.5 MW and 2 MW. The rotational speed (in rpm) is taken as a function of the power, P, such that N=24376$P^{-0.5}$ (taken by fitting wind turbine designs from Enercon, Fuhrlander and Vestas [44],[49],[127]). Flux density at no load is kept at B_g=0.6 T across all of the designs. The flux density in the steel is not allowed to saturate (i.e. B_{st}<1.4 T and B_{sp}<1.4 T). Deflection of the steel pieces is not allowed to exceed 10% of the airgap clearance, c. Appendix C contains more details of the 35 different machine designs.

Equations (7.24) and (7.29) altered for the C-core machine respectively become

$$T \propto R^2, \tag{7.43}$$

$$P \propto R^{4/3}. \tag{7.44}$$

Figure 7.19 shows the torque plotted against the airgap radius for the five different active lengths (each with a power curve fitted). The exponents of the curves are reproduced in Table 7.3. Similarly Fig. 7.20 gives the power

plotted against airgap radius, with the exponents used in the power curves given in Table 7.3.

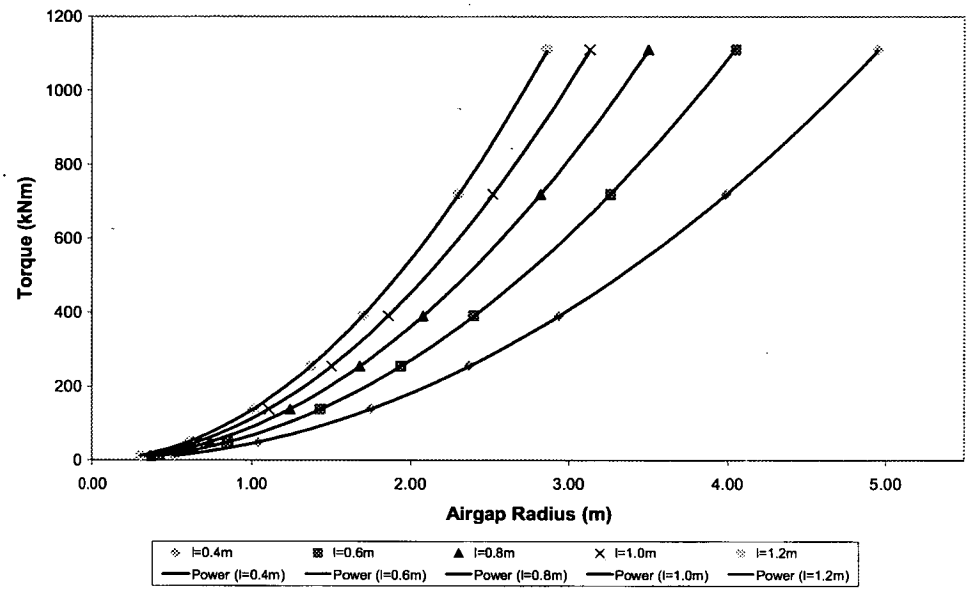

Figure 7.19. Torque plotted against airgap radius (curves for different active lengths)

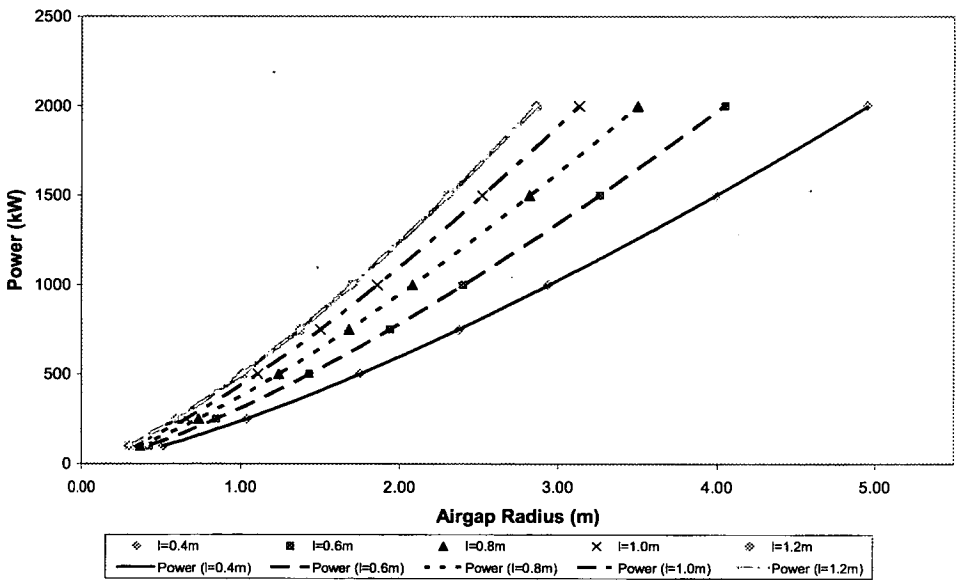

Figure 7.20 Power plotted against airgap radius (curves for different active lengths)

The active mass is counted as the copper, permanent magnet and electromagnetically active steel. This latter component is calculated from the minimum mass of steel in each module which does not lead to saturation.

The active mass is proportional to the airgap surface area, so for a constant axial length, then

$$m_{act} \propto R . \tag{7.45}$$

As was noted in the previous subsection, if the airgap clearance is assumed to be proportional to the airgap radius, then to produce the same no load flux density, the magnet thickness must increase with the airgap radius. As such the fitted curves in Fig. 7.21 have the following form (from Table 7.3):

$$m_{act} \propto R^{1.1} . \tag{7.45a}$$

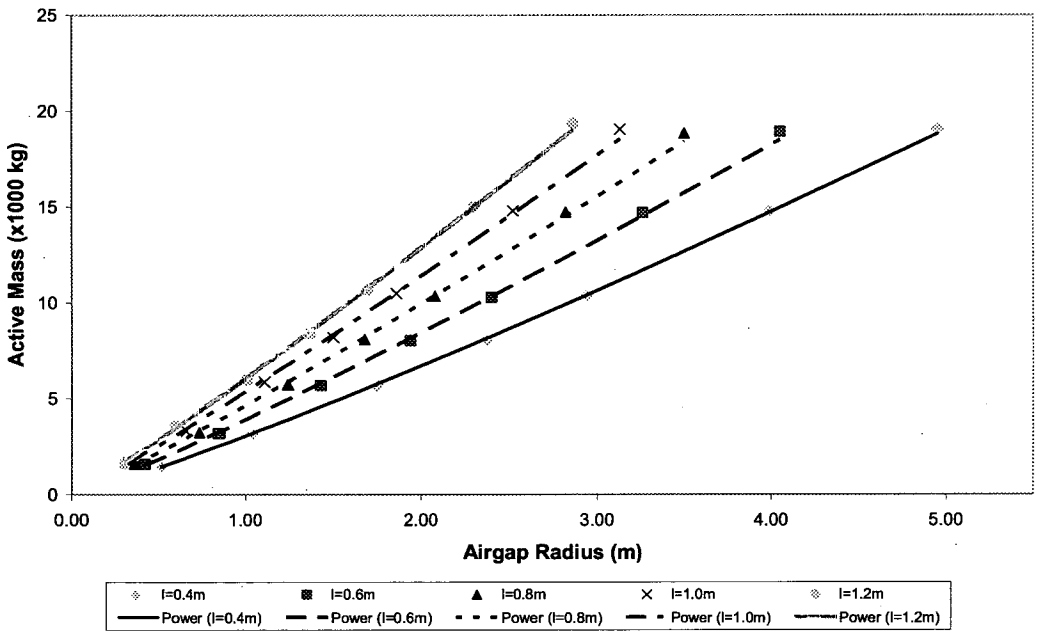

Figure 7.21 Active mass plotted against airgap radius (curves for different active lengths)

For the C-Core machine with a constant axial length, the active power density increases with radius and power rating:

$$\frac{P}{m_{act}} \propto R^{1/3} \tag{7.46}$$

$$\frac{P}{m_{act}} \propto P^{1/4} \tag{7.47}$$

Taking eqn. (7.44a) into account modifies (7.46) and (7.47), thus

$$\frac{P}{m_{act}} \propto R^{0.23} \quad (7.46a)$$

$$\frac{P}{m_{act}} \propto P^{0.17} \quad (7.47a)$$

Figures 7.22 and 7.23 show that the active power density increases with the airgap radius. The exponents of the power curve fits (Table 7.3) are close to those in eqns. (7.46a) and (7.47a).

The main difference between the active power density for the C-core machine and the conventional machine in the previous subsection is that a constant aspect ratio is not employed here. It has been previously argued in this thesis that using the same axial (active) length for all airgap radii is not appropriate for a conventional radial-flux machine. This is because the low aspect ratios at high power ratings would increase the need for structural material (and total mass). The next part of the analysis looks at the power density of structural material for the C-core machine.

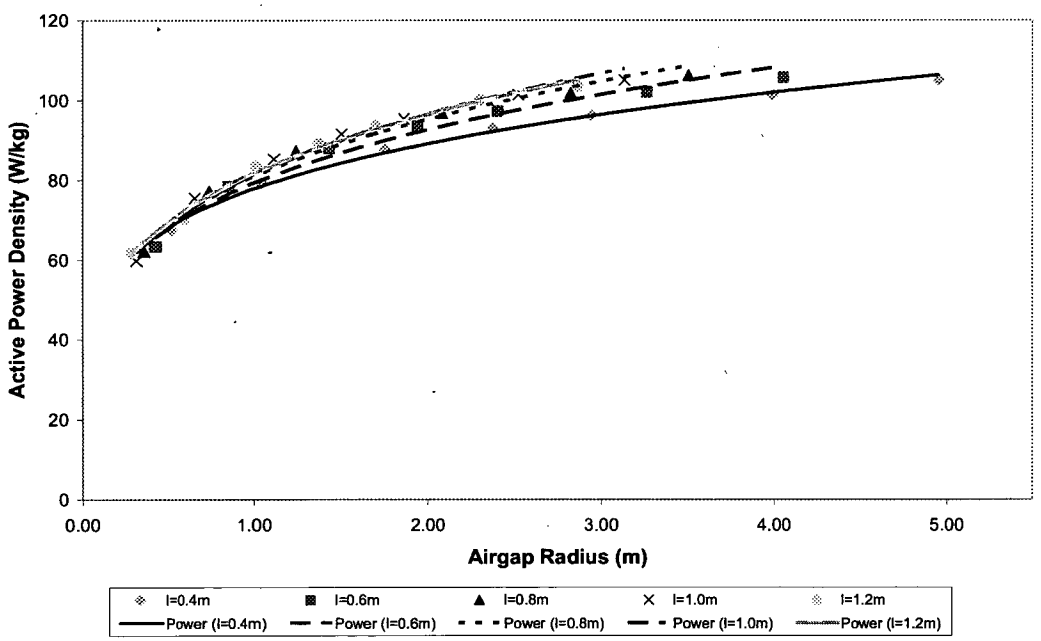

Figure 7.22 Power density (active material) plotted against airgap radius (curves for different active lengths)

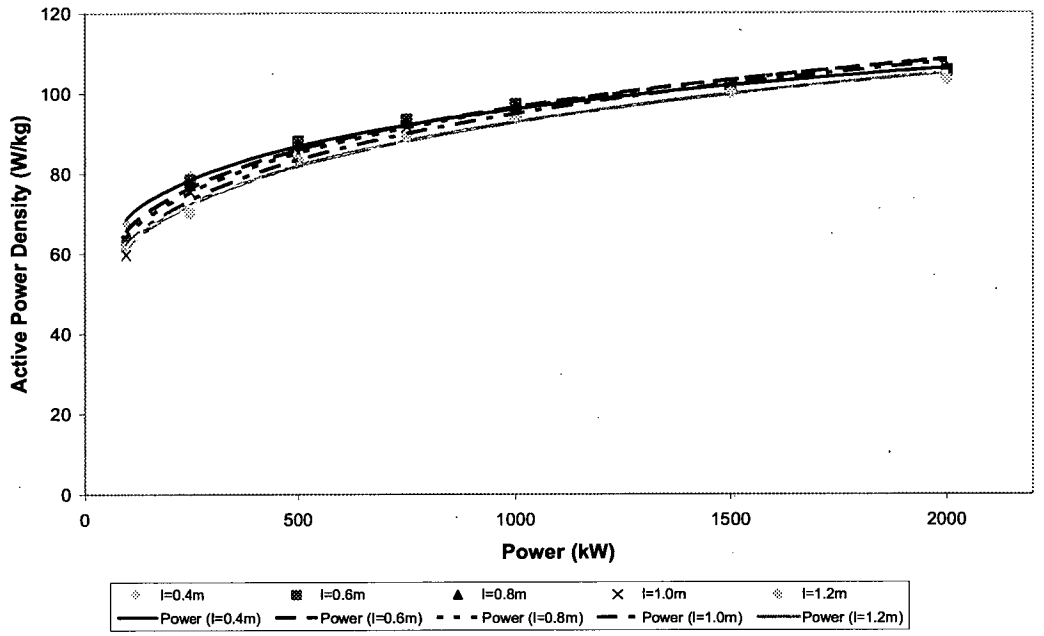

Figure 7.23 Power density (active material) plotted against power (curves for different active lengths)

Because the C-core machine is an air-cored machine, a valid approximation is that all the structural material is in the steel in the rotor. This structural mass can be divided into two parts according to section 7.2: the top and bottom pieces of the C-core modules. Equation (7.1) concerns the bottom piece. Simplifying this equation gives the deflection as

$$u \propto \frac{wl^4}{I}. \tag{7.48}$$

To simplify this further l and w can be assumed to be constant. If the pole pitch is constant, then the number of poles $p \propto R$. If the same flux density is used for all designs then the normal stress is constant.

$$w \propto q \tag{7.49}$$

$$\frac{u}{R} \propto \frac{1}{RI} \tag{7.50}$$

Assuming that the airgap clearance and permitted deflection are proportional to the airgap radius, then

$$I \propto \frac{1}{R} \tag{7.51}$$

A number of different cross sections can be used, the simplest (and worst) is the trapezoid, as shown in Fig. 7.9. Appendix D shows that this cross section has the following characteristic (when the pole pitch is constant and its depth is increased):

$$A \propto l^{0.36}. \tag{7.52}$$

The mass of these steel pieces is proportional to the pole number and their cross section, so that

$$m_{str} \propto RR^{-0.36} \propto R^{0.64}, \tag{7.53}$$

$$m_{str} \propto P^{0.52}. \tag{7.54}$$

Figures 7.24 and 7.25 show the curves fitted for the structural mass of these bottom steel pieces for the different designs. Equations (7.55) and (7.56) give the power density for the structural material in the bottom pieces. These are illustrated in Figs. 7.26 and 7.27.

$$\frac{P}{m_{str}} \propto R^{2/3}, \tag{7.55}$$

$$\frac{P}{m_{str}} \propto P^{1/2}. \tag{7.56}$$

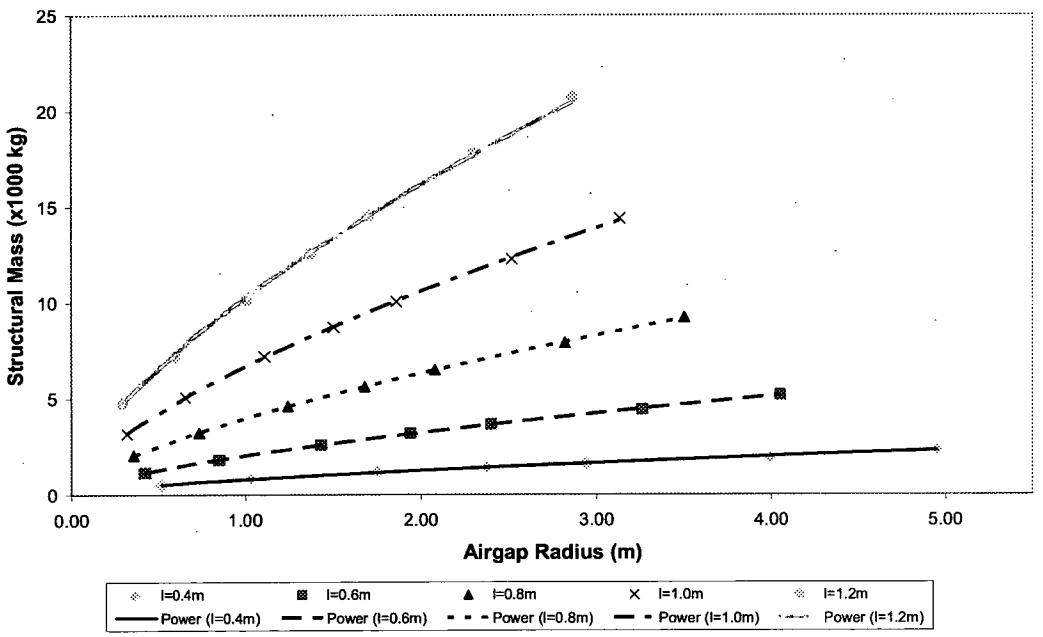

Figure 7.24 Structural mass (of bottom pieces) plotted against airgap radius (curves for different active lengths)

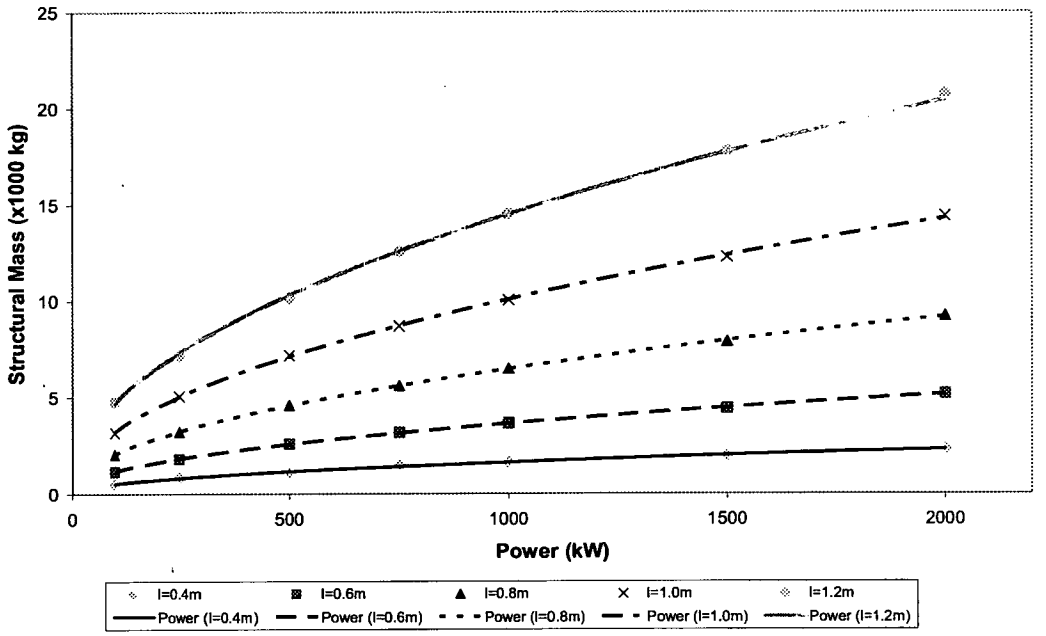

Figure 7.25 Structural mass (of bottom pieces) plotted against power (curves for different active lengths)

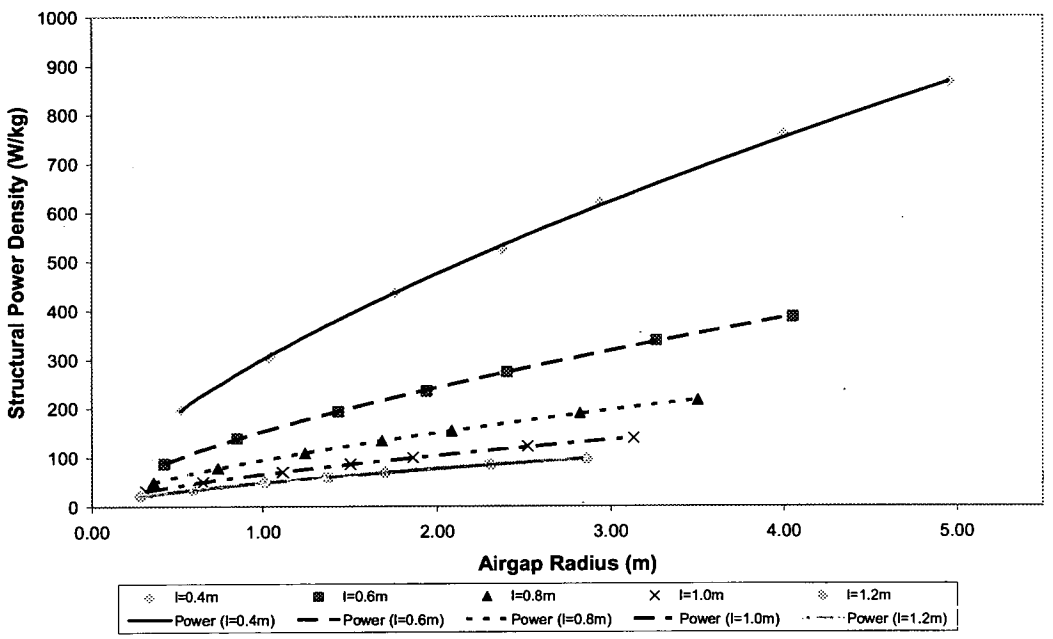

Figure 7.26 Power density (structural, bottom pieces) plotted against airgap radius (curves for different active lengths)

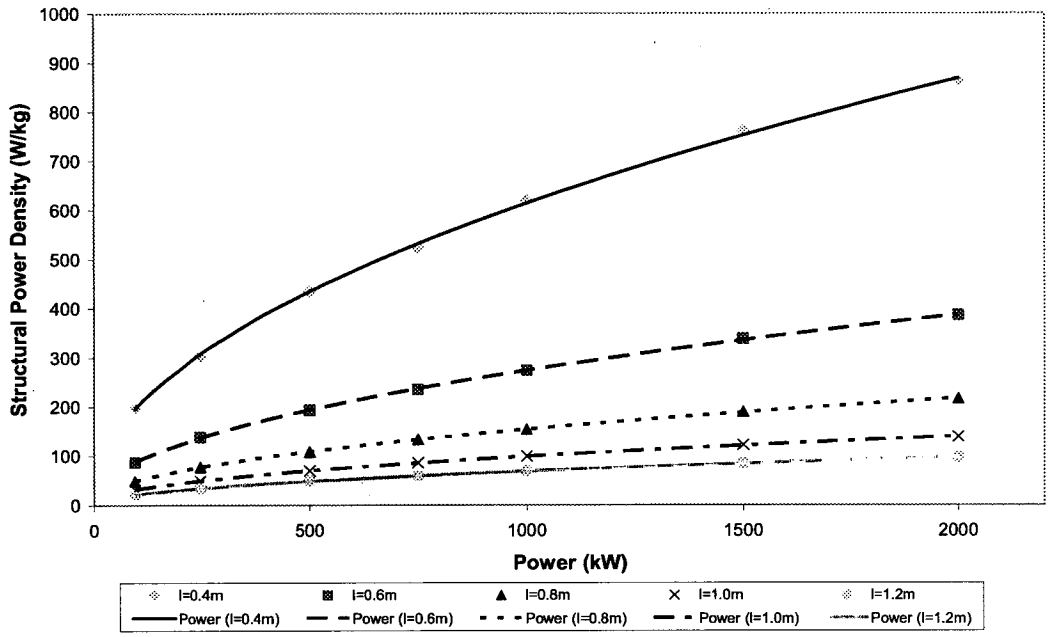

Figure 7.27 Power density (structural, bottom pieces) plotted against airgap radius (curves for different active lengths)

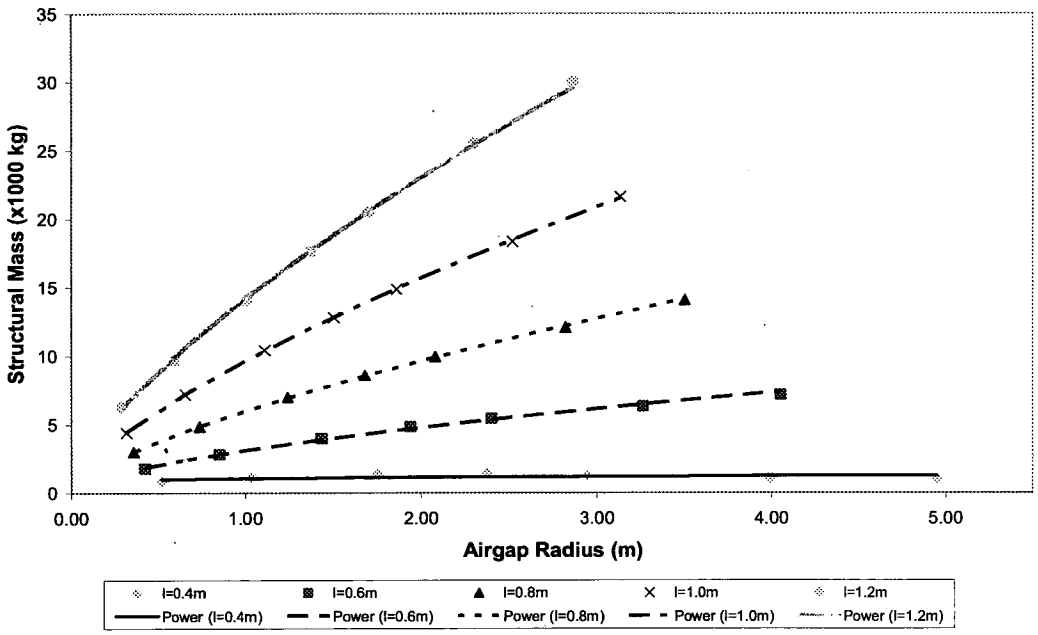

Figure 7.28 Total structural mass plotted against airgap radius (curves for different active lengths)

Including the mass of the top pieces into the structural mass calculation gives Fig. 7.28. Comparison of the power exponents from Fig. 7.25 with those in Fig. 7.28 shows similar results.

	Exponents, n						
	l=0.4m	l=0.6m	l=0.8m	l=1.0m	l=1.2m	Eqn.	For $m_{act} \propto R^{1.1}$
$T \propto R^n$ (7.43)	2.00	2.00	2.00	2.00	2.00	2	
$P \propto R^n$ (7.44)	1.33	1.34	1.33	1.33	1.33	$4/3$	
$m_{act} \propto R^n$ (7.45)	1.14	1.11	1.10	1.09	1.09	1	1.1
$\frac{P}{m_{act}} \propto R^n$ (7.46)	0.18	0.22	0.23	0.25	0.24	$1/3$	0.23
$\frac{P}{m_{act}} \propto P^n$ (7.47)	0.13	0.17	0.18	0.19	0.18	$1/4$	0.17
$m_{str} \propto R^n$ (7.53)	0.67	0.67	0.67	0.67	0.66	0.64	
$m_{str} \propto P^n$ (7.54)	0.50	0.50	0.50	0.50	0.49	0.52	
$\frac{P}{m_{str}} \propto R^n$ (7.55)	0.66	0.67	0.66	0.67	0.67	0.69	
$\frac{P}{m_{str}} \propto P^n$ (7.56)	0.50	0.50	0.50	0.50	0.51	0.56	
$m_{str,tot} \propto R^n$	0.11	0.62	0.69	0.70	0.70		
$m_{tot} \propto P^n$	0.73	0.69	0.66	0.63	0.61		

Table 7.3 Exponents from analysis and curve fitting of designs

7.4.3 Large scale designs for the C-Core machine

Figure 7.29 shows the total mass of the C-core machine for different power ratings achieved with different active lengths. The fitted curves are power functions with exponents of the range 0.61 to 0.73. Figure 7.30 shows how the C-core machine's power density increases when designed with the above assumptions.

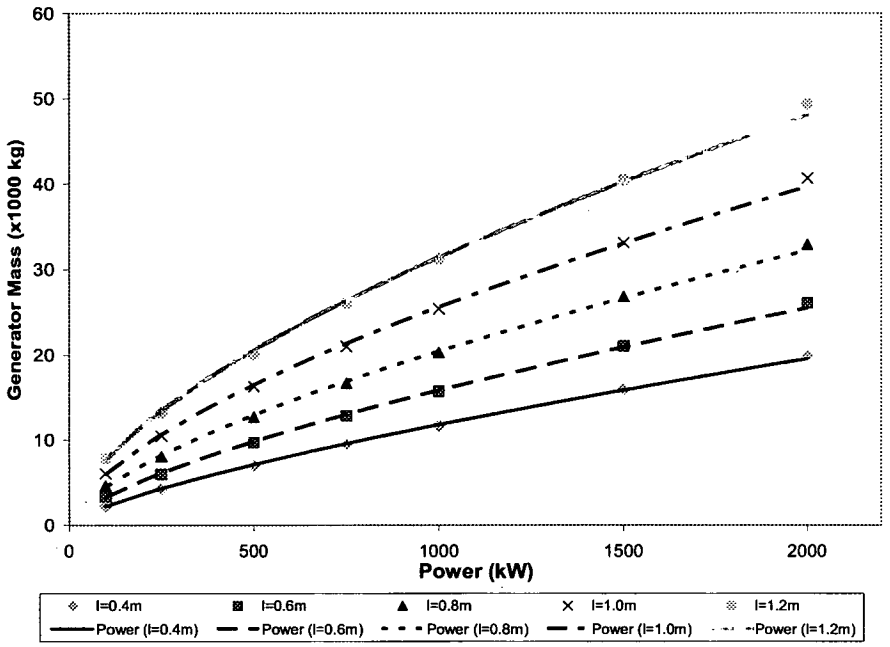

Figure 7.29 Generator mass plotted against power (curves for different active lengths)

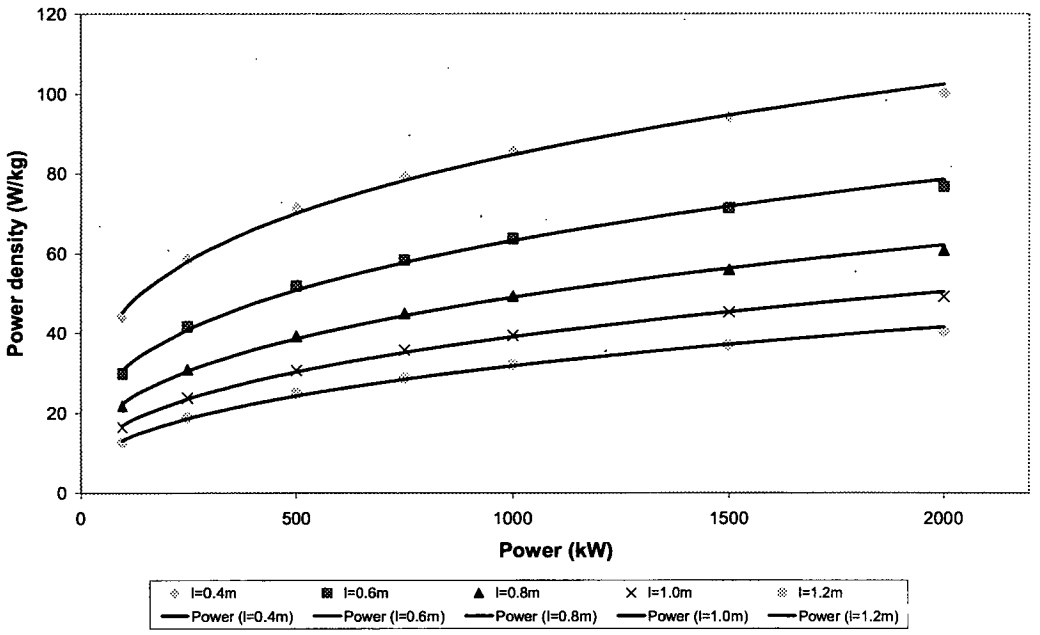

Figure 7.30 Power density plotted against power (curves for different active lengths)

7.4.4 Discussions

The lightest machines are those with low aspect ratios. These machines have a high power density with respect to active material because of the large

radius and also high power density with respect to structural material because of the short axial length. The large airgap radius for the machines with low axial length could be difficult to incorporate into a reasonably sized wind turbine nacelle. The machines with larger aspect ratios are dominated by structural material, particularly that structural material in the lower steel pieces in the C-cores. This part of the total mass is strongly influenced by axial length. By using back-to-back generators, it might be possible to reduce airgap radius without being penalised by the structural mass associated with the larger aspect ratios.

7.5 Conclusions

This chapter sets out some of the active and inactive modeling tools for an air-cored machine. The topology employs a rotor with steel C-core modules and permanent magnets placed either side of an airgap in which an air-cored winding is placed.

The C-core is the main distinguishing feature of the topology and allows the majority of structural material to also play an active role in the magnetic circuit. Scaling laws show that it has fundamental advantages over a conventional machine, mainly because low aspect ratios can be used without incurring the structural mass penalties that have been seen in Chapters 4 to 6.

Further improvements can be made by optimising the pole layout (winding thickness, pole pitch, magnet thickness and pitch), making use of other steel cross sections (with better I/A characteristics) and possibly by using back-to-back machines (in a similar way to Chapter 3). However even before these changes, it can be seen from the designs in this chapter that these are already lighter than conventional machines.

Chapter 8

Discussions and Conclusions

THIS thesis addresses the structural analysis of low speed, high torque electrical generators for direct drive renewable energy converters. In this chapter, a summary of each chapter is given and then the important themes are discussed and overall conclusions given.

8.1 Chapter summaries

Chapter 2 introduces renewable energy and the devices that are used to convert the fluid flows into electricity. In wind turbines the main design alternatives for the drivetrain are to use a gearbox to step up the low speed rotation of blades for a high speed conventional electrical machine, or to use a directly-driven generator. The latter has the advantages of being more reliable and more efficient and so it offers wind farm operators greater potential revenue. Unfortunately, to produce the same power as its gearbox driven counterpart, the direct drive generator must have a large torque rating and is thus large and heavy. While many investigators have addressed the mass of material that is actively involved in the electrical and magnetic circuits, less attention has been paid to the mass of material which is needed to maintain the structural integrity of the generator.

A consistent alternative approach has been adopted in Chapters 3, 4, 5 and 6. The airgap flux density is used as the link between the electromagnetic models and the structural models. Airgap flux density leads to shear stress and ultimately to the generation of voltage and electrical power. It also gives the normal component of Maxwell stress, which is the largest force in the electrical machine. For the structural modelling, the deflection into the airgap

is the most critical result. For all machines, a mode 0 deflection (deflection into the airgap, uniform across the airgap surface) is assumed. In all cases, the worst case scenario is addressed (i.e. assembly, when there is no balancing and cancelling out of forces). Simplified structures are used to model the deflection and wherever possible analytical expressions model the deflection.

Chapter 3 focuses on axial-flux machines. Rotor and stator discs are modelled using circular plate theory, with a uniformly distributed load to represent the normal component of Maxwell stress. These models can be verified with finite element analysis. For these machines, the rotor disc mass dominates the mass of structural material; this in turn dominates the total mass. Chapter 3 includes some simple optimisations for generators (for large wind turbines) using two dimensional plots of T/m and T, and treating aspect ratio, outer radius and airgap flux density as the independent variables. Different designs are shown to be best when minimising only electromagnetically active mass and then also including structural mass too. Multistage machines are shown to come out well when structural material is included in the optimisation process.

As most direct-drive generators for wind turbines are of the radial-flux type, Chapter 4 focuses on these topologies. Several different structures are used, those that are based around a disc and those that are based on arms. Because it can be difficult to model the deflection of the airgap deflection analytically, a hybrid finite element and polynomial method is used in Chapter 4. This method makes use of simple, generic structures. The essence of these structures is reduced down to four geometric variables and a further variable of the normal component of Maxwell stress. From a large database of discrete designs, attempts to synthesise functions relating these variables to the airgap deflection are made for both the rotor and stator of radial-flux machines. This method is quick to use once the polynomials are set up. The

disadvantage is that it can take a long time to set up, which would have to be done each time say a different material was chosen. Minimising the total mass of generators based upon aspect ratios generally gives the lightest machines when the axial length is 0.12-0.13 times the airgap length. The (outer) stator mass dominates and the mass of the structural mass dominates the mass of the electromagnetically active material.

Because of the problems with the method in Chapter 4, analytical methods are used to predict airgap deflection of radial-flux machines in Chapter 5. The deflection of armed and disc structures for both the rotor and the stator due to the normal component of Maxwell stress is found analytically. The deflection due to gravity in the axial direction of the structures is analysed and verified using finite element analysis. The mass is minimised using 2 dimensional plots, with structural variables used as the x and y axes and mass, radial deflection and axial deflection plotted.

Chapter 6 uses the work on axial-flux and radial-flux machines to optimise generators based upon total mass and a cost criterion. This cost criterion includes material cost - both active and structural mass - and the cost of lost energy. This chapter assumes a wind turbine subjected to a Weibull wind speed distribution, so that energy lost over the whole operating range - not just the nominal load point - is found. Machines rated at 2, 3 and 5 MW are optimised.

In Chapter 7 an air-cored topology is introduced. This uses steel C-core modules (with two permanent magnets in each module) to produce a finite airgap length. The module is analysed so that the deflection of the steel module into the airgap can be predicted. A simple lumped parameter magnetic circuit is used to find the airgap flux density. After this, generator designs for large wind turbines are produced and the scaling laws (linking generator mass and power density to generator power and airgap radius) are deduced.

8.2 Discussions and conclusions

8.2.1 The approach to the problem

The broad approach of this thesis includes three main ideas:

1. Simultaneously design the mechanical and electrical parts of these generators, using the airgap flux density at no load (and its corollary the normal component of Maxwell stress) to link the two.

2. Use simple structures that can represent the airgap deflection/mass characteristics of plausible generator designs used by industry.

3. Model the deflection of these structures using analytical expressions wherever possible. This allows quick calculations, straightforward optimisations and the identification of scaling laws.

The author believes that this should be the strategy for any design team trying to produce a lightweight low speed, high torque generator. It should be first used early on at the design study stage, so that the main design parameters can be chosen with low mass in mind.

How well do the design tools presented in this thesis realistically predict the actual mass of these generators? In Chapter 4, the amount of deflection (as a proportion of the airgap clearance) was varied so that the generator mass matched that of a commercial design. Generator material is needed for other roles: cooling, resisting thermal strain, bearings, helping transport and manufacturing requirements. All of these add mass and they have been ignored in this thesis. Every model is by its nature an approximation, and in this case it has been shown that the design tools in this thesis give a more sensible answer (to mass minimisation problems) than when just using active material. At least by including the structural mass it is a more realistic prediction than just using the active material for design studies and optimisations.

8.2.2 Revisiting the thesis statement

In Chapter 1, the thesis is stated as:

> "If there is to be a fair comparison to find the best topology for direct drive generators and if each topology is to be optimised for minimum mass and cost, then the inactive mass must be included."

Chapter 6 illustrates how a fair comparison between each topology might be conducted, and the results show how the exclusion of the inactive mass skews the result away from the optimum. Chapters 3, 4 and 5 show in greater detail the impact of not including the inactive mass on efforts to find a lighter direct-drive electrical generator. Chapter 7 shows how incorporating structural modelling in the design process can help to find electrical machine scaling laws. Overall, the thesis has been proved correct.

8.2.3 Contribution to knowledge

This thesis has contributed to knowledge in a number of ways. Structural design tools for large axial-flux and radial-flux machines have been introduced and verified. These have then been used to carry out total mass minimisations at what would be the early stage of generator design. The importance and dominance of inactive mass has been demonstrated. Indeed, it has been shown that these electrical machines can be made lighter (and more cheaply) by including this mass in the analysis. Simple magnetic and structural design tools for an unconventional PM machine have also been introduced. Finally, scaling laws (which show how alternatives to conventional PM machines may be needed for future, larger direct-drive generators) have been found.

The work in this thesis has contributed to a number of other publications: axial-flux machine modelling in Chapter 3 in [70] and [80]; radial-flux machine modelling in Chapter 4 in [71] and [95] and Chapter 5 in [73]; mass

and cost comparison of machines in Chapter 6 in [72]; scaling laws for conventional PM machines in Chapter 7 in [74].

8.2.4 Further work

In all of the design tools, a 'mode 0' deflection (whereby there is a uniform deflection into the airgap at every point along the airgap surface) has been assumed. Tavner and Spooner has shown using equivalent stiffness for the airgap and spokes that a 'mode 1' deflection is more appropriate [121]. This is where, say, for a radial-flux machine, the rotor cylinder maintains its shape but the centre of this cylinder moves eccentrically from the original centre. Because the strain energy needed for this type of deflection is less, the 'mode 0' deflection is likely to underestimate the need for structural stiffness and therefore structural mass. Further work should include the extension of the structural models to 'mode 1' deflection.

A further question that has been skirted by this thesis is where should one draw the line between the generator and the rest of the wind turbine? Direct drive machines are bespoke and tend to be integrated into the hub to some degree, rather than connected to it by a rotor shaft, as in a geared drivetrain. In these models the latter case has been assumed. This has allowed generic comparisons with no assumptions about the rest of the wind turbine. In individual cases where the likely hub and generator integration is known, then some of these design tools should be altered accordingly.

An attempt was made in Chapter 6 to link the stiffness/mass characteristics of the simple structures in Chapters 3, 4 and 5 to commercial structures. It is unclear what the optimal structures for either the axial-flux or radial-flux machines are. Further work should investigate what structures give the best stiffness/mass characteristics.

References

[1] Al-Badi, A., Gastli, A., Bourdoucen, H., and Jervase, J.: 'Evolution of axial-field electrical machines'. Science and Technology, Special Review (2000), Sultan Qaboos University, pp. 227-245

[2] ANSYS Workbench, www.ansys.com, last accessed January 2008

[3] AquaBuOY, www.finavera.com, last accessed January 2008

[4] Archimedes Wave Swing, www.waveswing.com, last accessed January 2008

[5] Arshad, W.M., Bäckström, T., and Sadarangani, C.: 'Analytical design and analysis procedure for a transverse flux machine'. IEEE International Electric Machines and Drives Conference, 2001. IEMDC 2001. pp.115-121

[6] Artemis Intelligent Power Ltd., www.artemisip.com, last accessed January 2008

[7] Baker, N.J.: 'Linear generators for direct drive marine renewable energy converters'. PhD Thesis, University of Durham, School of Engineering, 2003

[8] Barr, D.: 'Modern Wind Turbines: A Lubrication Challenge', *Machinery Lubrication Magazine*, September 2002

[9] Bianchi, N., and Lorenzoni, A.: 'Permanent magnet generators for wind power industry: an overall comparison with traditional generators'. IEE Conf. on Opportunities and Advances in International Power Generation, Durham, UK, 18-20 Mar. 1996, pp. 49-54

[10] Bonus Energy A/S, www.bonus.dk, last accessed January 2008

[11] *Ed.* Boyle, G.: 'Renewable energy – Power for a sustainable future' (Oxford University Press, Oxford, 2003)

[12] Braid, J., van Zyl, A., and Landy, C.: 'Design, analysis and development of a multistage axial-flux permanent magnet synchronous machine'. Proc. 6th IEEE Africon Conf. in Africa. 2-4 Oct. 2002, 2, pp. 675- 680

[13] Braid, J., van Zyl, A., and Landy, C.: 'Unbalanced load sharing in a prototype multistage axial-flux permanent magnet synchronous machine'. IEEE Int. Electric Machines and Drives Conference 2003 (IEMDC'03), 1-4 June 2003, 2, pp. 1935- 1940

[14] Brown, N., Haydock, L., and Bumby, J.R.: 'Foresight vehicle: a toroidal, axial flux generator for hybrid IC engine/battery electric vehicle applications'. Proc. SAE Conf. paper 2002-01-0829, Detroit, USA, March 2002

[15] Brown, N., Haydock, L., and Bumby, J.R.: 'An idealised geometric approach to electromagnetically comparing axial and radial flux permanent magnet machines'. Conf. Rec. of the 15th Int. Conf. on Electrical Machines (ICEM 2002), 25-28 Aug. 2002, Brugge, Belgium

[16] BTM Consult ApS: 'International Wind Energy Development World Market Update 2006 Forecast 2007-2011', Press Release, March 26, 2007, available at www.btm.dk/documents/pressrelease.pdf

[17] Bumby, J.R., and Spooner, E.: 'Torus Generator. Design, build and test of two prototypes'. Report, School of Engineering, Durham University, Durham, UK, July 2000

[18] Bumby, J.R., Martin, R., Mueller, M.A., Spooner, E., Brown, N.L., and Chalmers, B.J.: 'Electromagnetic design of axial-flux permanent magnet machines', *IEE Proc. Electr. Power Appl.*, 2004, **151**, (2), pp. 151-160

[19] Burton, T., Sharpe, D., Jenkins, N., and Bossanyi, E.: 'Wind Energy Handbook' (John Wiley & Sons Ltd, 2002)

[20] Bywaters, G. *et al.*: 'Northern Power Systems WindPACT Drive Train Alternative Design Study Report'. National Renewable Energy Laboratory report NREL/SR-500-35524. NREL, Golden, CO, USA. January 31, 2005.

[21] Caricchi, F., Crescimbini, F., Mezzetti, F., and Santini, E.: 'Multistage axial-flux PM machine for wheel direct drive', *IEEE Trans. on Ind. Appl.*, 1996, **32**, (4), pp. 882-888

[22] Caricchi, F., Crescimbini, F., Honorati, O., Bianco, G.L., and Santini, E.: 'Performance of coreless-winding axial-flux permanent-magnet generator with power output at 400 Hz, 3000 r/min', *IEEE Trans. on Ind. Appl.*, 1998, **34**, (6), pp. 1263-1269

[23] Caricchi, F., Chalmers, B.J., Crescimbini, F., and Spooner, E.: 'Advances in the design of torus machines'. Proc. Int. Conf. on Power Electronic Drives and Energy Systems for Ind. Growth (PEDES), Perth, Australia, 1998, 2, pp. 516-522

[24] Carlson, O., Grauers, A., Williamson, A., Engström, S., and Spooner, E.: 'Design and Test of a 40kW Directly Driven Permanent-Magnet Generator with a Frequency Converter', Proc. of European Wind Energy Conference, Nice, France, March 1-5, 1999

[25] Caricchi, F., Crescimbini, F., Honorati, O.: 'Modular axial-flux permanent-magnet motor for ship propulsion drives', *IEEE Trans. on Energy Conv.*, 1999, **14**, (3), pp. 673-679

[26] Chalmers, B.J., and Spooner, E.: 'An axial-flux permanent-magnet generator for a gearless wind energy system'. *IEEE Trans. on Energy Conv.*, 1999, **14**, (2), pp. 251-257

[27] Chen, J., Nayar, C.V., and Xu, L.: 'Design and finite-element analysis of an outer-rotor permanent magnet generator for directly coupled wind turbines', *IEEE Trans. on Magn.*, 2000, **36**, (5), pp. 3802-3809

[28] Chen, Y., Pillay, P., and Khan, A.: 'PM wind generator comparison of different topologies'. Conf. Rec. of the 2004 IEEE Ind. Appl. Conf. 39th IAS Annual Meeting, Seattle, WA, USA, 2004, 3, pp. 1405-1412

[29] COSMOSWorks, www.cosmosworks.com, last accessed January 2008

[30] Danielsson, O., Thorburn, K., Sjöstedt, E., Eriksson, M., and Leijon, M.: 'Permanent magnet fixation concepts for linear generator'. Proc. of the Fifth European Wave Energy Conf., Cork, Ireland, Sep 17-20, 2003

[31] Datta, R., and Ranganathan, V.T.: 'Variable-speed wind power generation using doubly fed wound rotor induction machine - a comparison with alternative schemes', *IEEE Trans. on Energy Conv.*, Sep. 2002, **17**, (3), pp. 414-421

[32] de Vries, E.: 'Global wind technology', *Renewable Energy World*, Jul.-Aug. 2004, **7**, (4)

[33] de Vries, E.: 'Multibrid, a new offshore wind turbine converter', *Renewable Energy World*, Sep.-Oct. 2004, **7**, (5), pp. 54

[34] de Vries, E.: 'Offshore boost for Bonus – Danish wind firm scales up', *Renewable Energy World*, Nov.-Dec. 2004, **7**, (6), pp. 84-91

[35] de Vries, E.: 'Trouble spots – Gearbox failures and design solutions', *Renewable Energy World*, Mar. 2006, **9**, (2), pp.37-47

[36] DTI: 'Our energy future – creating a low carbon economy', Energy White Paper, February 2003

[37] DTI, www.dti.gov.uk/energy/sources/renewables/renewables-explained/intro/

page14237.html, last accessed December 2007

[38] Dubois, M.R.: 'Review of electromechanical conversion in wind turbines'. Final Literature Review, Technical University of Delft, Electrical Power Processing Group, April 2000

[39] Dubois, M.R., Polinder, H., Ferreira, J.A.: 'Comparison of generator topologies for direct-drive wind turbines'. 2000 IEEE Nordic Workshop on Power and Industrial Electronics, Aalborg, Denmark, June 13-16 2000, p. 22-26

[40] Dubois, M.R., Polinder, H., Ferreira, J.A.: 'Axial and radial-flux permanent magnet generators for direct-drive wind turbines'. European Wind Energy Conf., Copenhagen, Denmark, 2-6 July 2001, pp. 5-8

[41] Dubois, M.R.: 'Optimized Permanent Magnet Generator Topologies for Direct-Drive Wind Turbines', PhD dissertation, Department of Electrical Engineering, Delft University of Technology, Delft, Netherlands, 2004

[42] Danish Windpower Industry Association, www.windpower.org, last accessed January 2008

[43] Ecotècnia, www.ecotecnia.es, last accessed January 2008

[44] Enercon GmbH, www.enercon.de, last accessed January 2008

[45] Engineering Business Ltd., www.engb.com, last accessed January 2008

[46] Éocycle Technologies, www.eocycle.com, last accessed January 2008

[47] European Wind Energy Association: 'Wind Energy The Facts An Analysis of Wind Energy in the EU-25' available at www.ewea.org, last accessed January 2008

[48] Evolving Generation Ltd., www.evolving-generation.co.uk, last accessed January 2008

[49] Fuhrländer AG, www.fuhrlaender.com, last accessed January 2008

[50] Gamesa Corporación Tecnológica S.A., www.gamesa.es, last accessed January 2008

[51] Geng, G., and Spooner, E.: 'Cancellation of noise and vibration in modular permanent-magnet wind turbine generators', IEE 7th International Conference on Electrical Machines and Drives, Durham, UK, 11-13 Sep. 1995, Conf. Pub. No. 412, pp. 467-471

[52] Gordon, P.: 'Aspects of, and new approaches to, the design of direct drive generators for wind turbines'. PhD thesis, University of Durham, School of Engineering, 2004

[53] Grauers, A.: 'Design of direct-driven permanent-magnet generators for wind turbines,' PhD dissertation, Department of Electric Power Engineering, Chalmers University of Technology, Göteburg, Sweden, 1996

[54] Grauers, A.: 'Direct Driven Generators: Technology and Development Trends'. Proc. Nordic Wind Power Conf., Trondheim, Norway, 13-14 March 2000, pp. 127-131

[55] Greaves, M.C., Simpson, A.G., Guymer, B.D., Walker, G.R., and Finn, D.A.: 'Ironless wheel motor for a direct drive vehicle application'. Australian Universities Power Engineering Conference 2003, Christchurch, New Zealand

[56] Hamlaoui, M.N., Mueller, M.A., Bumby, J.R., and Spooner, E.: 'Polynomial modelling of electromechanical devices: an efficient alternative to look-up tables', *IEE Proc. Electr. Power Appl.*, **151**, (6), pp. 758-768, 2004

[57] Harakosan Europe B.V., www.harakosan.nl, last accessed January 2008

[58] Harris, M.R., Pajooman, G.H., and Abu Sharkh, S.M.: 'The problem of power factor in VRPM (transverse-flux) machines'. Eighth Int. Conf. on Electrical Machines and Drives, 1997, (Conf. Publ. No. 444), pp. 386-390

[59] Hartkopf, T., Hofmann, M., Jöckel, S.: 'Direct-drive generators for megawatt wind turbines'. European Wind Energy Conf., Dublin, Ireland, 1997, pp. 668-671

[60] Hill-Cottingham, R.J., Coles, P.C., Eastham, J.F., Profumo, F., Tenconi, A., Gianolio, G., and Cerchio, M.: 'Plastic structure multi-disc axial flux PM motor'. Conf. Rec. of the 2002 IEEE Ind. Appl. Conf. 37th IAS Annual Meeting. Pittsburgh, PA, USA, 13-18 Oct. 2002, **2**, pp. 1274-1280

[61] International Energy Agency, 'Renewables in Global Energy Supply – An IEA Fact Sheet', September 2006, OECD-IEA, Paris

[61] Jöckel, S.: 'Gearless wind energy converters with permanent magnet generators – an option for the future?' Proc. of EUWEC 1996, Gothenburg, Sweden, 20-24 May 1996

[62] Keppola, H., Perälä, R., Söderlund, L., and Vihriälä, H.: 'Preliminary test results of an axial flux toroidal stator wind power generator'. Proc. Int. Conf. on Electr. Mach., Espoo, Finland, Aug. 28-30 2000, 3, pp. 1480-1484

[63] Knapp, W., Holmén, E., and Schilling, R.: 'Considerations for water turbines to be used in wave energy converters'. Proc. of the 4th European Wave Energy Conf., Aalborg, Denmark, 2000

[64] Lampola, P.: 'Directly driven, low-speed permanent-magnet generators for wind power applications', PhD thesis, Helsinki University of Technology, 2000

[65] Leitner AG, www.leitwind.com, last accessed January 2008

[66] Lombard, N.F., and Kamper, M.J.: 'Analysis and performance of an ironless stator axial flux PM machine', *IEEE Trans. on Energy Conv.*, 1999, **14**, (4), pp. 1051-1056

[67] Lovatt, H.C., Ramsden, V.S., and Mecrow, B.C.: 'Design of an in-wheel motor for a solar-powered electric vehicle', *IEE Proc. Electr. Power Appl.*, 1998, **145**, (5), pp. 402-408

[68] Manwell, J.F., McGowan, J.G., and Rogers, A.L.: 'Wind Energy Explained: Theory, Design and Application' (John Wiley & Sons, Chichester, 2002, 1st edn.), pp. 57-60

[69] Mbidi, D.N., van der Westhuizen, K.,Wang, R., Kamper, M.J., and Blom, J.: 'Mechanical design considerations of a double stage axial-flux PM machine'. Conf. Rec. of the 2000 IEEE Ind. Appl. Conf., 2000, **1**, pp. 198-201

[70] McDonald, A.S., Mueller, M.A.: 'Structural mass of axial-flux permanent magnet direct drive generators for wind turbines'. Proc. of the University Power Engineering Conf., Sept. 2005, Cork, Sep. 2005

[71] McDonald, A.S., Mueller, M.A.: 'Mechanical design tools for low speed high torque electrical machines'. Proc. IET 3rd Int. Conf. on Power Electronics, Machines & Drives, Dublin, March 2006

[72] McDonald, A.S., Mueller, M.A., Polinder, H.: 'Comparison of generator topologies for direct-drive wind turbines including structural mass'. Proc. XVII Int. Conf. on Electrical Machines ICEM 2006, Chania, Crete, Sep. 2006

[73] McDonald, A.S., Mueller, M.A. and Polinder, H.: 'Structural mass in direct-drive permanent magnet electrical generators'. Proc. European Wind Energy Conf., Milan, Italy, 2007, paper BS4.1

[74] McDonald, A.S., Mueller, M.A. and Polinder, H.: 'Structural mass in direct-drive permanent magnet electrical generators', *IET Renew. Power Gener.*, **2**, (1), EWEC 2007 Special Issue

[75] Meyer, N.I., and Nielsen, K.: 'The Danish wave energy programme second year status', Proc. of the Fourth Wave Energy Conference, Aalborg, 2000, pp. 10-18

[76] Mitsubishi Heavy Industries Ltd., www.mhi.co.jp/power/e_power/product/nature/wind_pdf/vol41_no3.pdf, last accessed January 2008

[77] MTorres, www.mtorres.com, last accessed January 2008

[78] Mueller, M.A.: 'Electrical generators for direct drive wave energy converters', *IEE Proc. Gen., Transm. and Distr.*, 2002, **149**, (4), pp. 446-456

[79] Mueller, M.A.: 'Wave energy: linear versus hydraulic generators for energy conversion', DTI Project Summary, Publication Code RPS003, DTI/Pub URN 01/1506

[80] Mueller, M.A., McDonald, A.S., and Macpherson, D.E.: 'Structural analysis of low-speed axial-flux permanent-magnet machines,' *IEE Proc. Electr. Power Appl.*, **152**, 6, pp. 1417-1426, 2005

[81] Mueller, M.A., *et al.*: 'Generator and magnetic flux conducting unit'. UK Patent, PCT/GB2007/000883, applied March 2007

[82] Mueller, M.A., McDonald, A.S., Ochije, K. and Jeffrey, J.: 'A novel lightweight permanent magnet generator for direct drive power take off in marine renewable energy converters'. European Wave and Tidal Energy Conf., Porto, Portugal, 2007, paper 1123

[83] Muljadi, E., Butterfield, C.P., and Wan, Y.-H.: 'Axial flux, modular, permanent magnet generator with a toroidal winding for wind turbine applications'. The 1998 IEEE Ind. Appl. Conf. 33rd IAS Annual Meeting, St. Louis, MO, USA, 12-15 Oct. 1998, **1**, pp. 174-178

[84] Multibrid GmbH, www.multibrid.com, last acccessed January 2008

[85] NEG Micon, www.boxer99.de/pressebox/neg/NEG_Micon_20020306.pdf, last accessed May 2007

[86] Nordex AG, www.nordex-online.com, last accessed January 2008

[87] OpenHydro Group Ltd., www.openhydro.com, last accessed January 2008

[88] Pelamis Wave Power, www.pelamiswave.com, last accessed January 2008

[89] Pippard, A.J.S.: 'Studies in Elastic Structures' (Edward Arnold, London, 1952, 1st edn.), pp. 76-78

[90] as above, pp. 84-87

[91] Polinder, H.: 'A linear permanent-magnet machine for the Archimedes Wave Swing: design and practical experience'. IEE Sem. on Electr. Aspects of Offshore Renewable Energy Systems, NaREC, Blyth, Northumberland, UK, 2004

[92] Polinder, H., de Haan, S.W.H., Slootweg, J.G., and Dubois, M.R.: 'Basic operation principles and electrical conversion systems of wind turbines'. Proc. of the Nordic Workshop on Power and Industrial Electronics, Tronheim, Norway, 14-16 June 2004, paper number 69

[93] Polinder, H., van der Pijl, F.F.A., de Vilder,G.-J., and Tavner, P.: 'Comparison of direct-drive and geared concepts for wind turbines'. Proc. of the IEEE International Electric Machine and Drives Conf., San Antonio, TX, USA, May 2005, pp 543-550

[94] Polinder, H., Mecrow, B.C., Jack, A.G., Dickinson, P.G. and Mueller, M.A.: 'Conventional and TFPM linear generators for direct-drive wave energy conversion,' *IEEE Trans. Energy Conv.*, **20**, (2), pp. 260-267, 2005

[95] Polinder, H., Bang, D., van Rooij, R.P.J.O.M., McDonald, A.S., Mueller, M.A.: '10 MW Wind Turbine Direct-Drive Generator Design with Pitch or Active Speed Stall Control', Proc. IEEE Int. Electric Machines & Drives Conf., Antalya, Turkey, May 2007, pp. 1390-1395

[96] Ponte di Archimede International SpA, www.pontediarchimede.com, last accessed January 2008

[97] REpower Systems AG, www.repower.de, last accessed January 2008

[98] Roark, R.J., and Young, W.C.: 'Roark's Formulas for Stress and Strain' (McGraw-Hill International Editions, Singapore, 1989, 6th edn.), pp. 398-427

[99] as above, pp. 100-107

[100] as above, pp. 530-536

[101] as above, pp. 518

[102] as above, pp. 268

[103] Rovio, T., Vihrälä, H., Söderlund, L., Kriikka, J., Hyppönen, M.: 'Axial and radial flux generators in small-scale wind power production'. European Wind Energy Conf., Copenhagen, Denmark, 2-6 July 2001, pp. 1094-1097

[104] Salter, S.H, Taylor, J.R.M., and Caldwell, N.J.: 'Power conversion mechanisms for wave energy', *IMechE Proc. Part M*, 2002, **216**, pp. 1-27

[105] ScanWind Group AS, www.scanwind.com, last accessed January 2008

[106] Scottish Executive, 'Securing a Renewable Future: Scotland's Renewable Energy', The Stationary Office, ISBN 0 7559 0766 3, Edinburgh, March 2003

[107] Scottish Executive, 'Matching Renewable Electricity Generation With Demand', April 2006, available at www.scotland.gov.uk/Publications/2006/04/24110728/0 last accessed January 2008

[108] Scottish Renewables Forum, *Review*, **32**, November 2006, available at http://www.scottishrenewables.com/MultimediaGallery/aeeb2c12-2406-47e1-977e-67518467f39b.pdf last accessed January 2008

[109] Siegfriedsen, S., and Böhmeke, G.: 'Multibrid technology a significant step to multi-megawatt wind turbines', *Wind Energy*, **1**, (2), pp. 89-100

[110] Söderlund, L., Eriksson, J-T., Salonen, J., Vihriälä, H., and Perälä, R.: 'A permanent-magnet generator for wind power applications', *IEEE Trans. on Magn.*, 1996, **32**, (4), pp. 2389-2392

[111] Söderlund, L., Koski, A., Vihriälä, H., Eriksson, J.-T., and Perälä, R.: 'Design of an axial flux permanent magnet wind power generator'. IEE 8th Int. Conf. on Electr. Mach. and Drives (EMD), Cambridge, UK, 1997, Conf. Publ. no. 444, pp. 224-228

[112] Söderlund, L., and Perälä, R.: 'Comparison of direct driven axial and radial flux permanent magnet generators for wind power applications'. Proc. of 15th Int. Conf. on Magnet Technology, Beijing, China, Oct. 20-24, 1997, **2**, pp. 940-943

[113] Spooner, E., and Chalmers, B.J.: '"TORUS": A slotless, toroidal-stator, permanent-magnet generator', *IEE Proc. B*, 1992, **139**, (6), pp. 497-506

[114] Spooner, E., and Williamson, A.: 'Modular, permanent-magnet wind-turbine generators'. Conf. Rec. of the 1996 IEEE Ind. Appl. Conf. 31st IAS Annual Meeting, San Diego, CA, USA, 1996, **1**, pp. 497-502

[115] Spooner, E., Williamson, A.C., and Catto, G.: 'Modular design of permanent-magnet generators for wind turbines', *IEE Proc. Electr. Power Appl.*, 1996, **143**, (5), pp. 388-395

[116] Spooner, E. and Williamson, A.C.: 'Parasitic losses in modular permanent-magnet generators', *IEE Proc. Electr. Power Appl.*, 1998, **145**, (6), pp. 485-496

[117] Spooner, E. and Mueller, M.A.: 'Comparative study of linear generators and hydraulic systems for wave energy converters', ETSU V/06/00189/REP, DTI/Pub URN 01/783, University of Durham, School of Engineering, 2001

[118] Spooner, E.: 'Spoked lightweight machine (SLiM) for direct drive wind energy converters'. IEE Sem. on Electr. Aspects of Offshore Renewable Energy Systems, NaREC, Blyth, Northumberland, UK, 2004

[119] Spooner, E., Gordon, P., Bumby, J.R., and French, C.D.: 'Lightweight ironless-stator PM generators for direct-drive wind turbines'. *IEE Proc. Electr. Power Appl.*, 2005, **152**, (1), pp. 17-26

[120] Sustainable Development Commission: 'Wind Power in the UK', available at www.sd-commission.org.uk/publications/downloads/Wind_Energy-NovRev2005.pdf last accessed January 2008

[121] Tavner, P.J. and Spooner, E.: 'Light structures for large low-speed machines for direct-drive applications'. Proc. XVII Int. Conf. on Electrical Machines ICEM 2006, Chania, Crete, Sep. 2006

[122] Thorpe, T.W.: 'A brief review of wave energy', DTI Report, ETSU-R120, May 1999

[123] www.upwind.eu/fileadmin/ewea_documents/documents/press_releases/2006/0411-Upwind.pdf, last accessed January 2008

[124] Vector Fields, www.vectorfields.com, last accessed January 2008

[125] VENSYS Energy AG, www.vensys.de, last accessed January 2008

[126] Versteegh, C.J.A.: 'Low speed direct drive PM generator for application in the Zephyros Z72 wind turbine'. IEE Seminar on Electr. Aspects of Offshore Renewable Energy Systems, NaREC, Blyth, Northumberland, UK, 2004

[127] Vestas Wind Systems A/S, www.vestas.com, last accessed January 2008

[128] Vihriälä, H., Perälä, R., Söderlund, L., Eriksson, J.-T.: 'Reducing costs of wind power with a gearless permanent-magnet generator'. Proc. of the European Wind Energy Association (EWEC) Special Topic Conf.: The Economics of Wind Energy, 5-7 September 1995, Helsinki, Finland, pp. 225-229

[129] Vilsbøll, N., Pinegin, A., Goussarov, D., and Bugge, J.: 'The experience of designing and testing a 20kW multi pole permanent magnet generator for wind turbines', *DEWI Magazine*, Nr. 9, August 1996, pp. 74-83

[130] Vizireanu, D., Kestelyn, X., Brisset, S., Brochet, P., Milet, Y., and Laloy, D.: 'Polyphased modular direct-drive wind turbine generator', Proc. European Conf. on Power Electronics and Applications, 11-15 Sep. 2005, Dresden, 2005

[131] Voith WinDrive, www.voithturbo.com, last accessed January 2008

[132] Wang, R.-J., Kamper, M.J., VanderWesthuizen, K., and Gieras, J.F.: 'Optimal design of a coreless stator axial flux permanent-magnet generator', *IEEE Trans. on Magn.*, 2005, **141**, (1), pp. 55-64

[133] Wave Dragon, www.wavedragon.net, last accessed January 2008

[134] Wavegen, www.wavegen.co.uk, last accessed January 2008

[135] WaveNet: 'Results from the work of the European Thematic Network on Wave Energy', Report ERK5-CT-1999-20001, March 2003, available at www.wave-energy.net/Library/WaveNet%20Full%20Report(11.1).pdf last accessed January 2008

[136] Weh, H., Hoffmann, H., and Landrath, J.: 'New permanent magnet excited synchronous machine with high efficiency at low speeds'. Proc. of the Int. Conf. on Electrical Machines, Pisa, Italy, Sep. 1988, pp. 35-40

[137] Winwind Oy, www.winwind.fi, last accessed January 2008

Appendix A

Flat circular plates

Flat circular plate constants

$$C_1 = \tfrac{1+\nu}{2}\left(\tfrac{b}{a}\right)\ln\left(\tfrac{a}{b}\right) + \tfrac{1-\nu}{4}\left(\tfrac{a}{b} - \tfrac{b}{a}\right)$$

$$C_2 = \tfrac{1}{4}\left[1 - \left(\tfrac{b}{a}\right)^2\left(1 + 2\ln\left(\tfrac{a}{b}\right)\right)\right]$$

$$C_3 = \tfrac{b}{4a}\left\{\left[\left(\tfrac{b}{a}\right)^2 + 1\right]\ln\left(\tfrac{a}{b}\right) + \left(\tfrac{b}{a}\right)^2 - 1\right\}$$

$$C_4 = \tfrac{1}{2}\left[(1+\nu)\tfrac{b}{a} + (1-\nu)\tfrac{a}{b}\right]$$

$$C_5 = \tfrac{1}{2}\left[1 - \left(\tfrac{b}{a}\right)^2\right]$$

$$C_6 = \tfrac{b}{4a}\left[\left(\tfrac{b}{a}\right)^2 - 1 + 2\ln\tfrac{a}{b}\right]$$

$$C_7 = \tfrac{1}{2}\left(1+\nu^2\right)\left(\tfrac{a}{b} - \tfrac{b}{a}\right)$$

$$C_8 = \tfrac{1}{2}\left[1 + \nu + (1-\nu)\left(\tfrac{b}{a}\right)^2\right]$$

$$C_9 = \tfrac{b}{a}\left\{\tfrac{1+\nu}{2}\ln\left(\tfrac{a}{b}\right) + \tfrac{1-\nu}{4}\left[1 - \left(\tfrac{b}{a}\right)^2\right]\right\}$$

Flat circular plate loading constants

$$L_{11} = \tfrac{1}{64}\left\{1 + 4\left(\tfrac{r_o}{a}\right)^2 - 5\left(\tfrac{r_o}{a}\right)^4 - 4\left(\tfrac{r_o}{a}\right)^2\left[2 + \left(\tfrac{r_o}{a}\right)^2\right]\ln\left(\tfrac{a}{r_o}\right)\right\}$$

$$L_{14} = \tfrac{1}{16}\left\{1 - \left(\tfrac{r_o}{a}\right)^4 - 4\left(\tfrac{r_o}{a}\right)^2\ln\left(\tfrac{a}{r_o}\right)\right\}$$

$$L_{17} = \tfrac{1}{4}\left\{1 - \tfrac{1-\nu}{4}\left[1 - \left(\tfrac{r_o}{a}\right)^4\right] - \left(\tfrac{r_o}{a}\right)^2\left[1 + (1+\nu)\ln\left(\tfrac{a}{r_o}\right)\right]\right\}$$

Cylindrical shells

Cylindrical shell functions

$$F_1 = \cosh(\lambda x)\cos(\lambda x)$$

$$F_2 = \cosh(\lambda x)\sin(\lambda x) + \sinh(\lambda x)\cos(\lambda x)$$

$$F_4 = \cosh(\lambda x)\sin(\lambda x) - \sinh(\lambda x)\cos(\lambda x)$$

$$F_{a4} = \cosh(\lambda\langle x-a\rangle)\sin(\lambda\langle x-a\rangle) - \sinh(\lambda\langle x-a\rangle)\cos(\lambda\langle x-a\rangle)$$

Cylindrical shell constants

$$\lambda = \left[\frac{3\left(1-\nu^2\right)}{R^2t^2}\right]^{1/4}$$

$$D = \frac{Et^3}{12(1-\nu^2)}$$

$$C_2 = \cosh(\lambda l_s)\sin(\lambda l_s) + \sinh(\lambda l_s)\cos(\lambda l_s)$$

$$C_3 = \sinh(\lambda l_s)\sin(\lambda l_s)$$

$$C_4 = \cosh(\lambda l_s)\sin(\lambda l_s) - \sinh(\lambda l_s)\cos(\lambda l_s)$$

$$C_{11} = \sinh^2(\lambda l_s) - \sin^2(\lambda l_s)$$

$$C_{13} = \cosh(\lambda l_s)\sinh(\lambda l_s) - \cos(\lambda l_s)\sin(\lambda l_s)$$

$$C_{14} = \sinh^2(\lambda l_s) + \sin^2(\lambda l_s)$$

$$C_{a1} = \cosh(\lambda(l_s - a))\cos(\lambda(l_s - a))$$
$$= \cosh(\lambda l_s/2)\cos(\lambda l_s/2)$$

$$C_{a2} = \cosh(\lambda(l_s - a))\sin(\lambda(l_s - a)) + \sinh(\lambda(l_s - a))\cos(\lambda(l_s - a))$$
$$= \cosh(\lambda l_s/2)\sin(\lambda l_s/2) + \sinh(\lambda l_s/2)\cos(\lambda l_s/2)$$

$$K_2 = \cosh(\lambda l)\sin(\lambda l) + \sinh(\lambda l)\cos(\lambda l)$$

$$K_3 = \sinh(\lambda l)\sin(\lambda l)$$

$$K_4 = \cosh(\lambda l)\sin(\lambda l) - \sinh(\lambda l)\cos(\lambda l)$$

$$K_{11} = \sinh^2(\lambda l) - \sin^2(\lambda l)$$

$$K_{a1} = \cosh[\lambda(l-a)]\cos[\lambda(l-a)]$$

$$K_{a4} = \cosh[\lambda(l-a)]\sin[\lambda(l-a)] - \sinh[\lambda(l-a)]\cos[\lambda(l-a)]$$

Appendix B

The reader is referred to [93] for full details of the active modelling of permanent magnet synchronous generators in Chapter 5. A summary is included below.

The generator is modelled as the equivalent circuit and phasor diagrams shown in Figure B.1.

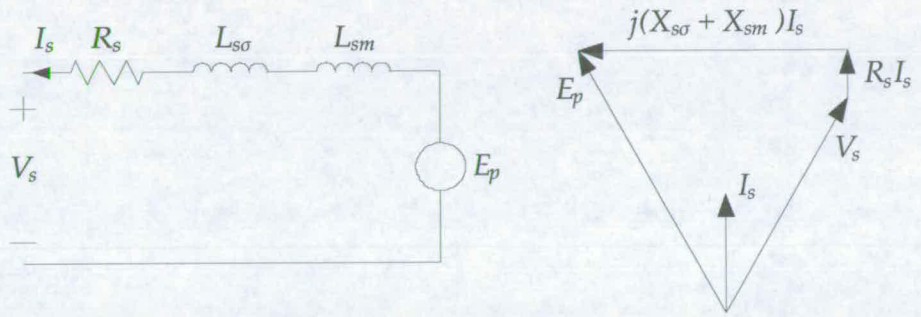

Figure B.1. Equivalent circuit of the permanent-magnet synchronous machine and the applied phasor diagram (taken from [93])

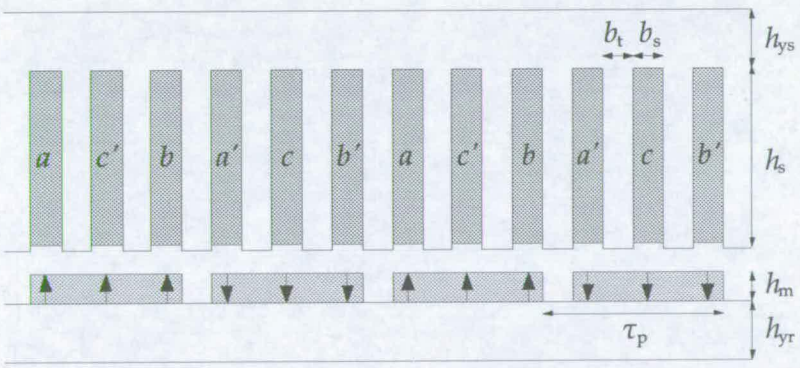

Figure B.2. Sketch of a cross section of four poles of a permanent magnet synchronous generator with full pitch winding (taken from [93])

The magnetising inductance is given as

$$L_{sm} = \frac{6\mu_0 l_s r_s (k_w N_s)^2}{p^2 g_{eff} \pi}. \qquad \text{(B.1)}$$

where l_s is the stack length in the axial distance, r_s is the stator radius, N_s is the number of turns of the phase winding, k_w is the winding factor, p is the number of pole pairs and g_{eff} is the effective airgap. For the permanent magnet machine,

$$g_{eff} = k_{sat} k_{Cs} g_1 . \tag{B.2}$$

The Carter factor for the stator slots is given by

$$k_{Cs} = \frac{\tau_s}{\tau_s - g_1 \gamma}, \tag{B.3}$$

$$g_1 = g + \frac{h_m}{\mu_r}, \tag{B.4}$$

$$\gamma = \frac{4}{\pi}\left(\frac{b_{so}}{2g_1} \arctan\left(\frac{b_{so}}{2g_1}\right) - \log\sqrt{1+\left(\frac{b_{so}}{2g_1}\right)^2} \right), \tag{B.5}$$

where τ_s is the slot pitch and b_{so} is the slot opening width.

The factor representing the reluctance of the iron in the magnetic circuit is

$$k_{sat} = 1 + \frac{1}{H_g g_{eff}} \int_0^{l_{Fe}} H_{Fe} dl_{Fe} , \tag{B.6}$$

where H_{Fe} is the magnetic field intensity in the iron, taken from the BH curve. The leakage inductance is made up of slot, end winding and airgap components:

$$L_{s\sigma} = L_{s\sigma_s} + L_{s\sigma_{ew}} + L_{s\sigma_g} \tag{B.7}$$

$$L_{s\sigma_s} = \frac{2\mu_0 l_s N_s^2}{pq}\left(\frac{h - 0.004}{3b_s} + \frac{0.004}{b_{so}} \right) \tag{B.8}$$

$$L_{s\sigma_{ew}} = \frac{\mu_0 N_s^2}{p} 1.2\left(\tfrac{2}{3}\tau_p + 0.01\right) \tag{B.9}$$

$$L_{s\sigma_g} = \frac{2\mu_0 l_s N_s^2}{pq} \frac{\frac{5(g+h_m)}{b_{so}}}{5 + \frac{4(g+h_m)}{b_{so}}}, \tag{B.10}$$

where q is the number if slots per pole per phase and τ_p is the pole pitch.

The flux density above a magnet in the airgap of a permanent magnet machine is

$$B_g = \frac{h_m}{\mu_r g_{eff}} B_r . \tag{B.11}$$

Using Fourier analysis, the fundamental space harmonic of this flux density is

$$\hat{B}_g = B_g \frac{4}{\pi} \sin\left(\frac{\pi b_p}{2\tau_p}\right), \tag{B.12}$$

where B_r is the remanent flux density of the magnets and b_p is the width of the magnets.

The no load voltage in stator winding is

$$E_p = \sqrt{2} k_w N_s \omega_m r_s l_s \hat{B}_g , \tag{B.13}$$

where ω_m is the mechanical angular speed of the rotor. The phase resistance is

$$R_s = \frac{\rho_{Cu} l_{Cu}}{A_{Cu}} , \tag{B.14}$$

where

$$l_{Cu} = N_s (2l_s + 4\tau_p), \tag{B.15}$$

$$A_{Cu} = \frac{pqk_{fill} b_{sav} h_s}{N_s} , \tag{B.16}$$

where k_{fill}, the fill factor is 60%, b_{sav} is the average slot width and h_s is the slot height.

Specific iron losses are

$$P_{Fe} = 2P_{Fe0h}\left(\frac{f_e}{f_0}\right)\left(\frac{\hat{B}_{Fe}}{\hat{B}_0}\right)^2 + 2P_{Fe0e}\left(\frac{f_e}{f_0}\right)^2\left(\frac{\hat{B}_{Fe}}{\hat{B}_0}\right)^2 \tag{B.17}$$

where f_e is the frequency of the field in the iron. P_{Fe0h} is the hysteresis loss per unit mass of laminations and P_{Fe0e} is the eddy current loss per unit mass of laminations at frequency f_0 and flux density B_0. (P_{Fe0h} = 2 W/kg and P_{Fe0e} = 0.5 W/kg for f_0 = 50 Hz and B_0 = 1.5 T).

In the slotted axial-flux machine, l_s is be replaced by (r_o-r_i). The calculation of the slotted machine no load voltage is based on the idea that flux density is limited to a certain value in the areas that saturation happens.

$k_{r,sat}$ is the ratio of the saturation radius to outer radius,

$$k_{r,sat} = \frac{mqb_s}{\tau_{po}}\left(\frac{B_{Fesat}}{B_{Fesat} - B_g}\right), \tag{B.18}$$

where B_{Fesat} is the saturation flux density of the iron.

If the teeth at the inner radius saturate but the teeth at the outer radius do not saturate (such as in Fig. B.3) then B_g in eqn. (B.13) is replaced by

$$\frac{A_{po}B_g + (A_{pi} - mq(r_{lo}k_{r,sat} - r_{li})b_s)B_{Fesat}}{A_p}, \tag{B.19}$$

where A_p is the area of one pole and

$$A_{po} = A_p\left(\frac{k_r}{k_{r,sat}}\right)^2, \tag{B.20}$$

$$A_{pi} = A_p - A_{po}. \tag{B.21}$$

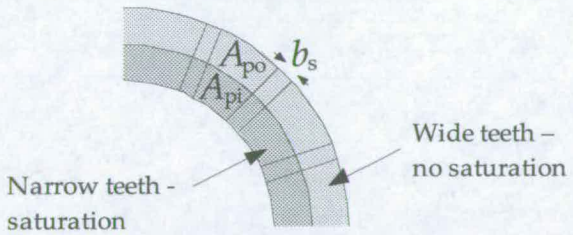

Figure B.3. Slotted axial-flux permanent magnet machine with saturation in teeth at inner radius and no saturation in outer teeth (taken from [41])

Appendix C

l_m/m	0.4	0.6	0.8	1.0	1.2
R_g/m	0.52	0.43	0.37	0.33	0.3
Poles	40	32	28	24	24
Coils	30	24	21	18	18
h_m/m	0.015	0.015	0.015	0.015	0.015
h_w/m	0.025	0.025	0.025	0.025	0.025
m_{cu}/kg	107	122	136	145	155
m_{PM}/kg	259	321	368	411	448
m_{st}/kg	1892	2910	4093	5516	7383
m_{tot}/kg	2258	3352	4595	6072	7985

Table C.1 100 kW, 77 rpm

l_m/m	0.4	0.6	0.8	1.0	1.2
R_g/m	1.04	0.85	0.74	0.66	0.60
Poles	80	64	56	52	44
Coils	60	48	42	39	33
h_m/m	0.016	0.016	0.015	0.015	0.015
h_w/m	0.025	0.025	0.025	0.025	0.025
m_{cu}/kg	214	241	267	289	310
m_{PM}/kg	535	656	737	821	896
m_{st}/kg	3530	5113	7076	9397	12025
m_{tot}/kg	4279	6010	8080	10508	13230

Table C.2 250 kW, 49 rpm

l_m/m	0.4	0.6	0.8	1.0	1.2
R_g/m	1.75	1.43	1.24	1.11	1.01
Poles	132	108	96	84	76
Coils	99	81	72	63	57
h_m/m	0.017	0.017	0.016	0.016	0.016
h_w/m	0.025	0.025	0.025	0.025	0.025
m_{cu}/kg	360	405	447	487	521
m_{PM}/kg	987	1174	1316	1473	1558
m_{st}/kg	5668	8076	10960	14327	17984
m_{tot}/kg	7015	9684	12723	16287	20063

Table C.3 500 kW, 34.5 rpm

l_m/m	0.4	0.6	0.8	1.0	1.2
R_g/m	2.37	1.94	1.68	1.5	1.37
Poles	180	148	128	112	104
Coils	135	111	96	84	78
h_m/m	0.019	0.018	0.017	0.017	0.017
h_w/m	0.025	0.025	0.025	0.025	0.025
m_{cu}/kg	488	550	606	658	707
m_{PM}/kg	1454	1689	1895	2053	2250
m_{st}/kg	7539	10611	14161	18274	23086
m_{tot}/kg	9481	12850	16662	20984	26042

Table C.3 750 kW, 28.1 rpm

l_m/m	0.4	0.6	0.8	1.0	1.2
R_g/m	2.94	2.40	2.08	1.86	1.70
Poles	224	184	160	140	132
Coils	168	138	120	105	99
h_m/m	0.020	0.019	0.018	0.018	0.017
h_w/m	0.025	0.025	0.025	0.025	0.025
m_{cu}/kg	605	680	751	815	877
m_{PM}/kg	1902	2210	2484	2700	2876
m_{st}/kg	9186	12814	17050	21856	27478
m_{tot}/kg	11693	15703	20285	25371	31232

Table C.5 1000 kW, 24.4 rpm

l_m/m	0.4	0.6	0.8	1.0	1.2
R_g/m	3.99	3.26	2.82	2.52	2.3
Poles	304	248	212	192	176
Coils	228	186	159	144	132
h_m/m	0.022	0.020	0.020	0.019	0.018
h_w/m	0.025	0.025	0.025	0.025	0.025
m_{cu}/kg	821	923	1018	1105	1187
m_{PM}/kg	2846	3245	3647	3867	4120
m_{st}/kg	12259	16850	22148	28170	35214
m_{tot}/kg	15926	21018	26814	33142	40521

Table C.6 1500 kW, 19.9 rpm

l_m/m	0.4	0.6	0.8	1.0	1.2
R_g/m	4.95	4.05	3.50	3.13	2.86
Poles	376	308	268	240	220
Coils	282	231	201	180	165
h_m/m	0.024	0.022	0.021	0.020	0.020
h_w/m	0.025	0.025	0.025	0.025	0.025
m_{cu}/kg	1018	1147	1263	1372	1476
m_{PM}/kg	3859	4333	4761	5192	5550
m_{st}/kg	15102	20602	26897	34103	42330
m_{tot}/kg	19979	26082	32921	40667	49356

Table C.7 2000 kW, 17.2 rpm

Appendix D

$$I_i = \frac{d^3}{36}\frac{b^2+4bc+c^2}{b+c}. \quad \text{(D.1)}$$

$$A = \tfrac{1}{2}d(b+c) \quad \text{(D.2)}$$

The pole pitch and c are kept constant, but the depth, d is varied according to

$$d = 0.05n \quad \text{(D.3)}$$

n	1	2	3	4	5	6	7	8
c/m	0.0875	0.0875	0.0875	0.0875	0.0875	0.0875	0.0875	0.0875
b/m	0.0962	0.101	0.105	0.109	0.114	0.118	0.122	0.127
d/m	0.05	0.075	0.1	0.125	0.15	0.17	0.2	0.225
A/m^2	0.0046	0.0071	0.0096	0.0123	0.0151	0.0180	0.0210	0.0241
I/m^4	9.56×10^{-7}	3.30×10^{-6}	8.00×10^{-6}	1.60×10^{-5}	2.81×10^{-5}	4.56×10^{-5}	6.93×10^{-5}	1.01×10^{-4}

Table D.1. Dimensions, area and second moment of area of trapezoids

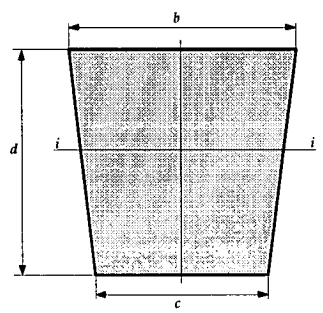

Figure D.1. Cross section of steel piece for calculating second moment of area

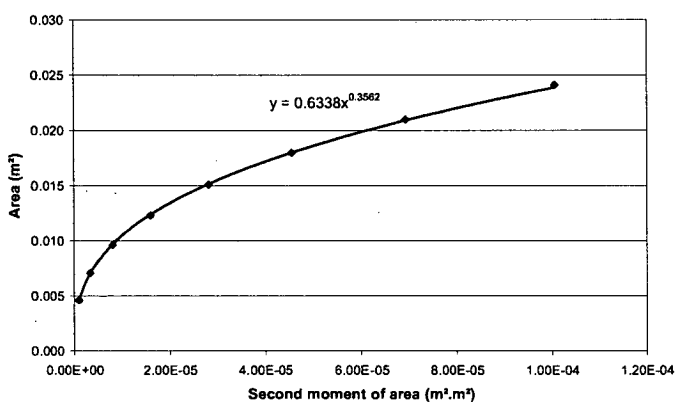

Figure D.2. Results from Table D.1. fitted with power trendline to find $A \propto I^{0.36}$